Mémoire

présenté

à l'Université de Nantes

pour obtenir une

Habilitation à Diriger des Recherches

spécialité: Géophysique interne

par

Hagay Amit

sujet:

Planetary dynamo features inferred from rapid core dynamics and mantle control

soutenance le 25/1/2018 devant le jury composé de

Mr Thierry Alboussière, Directeur de Recherche, Rapporteur
Mr Andy Biggin, Professeur, Examinateur
Mr Philippe Cardin, Directeur de Recherche, Rapporteur
Mr Alexandre Fournier, Professeur, Rapporteur
Mr Benoit Langlais, Directeur de Recherche, Examinateur

February 5, 2018

Acknowledgements

Since HDR is primarily about the right to mentor students, first I thank my students. I feel fortunate that I had the opportunity to work with competent, motivated and eager to learn students. It requires some courage to take a foreigner as an advisor...

I thank Benoit Langlais and Gaël Choblet, my closest collaborators in LPG. I thank numerous collaborators outside LPG. In France I thank Julien Aubert and Gauthier Hulot (IPGP, Paris) and to Julien Monteux (LMV, Clermont Ferrand). Outside France I thank Uli Christensen (Max-Planck, Göttingen, Germany), Alexandra Pais (University of Coimbra, Portugal), Katia Pinheiro (ON, Rio de Janeiro, Brazil) and Gelvam Hartmann and Ricardo Trinidade (USP, São Paulo, Brazil).

Special thanks to my family. To my wife Beatriz Funatsu and my son Eder – no way I could have done any of this without you! I thank my parents, brother and sister in Israel – my core. I also thank my friends along the way – from Israel, US and France.

Finally, I am grateful to my Ph.D. advisor and my main collaborator until today, Peter Olson. Peter is a huge inspiration to me, scientifically and personally. While I cannot give my students Peter's scientific knowledge, I try to give them the endless attention and patience that he devoted to me when I was a student.

Résumé

Les champs magnétiques planétaires sont générés par l'effet dynamo dans leur intérieurs profonds. Dans le cas de planètes telluriques ces dynamos proviennent des mouvements convectifs dans les noyaux extérieurs de métal liquide. Les mesures de champs magnétiques planétaires peuvent donc fournir des informations vitales sur la dynamique, structure interne et évolution des planétes.

Le champ géomagnétique varie sur différentes échelles de temps. Les échelles de temps les plus fondamentales de la dynamique du noyau sont le temps caractéristique d'advection magnétique de $\sim$60 yr et le temps caractéristique de diffusion magnétique de $\sim$30 kyr (e.g. Holme, 2007). Les observations révèlent plusieurs échelles de temps supplémentaires, depuis changements abrupts appelés secousses géomagnétiques (ou "jerks") qui se produisent pendant $\sim$1-2 yr (Alexandrescu et al., 1996), à la durée des inversions de $\sim$5-10 kyr, jusqu'à durée des superchrons de 40 Myr (e.g. Merrill et al., 1998).

Ma recherche couvre diverses échelles de temps de la dynamique du noyau. La dynamique rapid du noyau, caractérise par des échelles de temps de 10s à 100s yr, sont étudiés par l'analyse de modèles de la variation séculaire géomagnétique (SV). Ces études comprennent des inversions de vitesse au sommet de noyau et des déductions additionelles de la SV géomagnétique. Parce que le champ géomagnétique est dominé par sa composante dipolaire, une implémentation spéciale implique l'étude les changements du dipôle. Sur échelles de temps millénaires, la dynamique du noyau est étudiée par l'analyse des taches de flux intenses qui apparaissent dans les modèles de champs archéomagnétiques. Structures persistant sur des périodes de Myr sont explorées en invoquant le contrôle de manteau sur les dynamos planétaires. Dans ces études, différents modèles de flux de chaleur hétérogène à la frontière noyau-manteau (CMB) sont imposées à la limite extérieure de simulations numériques de dynamo pour reproduire les observations liées aux dynamos de la Terre, Mars et Mercure. Enfin, sur la plus longue échelle de temps 100s Myr, la fréquence variable de inversions paléomagnétiques est modélisée en utilisant des dynamos numériques avec évolution du flux de chaleur à la CMB.

L'application la plus commune des modèles de champs et SV géomagnétiques est leur inversion pour obtenir la vitesse au sommet du noyau (e.g. Hulot et al., 2002; Holme and Olsen, 2006). Nous avons introduit une nouvelle méthode et une nouvelle hypothèse physique pour en déduire la vitesse au sommet du noyau. Dans notre inversion nous supposons un écoulement hélicoïdal basé sur des résultats de dynamos numériques (Olson et al., 2002), quelques exemples analytiques (Amit et Olson, 2004) et le besoin fondamental d'une fort hélicité pour soutenir une dynamo (e.g. Moffatt, 1978). Ces modèles de vitesse ont été utilisés pour diverses applications, notamment la décomposition de l'écoulement en une part correspondant à la moyenne temporelle et une part dépendant du temps. La part liée à la moyenne temporelle a été interpréte en termes de couplage thermique noyau-manteau à long terme, tandis que la partie dépendant du temps a été interpréte en termes d'échange de moment angulaire entre le noyau et le

manteau (Amit et Olson, 2006). Nous avons également proposé un modèle de diffusion magnétique basé sur des dynamos numériques (Amit et Christensen, 2008) qui permet de ne pas avoir recours à l'hypothèse communément formulée de flux gelé ("frozen flux", Roberts and Scott, 1965). Dans le cadre de la quasi-géostrophie (Pais and Jault, 2008; Gillet et al., 2009), nous avons développé une théorie qui permet de relier les composants toroïdale et poloïdale du champ de vitesse au sommet du noyau et produit une comparaison avec l'hypothèse de géostrophie tangentielle (LeMouël, 1984) fréquemment utilisée jusqu'à présent en termes de conservation de la masse, non-unicité et symétrie équatoriale du champ de vitesse inversé à partir de la SV (Amit et Pais, 2013).

Diverses incertitudes inhérentes aux inversions pour obtenir le vitesse au sommet du noyau à partir de la SV géomagnétique limitent la teneur de leur interprétation (les revues de Bloxham and Jackson, 1991; Holme, 2007). Il est donc utile d'envisager des façons alternatives de déduire les propriétés de la dynamique de noyau à partir de la SV géomagnétique. Par exemple, l'amplitude de la vitesse au sommet du noyau peut être évaluée d'information sur les interactions champ-vitesse (Finlay et Amit, 2011). Des études d'échelle régional peuvent révéler la signature locale de upwelling/downwelling au sommet du noyau (Olson and Aurnou, 1999; Chulliat et al., 2010). L'analyse de la SV associée aux taches intenses de flux géomagnétiques peut indiquer l'existence d'un écoulement poloïdal au sommet du noyau ainsi renseigner sur l'état convectif de la géodynamo (Amit, 2014).

Nous avons développé une théorie pour calculer la distribution spatiale des sources advectives à changements du dipôle. En combinant des modèles de champs et nos modèles de vitesse hélicoïdale, cette théorie a été mis en œuvre pour étudier la diminution historique de l'intensité du dipôle (Olsen et Amit, 2006). Notre théorie a récemment été revisite par (Finlay et al., 2016). En combinant des modèles de champs géomagnétique par satellite et un système d'assimilation de données pour inverser la SV pour la vitesse au sommet du noyau (Aubert et al., 2013), Finlay et al. (2016) ont corroboré nos principaux résultats malgré l'utilisation de modèles distinctifs de vitesse. Nous avons aussi mis en œuvre la théorie pour les contributions advectives à changements du dipôle équatorial pour identifier les sources et puits régionaux qui ont causés la récente diminution de l'inclinaison du dipôle (Amit et Olson, 2008).

Sur des échelles de temps millénaires, nous avons analysé les modèles de champs archéomagnétiques. Nous nous sommes concentrés sur les taches de flux intense qui peuvent être robustes même dans ces modèles à faible résolution. Nous avons démontré que les taches oscillent autour de positions préférées possiblement prescrites par l'hétérogénéité du manteau inférieur et présentent occasionnellement une dérive depuis une position prescrite vers une autre (Amit et al., 2011b), en accord avec la mobilité de taches dans les dynamos numériques avec flux de chaleur tomographique à limite extérieure (Amit et al., 2010a). Ces résultats suggèrent que le noyau externe est chaotique et fortement dépendant du temps, contrairement au scénario proposé de blocage de champ magnétique par l'hétérogénéité du manteau (Gubbins

et al., 2007; Willis et al., 2007). Néanmoins, selon nos résultats sur des échelles de temps millénaires, le contrôle du manteau fonctionne dans un sens statistique, i.e. l'hétérogénéité du manteau prescrit des positions préférés de downwellings (Gubbins, 2003) qui concentrent le flux magnétique dans ces régions plus qu'ailleurs (Olson and Christensen, 2002).

Le contrôle du manteau sur dynamos planétaires a été invoqué pour expliquer diverses observations liées au noyau (Amit et al., 2015a). En particulier, les écarts persistants de champs magnétiques planétaires et/ou des vitesse au noyau de axisymétrie ou de la symétrie équatoriale sont très probablement dues à des conditions limites hétérogènes. Nous avons démontré qu'un modèle de dynamo numérique avec flux de chaleur tomographique imposée sur le CMB peut reproduire plusieurs observations de géodynamo importantes (Aubert et al., 2008), y compris les positions des taches intenses de flux paléomagnétiques (Kelly and Gubbins, 1997), les positions des cyclones au sommet du noyau en moyenne temporelle (Amit et Olson, 2006) et la dichotomie hémisphérique est-ouest dans les propriétés sismiques de la graine (e.g. Tanaka and Hamaguchi, 1997). En revanche, plus récemment, Aubert et al. (2013) ont imposé un taux de croissance hétérogène de la graine (plutôt que l'obtenir comme résultat comme dans Aubert et al. 2008) pour récupérer la forte SV équatoriale et à la dérive vers l'ouest dans les basses latitudes de l'hémisphère Atlantique.

Une caractéristique du champ géomagnétique qui est difficile à obtenir à partir des dynamos numériques concerne les taches de flux intense observes aux basses latitudes (Jackson et al., 2000). Même avec une condition limite tomographique, ce problème reste parce que le Y_2^2 qui domine dans les modèles sismiques prescrit généralement des valeurs préférées de longitudes tandis que les effets de cylindre tangential (Christensen et al., 1998; Olson et al., 1999; Aurnou et al., 2003) fixent les taches intenses des latitudes d'environ 70°. Une solution possible pourrait être que les modèles tomographiques ne capturent pas de manière adéquate l'hétérogénéité thermique à la base du manteau. Nous avons examiné quelques scénarios de dynamique du manteau inférieur pour imposer des modèles alternatives de flux de chaleur à la CMB dans des dynamos numériques. Ces modàles prennent compte des anomalies linéaires chaudes (Amit et Choblet, 2012) ou bien isolent la composante thermique par le biais de la tomographie probabilistique (Amit et al., 2015b). Dans les deux cas, ces modèles permettent de mieux reproduire les taches de flux intenses de basse latitudes sur la CMB.

Sur des échelles de temps plus longues, un défi majeur reste à expliquer l'enorme variabilité de la fréquence des inversions paléomagnétique, y compris de très longs superchrons, périodes pendant lesquelles la polarité du champ reste inchangé sur 10s de Myr (Merrill et al., 1998). La durée des superchrons rappelle les échelles de temps de la convection dans le manteau, ce qui a conduit à proposer que la fréquence d'inversion paléomagnétique variable est entraînée par des changements dans la vigueur et/ou pattern de convection du manteau (Glatzmaier et al., 1999; Kutzner and Christensen, 2004; Olson

et al., 2010). Zhang and Zhong (2011) ont imposé l'histoire de la tectonique des plaques sur les modèles de convection du manteau pour évaluer le flux de chaleur à la CMB au cours des dernières 100s de Myr. Olson et al. (2013) ont imposé le flux de chaleur de CMB de Zhang and Zhong (2011) sur des dynamos numériques et comparé ces résultats avec les données paléomagnétiques. Le problème principal est que pendant le Cretaceous Normal Superchron (CNS) les vitesses de plaque sont grandes, donc la convection dans le manteau devrait être forte, de manière que le flux de chaleur à la CMB est probablement élevé pour cette période, entraînant une convection vigoureuse dans le noyau et une valeur élevée pour la fréquence d'inversion (Olson et al., 2013). Nous avons proposé que la dépendance temporelle de la hauteur de superplumes dans le manteau contrôle la fréquence d'inversion (Amit et Olson, 2015; Olson et Amit, 2015). Ce mécanisme peut être découplé de la vitesse du manteau associé avec les plaques sur la surface. Selon notre modèles de dynamo numérique la croissance et la decroissance des superplumes peut avoir induit la fin et initié les superchrons, respectivement.

La dichotomie hémisphérique dans le champ magnétique crustal de Mars a été modélisé en imposant un pattern de type Y_1^0 comme flux de chaleur à la CMB sur les dynamos numériques (Stanley et al., 2008). Nous avons élaboré et exploré une certaine gamme de paramètres de contrôle de la dynamo (Amit et al., 2011a). Nous avons également expliqué l'efficacité supérieure d'un pattern Y_1^0 de flux de chaleur à la CMB pour produire l'asymétrie magnétique nord-sud par rapport à un pattern Y_1^1 de flux de chaleur à la CMB pour produire une asymétrie magnétique est-ouest en termes de vitesse zonale dans les dynamos (Aubert, 2005). Ces résultats peuvent expliquer l'orientation de la dichotomie du champ crustal de Mars même si le panache du manteau n'était pas exactement polaire. Nous avons également proposé un scénario du manteau correspondant à un chauffage par un impact géant (Monteux et al., 2015). Nous avons montré que les modèles de flux de chaleur à la CMB représentant l'effet d'un impact géant sont plus efficaces que les modèles de degré-1 pour produire la dichotomie magnétique pour une forçage horizontal donné.

Il est évident que l'objectif principal de ce document est d'obtenir l'autorisation oficielle d'encadrer les étudiants. Par conséquent, je souligne dans les paragraphs suivants les travaux des étudiants que j'ai déjà encadré. À titre d'exemples je me concentre sur les étudiants pour lesquels j'ai été l'encadrant principal.

Ludovic Huguet a développé une théorie permettant suivre le transfert d'énergie d'un degré d'harmonique sphérique à un autre. Il a combiné des modèles de champ géomagnétique et des modèles de vitesse au sommet du noyau pour obtenir des matrices détaillées décrivant le transfert d'énergie magnétique à magnétique. Son travail a des implications pour les changements de dipôle et quant au rôle de la turbulence dans la SV du champ à grande échelle dans le noyau. Un premier article résumant le travail de Master 2 de Ludovic a été publié (Huguet et Amit, 2012). Plus tard, Ludovic a suivi avec un doc-

torat à l'ENS Lyon. En parallèle à son travail de doctorat, il a poursuivi ses travaux au sujet du transfert d'énergie. Avec son directeur de thèse Thierry Alboussière nous avons affiné la théorie pour décrire les transferts magnétique à magnétique et cinétique à magnétique (Huguet et al., sous presse). Ce travail a des répercussions sur l'état convectif de la partie supérieure du noyau. Certaines études de physique minérale font valoir que la conductivité thermique du noyau externe est plus grande que précédemment pensé et donc la partie supérieure du noyau doit être stratifiée (par exemple Pozzo et al., 2012), tandis que d'autres études trouvent des valeurs de conductivité thermique plus faibles, compatibles avec la convection du noyau entier (Konôpková et al., 2016). L'article de Huguet et al. (sous presse) apporte des contraintes géomagnétiques au débat sur l'état convectif de noyau supérieur. Actuellement Ludovic continue sa carrière academique en tant que postdoc dans la Case Western Reserve University, Cleveland, États-Unis.

J'ai initié une collaboration avec le Brésil qui me permet d'accueillir les étudiants compétents pour travailler sur mes sujets de recherche. Filipe Terra-Nova, un étudiant de doctorat en LPG, a développé des algorithmes pour identifier et suivre les taches de flux géomagnétiques inverses (RFPs). Il a appliqué ses algorithmes aux modèles de champ archéomagnétiques pour déduire la dynamique de noyau sur des échelles de temps millénaires. Dans un premier article (Terra-Nova et al., 2015), Filipe a présenté ses algorithmes, a examiné le rôle des RFPs dans les changements de dipôle axial et effectué quelques tests de robustesse basés sur le filtrage. Dans un second article (Terra-Nova et al., 2016), Filipe a analysé 20 modèles de champ archéomagnétiques de divers auteurs, y compris l'échantillonnage d'ensembles de modèles (Korte et al., 2009; Korte and Constable, 2011; Licht et al., 2013; Nilsson et al., 2014). Cela a permis un test beaucoup plus rigoureux de la robustesse de l'existence et de la mobilité des RFPs. Le comportement des RFPs dans les modèles de champs archéomagnétiques a été comparé avec le modèle le plus fiable de champ historique (Jackson et al., 2000) pour sélectionner un modèle de champ archéomagnétique préféré. Ce modèle préféré a été analysé en termes de contrôle du manteau sur le géodynamo et d'orientation des lignes du champ toroïdal dans le noyau. En outre, nous avons calculé une limite supérieure pour l'épaisseur de la couche limite magnétique en dessous de la CMB, qui est compatible avec des estimations indépendantes de dynamos numériques (Amit et Christensen, 2008) et modèles de champ géomagnétique par satellite (Chulliat and Olsen, 2010). Ces deux articles (Terra-Nova et al., 2015, 2016) ont été publiés alors que Filipe commence juste la deuxième année de son doctorat.

La thèse de Diego Peña est rendu plus complexe par le fait qu'il est un étudiant d'Observatério Nacional (ON) Brésil. Diego a visité le LPG pour des périodes de $\sim$3 mois par an et nous communiquons régulièrement par mail et skype. Malgré les difficultés géographiques Diego a déjà publié un article (Peña et al., 2016) sur effets d'étirement du champ magnétique au sommet de la coquille des dynamos numériques. Dans cet article, nous avons constaté que la rôle de l'étirement dans la SV est plus grand

que la vitesse poloïdale relative, en particulier au voisinage de régions de taches magnétique intenses. Les similitudes entre les morphologie de la SV dominée par l'étirement associées aux taches de flux intenses dans les modèles de dynamo et celles présentes au voisinage des taches géomagnétiques dans les observations (Amit, 2014) peut suggérer que la convection procède dans le noyau entier. Diego travaille actuellement sur un second article où nous examinons des effets de étirement magnétique en profondeur, notamment en mettant l'accent sur les racines profondes de taches de flux intenses sur le CMB.

Le travail de master de Maélie Coutelier a porté sur deux sujets relatifs à la dynamique rapide du noyau. Tout d'abord, nous avons proposé de nouvelles lois d'échelle pour les échelles de temps de la SV géomagnétique. Des études antérieures issues de modèles de champ géomagnétique et de dynamos numériques ont constaté que les échelles de temps de SV sont inversement proportionnelles au degré d'harmonique sphérique (Christensen and Tilgner, 2004; Lhuillier et al., 2011; Christensen et al., 2012). Nous avons montré que la même loi d'échelle est valable pour les sous-familles symétriques et asymétriques par rapport à l'equateur des échelles de temps de la SV. Ensuite, nous avons developpé de nouvelles expressions analytiques pour le couplage de vitesse toroïdale et poloidale dans le cadre d'une dynamique quasi-géostrophique du noyau (Pais and Jault, 2008; Gillet et al., 2009, 2011, 2015). Des études antérieures ont établi la relation pour un écoulement en forme de colonne sous l'hypothèse que la variation de l'écoulement axial le long d'une colonne axiale est linéaire (Amit et Olson, 2004; Amit et Pais, 2013). En relâchant cette contrainte, nous montrons que l'amplitude de ce couplage peut varier en fonction du profil de vitesse axiale dans la colomne. Ces deux articles sont en préparation.

Le document est présenté comme suit. Dans la section 2 je donne mon Curriculum Vitae incluant une liste complète des articles publiés par des journaux peer-reviewed. Dans la section 3, je décris mes axes principaux de recherche. Les perspectives de future recherche (la plupart déjà en cours) sont fournies dans la section 4. Enfin, cinq articles sélectionnés sont donnés dans les annexes. Tout au long du document, j'ai tenté de mettre en évidence le travail accompli par les étudiants.

Abstract

Planetary magnetic fields are generated by dynamo action in their deep interior. In the case of terrestrial planets these dynamos originate from convective motions in the metallic liquid outer cores. Measurements of planetary magnetic fields may therefore provide vital information on the planets' dynamics, interior and evolution.

The geomagnetic field varies on various timescales. The most fundamental timescales of core dynamics are the magnetic advection time of ~ 60 yr and the magnetic diffusion time of ~ 30 kyr (e.g. Holme, 2007). Observations reveal several additional timescales, from abrupt changes termed geomagnetic jerks that occur during $\sim 1-2$ yr (Alexandrescu et al., 1996), to duration of reversals of $\sim 5-10$ kyr, up to duration of superchrons of ~ 40 Myr (e.g. Merrill et al., 1998).

My research spans various core dynamics timescales. Rapid core dynamics characterized by decadal to centennial timescales are studied by analysis of geomagnetic secular variation (SV) models. These studies include core flow inversions and additional inferences from the geomagnetic SV. Because the geomagnetic field is dominated by its dipole component, a special implementation involves the study of dipole changes. Millennial timescale core dynamics is investigated by analysis of intense flux patches in archeomagnetic field models. Persistent features over periods of Myr are explored by invoking mantle control on planetary dynamos. In these studies various models of heterogeneous core-mantle boundary (CMB) heat flux are imposed on the outer boundary of numerical dynamo simulations to reproduce observations related to the dynamos of Earth, Mars and Mercury. Finally, on the longest timescale of 100s Myr, the variable frequency of paleomagnetic reversals is modeled using numerical dynamos with evolving CMB heat flux.

The most common application of geomagnetic field and SV models is their inversion for the flow at the top of the core (e.g. Hulot et al., 2002; Holme and Olsen, 2006). We introduced a new method and physical assumption to infer the core flow. In our inversions we assume helical flow based on results from numerical dynamos (Olson et al., 2002), some analytical examples (Amit and Olson, 2004) and the fundamental need for strong helicity to sustain a dynamo (e.g. Moffatt, 1978). These core flow models were used for various applications, most notably the decomposition of the flow to time-average and time-dependent parts. The time-average part was interpreted in terms of long-term thermal core-mantle coupling, while the time-dependent part was interpreted in terms of angular momentum exchange between the core and the mantle (Amit and Olson, 2006). We also proposed a model of magnetic diffusion based on numerical dynamos (Amit and Christensen, 2008) to remove the need for the commonly used assumption of frozen-flux (Roberts and Scott, 1965). In the quasi-geostrophic framework (Pais and Jault, 2008; Gillet et al., 2009), we developed the theory to relate toroidal and poloidal core flows and compared it with the previously used tangential geostrophy assumption (LeMouël, 1984) in terms of conservation

of mass, non-uniqueness and equatorial symmetry of SV inverted flows (Amit and Pais, 2013).

Various uncertainties inherent to core flow inversions from geomagnetic SV limit their interpretations (for reviews see Bloxham and Jackson, 1991; Holme, 2007). It is therefore worth considering alternative ways to infer core dynamics properties from the geomagnetic SV. For example, the magnitude of the core flow can be assessed based on information about field-flow interactions (Finlay and Amit, 2011). Regional scale studies may reveal local signature of core upwelling/downwelling (Olson and Aurnou, 1999; Chulliat et al., 2010). Analysis of the SV associated with intense geomagnetic flux patches may shed light on the existence of poloidal flow at the top of the core and the convective state of the geodynamo (Amit, 2014).

We developed a theory for mapping the advective contributions to dipole changes. Combining core field models and our helical flow models, this theory was implemented to study the historical decrease in the dipole intensity (Olsen and Amit, 2006). Our theory was recently revisited by Finlay et al. (2016). Combining satellite geomagnetic field models and a data assimilation scheme to invert for the core flow (Aubert et al., 2013), Finlay et al. (2016) corroborated our main results despite using distinctive core flow models. We also implement the theory to map the advective contributions to equatorial dipole changes in order to identify regional sources and sinks that led to the recent decrease of the dipole tilt (Amit and Olson, 2008).

On millennial timescales, we analyzed archeomagnetic field models. We focused on intense flux patches that may be robust even in these low resolution models. We demonstrated that the patches oscillate about preferred locations possibly prescribed by lower mantle heterogeneity while occasionally drift from one prescribed location to another (Amit et al., 2011b), in agreement with patches mobility behavior in numerical dynamos with tomographic outer boundary heat flux (Amit et al., 2010a). These results suggest that the outer core is chaotic and strongly time-dependent, in contrast to the proposed scenario of magnetic field locking to mantle heterogeneity (Gubbins et al., 2007; Willis et al., 2007). Nevertheless, according to our results on millennial timescales mantle control acts in a statistical sense, i.e. the mantle heterogeneity leads to preferred locations of flow downwellings (Gubbins, 2003) which concentrate magnetic flux in these regions more than elsewhere (Olson and Christensen, 2002).

Mantle control on planetary dynamos was invoked to explain various core related observations (Amit et al., 2015a). In particular persistent deviations of planetary magnetic fields and/or core flows from axisymmetry or from equatorial symmetry are most likely due to heterogeneous boundary conditions. We demonstrated that a numerical dynamo model with imposed tomographic outer boundary heat flux may reproduce several important geodynamo observations (Aubert et al., 2008), including the locations of intense paleomagnetic flux patches (Kelly and Gubbins, 1997), the locations of time-average cyclones at the top of the core (Amit and Olson, 2006) and the east-west hemispheric dichotomy in inner core

seismic properties (e.g. Tanaka and Hamaguchi, 1997). In contrast, more recently Aubert et al. (2013) imposed inner boundary heterogeneous growth rate (rather than obtaining it as a result as in Aubert et al., 2008) to recover the strong equatorial SV and westward drift in low-latitudes of the Atlantic hemisphere.

A feature of the geomagnetic field that is difficult to recover with numerical dynamos is the intense flux patches observed at low-latitudes (e.g. Jackson et al., 2000). Even with tomographic boundary conditions this problem remains because the dominant Y_2^2 seismic patterns typically prescribes preferred longitudes while tangent cylinder effects (Christensen et al., 1998; Olson et al., 1999; Aurnou et al., 2003) fixate the intense patches to about 70°. A possible solution could be that the tomographic models do not capture adequately the thermal heterogeneity at the base of the mantle. We examined some dynamical scenarios of the lower mantle to impose alternative CMB heat flux models on numerical dynamos. These models either account for sharp hot ridges (Amit and Choblet, 2012) or isolated the thermal component based on probabilistic tomography (Amit et al., 2015b), in both cases in order to reproduce low-latitudes intense flux patches on the CMB.

On longer timescales, a major challenge remains to explain the huge variability in paleomagnetic reversal frequency, including very long superchrons, periods in which the polarity of the field remain unchanged over 10s of Myr (Merrill et al., 1998). The duration of superchrons is reminiscent of mantle convection overturn, which led to argue that the variable paleomagnetic reversal frequency is driven by changes in mantle convection vigor and/or pattern (Glatzmaier et al., 1999; Kutzner and Christensen, 2004; Olson et al., 2010). Zhang and Zhong (2011) imposed plate tectonics history on mantle convection models to assess the CMB heat flux over the past 100s of Myr. Olson et al. (2013) imposed the time-dependent CMB heat flux of Zhang and Zhong (2011) on numerical dynamos and compared with the paleomagnetic record. The main problem is that during the Cretaceous Normal Superchron (CNS) plate speeds are large, hence mantle convection is expected to be strong, CMB heat flux is expected to be large, core convection is expected to be strong, and reversal frequency is expected to be large (Olson et al., 2013). We proposed that time-dependent superplumes height controls reversal frequency (Amit and Olson, 2015; Olson and Amit, 2015). This mechanism may be decoupled from the mantle flow associated with the surface plates. According to our numerical dynamo models growth and collapse of superplumes may have terminated and initiated superchrons, respectively.

The hemispheric dichotomy in the crustal magnetic field of Mars has been modeled by imposing a Y_1^0 pattern on the CMB heat flux of numerical dynamos (Stanley et al., 2008). We elaborated and explored some range of dynamo control parameters (Amit et al., 2011a). We also explained the higher efficiency of a Y_1^0 CMB heat flux pattern to produce north-south magnetic asymmetry compared to a Y_1^1 CMB heat flux pattern to produce east-west magnetic asymmetry in terms of the background zonal dynamo flow (Aubert, 2005). These findings may explain the orientation of the Martian crustal field dichotomy even if

the mantle plume was not exactly polar. We also proposed a more realistic mantle scenario corresponding to heating by a giant impact (Monteux et al., 2015). We showed that impact-driven CMB heat flux patterns are more efficient than degree-1 patterns in producing field dichotomy for a given horizontal forcing.

Obviously the main objective of this document is to obtain the permission to mentor students. Therefore I would like to highlight work of students that I have already been mentoring (non-officially of course). As examples I focus on students that I served as their main advisor.

Ludovic Huguet developed the theory to track energy transfer from one spherical harmonic degree to another. He combined geomagnetic field models and core flow models to obtain detailed matrices describing the magnetic to magnetic energy transfer. His work has implications to dipole changes and to the role of turbulence in the SV of the large-scale field in the core. A first paper summarizing Ludovic's Master 2 work was published (Huguet and Amit, 2012). Later Ludovic followed with a Ph.D. in ENS Lyon. In parallel to his Ph.D. work he continued to develop the topic of energy transfer. Together with his Ph.D. advisor Thierry Alboussière we refined the theory to depict the magnetic to magnetic and kinetic to magnetic energy transfers (Huguet et al., submitted). This work has implications for the convective state of the top of the core. Some mineral physics studies argue that the thermal conductivity of the outer core is larger than previously thought and therefore the top of the core must be stably stratified (e.g Pozzo et al., 2012), while other studies find lower thermal conductivity values consistent with whole core convection (Konôpková et al., 2016). Our study brings geomagnetic constraints to the debate on the convective state of the upper core. Currently Ludovic continues his academic career as a postdoc in Case Western Reserve University, Cleveland, USA.

I initiated a collaboration with Brazilian researchers which allowed me to welcome competent Brazilian students to work on my research topics. Filipe Terra-Nova, a Ph.D. student in LPG, developed algorithms to identify and track reversed flux patches (RFPs). He applied his algorithms to archeomagnetic field models to infer core dynamics on millennial timescales. In a first paper (Terra-Nova et al., 2015), Filipe introduced his algorithms, examined the role of RFPs in axial dipole changes and performed some robustness tests based on low-pass filtering. In a second paper (Terra-Nova et al., 2016), Filipe analyzed 20 archeomagnetic field models from various authors including sampling of ensembles of models (Korte et al., 2009; Korte and Constable, 2011; Licht et al., 2013; Nilsson et al., 2014). This allowed a much more rigorous robustness test for the existence and mobility of RFPs. The behavior of RFPs in the archeomagnetic field models was compared with the more reliable historical field model (Jackson et al., 2000) to select a preferred archeomagnetic field model. This preferred model was analyzed in terms of mantle control on the geodynamo and orientation of toroidal field lines in the core. In addition, we calculated an upper bound for the thickness of the magnetic boundary layer below the CMB, which is consistent with independent estimates from numerical dynamos (Amit and Christensen, 2008) and satellite geomagnetic

field models (Chulliat and Olsen, 2010). These two papers (Terra-Nova et al., 2015, 2016) were published while Filipe is just starting the second year of his Ph.D.

The Ph.D. of Diego Peña is challenging because he is a student of the Observatório Nacional (ON) Brazil. Diego has been visting LPG for periods of $\sim$ 3 months per year and we communicate regularly by emails and skype. Despite the geographical difficulties Diego has already published a paper (Peña et al., 2016) about magnetic field stretching effects at the top of the shell of numerical dynamos. In this paper we found that the role of stretching in the SV is larger than the relative poloidal flow, in particular near regions of intense magnetic flux patches. Similarities between the stretching dominated SV patterns associated with intense flux patches in the dynamo models and geomagnetic SV patterns near observed patches (Amit, 2014) may suggest whole core convection. Diego is currently working on a second paper where we examine stretching effects at depth, in particular focusing on the deep roots of intense flux patches on the CMB.

The Master work of Maélie Coutelier covered two topics relevant to rapid core dynamics. First, we proposed new scaling laws for the geomagnetic SV timescales. Previous studies of geomagnetic field models and numerical dynamos found that the SV timescales are inversely proportional to the spherical harmonic degree (Christensen and Tilgner, 2004; Lhuillier et al., 2011; Christensen et al., 2012). We showed that the same scaling law holds for the equatorially-symmetric and asymmetric sub-families of the SV timescales. Second, we derived new analytical expressions for toroidal-poloidal flow coupling in the framework of quasi-geostrophic core flow (Pais and Jault, 2008; Gillet et al., 2009, 2011, 2015). Previous studies established the columnar flow relation under the assumption that the variation of the axial flow along an axial column is linear (Amit and Olson, 2004; Amit and Pais, 2013). By relaxing this constraint we show that the magnitude of this coupling may vary depending on the particular columnar profile of the axial flow. These two papers are in preparation.

The document is outlined as follows. In section to I give Curriculum Vitae including a complete list of peer-reviewed published papers. In section 3 I describe my main research axes. Future research perspectives (mostly already ongoing) are provided in section 4. Finally, five selected papers are given in the Appendices. Throughout the document I tried to highlight work done by students.

Contents

Chapter 1

Foreword

I wish to mention two personal issues. The first concerns the multiple languages that affect my life, which I will use to defend my choice of writing this document in English (rather than in French as may be expected). The second is related to my educational philosophy, which is not necessarily ideal, but stems from my positive experience as a student.

1.1 Languages...

I live in four languages. My maternal language is Hebrew. I speak to my family and to my friends in Israel in Hebrew. I speak to me four-years old son in Hebrew which is his preferred language (despite being born and raised here in France). The majority of books I read, music I listen to, crosswords I solve, is all in Hebrew.

My wife is Brazilian. I hear her speaking to her family and friends in Portuguese. I hear her speaking to our son in Portuguese which he is fluent in too. In addition, in recent years I have been mentoring several Brazilian students and I have been collaborating with several Brazilian colleagues.

We all write papers in English and present our results in conferences and workshops (talks, posters) in English. For me science is most natural in English. Apart from that, I met my wife during my thesis in US and we speak between us English.

Finally, I live and work in France for the past 11 years. French is a must in order to have the minimal integration in society. Upon arriving to France I took some intensive French courses. However, in Paris my colleagues spoke English with me and my social circle was very international, which slowed my progress in French. Since arriving to Nantes I feel that I am advancing. I gave short Master courses in French and I had some French students with which I mostly interacted in French. Still my grammar is poor and I cannot really write French, but I survive.

For all these reasons I chose to write this document in English.

1.2 Educational philosophy

There are two endmember educational philosophies. The first approach is to give the student as much time and guidance as possible. In this approach the student my gain a lot of knowledge from his/her mentor but he/she will not develop independent thinking. The second approach is to teach how to swim by throwing the student to deep water. In this approach will develop independent thinking but he/she will not gain a lot of knowledge from his/her mentor.

In both my Master and Ph.D. I had advisors that devoted plenty of time to explain to me all possible aspects of research. In particular I spend hours on daily basis discussing with my Ph.D. advisor Peter Olson. These discussions gave me endless ideas which I use up until today.

I believe that there is no better endmember educational philosophy, and the right approach may be student-dependent. However, I am so grateful to Peter Olson for everything he gave me, that I feel the need to give my students similar attention and guidance.

Chapter 2

Curriculum Vitae (valid for August 2017)

2.1 Education

- 10/2005-9/2008: Postdoc at Equipe de Géomagnétisme, Institut de Physique du Globe de Paris, France.
- 1/2001-9/2005: Ph.D. in Geophysics, The Johns Hopkins University, USA. Thesis: Imaging core flow from geomagnetic secular variation: Consequences for core-mantle interactions and geomagnetic dipole moment changes.
- 10/1998-12/2000: M.Sc. in Hydrology, The Hebrew University of Jerusalem, Israel. Thesis: The interpretation of hydrographs from springs and wells.
- 10/1994-5/1998: B.Sc. in Physics and Atmospheric Sciences, The Hebrew University of Jerusalem, Israel.

2.2 Research experience

- 10/2006-9/2008: Postdoc at Equipe de Géomagnétisme, Institut de Physique du Globe de Paris, Marie Curie Intra-European Fellowship FP6.
- 10/2005-9/2006: Postdoc at Equipe de Géomagnétisme, Institut de Physique du Globe de Paris, departamental grants.

I was mentored by the following advisors:

- Gauthier Hulot, Institut de Physique du globe de Paris: Postdoc advisor 2005-2008.

- Peter L. Olson, The Johns Hopkins University: Ph.D. advisor 2001-2005.
- Vladimir Lyakhovsky, Abraham Starinsky, Amitai Katz, The Hebrew University: M.Sc. advisors 1999-2000.

2.3 Grants and awards

- EPS excellent reviewer 2013.
- Bourse de Programme National de Planétologie - PNP, 2012.
- Marie Curie European Reintegration Grant - FP7, 2008 (which I declined in favor of my current permanent CNRS position).
- Marie Curie Intra-European Fellowship - FP6, 2006.
- Bourse de recherche post-doctorale - CNES, 2006 (which I declined in favor of the Marie Curie grant mentioned above).
- Krieger School of Arts and Sciences Fellowship, 2002.

2.4 Teaching

I served as a teaching assistant in the following courses:

- Natural Catastrophes (Johns Hopkins University 2004).
- Guided Tour of the Planets (Johns Hopkins University 2002).
- The Planet Earth (Johns Hopkins University 2001 & 2003).
- Groundwater (Hebrew University Jerusalem 2000).
- Geophysical methods (Hebrew University Jerusalem 1999 & 2000).

I taught the following courses:

- Fluid dynamics and dynamo action in planetary cores (LPG, for Master 2 in 2010; for Master 1 in 2011 and 2012).

2.5 Mentoring

- Co-supervisor of the Ph.D. thesis of Joana Oliveira, LPG 2012-2015, defended in Nantes University on 1/4/2015. The main supervisor was Benoit Langlais (LPG), my part in this thesis was 30%. Thesis: The magnetic field of Mercury as measured by the MESSENGER spacecraft. A peer-reviewed paper was published based on this Ph.D. work (Oliveira et al., 2015). Joana followed to a postdoc in IPGP.

- Co-supervisor of the Ph.D. thesis of Diana Saturnino, LPG 2013-2015, defended in Nantes University on 30/11/2015. The main supervisor was Benoit Langlais (LPG), my part in this thesis was 30%. Thesis: Describing temporal variations of the geomagnetic field using a modified virtual observatory scheme: application to Swarm measurements. Diana followed to a postdoc in DTU, Denmark.
- Supervisor of the Ph.D. thesis of Diego Peña, Observatório Nacional (ON) 2014-2017, defended in ON Rio de Janeiro Brazil on 17/2/2017. I am the co-supervisor together with Katia Pinheiro (ON, Brazil), my part in this thesis is 70%. Thesis: Magnetic field stretching at the top of Earth's core. A peer-reviewed paper was published based on this Ph.D. work (Peña et al., 2016).
- Supervisor of the Ph.D. thesis of Filipe Terra-Nova, LPG 2015-2018. I am the co-supervisor together with Gaël Choblet (LPG), my part in this thesis is 70%. Three peer-reviewed papers have already been published based on this Ph.D. work (Terra-Nova et al., 2015, 2016, 2017).
- Supervisor of the Master 2 of Ludovic Huguet, LPG 2011. Thesis: Transfert d'energie magnétique dans le noyau de la Terre. Two peer-reviewed papers were published based on this Master work (Huguet and Amit, 2012; Hugeut et al., 2016). Ludovic followed to a Ph.D. in Lyon and later to a postdoc at Case Western Reserve University, Cleveland, USA.
- Supervisor of the Master 1 of Maélie Coutelier, LPG 2015. Thesis: Geomagnetic secular variation timescales under rapid rotation constraints.
- Co-supervisor of the B.Sc. internship of Hugo Larnier, LPG 2013.

2.6 Service as a reviewer

- International journals
  - Geophysical Journal International.
  - Physics of the Earth and Planetary Interiors.
  - Earth Planets Space.
  - Proceedings of the National Academy of Sciences.
  - Journal of Geophysical Research.
  - Nature Geosciences.
  - Icarus.
  - Earth and Planetary Science Letters.
  - Geophysical Research Letters.
  - Progress in Earth and Planetary Sciences.
  - Nature Communications.
  - Journal of Atmospheric and Solar Physics.

- Grant proposals
  - PNP (Programme National de Planétologie).
  - GIF (the German Israeli Foundation for scientific research and developement).
  - IDEX (Initiative D'EXellence).
  - CEFIPRA (Indo French Centre for the Promotion of Advanced Research).
  - NERC (Natural Environment Research Council) UK.
  - GAČR (Czech Science Foundation).
  - NSF (National Science Foundation) USA.
- Jury committee
  - Master of Camilo Valbuena Sánchez, Bogotá Columbia. Thesis: Study on polarity reversal of the geomagnetic field.

2.7 Conference organization

- Convener of sessions in AGU, EGU.
- Core officer in the Geodynamics section of EGU 2011-2015.
- Member of scientific and local committees of the SEDI (Study of the Earth Deep Interior) conference, Nantes July 2016.
- Guest editor in the PEPI special issue dedicated for the SEDI conference in Nantes July 2016.

2.8 Scientific productivity

2.8.1 Peer-reviewed publications

1. Terra-Nova, F., **Amit, H.,** Hartmann, G. A., Trinidade, R. I. F., Pinheiro, K. J., 2017. Relating the South Atlantic Anomaly and geomagnetic flux patches. Phys. Earth Planet. Inter., 266, 39-53.
2. Choblet, G., **Amit, H.,** Husson, L., 2016. Constraining mantle convection models with palaeomagnetic reversals record and numerical dynamos. Geophys. J. Int., 207, 1165-1184.
3. Huguet, L., **Amit, H.,** Alboussière, T., 2016. Magnetic to magnetic and kinetic to magnetic energy transfers at the top of the Earth's core. Geophys. J. Int., 207, 934-948.
4. Terra-Nova, F., **Amit, H.,** Hartmann, G. A., Trinidade, R. I. F., 2016. Using archaeomagnetic field models to constrain the physics of the core: robustness and preferred locations of reversed flux patches. Geophys. J. Int., 206, 1890-1913.
5. Peña, D., **Amit, H.,** Pinheiro, K. J., 2016. Magnetic field stretching at the top of the shell of numerical dynamos. Earth Planets Space, 68:78.

6. Sahoo, S., Sreenivasan, B., **Amit, H.,** 2016. Dynamos driven by weak thermal convection and heterogeneous outer boundary heat flux. Phys. Earth Planet. Inter., 250, 35-45.
7. **Amit, H.,** Choblet, G., Olson, P., Monteux, J., Deschamps, F., Langlais, B., Tobie, G., 2015a. Towards more realistic core-mantle boundary heat flux patterns: a source of diversity in planetary dynamos. Prog. Earth Planet. Sci., 2:26, DOI: 10.1186/s40645-015-0056-3.
8. **Amit, H.,** Deschamps, F., Choblet, G., 2015b. Numerical dynamos with outer boundary heat flux inferred from probabilistic tomography–consequences for latitudinal distribution of magnetic flux. Geophys. J. Int., 203, 840-855.
9. Olson, P., **Amit, H.,** 2015. Mantle superplumes induce geomagnetic superchrons. Front. Earth Sci., 3:38, doi: 10.3389/feart.2015.00038.
10. Oliveira, J. S., Langlais, B., Pais, M. A., **Amit, H.,** 2015. A modified Equivalent Source Dipole method to model partially distributed magnetic field measurements, with application to Mercury. J. Geophys. Res., 120, doi:10.1002/2014JE004734.
11. Terra-Nova, F., **Amit, H.,** Hartmann, G. A., Trinidade, R. I. F., 2015. The time dependence of reversed archeomagnetic flux patches. J. Geophys. Res., 120, 691-704.
12. Monteux, J., **Amit, H.,** Choblet, G., Langlais, B., Tobie, G., 2015. Giant impacts, heterogeneous mantle heating and a past hemispheric dynamo on Mars. Phys. Earth Planet. Inter., 240, 114-124.
13. **Amit, H.,** Olson, P., 2015. Lower mantle superplume growth excites geomagnetic reversals. Earth Planet. Sci. Lett., 414, 68-76.
14. Pinheiro, K.J., Jackson, A., **Amit, H.,** 2015. On the applicability of Backus' mantle filter theory. Geophys. J. Int., 200, 1336-1346.
15. Langlais, B., **Amit, H.,** Larnier, H., Thébault, E., Mocquet, A., 2014. A new model for the (geo)magnetic power spectrum, with application to planetary dynamo radii. Earth Planet. Sci. Lett., 401, 347-358.
16. **Amit, H.,** 2014. Can downwelling at the top of the Earth's core be detected in the geomagnetic secular variation? Phys. Earth Planet. Inter., 229, 110-121.
17. Olson, P., **Amit, H.,** 2014. Magnetic reversal frequency scaling in dynamos with thermochemical convection. Phys. Earth Planet. Inter., 229, 122-133.
18. **Amit, H.,** Pais, M.A., 2013. Differences between tangential geostrophy and columnar flow. Geophys. J. Int., 194, 145-157.
19. Monteux, J., Schaeffer, N., **Amit, H.,** Cardin, P., 2012. Can a sinking metallic diapir generate a dynamo? J. Geophys. Res., 117, E10005, doi:10.1029/2012JE004075.
20. Huguet, L., **Amit, H.,** 2012. Magnetic energy transfer at the top of Earth's core. Geophys. J. Int., 190, 856-870.

21. **Amit, H.,** Choblet, G., 2012. Mantle-driven geodynamo features - effects of compositional and narrow D" anomalies. Phys. Earth Planet. Inter., 190-191, 34-43.

22. **Amit, H.,** Korte, M., Aubert, J., Constable, C., Hulot, G., 2011b. The time-dependence of intense archeomagnetic flux patches. J. Geohys. Res., 116, B12106, doi:10.1029/2011JB008538.

23. **Amit, H.,** Christensen, U., Langlais, B., 2011a. The influence of degree-1 mantle heterogeneity on the past dynamo of Mars. Phys. Earth Planet. Inter., 189, 63-79.

24. Finlay, C.C., **Amit, H.,** 2011. On flow magnitude and field-flow alignment at Earth's core surface. Geophys. J. Int., 186, 175-192.

25. **Amit, H.,** Leonhardt, R., Wicht, J., 2010b. Polarity reversals from paleomagnetic observations and numerical dynamo simulations. Space Sci. Rev., 155, 293-335.

26. **Amit, H.,** Aubert, J., Hulot, G., 2010a. Stationary, oscillating or drifting mantle-driven geomagnetic flux patches? J. Geophys. Res., 115, B07108, doi:10.1029/2009JB006542.

27. **Amit, H.,** Olson, P., 2010. A Dynamo Cascade Interpretation of the Geomagnetic Dipole Decrease. Geophys. J. Int., 181, 1411-1427.

28. **Amit, H.,** Choblet, G., 2009. Mantle-driven geodynamo features - effects of post-Perovskite phase transition. Earth Planets Space, 61, 1255-1268.

29. Olson, P., Driscoll, P., **Amit, H.,** 2009. Dipole collapse and reversal precursors in a numerical dynamo. Phys. Earth Planet. Inter., 173, 121-140.

30. **Amit, H.,** Christensen, U., 2008. Accounting for magnetic diffusion in core flow inversions from geomagnetic secular variation. Geophys. J. Int., 175, 913-924.

31. Langlais, B., **Amit, H.,** 2008. The Past Martian Dynamo, Science, 321, 1784-1785.

32. **Amit, H.,** Aubert, J., Hulot, G., Olson, P., 2008. A simple model for mantle-driven flow at the top of Earth's core. Earth Planets Space, 60, 845-854.

33. Aubert, J., **Amit, H.,** Hulot, G., Olson, P., 2008. Thermo-chemical flows couple the Earth's inner core growth to mantle heterogeneity. Nature, 454, 758-761.

34. **Amit, H.,** Olson, P., 2008. Geomagnetic dipole tilt changes induced by core flow. Phys. Earth Planet. Inter., 166, 226-238.

35. Aubert, J., **Amit, H.,** Hulot, G., 2007. Detecting thermal boundary control in surface flows from numerical dynamos. Phys. Earth Planet. Inter., 160, 143-156.

36. **Amit, H.,** Olson, P., Christensen, U., 2007. Tests of core flow imaging methods with numerical dynamos. Geophys. J. Int., 168, 27-39.

37. Olson, P., **Amit, H.,** 2006. Changes in Earth's dipole. Naturwissenschaften, 93, 11, 519-542.

38. **Amit, H.,** Olson, P., 2006. Time-average and time-dependent parts of core flow. Phys. Earth Planet. Inter., 155, 120-139.
39. **Amit, H.,** Olson, P., 2004. Helical core flow from geomagnetic secular variation. Phys. Earth Planet. Inter., 147, 1-25.
40. **Amit, H.,** Lyakhovsky, V., Katz, A., Starinsky, A., Burg, A., 2002. Interpretation of spring recession curves. Groundwater, 40, 543-551.

2.8.2 Conference talks

1. Choblet, G., **Amit., H.,**, Husson, L., Constraining mantle convection models with paleomagnetic reversals record and numerical dynamos. American Geophysical Union Fall meeting, San Francisco, California, December 2016.
2. Monteux, J., **Amit., H.,** Arkani-Hamed, J., Choblet, G., Langlais, B., Tobie, G., Johnson, C., Jellinek, M., Consequences of Giant Impacts on the Martian dynamo. American Geophysical Union Fall meeting, San Francisco, California, December 2015.
3. Thébault, E., Oliveira, J., Langlais, B., **Amit., H.,** A model of the Hermean magnetic field using a quasi-hemispheric method. Int. Union Geodesy Geophysics, Pragues, Czech Republic, June 2015.
4. Oliveira, J. S., Langlais, B., Pais, A., **Amit, H.,** A new method to model partially distributed magnetic field measurements, with application to Mercury. European Geosciences Union, Vienna, Austria, April 2015.
5. Saturnino, D., Langlais, B., **Amit, H.,** Mandea, M., Describing temporal variations of the geomagnetic field using a modified virtual observatory scheme: application to Swarm data. European Geosciences Union, Vienna, Austria, April 2015.
6. Olson, P., **Amit, H.,** Lower Mantle Superplume Growth Stimulates Geomagnetic Reversals. American Geophysical Union Fall meeting, San Francisco, California, December 2014.
7. **Amit, H.,** Choblet, G., Olson, P., Monteux, J., Deschamps, F., Langlais, B., Tobie, G., Planetary dynamo features driven by exotic models of core-mantle boundary heat flux. Study of the Earth Deep Interior, Shonan village, Japan, August 2014.
8. Oliveira, J.S., Langlais, B., **Amit, H.,** Pais, M.A., Modeling the magnetic field of Mercury using the Time Dependent Equivalent Source Dipole method. European Geosciences Union, Vienna, Austria, April 2014.
9. Choblet, G., **Amit, H.,** Relating plate tectonics, mantle convection and variations in paleomagnetic reversal frequency. American Geophysical Union Fall meeting, San Francisco, California, December 2013.

10. Olson, P., **Amit, H.,** Interpreting geomagnetic reversal frequency using numerical dynamos. American Geophysical Union Fall meeting, San Francisco, California, December 2013.
11. Lefevre, A., Tobie, G., **Amit, H.,** Cadek, O., Choblet, G., Le Mouelic, S., Mitri, G., Sotin, C. Evolution of Titan's outer icy shell: Role of ocean crystallization and surface weathering. American Geophysical Union Fall meeting, San Francisco, California, December 2013.
12. **Amit, H.,** Mantle control on planetary dynamos. Dynamics of Earth and planetary cores, Bangalore, India, September 2013.
13. Monteux, J., Schaeffer, N., **Amit, H.,** Cardin, P., Can a sinking metallic diapir generate a dynamo? Paléomagnétisme en France, IPGP Paris, France, March 2013.
14. Oliveira, J.S., Langlais, B., **Amit, H.,** Pais, M.A., Time Dependent Equivalent Source Dipole - a new method to model the internal magnetic field of Mercury. Paléomagnétisme en France, IPGP Paris, France, March 2013.
15. **Amit, H.,** Christensen, U., Langlais, B., The influence of degree-1 mantle heterogeneity on the past dynamo of Mars. Paléomagnétisme en France, IPGP Paris, France, March 2013.
16. Choblet, G., Husson, L., **Amit, H.,** Relating plate tectonics, mantle convection and variations in paleomagnetic reversal frequency. Paléomagnétisme en France, IPGP Paris, France, March 2013.
17. Choblet, G., **Amit, H.,** Mantle-driven geodynamo features - accounting for non-thermal lower mantle effects. American Geophysical Union Fall meeting, San Francisco, California, December 2011.
18. **Amit, H.,** Christensen, U., Langlais, B., The influence of degree-1 mantle heterogeneity on the past dynamo of Mars. EPSC-DPS Joint Meeting, Nantes, France, October 2011.
19. Monteux, J., Schaeffer, N., **Amit, H.,** Cardin, P., Can a sinking metallic diapir generate a dynamo? EPSC-DPS Joint Meeting, Nantes, France, October 2011.
20. **Amit, H.,** On magnetic diffusion and energy cascade in core dynamics. I Magnet Brazil, Buzios, Brazil, June 2011.
21. Christensen, U.R., Dietrich, W., Hori, K., Wicht, J., **Amit, H.,** Langlais, B., Magnetic fields and dynamos in terrestrial planets. American Geophysical Union Fall meeting, San Francisco, California, December 2010.
22. Tobie, G., **Amit, H.,** Grasset, O., Langlais, B., Le Feuvre, M., Mocquet, A., Verhoeven, O., Probing Jupiter's moons' interiors with tidal deformation and magnetic fields. European Planetary Science Congress, Rome, Italy, September 2010.
23. **Amit, H.,** Core dynamics on various time scales. Study of the Earth Deep Interior, Santa Barbara, California, USA, July 2010.

24. **Amit, H.,** Aubert, J., Hulot. G., Stationary, oscillating or drifting mantle-driven geomagnetic flux patches? American Geophysical Union Fall meeting, San Francisco, California, December 2009.
25. **Amit, H.,** Choblet, G., Mantle-driven geodynamo features - effects of post-Perovskite phase transition. Natural Dynamos, Slovakia, September 2009.
26. **Amit, H.,** Christensen, U., Accounting for magnetic diffusion in core flow inversions from geomagnetic secular variation. Natural Dynamos, Slovakia, September 2009.
27. **Amit, H.,** Christensen, U., Accounting for magnetic diffusion in core flow inversions from geomagnetic secular variation. European Geosciences Union, Vienna, Austria, April 2009.
28. Olson, P., Driscoll, P., **Amit, H.,** Identifying the causes of reversals from theory and simulations. ISSI workshop on terrestrial magnetism, Bern, Switzerland, March 2009.
29. Aubert, J., **Amit, H.,** Hulot, G., Olson, P., Thermo-chemical coupling between the mantle, core and inner core. Study of the Earth Deep Interior, Kunming, China, 2008.
30. Aubert, J., **Amit, H.,** Hulot, G., Olson, P., A possible mechanism for coupling the Earth's inner core to thermal mantle structures. International Union of Geodesy and Geophysics, Perugia, Italy, July 2007.

2.8.3 Conference posters

1. **Amit., H.,**, Coutelier, M., A generalized quasi-geostrophic core flow formalism. American Geophysical Union Fall meeting, San Francisco, California, December 2016.
2. Choblet, G., **Amit., H.,** Husson, L., Constraining mantle convection models with paleomagnetic reversals record and numerical dynamos. Study of the Earth Deep Interior, Nantes, France, July 2016.
3. Pinheiro, K., **Amit., H.,** Terra-Nova, F., Magnetic jerks induced by field roughness. Study of the Earth Deep Interior, Nantes, France, July 2016.
4. Terra-Nova, F., **Amit., H.,** Hartmann, G., Trinidade, R., Using archaeomagnetic field models to constrain the physics of the core: robustness and preferred locations of reversed flux patches. Study of the Earth Deep Interior, Nantes, France, July 2016.
5. Saturnino, D., Langlais, B., **Amit., H.,** Mandea, M., Civet, F., VO-ESD: a modified virtual observatory approach with application to Swarm measurements. Study of the Earth Deep Interior, Nantes, France, July 2016.
6. Huguet, L., **Amit, H.,** Alboussiere, T., Magnetic to magnetic and kinetic to magnetic energy transfers at the top of the Earth's core. Study of the Earth Deep Interior, Nantes, France, July 2016.
7. Thébault, E., Langlais, B., Oliveira, J., **Amit, H.,** A time-averaged regional model of the Hermean magnetic field. Study of the Earth Deep Interior, Nantes, France, July 2016.

8. Oliveira, J., Langlais, B., Pais, A., **Amit, H.,** A New Hermean Magnetic Field Model. Study of the Earth Deep Interior, Nantes, France, July 2016.
9. Pinheiro, K. J., **Amit, H.,** Magnetic jerks induced by field roughness, European Geosciences Union, Vienna, Austria, April 2016.
10. Terra-Nova, F., **Amit, H.,** Hartmann, G. A., Trindade, R. I. F., The time dependence of reversed archeomagnetic flux patches. European Geosciences Union, Vienna, Austria, April 2016.
11. Pinheiro, K. J., Jackson, A., **Amit, H.,** On the applicability of Backus' mantle filter theory. European Geosciences Union, Vienna, Austria, April 2016.
12. Coutelier, M., **Amit, H.,** Christensen, U., Geomagnetic secular variation timescales under rapid rotation constraints. European Geosciences Union, Vienna, Austria, April 2016.
13. **Amit, H.,** Deschamps, F., Choblet, G., Numerical dynamos with outer boundary heat flux inferred from probabilistic tomography – Consequences for latitudinal distribution of magnetic flux. American Geophysical Union Fall meeting, San Francisco, California, December 2015.
14. Oliveira, J.S., Langlais, B., Pais, M.A., **Amit, H.,** Hermean magnetic field models based on MESSENGER measurements. EPSC, Nantes, France, September 2015.
15. Monteux, J., **Amit, H.,** Choblet, G., Langlais, B., Tobie, G., Giant impacts, heterogeneous mantle heating and a past hemispheric dynamo on Mars. EPSC, Nantes, France, September 2015.
16. Peña, D., **Amit, H.,** Pinheiro, K., Magnetic field stretching at the top of Earth's core. European Geosciences Union, Vienna, Austria, April 2015.
17. **Amit, H.,** Deschamps, F., Choblet, G., Numerical dynamos with outer boundary heat flux inferred from probabilistic tomography – Consequences for latitudinal distribution of magnetic flux. European Geosciences Union, Vienna, Austria, April 2015.
18. **Amit, H.,** Olson, P., Lower mantle superplume growth excites geomagnetic reversals. European Geosciences Union, Vienna, Austria, April 2015.
19. Monteux, J., **Amit, H.,** Choblet, G., Langlais, B., Tobie, G., Giant impacts, heterogeneous mantle heating and a past hemispheric dynamo on Mars. European Geosciences Union, Vienna, Austria, April 2015.
20. Saturnino, D., Langlais, B., **Amit, H.,** Mandea, M., Describing Temporal Variations of the Geomagnetic Field through a Modified Virtual Observatory Scheme: Application to SWARM Measurements. American Geophysical Union Fall meeting, San Francisco, California, December 2014.
21. **Amit, H.,** Can downwelling at the top of the Earth's core be detected in the geomagnetic secular variation? Study of the Earth Deep Interior, Shonan village, Japan, August 2014.
22. Olson, P., **Amit, H.,** Magnetic reversal frequency scaling in dynamos with thermochemical convection. European Geosciences Union, Vienna, Austria, April 2014.

23. **Amit, H.,** Can downwelling at the top of the Earth's core be detected in the geomagnetic secular variation? European Geosciences Union, Vienna, Austria, April 2014.
24. Choblet, G., **Amit, H.,** Husson, L., Relating plate tectonics, mantle convection and variations in paleomagnetic reversal frequency. European Geosciences Union, Vienna, Austria, April 2014.
25. Oliveira, J.S., Langlais, B., **Amit, H.,** Pais, M.A., Modeling the magnetic field of Mercury using the Time Dependent Equivalent Source Dipole method. American Geophysical Union Fall meeting, San Francisco, California, December 2013.
26. Langlais, B., **Amit, H.,** Larnier, H., Thébault, E., A new model for the geomagnetic power spectrum, with application to planetary core size. European Geosciences Union, Vienna, Austria, April 2013.
27. **Amit, H.,** Pais, M.A., Differences between tangential geostrophy and columnar flow. European Geosciences Union, Vienna, Austria, April 2013.
28. **Amit, H.,** Pais, M.A., Differences between tangential geostrophy and columnar flow. Paléomagnétisme en France, IPGP Paris, France, March 2013.
29. Langlais, B., **Amit, H.,** Larnier, H., Thébault, E., A new model for the geomagnetic power spectrum, with application to planetary core size. American Geophysical Union Fall meeting, San Francisco, California, December 2012.
30. Oliveira, J.S., Langlais, B., **Amit, H.,** Pais, M.A., Time Dependent Equivalent Source Dipole - a new method to model the internal magnetic field of Mercury. American Geophysical Union Fall meeting, San Francisco, California, December 2012.
31. **Amit, H.,** Pais, M.A., Differences between tangential geostrophy and columnar flow. American Geophysical Union Fall meeting, San Francisco, California, December 2012.
32. Huguet, L., **Amit, H.,** Magnetic energy transfer at the top of the Earth's core. American Geophysical Union Fall meeting, San Francisco, California, December 2012.
33. Monteux, J., Schaeffer, N., **Amit, H.,** Cardin, P., Can a sinking metallic diapir generate a dynamo? American Geophysical Union Fall meeting, San Francisco, California, December 2012.
34. **Amit, H.,** Choblet, G., Mantle-driven geodynamo features - accounting for non-thermal lower mantle effects. Study of the Earth Deep Interior, Leeds, UK, July 2012.
35. **Amit, H.,** Christensen, U., Langlais, B., The influence of degree-1 mantle heterogeneity on the past dynamo of Mars. Study of the Earth Deep Interior, Leeds, UK, July 2012.
36. **Amit, H.,** Korte, M., Aubert, J., Constable, C., Hulot, G., The time-dependence of intense archeomagnetic flux patches. Study of the Earth Deep Interior, Leeds, UK, July 2012.
37. Huguet, L., **Amit, H.,** Magnetic energy transfer at the top of the Earth's core. Study of the Earth Deep Interior, Leeds, UK, July 2012.

38. Monteux, J., Schaeffer, N., **Amit, H.,** Cardin, P., Can a sinking metallic diapir generate a dynamo? Study of the Earth Deep Interior, Leeds, UK, July 2012.
39. **Amit, H.,** Christensen, U., Langlais, B., The influence of degree-1 mantle heterogeneity on the past dynamo of Mars. The International Conference on Exploring Mars Habitability, Lisbon, Portugal, June 2011.
40. **Amit, H.,** Olson, P., A Dynamo Cascade Interpretation of the Geomagnetic Dipole Decrease. Study of the Earth Deep Interior, Santa Barbara, California, USA, July 2010.
41. **Amit, H.,** Olson, P., A Dynamo Cascade Interpretation of the Geomagnetic Dipole Decrease. European Geosciences Union, Vienna, Austria, May 2010.
42. **Amit, H.,** Choblet, G., Mantle-driven geodynamo features - effects of post-Perovskite phase transition. European Geosciences Union, Vienna, Austria, May 2010.
43. **Amit, H.,** Aubert, J., Hulot, G., Stationary, oscillating or drifting mantle-driven geomagnetic flux patches? Natural Dynamos, Slovakia, September 2009.
44. **Amit, H.,** Olson, P., Geomagnetic Dipole Tilt Changes Induced by Core Flow. American Geophysical Union Fall meeting, San Francisco, California, December 2007.
45. Aubert, J., **Amit, H.,** Hulot, G., Olson, P., A thermo-chemical wind coupling the Earth's inner core and deep mantle. American Geophysical Union Fall meeting, San Francisco, California, December 2007.
46. **Amit, H.,** Aubert, J., Hulot, G., Olson, P., Thermal wind at the top of the core. American Geophysical Union Fall meeting, San Francisco, California, December 2006.
47. Aubert, J., **Amit, H.,** Hulot, G., Can thermal mantle control be identified in Earth's core surface flows? American Geophysical Union Fall meeting, San Francisco, California, December 2006.
48. **Amit, H.,** Aubert, J., Hulot, G., Olson, P., Mantle-driven thermal wind at the top of the core. Study of the Earth Deep Interior, Prague, Czech Republic, July 2006.
49. Aubert, J., **Amit, H.,** Hulot, G., Can thermal mantle control be identified in Earth's core surface flows? Study of the Earth Deep Interior, Prague, Czech Republic, July 2006.
50. **Amit, H.,** Aubert, J., Hulot, G., Olson, P., Mantle-driven thermal wind at the top of the core. 26rd International Conference on Mathematical Geophysics, Sea of Galilee, Israel, June 2006.
51. Andrews, D., **Amit, H.,** Olson, P., Rapidly evolving sources of geomagnetic dipole tilt on the core-mantle boundary. American Geophysical Union Fall meeting, San Francisco, California, December 2005.
52. Aurnou, J., Aubert, J., **Amit, H.,** Andreadis, S., Olson, P., Thermal Winds in the Tangent Cylinder. American Geophysical Union Fall meeting, San Francisco, California, December 2005.

53. **Amit, H.,** Olson, P., The origin of the geomagnetic dipole and tilt. European Geosciences Union, Vienna, Austria, April 2005.
54. Olson, P., **Amit, H.,** The origin of the rapid decrease of the geomagnetic dipole moment. European Geosciences Union, Vienna, Austria, April 2005.
55. **Amit, H.,** Olson, P., Time-Average Core Flow: Mantle vs. Core Origins. American Geophysical Union Fall meeting, San Francisco, California, December 2004.
56. Olson, P. **Amit, H.,** Andreadis, S., Liu, L., A Dynamo Mechanism for Rapid Decrease of the Geomagnetic Dipole Moment. American Geophysical Union Fall meeting, San Francisco, California, December 2004.
57. **Amit, H.,** Olson, P., Helical core flow from geomagnetic secular variation. Study of the Earth Deep Interior, Garmisch-Partenkirchen, Germany, July 2004.
58. **Amit, H.,** Olson, P., Christensen, U., Core flow inversions: Constraints from dynamo theory. Study of the Earth Deep Interior, Garmisch-Partenkirchen, Germany, July 2004.
59. **Amit, H.,** Olson, P., A new Method for Determining the Fluid Flow Below the Core-Mantle Boundary From Global Geomagnetic Field Models. Planetary Dynamos, Les Houches, France, March 2003.
60. **Amit, H.,** Olson, P., A new Method for Determining the Fluid Flow Below the Core-Mantle Boundary From Global Models of the Geomagnetic Field. American Geophysical Union Fall meeting, San Francisco, California, December 2002.
61. **Amit, H.,** Lyakhovsky, V., Katz, A., Starinsky, A., Burg, A., Spring discharge anomaly: effect of low magnitude earthquakes. 23rd International Conference on Mathematical Geophysics, Villefranche sur mer, France, June 2000.
62. **Amit, H.,** Lyakhovsky, V., Katz, A., Starinsky, A., Burg, A., Groundwater flow mechanisms in perched carbonate aquifers. Israel Geological Society annual meeting, Maalot, April 2000.

2.8.4 Invited seminars

1. October 2013, Coimbra Portugal: “Magnetic reversal frequency scaling in dynamos with thermo-chemical convection”.
2. January 2013, BGU Beer Sheva Israel: “Mantle control on planetary dynamos: Mars, Earth, long term, shorter term”.
3. March 2011, ENS Lyon France: “Mantle control on planetary dynamos: Mars, Earth, long term, shorter term”.
4. June 2010, GFZ Potsdam Germany: “Geomagnetic field dynamics on various time scales”.

5. January 2008, The Hebrew University Jerusalem Israel: “Magnetic field and fluid dynamics of Earth’s outer core from observations, numerical simulations and theory”.
6. December 2007, IGS Jerusalem Israel: “Magnetic field and fluid dynamics of Earth’s outer core from observations, numerical simulations and theory”.
7. December 2007, University of Nantes France: “Probing the planets using magnetic fields: Application for dynamo action in Earth’s core”.
8. November 2007, ENS Paris France: “Combining geomagnetic observations, numerical simulations and theory to study dynamo action in Earth’s outer core”.
9. November 2007, ENS Lyon France: “Combining geomagnetic observations, numerical simulations and theory to study dynamo action in Earth’s outer core”.
10. June 2007, University of Cologne Germany: “Magnetohydrodynamics of earth’s outer core from observations, numerical simulations and theory”.
11. January 2007, LGIT Grenoble France: “Imaging core flow from geomagnetic secular variation: Consequences for core-mantle interactions and geomagnetic dipole moment changes”.
12. January 2007, BGI Bayreuth Germany: “Imaging core flow from geomagnetic secular variation: Consequences for core-mantle interactions and geomagnetic dipole moment changes“.
13. March 2006, IPGP Paris France: “Imaging core flow from geomagnetic secular variation: Consequences for core-mantle interactions and geomagnetic dipole moment changes”.
14. November 2005, IPGP Paris France: “Core flow models from geomagnetic secular variation”.

2.9 Main collaborations

2.9.1 Within LPG

Since obtaining my CNRS position in 2008, my main collaborators within LPG have been Benoit Langalis and Gaël Choblet. With Benoit we mostly studied mantle control causing the hemisphericity of the Martian crustal magnetic field (Langlais and Amit, 2008; Amit et al., 2011a; Monteux et al., 2015). We also inferred magnetic CMB radii of planets from spectra of field models (Langlais et al., 2014).

With Gaël we modeled alternative CMB heat flux patterns that correspond to various lower mantle dynamical scenarios and explored their effect on observed morphological dynamo features (Amit and Choblet, 2009, 2012; Amit et al., 2015a, 2015b). We also collaborated on the Martian magnetic hemisphericity (Monteux et al., 2015).

I benefited from working with several competent students in LPG. Together with my LPG Master student Ludovic Huguet we developed and formulated the theory to track energy transfers from one

spherical harmonic degree to another and implemented it on historical and modern core field and flow models (Huguet and Amit, 2012; Huguet et al., 2016). With my LPG Ph.D. student Filipe Terra-Nova we designed topological algorithms to identify and track reversed flux patches in archeomagnetic field models (Terra-Nova et al., 2015, 2016) and to relate these patches to minimum surface field intensity (Terra-Nova et al., 2017).

2.9.2 In France

During my postdoc in IPGP I collaborated with Julien Aubert and Gauthier Hulot on two main topics. We focused on mantle control explaining robust morphological features of the geodynamo (Aubert et al., 2007, 2008; Amit et al., 2008). In addition, we developed algorithms to identify and track intense magnetic flux patches in numerical dynamos (Amit et al., 2010a) and in an archeomagnetic field model (Amit et al., 2011b).

During the postdoc of Julien Monteux in LPG (currently a CNRS agent in LMV, Clermont Ferrand) we have been working on the effects of giant impacts on the magnetic evolution of Mars. We examined the possibility to generate a transient dynamo from sinking metallic diapirs (Monteux et al., 2012). We imposed localized CMB heat flux heterogeneity consistent with mantle heating from giant impacts on numerical dynamos and explored the resulting crustal magnetic hemisphericity (Monteux et al., 2015).

2.9.3 Outside France

My main collaborator up until today is my Ph.D. advisor Peter Olson (USA). During my Ph.D. thesis Peter and I designed a new method and physical assumption for core flow inversions from geomagnetic SV (Amit and Olson, 2004) which we implemented on the historical geomagnetic field model (Amit and Olson, 2006) and tested with synthetic data from numerical dynamos (Amit et al., 2007). We also developed a new theory to study geomagnetic dipole changes and implemented it for geomagnetic dipole intensity changes (Olson and Amit, 2006) and for dipole collapse events in numerical dynamos (Olson et al., 2009) as well as for geomagnetic dipole tilt changes (2008). Later we examined the possibility that the decay of the geomagnetic dipole is caused by energy cascade to higher degrees (Amit and Olson, 2010). We also collaborated on recovering persistent geodynamo observations by invoking heterogeneous mantle control on numerical dynamos, in particular robust morphological features (Amit et al., 2008, 2015a; Aubert et al., 2008) and the variable paleoemagnetic reversal frequency (Olson and Amit, 2014, 2015; Amit and Olson, 2015).

I have been collaborating with Uli Christensen (Max-Planck, Göttingen, Germany) on various topics. We tested core flow inversions using synthetic SV from numerical dynamos (Amit et al., 2007). We

modeled the contribution of radial diffusion to the SV and accounted for it in core flow inversions (Amit and Christensen, 2008). We studied the effects of a degree-1 mantle heterogeneity on the past Martian dynamo and the formation of hemisphericity in the crustal magnetic field (Amit et al., 2011a).

I have been working with Alexandra Pais (University of Coimbra, Portugal) on different physical assumptions for core flow inversions, including theoretical and practical consequences (Amit and Pais, 2013). We also collaborated on modeling the magnetic field of Mercury from MESSENGER data (Oliveira et al., 2015). The latter study is part of the Ph.D. thesis of Joana Oliveira in LPG which Alexandra and I co-advised.

Katia Pinheiro (ON, Rio de Janeiro, Brazil) has been working in LPG for two years. We have been collaborating on mantle filter theory for the propagation of geomagnetic jerks' signal from the CMB to Earth's surface (Pinheiro et al., 2015). We are also co-advising the Ph.D. thesis of Diego Peña in ON on magnetic field stretching effects in numerical dynamos (Peña et al., 2016).

Finally, I have a fruitful ongoing collaboration with Gelvam Hartmann and Ricardo Trinidade (USP, São Paulo, Brazil) via the Ph.D. thesis of Filipe Terra-Nova in LPG. This collaboration has already led to three papers (Terra-Nova et al., 2015, 2016, 2017).

Chapter 3

Research

My research focuses on the fluid dynamics in planetary cores that generates magnetic fields by dynamo action. More specifically, my research activities focus on two main axes, rapid dynamics in Earth's core and mantle control on planetary dynamos. Rapid core dynamics includes core flow modeling and other inferences from the geomagnetic secular variation, geomagnetic dipole changes and kinematics of intense geomagnetic flux patches on decadal to millennial timescales. Mantle control is invoked to explain persistent morphological features of the geodynamo, the variable paleomagnetic reversal frequency and the hemispheric dichotomy in the crustal magnetic field of Mars. Below I give some examples of my results for each of these research axes. For references to my papers see section 2.8.1, for other referred papers see the Bibliography at the end of the document.

3.1 Rapid core dynamics

Geomagnetic field and secular variation (SV) models based on observations provide vital insight into the dynamics at the top of the Earth's core. These models may be inverted for the flow at the top of the core (for reviews see Bloxham and Jackson, 1991; Holme, 2007) and thus provide an important insight into core dynamics and geodynamo action. However, various uncertainties in these inversions limit the interpretation of the results. These limitations motivate additional ways to extract complimentary information about core dynamics properties from the geomagnetic SV.

In these studies I collaborated with the following researchers:

- LPG: Ludovic Huguet and Filipe Terra-Nova
- IPGP: Julien Aubert and Gauthier Hulot
- ENS Lyon: Thierry Alboussière
- Max-Planck, Göttingen, Germany: Uli Christensen

- GFZ, Potsdam, Germany: Monika Korte
- DTU, Copenhagen, Denmark: Chris Finlay
- University of Coimbra, Portugal: Alexandra Pais
- DTM, Washington D.C., USA: Peter Driscoll
- USA: Peter Olson
- Scripps, San Diego, USA: Catherine Constable
- ON, Rio de Janeiro, Brazil: Diego Peña and Katia Pinheiro
- USP, São Paulo, Brazil: Gelvam Hartmann and Ricardo Trinidade

3.1.1 Core flow models inferred from the geomagnetic secular variation

Core flow inversions from geomagnetic SV image the geodynamo at the top of its region of generation. In Amit and Olson (2004) we inverted the geomagnetic SV for the fluid flow below the CMB assuming a new physical assumption termed *helical flow* in which the tangential divergence correlates with the radial vorticity. Helical flow introduces streamfunction diffusion to the magnetic induction equation and removes non-uniqueness from the inversion. In Amit and Olson (2006) we applied the helical core flow modeling technique for the historical geomagnetic field model gufm1 (Jackson et al., 2000). We decomposed the flow model to time-average and time-dependent parts. The most prominent time-average flow structure is a large anti-cyclonic vortex in the southern hemisphere beneath the Atlantic and Indian Oceans (Fig. 3.1a). The time-average zonal core flow outside the inner core tangent cylinder is significantly westward in the southern hemisphere but nearly zero in the northern hemisphere (Fig. 3.1b). Westward polar vortices occur inside the tangent cylinder in both hemispheres, particularly in the north. In terms of mantle versus core origins, mantle driving appears to be responsible for the mid-latitude asymmetry in the zonal core flow, whereas core driving appears to be responsible for the flow at high latitudes. We also compared changes in the core's angular momentum calculated from our time-dependent core flow with changes in the mantle's angular momentum derived from decade-scale length-of-day variations and found adequate agreement. A fit of our time-dependent core flow to a torsional oscillations model yielded dominant periods of 110 and 53 years.

In Amit and Christensen (2008) we used numerical dynamos to investigate the possible role of magnetic diffusion at the top of the core. We found that the contribution of radial magnetic diffusion to the SV is correlated with that of tangential magnetic diffusion (Fig. 3.2) for a range of control parameters. The correlation between the two diffusive terms was interpreted in terms of the variation in the strength of poloidal flow along a columnar flow tube. The amplitude ratio of the two diffusive terms was used to estimate the probable contribution of radial magnetic diffusion to the SV at Earth-like conditions. We

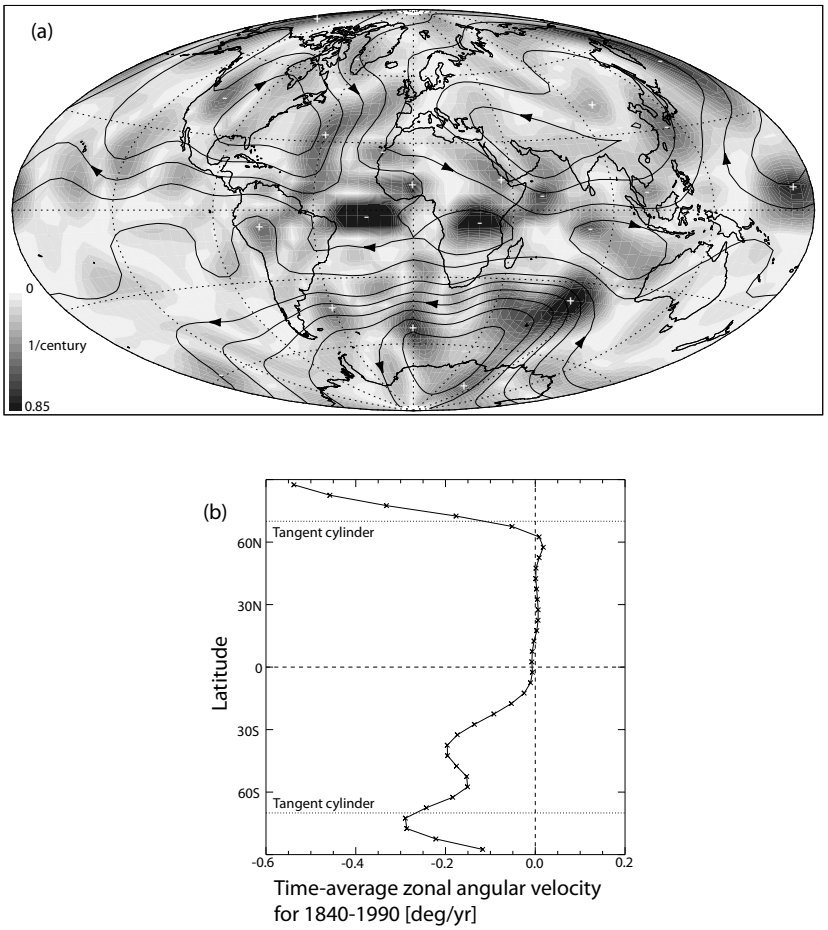

Figure 3.1: Time-average core flow for 1840-1990 (a), and time-average zonal angular velocity for the same time period (b). Contours in (a) are streamlines of the toroidal flow; grey scale represents absolute upwelling value with + and - signs indicating upwelling and downwelling, respectively. From Amit and Olson (2006).

then applied a model where radial magnetic diffusion was proportional to tangential diffusion to core flow inversions of geomagnetic SV data. We found that including magnetic diffusion does not change dramatically the global flow but some significant local variations appear. In the non frozen-flux core flow models (termed 'diffusive'), the hemispherical dichotomy between the active Atlantic and quiet Pacific is weaker, a cyclonic vortex below North America emerges and the vortex below Asia is stronger. Our results had several important geophysical implications. First, our diffusive flow models contain some flow activity at low latitudes in the Pacific, suggesting a local balance between magnetic field advection and diffusion in that region. Second, the cyclone below North America in our diffusive flows reconciles the difference between mantle-driven thermal wind predictions and frozen-flux core flow models, and is consistent with the prominent intense magnetic flux patch below North America in geomagnetic field models. Finally, we hypothesized that magnetic diffusion near the core surface plays a larger role in the geomagnetic SV

than usually assumed.

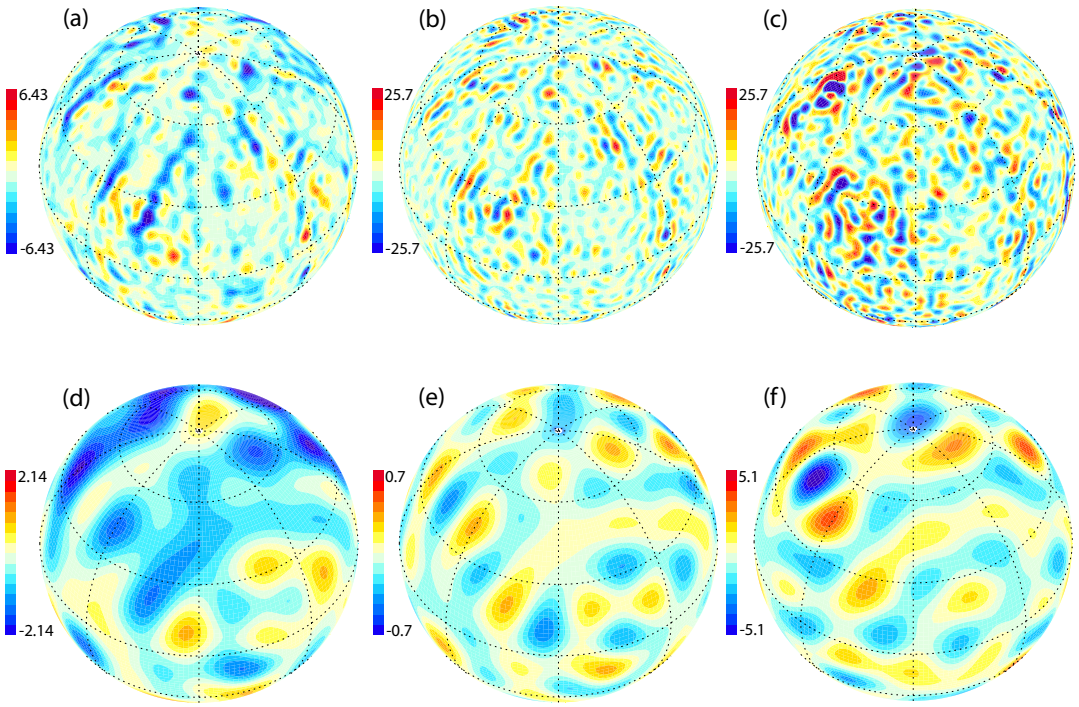

Figure 3.2: Radial magnetic field (a), tangential magnetic diffusion (b) and radial magnetic diffusion (c) for a snapshot from a dynamo model (case 7 of Amit and Christensen, 2008). The corresponding quantities for a low-pass filtered field are given in (d)-(f), respectively. All images are at the top of the free stream. Note differences in color scales. In this snapshot the correlation coefficients between the two radial and tangential diffusion terms are 0.59 (non-filtered) and 0.48 (filtered) and their RMS ratios are 1.48 (non-filtered) and 6.72 (filtered). From Amit and Christensen (2008).

In Huguet and Amit (2012) we introduced a formalism to track magnetic energy transfer between spherical harmonic degrees due to the interaction of fluid flow and radial magnetic field at the top of the Earth's core. Large-scale synthetic single harmonic flows were characterized by a fixed difference between harmonics participating in the transfer. Large-scale toroidal flows resulted in more local energy transfer than small-scale poloidal flows. Axisymmetric poloidal flows were most efficient in producing energy transfer and dipole changes. The azimuthal phase relation between the field and the flow may play a major role in the energy transfer. Geomagnetic energy transfer induced by core flow models exhibited a striking transfer spectrum pattern of alternating extrema suggestive of energy cascade, but the detailed transfer spectrum matrix revealed rich behaviour with both local Kolmogorov-like transfer and non-local transfer, the latter about twice larger. The transfer spectrum reversed from even maxima and odd minima between 1840 and 1910 to odd maxima and even minima between 1955 and 1990. The transfer spectrum matrix showed geomagnetic energy cascade from low to high degrees as well as non-local transfer from the dipole directly to higher degrees, explaining the simultaneous dipole decrease and non-dipole increase

during the historical period. This paper summarizes the Master thesis of Ludovic Huguet in LPG under my supervision.

We extended the work of Huguet and Amit (2012) and developed the theory for the magnetic to magnetic as well as kinetic to magnetic energy transfer between different spherical harmonic degrees due to the interaction of fluid flow and radial magnetic field at the top of the Earth's core (Huguet et al., 2016). We showed that non-zero SV of the total magnetic energy is likely numerically significant and may provide evidence for the existence of stretching SV, which suggests the existence of radial motions at the top of the Earth's core - whole core convection or MAC waves. Combining core field and flow models we calculated the detailed magnetic to magnetic and kinetic to magnetic energy transfer matrices. Our results showed that the magnetic to magnetic energy transfer has a complex behavior with local and non-local transfers (Fig. 3.3). The spectra of magnetic to magnetic energy transfers show clear maxima and minima, suggesting an energy cascade. The kinetic to magnetic energy transfers, which are much weaker due to the weak poloidal flow, are either local or non-local between degree one and higher degrees. The patterns observed in the matrices resemble energy transfer patterns that are typically found in 3D MHD numerical simulations.

In the same topic of core flows inferred from the geomagnetic SV, in Amit and Pais (2013) we compared two assumptions similar in form yet different in essence: tangential geostrophy (TG, LeMouël, 1984) and columnar flow (CF, Amit and Olson, 2004). We recalled that CF is theoretically consistent with the quasi-geostrophy (QG) theory for an incompressible fluid with spherical solid boundaries whereas TG is not. As such, we highlighted the importance of applying the CF assumption when inverting geomagnetic data for interior core (columnar) flows that can be used in kinematic dynamo and thermal convection models in the Boussinesq approximation. Next we evaluated the non-uniqueness associated with CF flows. The areas of ambiguous patches at the core surface where invisible TG or CF flows reside were roughly comparable. The spatial distribution of ambiguous patches for both TG and CF is quite asymmetric about the equator, so assuming equatorial symmetry is expected to reduce the non-uniqueness significantly. In fact, for assumed equatorial symmetry, the only possible non-unique flows will be those along hypothetical invisible flow contours in the opposite hemispheres that their equatorial plane projections are parallel. TG flows exhibited a strong Atlantic/Pacific hemispheric dichotomy and a well-defined eccentric gyre whereas in CF flows the dichotomy between these two hemispheres was weaker and the gyre was less clear suggesting that the eccentric gyre might not conserve mass. Both TG and CF upwelling/downwelling patterns were strongly localized in the equatorial region. In addition, in both cases upwelling/downwelling was correlated with equatorward/poleward flow respectively, as expected for QG convection. CF upwelling was more intense than TG upwelling but the magnitude ratio was smaller than the factor 2 distinguishing the analytical expressions of the two assumptions. This

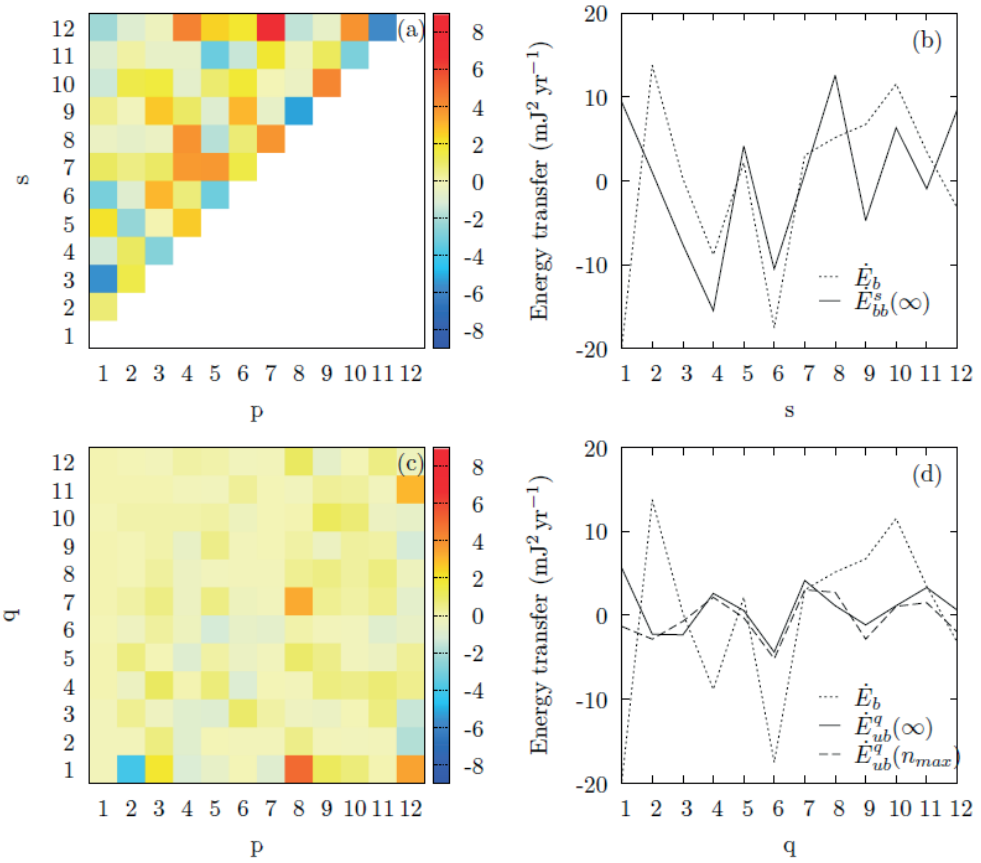

Figure 3.3: Energy transfer spectra for the year 2005 for the geomagnetic field model CHAOS-4 (Olsen et al., 2014). Magnetic to magnetic (a) and kinetic to magnetic (c) energy transfer matrices $\dot{E}_{bb}(p,s)$ and $\dot{E}_{ub}(p,q)$ respectively. (b) and (d): The observed energy transfer $\dot{E}_b$ (dotted line), the total energy transfers $\dot{E}^s_{bb}(\infty)$ and $\dot{E}^q_{ub}(\infty)$ (solid black lines) and the kinetic to magnetic energy transfer within the observed spectrum $\dot{E}^q_{ub}(n_{max})$ (dashed line), all in mJ^2/yr. In (b), the dashed line is practically identical to the solid line. From Hugeut et al. (2016).

smaller magnitude ratio is due to the fact that presently observed geomagnetic SV features are mostly explained by magnetic field advection by toroidal core flow in the frozen-flux approximation (Fig. 3.4). Robust upwelling features below India/Indonesia may be viewed as geomagnetic evidence for whole core convection.

3.1.2 More inferences from the geomagnetic secular variation

Fundamental insight into core dynamics was obtained without relying on core flow inversions from geomagnetic SV. In Finlay and Amit (2011) we presented a method to estimate the typical magnitude of flow close to Earth's core surface based on observational knowledge of the geomagnetic field and its SV together with prior information concerning field-flow alignment gleaned from numerical dynamo models. An expression linking the core surface flow magnitude to spherical harmonic spectra of the field and SV

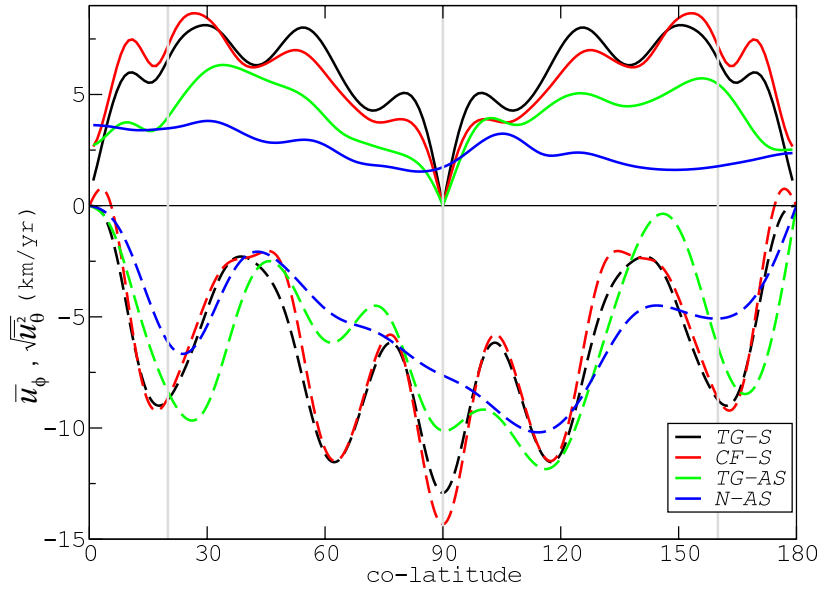

Figure 3.4: Zonal profiles $\overline{u}_\phi$ (dashed) and $\sqrt{\overline{u_\theta^2}}$ (solid) as a function of co-latitude for core surface flow models derived based on four different physical assumptions: Tangential geostrophy with equatorial symmetry (black), columnar flow with equatorial symmetry (red), tangential geostrophy without equatorial symmetry (green) and non-constrained (blue). Different physical assumptions result in significantly different geomagnetic SV inverted core flows. From Amit and Pais (2013).

was derived from the magnetic induction equation. This involves the angle between the flow and the horizontal gradient of the radial field. We studied this angle in a suite of numerical dynamo models and discussed the physical mechanisms that control it. Horizontal flow was observed to approximately follow contours of the radial field close to high-latitude flux bundles, while more efficient induction occurred at lower latitudes where predominantly zonal flows are often perpendicular to contours of the radial field. We showed that the amount of field-flow alignment depends primarily on a magnetic modified Rayleigh number Ra that measures the vigor of convective driving relative to the strength of magnetic dissipation. Synthetic tests of the flow magnitude estimation scheme were encouraging, with results differing from true values by less than 8%. Application to a high-quality geomagnetic field model based on satellite observations led to a flow magnitude estimate of 11-14 km/yr, in accordance with previous estimates. When applied to the historical geomagnetic field model gufm1 for the interval 1840-1990, the method predicted temporal variations in flow magnitude similar to those found in earlier studies. The calculations rely primarily on knowledge of the field and SV spectra; by extrapolating these beyond observed scales the influence of small scales on flow magnitude estimates was assessed. Exploring three possible spectral extrapolations we found that the magnitude of the core surface flow, including small scales, is likely less than 50 km/yr.

In the same topic of inferring core dynamics properties without global SV inversions, in Amit (2014)

I analyzed persistent geomagnetic SV features on the CMB to examine whether a kinematic signature of core fluid upwelling/downwelling can be detected. I focused on regions of intense high-latitude geomagnetic flux patches that may be maintained by fluid downwelling. In order to identify persistent patterns, the radial field and its SV were stacked in the flux patch moving reference frame. These stacked images were compared with forward solutions to the radial induction equation based on idealized field-flow models. Clear advective SV signature below North America indicated that these intense flux patches may exhibit significant mobility. Stretching signature in the form of persistent positive SV correlated with the intense flux patch below the Southern Indian Ocean may be considered as regional scale geomagnetic evidence for whole core convection (Fig. 3.5), although pure toroidal flow cannot be outruled.

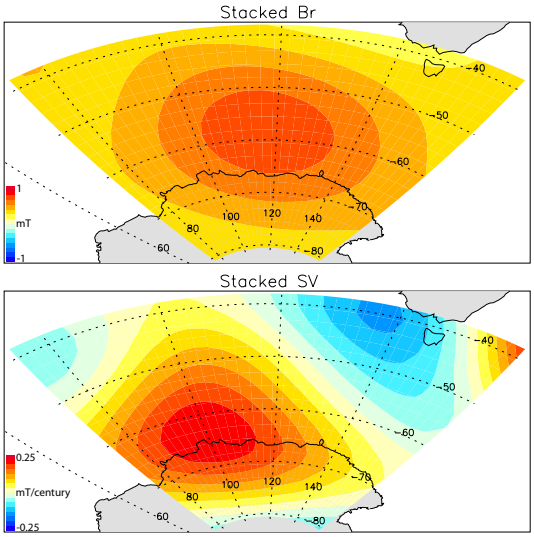

Figure 3.5: Stacked radial field (top) and SV (bottom) centered below the Southern Indian Ocean geomagnetic flux patch based on the historical field model gufm1 of Jackson et al. (2000). The stacking is performed over the period 1920-1990 when this patch was classified as intense by Amit et al. (2011b). Same sign stacked radial field and SV is suggestive of persistent core fluid downwelling in this region. From Amit (2014).

Peña et al. (2016) studied magnetic field stretching at the top of the shell of numerical dynamos, focusing on specific regions. High-latitude intense NFPs may be concentrated by flow convergence. RFPs may emerge due to expulsion of toroidal field advected to the core-mantle boundary by fluid upwelling. We found that stretching at the top of the shell has a significant influence on the SV despite the relatively weak poloidal flow. In addition, locally stretching is often more effective than advection in particular at regions of significant field-aligned flow. Morphological resemblance between local stretching in the dynamo models of Peña et al. (2016) and local observed geomagnetic SV (Amit, 2014) may suggest the presence of stretching at the top of the Earth's core. This paper summarizes the first part of the Ph.D. thesis of Diego Peña in ON (Rio de Janeiro, Brazil) under my supervision.

3.1.3 Geomagnetic dipole changes

The dipole moment of Earth's magnetic field has decreased by nearly 9% over the past 150 years, and by about 30% over the past 2000 years according to archeomagnetic measurements. In Olson and Amit (2006) we explored the causes and the implications of this rapid change. Growth of reversed flux regions has occurred over the past century or longer and is associated with the expansion of the South Atlantic Anomaly, a low-intensity region in the geomagnetic field that presents a radiation hazard at satellite altitudes. We addressed the speculation that the present episode of dipole moment decrease is a precursor to the next geomagnetic polarity reversal. The paleomagnetic record contains a broad spectrum of dipole moment fluctuations with polarity reversals typically occurring during dipole moment lows. However, the dipole moment is stronger today than its long time average, indicating that polarity reversal is not likely unless the current episode of moment decrease continues for a thousand years or more. Maps of the geomagnetic field on the CMB reveal that most of the present episode of dipole moment decrease originates in the southern hemisphere. We developed a new theory to map advective sources and sinks of axial dipole change. Weakening and equatorward advection of normal polarity magnetic field by the core flow (Fig. 3.6), combined with proliferation and growth of regions where the magnetic polarity is reversed, are reducing the dipole moment on the CMB. This theory was applied to dipole collapse events in numerical dynamos (Olson et al., 2009). Recently, our theory was applied by Finlay et al. (2016) for new core field and flow models in the framework of geomagnetic data assimilation.

The theory for the advective sources of dipole change was further applied for the equatorial dipole moment in order to study tilt changes. The tilt of the geomagnetic dipole decreased from about 11.7° in 1960 to 10.5° in 2005, following more than a century when it remained nearly constant. The recent poleward motion of the dipole axis is primarily due to a rapid decrease in the equatorial component of the dipole moment vector. Using maps of the equatorial dipole moment density and its SV derived from core field models, in Amit and Olson (2008) we identified regions on the CMB where the present-day tilt decrease is concentrated. We showed that magnetic flux transport can account for most of the observed equatorial dipole moment change. Core flow models derived from geomagnetic SV reveal a nearly balanced pattern of advective sources and sinks for the equatorial dipole moment below the CMB. The recent tilt decrease originates from two advective sinks, one beneath Africa where positive radial magnetic field is transported westward away from the equatorial dipole axis, the other beneath North America where negative radial magnetic field is transported northward away from the equatorial dipole axis (Fig. 3.7). Each of these sinks is related to a prominent gyre that has evolved significantly over the past few decades, indicating the strong variability of the large-scale circulation in the outer core on this time scale.

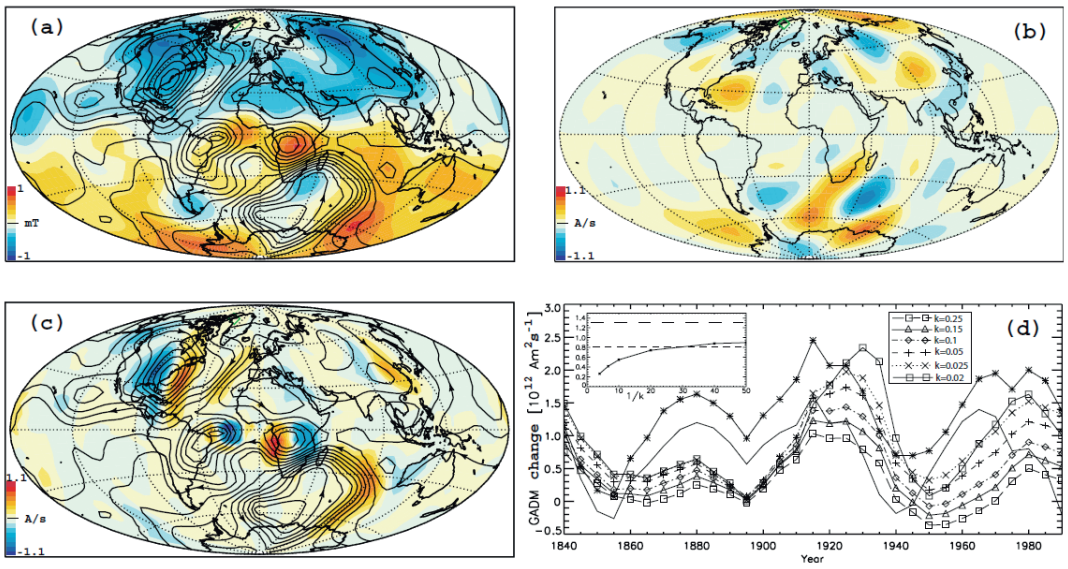

Figure 3.6: (a) Radial magnetic field (colors) and streamlines of a core flow model (solid curves with arrows indicating circulation direction) at 1980. (b) Axial dipole moment density change at 1980. (c) Advective contributions to axial moment change (colors) with streamlines of a core flow model at 1980. (d) Advective axial moment change for different k values (see legend) vs. the observed total axial moment change (solid, asterisk) and reduced axial moment change (solid) from 1840 to 1990. Inlet: time-averaged advective axial moment change (solid, asterisk) vs. k. Also shown are the observed time-averaged change (long dash) and the time-averaged reduced change (short dash). From Olson and Amit (2006).

3.1.4 Kinematics of intense geomagnetic flux patches

Archeomagnetic field models provide vital information about the field behavior on millennial timescales. However, their low spatio-temporal resolution prevents inversions for the core flow. In contrast, following the temporal evolution of some field features may allow a glimpse into the dynamo behavior on these longer timescales. We designed algorithms to identify and track intense magnetic flux patches in numerical dynamos (Amit et al., 2010a) and in archeomagnetic field models (Amit et al., 2011b). In the latter we found that most intense flux patches appear near the edge of the tangent cylinder. Quasi-stationary periods with small oscillations of patches occurred more than drifts (Fig. 3.8). Detailed comparison of the archeomagnetic patches' behavior with that seen in numerical dynamos with tomographic heat flux boundary conditions suggested that core-mantle thermal coupling could be the cause of a statistical preference for some longitudes on the long term, which does not exclude significant time spent away from the preferred longitudes. This could explain the roughly coincident locations of high-latitude patches in the historical geomagnetic field with that of the time-average paleomagnetic field together with the much weaker patches intensity in the latter. Alternating eastward and westward drifts were also observed. The drifts were more westward than eastward, especially in the southern hemisphere, indicating that the time-average zonal core flow may also be driven by core-mantle thermal coupling. An average patch lifetime

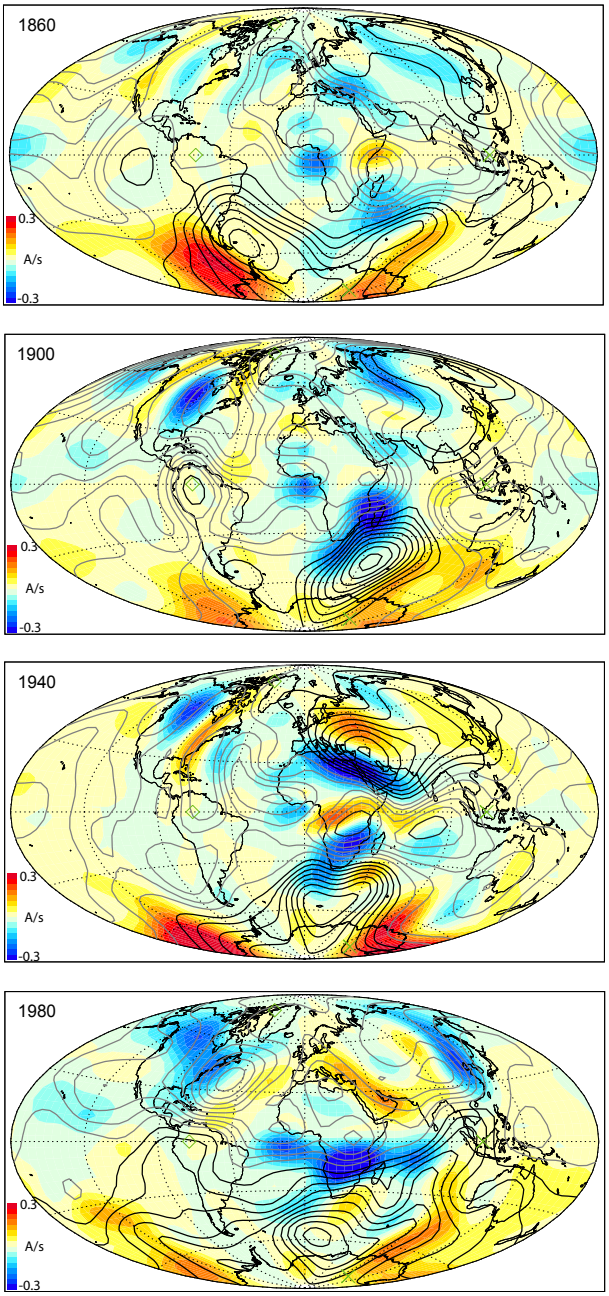

Figure 3.7: Advective contributions to equatorial dipole moment change with toroidal streamlines (black/grey denotes counter-clockwise/clockwise flow) of a helical core flow model of Amit and Olson (2006) superimposed for four snapshots. Streamline intervals are the same for all epochs. From Amit and Olson (2008).

of $\sim$ 300 years was found, which we hypothesized may indicate the vortex lifetime in the outer core.

In the same topic of tracking flux patches in archeomagnetic field models, in Terra-Nova et al. (2015) we investigated the existence and mobility of reversed flux patches (RFPs) in an archeomagnetic field model. We introduced topological algorithms to define, identify, and track RFPs. In addition, we explored the relations between RFPs and dipole changes and applied robustness tests to the RFPs. This paper is the

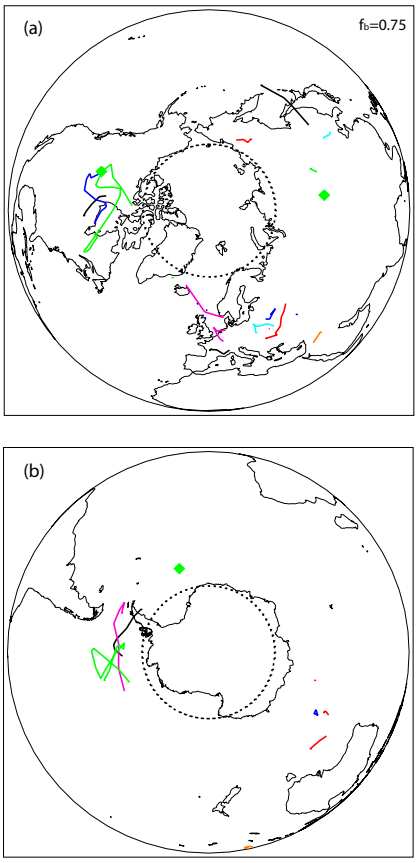

Figure 3.8: Polar views of tracked intense flux patches based on the archeomagnetic field model CALS3k.3 of Korte et al. (2009). Dotted horizontal lines denote the tangent cylinder. The locations of the time-average intense paleomagnetic flux patches of Kelly and Gubbins (1997) are denoted by green diamonds. Patches appear to be oscillated about preferred locations possibly prescribed by the lower mantle thermal heterogeneity. From Amit et al. (2011b).

outcome of an internship of Filipe Terra-Nova and serves as a methodological base for his Ph.D. thesis, both in LPG under my supervision.

Next, in Terra-Nova et al. (2016) we characterized and compared the identification and tracking of RFPs in various archaeomagnetic field models in order to assess the RFPs robustness. We found similar behaviour within a family of models but differences among different families. Similarities involve recurrent positions of RFPs, but no preferred direction of motion is found. The tracking of normal flux patches (NFPs) shows similar qualitative behaviour confirming that RFPs identification and tracking is not strongly biased by their relative weakness. We also compared the tracking of RFPs with that of the historical field model gufm1 and with seismic anomalies of the lowermost mantle to explore the possibility that RFPs have preferred locations prescribed by lower mantle lateral heterogeneity. The archaeomagnetic field model that most resembles the historical field exhibits correlation between RFPs and low seismic shear velocity in co-latitude and a shift in longitude, which we interpreted to be related

to the toroidal field lines azimuthal orientation below the CMB (Fig. 3.9). In addition, we inferred large fluid upwelling structures with a width of about 80° (Africa) and 110° (Pacific) at the top of the core. Finally, similar preferred locations of RFPs in the past 9 kyr and 3 kyr of the same archaeomagnetic field model suggests that a 3 kyr period is sufficiently long to reliably detect mantle control on core dynamics. This allows estimating an upper bound of 220-310 km for the magnetic boundary layer thickness below the CMB. This study is part of the Ph.D. thesis of Filipe Terra-Nova in LPG under my supervision.

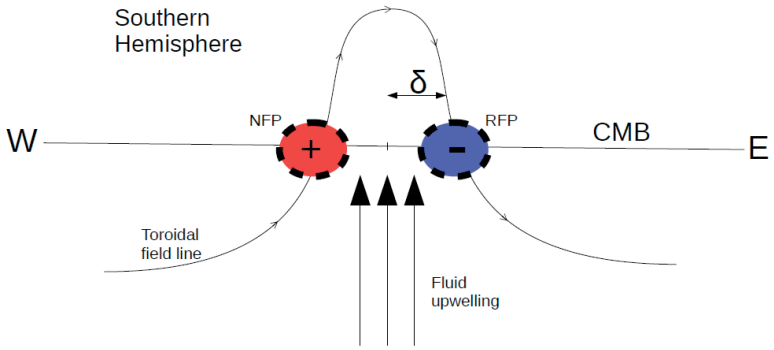

Figure 3.9: Schematic illustration of RFP emergence on the CMB due to flux expulsion of a toroidal field line by fluid upwelling. Red represents normal flux and blue reversed flux in the Southern Hemisphere. δ is the shift between the center of fluid upwelling and the center of an RFP (or an NFP). From Terra-Nova et al. (2016).

Finally, in Terra-Nova et al. (2017) we established the relation between RFPs on the CMB and minimum field intensity at Earth's surface. The South Atlantic Anomaly (SAA) is a region of strong non-dipolar field influence. The SAA is commonly attributed to RFPs on the CMB. While the SAA is clearly related to the reversed flux region below the South Atlantic, we showed that the SAA minimum intensity field point is not straightforward related to RFPs. We applied a non-linear kernel to relate the radial field at the CMB to the surface field intensity. Our results showed that the level of axial dipolarity of the field determines the stability of the relation between the SAA minimum and RFPs. The kernel analysis highlights the role of RFPs as SAA attractors and NFPs as SAA repulsors. The present position of the SAA is determined by the interplay among four robust features of the radial geomagnetic field at the CMB: the RFP below Patagonia, the South Pacific high-latitude NFP, the equatorial intense NFPs and the extent of the reversed flux region in the South Atlantic (Fig. 3.10). This paper is part of the Ph.D. thesis of Filipe Terra-Nova in LPG under my supervision.

3.2 Mantle control on planetary dynamos

Heterogeneous boundary conditions (CMB or ICB) has been invoked to explain numerous dynamo features for the Earth (e.g. Gubbins et al., 2011; Olson and Deguen, 2012; Aubert et al., 2013), Mercury (Cao

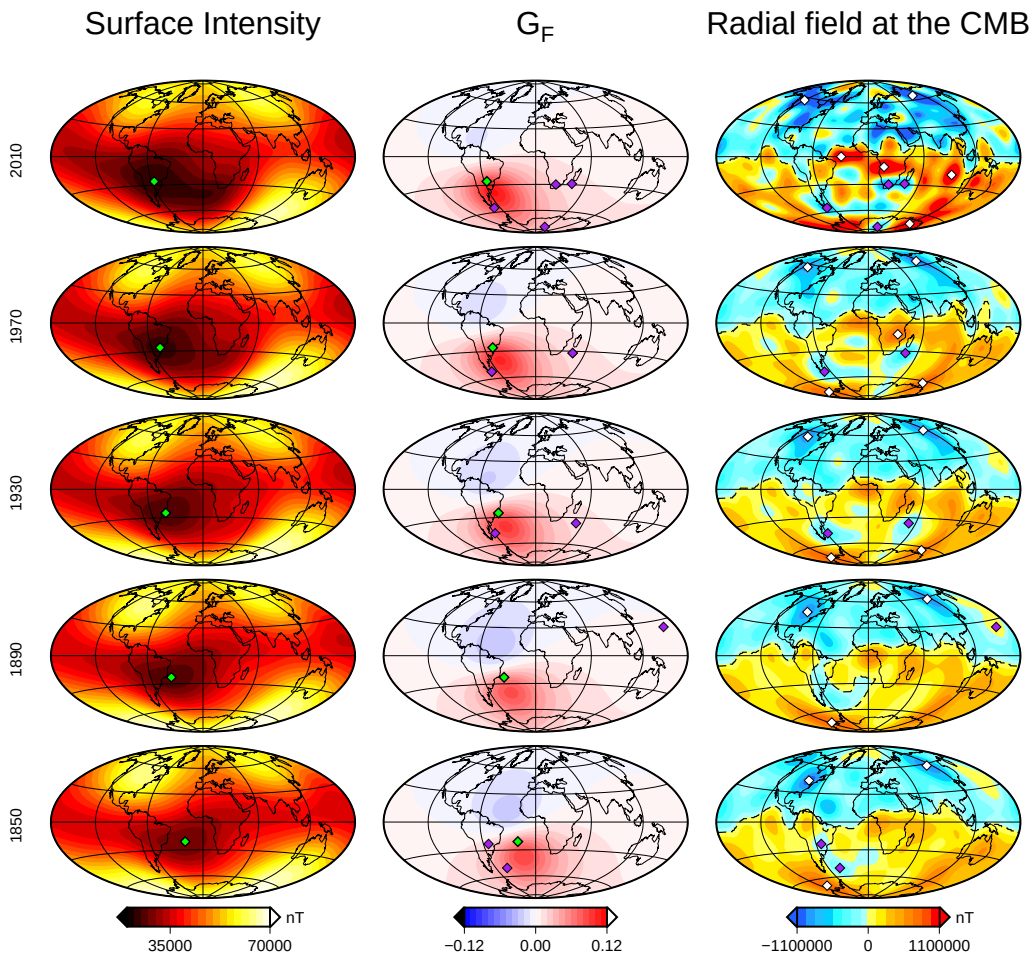

Figure 3.10: Geomagnetic field intensity at the surface (left), intensity kernel G_F (middle) and radial field at the CMB (right) for 1850, 1890, 1930, 1970 (gufm1, Jackson et al., 2000) and 2010 (CHAOS-5, Finlay et al., 2015). The SAA is denoted by green diamonds (left and middle) and the identified RFPs are denoted by purple diamonds (middle and right). Dashed lines denote the identified magnetic equator (right). Both CMB and surface fields are in nT. From Terra-Nova et al. (2017).

et al., 2014), Mars (e.g. Stanley et al., 2008) and Saturn (Stanley, 2010). For the CMB these studies often use either seismic tomography (Earth) or single harmonics (Earth and other planets) as thermal boundary conditions for their dynamo models (e.g. Olson and Christensen, 2002). Other papers about numerical dynamos affected by alternative (i.e. neither tomographic nor single harmonic) heterogeneous CMB heat flux models were summarized in a review paper (Amit et al., 2015a). For present-day Earth, the alternative patterns reflected non-thermal contributions to seismic anomalies or sharp features not resolved by global tomography models (Fig. 3.11a). Time-dependent mantle convection was invoked for capturing past conditions on Earth's CMB. For Mars, alternative patterns accounted for localized heating by a giant impact or a mantle plume (Fig. 3.11b). Recovered geodynamo-related observations included persistent morphological features of present-day core convection and the geomagnetic field as well as the variability

in the geomagnetic reversal frequency over the past several hundred Myr. On Mars the models aimed at explaining the demise of the paleodynamo or the hemispheric crustal magnetic dichotomy. We reported the main results of these studies, discussed their geophysical implications, and speculated on some future prospects.

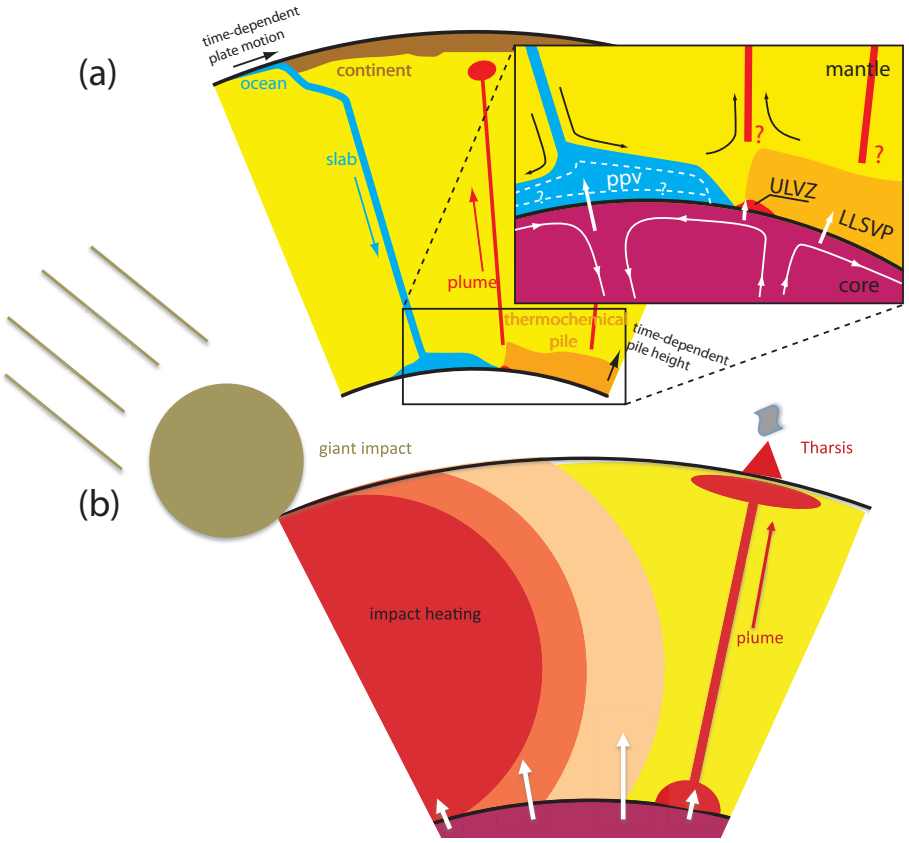

Figure 3.11: Cartoons showing various possible dynamical complexities in the Earth's (a) and Mars' (b) lowermost mantles that may motivate alternative CMB heat flux models. From Amit et al. (2015a).

In these studies I collaborated with the following researchers:

- LPG: Benoit Langalis, Gaël Choblet and Gabriel Tobie
- IPGP: Julien Aubert and Gauthier Hulot
- LMV, Clermont Ferrand: Julien Monteux
- ISTerre, Grenoble: Laurent Husson
- Max-Planck, Göttingen, Germany: Uli Christensen and Johaness Wicht
- ZAMG, Vienna, Austria: Roman Leonhardt
- USA: Peter Olson
- Academia Sinica, Taipei, Taiwan: Frédéric Deschamps
- IISC, Bangalore, India: Swarandeep Sahoo and Binod Sreenivasan

3.2.1 Persistent geodynamo features

Heterogeneity at the lowermost mantle is expected to affect dynamo morphologies via non-uniform thermal outer boundary condition on core dynamics. Seismic waves sampling the top 100 km of the Earth's inner core reveal that the eastern hemisphere is seismically faster, more isotropic and more attenuating than the western hemisphere (e.g. Tanaka and Hamaguchi, 1997). Fluid flow in the outer core can induce textural heterogeneity on the inner core solidification front. In Aubert et al. (2008) we showed that a numerical dynamo model produces a large-scale, long-term outer core flow that couples the heterogeneity of the inner core with that of the lower mantle. The main feature of this thermochemical 'wind' is a cyclonic circulation below Asia which concentrates magnetic field on the CMB at the same location, in agreement time-average palaeomagnetic field over the past 5Myr (Kelly and Gubbins, 1997) and preferred eddy locations in the time-average core flow inferred from the historical geomagnetic SV (Amit and Olson, 2006). This wind also causes anomalously high rates of light element release in the eastern hemisphere of the inner core boundary, suggesting that lateral seismic anomalies at the top of the inner core result from mantle-induced variations in its freezing rate.

Most numerical dynamo studies impose core-mantle boundary (CMB) heat flux patterns inferred from seismic tomography models. However, seismic heterogeneity may be affected by non-thermal sources, e.g. compositional or mineralogical, i.e. the seismic-thermal relation is complex. In Amit and Choblet (2012) we studied the possible impact on the geodynamo of narrow thermal anomalies in the base of the mantle, originating from either compositional heterogeneity or sharp margins of large-scale features. A heat flux boundary condition composed of a large-scale pattern and narrow ridges separating the large-scale positive and negative features was imposed on numerical dynamos. We found that hot ridges located to the west of a positive large-scale CMB heat flux anomaly produce a time-average narrow elongated upwelling, a flow barrier at the top of the core and intensified low-latitudes magnetic flux patches (Fig. 3.13). When the ridge is located to the east of a positive CMB heat flux anomaly, the associated upwelling is weaker and the homogeneous dynamo westward drift leaks, precluding persistent intense low-latitudes magnetic flux patches. These signatures of the CMB heat flux ridge are evident in the north-south component of the thermal wind balance. Based on the pattern of lower mantle seismic tomography (Masters et al., 2000), we hypothesized that hot narrow thermal ridges below central Asia and the Indian Ocean and below the American Pacific coast produce time-average fluid upwelling and a barrier for azimuthal flow at the top of the core. East of these ridges, below east Asia and Oceania and below the Americas, time-average intense geomagnetic flux patches are expected.

In the same topic of the seismic-thermal relation, in Amit et al. (2015b) we used a probabilistic tomography model to isolate the thermal part of the seismic anomaly in order to impose a more realistic

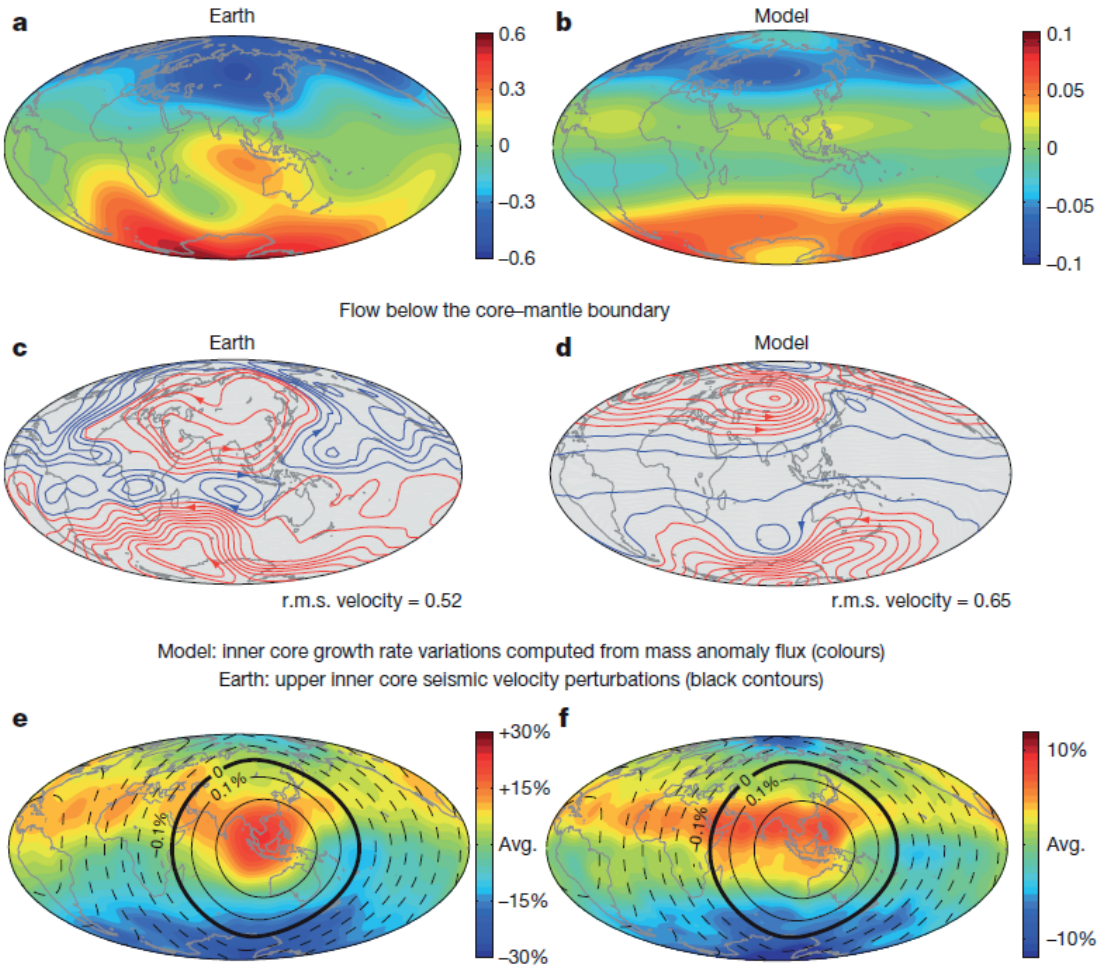

Figure 3.12: (a) Time-average palaeomagnetic field model at the CMB over the normal polarity periods of the past 5Myr (Kelly and Gubbins, 1997). (b) Time-average magnetic field at the outer boundary for the dynamo model, taken over the stable polarity periods of 0.7Myr, and filtered to spherical harmonic degree and order 5. In (a) and (b) the amplitudes are normalized relative to the values predicted by a systematic scaling study (Christensen and Aubert, 2006). (c) Streamlines of the time-average flow below the CMB obtained from geomagnetic SV inversions for the period 1840-1990 (Amit and Olson, 2006). (d) Streamlines of the time-average flow at the top of the free stream for the dynamo model. In (c) and (d) the root-mean-squared velocity is normalized relative to the values predicted by thermal wind scaling (Aubert et al., 2007). (e) Anomalies of buoyancy flux extracted from the inner boundary for the dynamo model. The black contours show an upper inner core seismic velocity perturbation model (Tanaka and Hamaguchi, 1997). (f) As in (e) for another dynamo model. From Aubert et al. (2008).

CMB heat flux pattern on the outer boundary of numerical dynamo simulations.We demonstrated that on time-average these dynamo models have more low-latitude convective and magnetic activity than corresponding models with conventional tomographic heat flux. In addition, the low-latitude magnetic flux and kinetic energy contributions are more time-dependent in the dynamo models with a probabilistic tomography heat flux, and thus may recover the observed latitudinal distribution of geomagnetic flux on the CMB, which we proposed as a morphological criterion for Earth-like dynamo models.

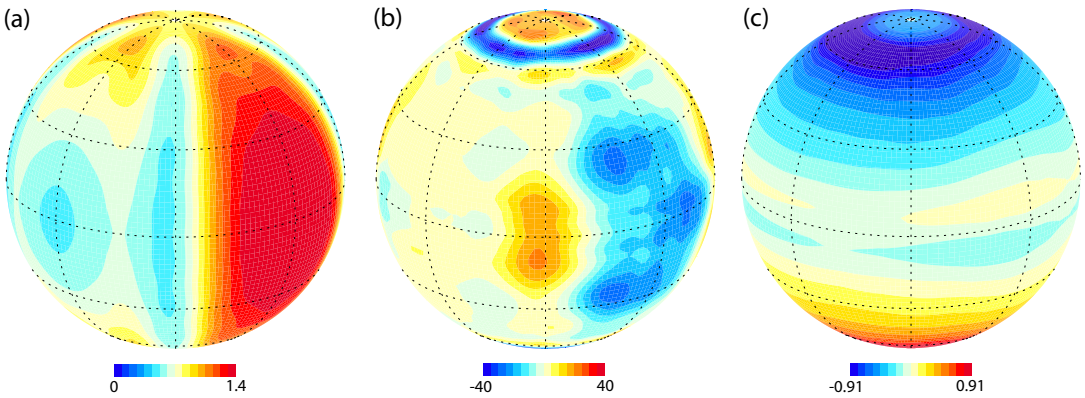

Figure 3.13: Images from a numerical dynamo simulation with a CMB heat flux of spherical harmonic Y_2^2 with superimposed hot ridges at the boundaries of hot and warm large-scale structures. (a) Imposed outer boundary heat flux normalized by the mean heat flux; (b) Time-average upwelling at the top of the free stream just below the Ekman boundary layer; (c) Time-average radial magnetic field on the outer boundary. The upwelling is given in units of ν/D^2. The radial magnetic field is given in units of $\sqrt{\rho\mu_0\lambda\Omega}$, where ρ is the fluid density and μ_0 the permeability of free space. The hot ridge separating the large-scale CMB heat flux structures (a) induces local elongated fluid upwelling (b) that concentrates magnetic field at the equatorial region east of the ridge (c). From Amit and Choblet (2012).

3.2.2 Paleomagnetic reversal frequency

Both the amplitude and the pattern of CMB heat flux may affect reversal frequency. Therefore, time-dependent mantle convection may explain the large variability of paleomagnetic reversal frequency. However, the Cretaceous Normal Superchron occurred when plates moved fast, in contrast to the expected quite conditions for the geodynamo during that period (Olson et al., 2013). In Olson and Amit (2014) we derived scaling relationships for the frequency of magnetic polarity reversals in numerical dynamos powered by thermochemical convection. We showed that the average number of reversals per unit of time scales with the local Rossby number Ro_ℓ of the convection. With uniform CMB heat flux, polarity reversals were absent below a critical value $Ro_{\ell crit} \equiv 0.05$, beyond which reversal frequency increased approximately linearly with Ro_ℓ. The relative standard deviation of the dipole intensity fluctuations increases with reversal frequency and Ro_ℓ. With heterogeneous CMB heat flux that models the large-scale seismic heterogeneity in Earth's lower mantle, reversal frequency also exhibited linear dependence on Ro_ℓ, and increased approximately as the square root of the amplitude of the CMB heterogeneity (Fig. 3.14). Applied to the history of the geodynamo, these results implied lower CMB heat flux with $Ro_\ell < Ro_{\ell crit}$ during magnetic superchrons and higher, more heterogeneous CMB heat flux with $Ro_\ell > Ro_{\ell crit}$ when geomagnetic reversals were frequent. They also suggested that polarity reversals may have been commonplace in the early history of other terrestrial planets. We found that zonal heterogeneity in CMB heat flux produces special effects. Close to $Ro_{\ell crit}$ enhanced equatorial cooling

at the CMB increases reversal frequency by concentrating magnetic flux at low latitudes, whereas far beyond $Ro_{\ell crit}$ enhanced polar cooling at the CMB increases reversal frequency by amplifying outer core convection.

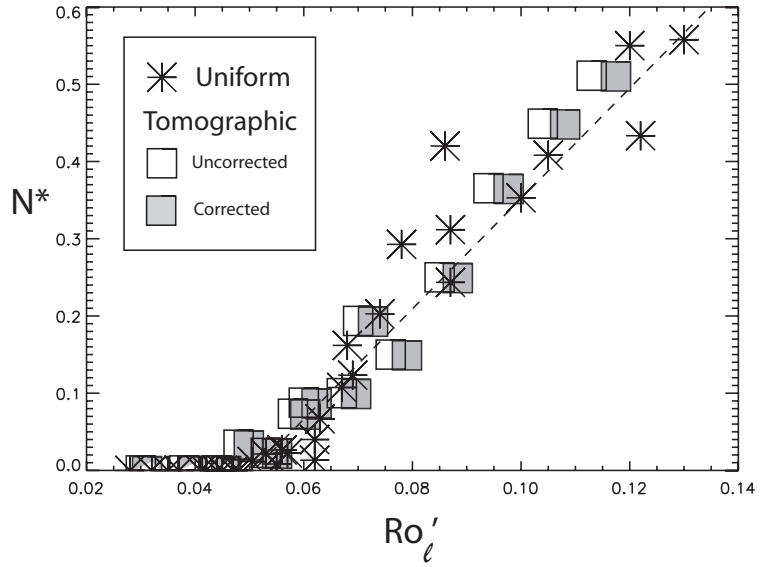

Figure 3.14: Non-dimensional reversal frequency versus corrected local Rossby number for boundary heterogeneity from dynamos with uniform and tomographic boundary conditions. Dashed line is the fit to the corrected values. Open symbols are tomographic dynamos with uncorrected local Rossby number. Reversal frequency increases linearly with the level of inertia in the core, which may also be augmented by the CMB heterogeneity. From Olson and Amit (2014).

In the same topic of unraveling the causes of the reversal frequency variability, in Amit and Olson (2015) we showed that time variations in the height of lower mantle thermochemical piles produce variations in CMB heat flux that can control the rate at which geomagnetic polarity reversals occur. Superplumes growth increased the mean CMB heat flux and its lateral heterogeneity, thereby stimulating polarity reversals, whereas superplumes collapse decreased the mean CMB heat flux and its lateral heterogeneity, inhibiting polarity reversals (Fig. 3.15). Our results suggested that the long, stable polarity geomagnetic superchrons such as occurred in the Cretaceous, Permian, and earlier in the geologic record were initiated and terminated by the collapse and growth of lower mantle superplumes, respectively.

Based on the results of Amit and Olson (2015), we inverted the paleomagnetic record of reversals to the changes in CMB heat flux during the past 300 Myrs. In Olson and Amit (2015) we quantified the hypothesis that the modulation of geomagnetic reversal frequency, including geomagnetic superchrons, results from changes in CMB heat flux related to growth and partial collapse of the two seismically-imaged lower mantle superplumes. We parameterized the reversal frequency sensitivity from numerical dynamos in terms of average CMB heat flux normalized by the difference between the present-day CMB heat flux and the CMB heat flux at geomagnetic superchron onset. A low-order polynomial fit to the

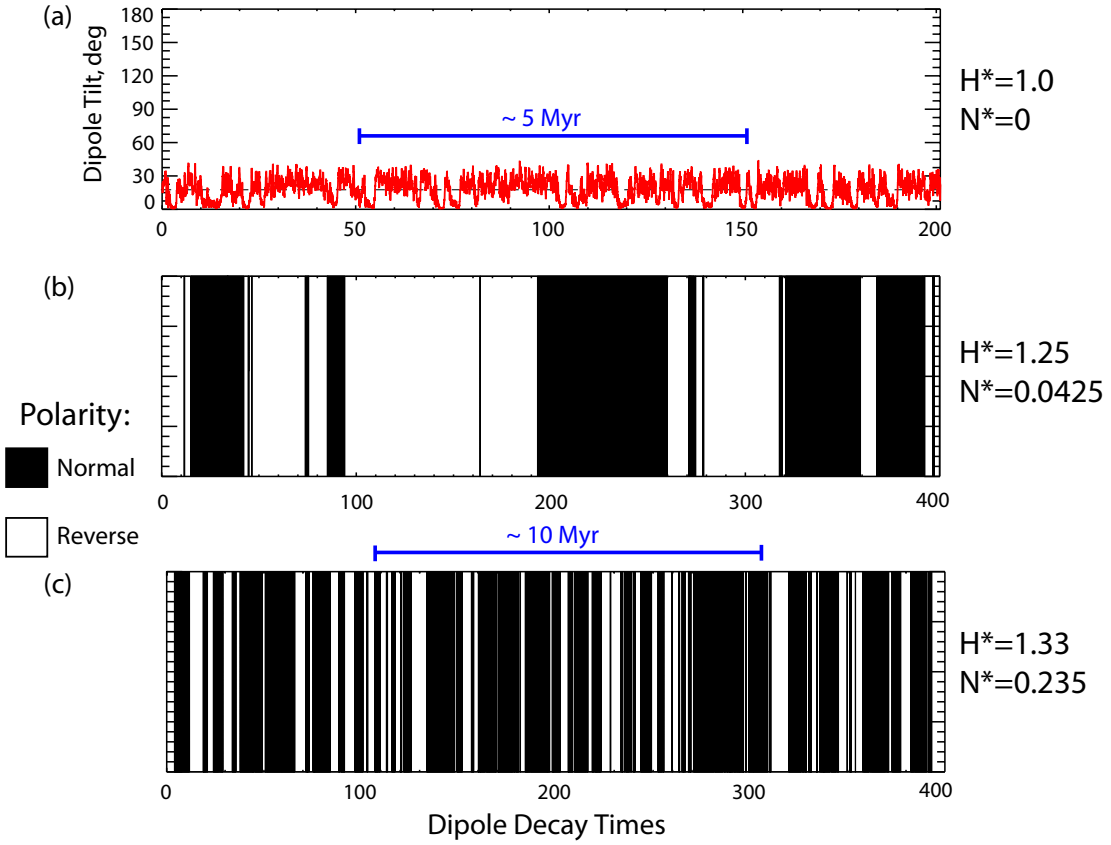

Figure 3.15: Magnetic polarity timeseries in the dual pile dynamos with increasing D" thickness H^*. Time is given in units of dipole decay time, mean non-dimensional reversal frequency is N^*. (a) Dipole tilt timeserie (red) and its average (dashed black) in a non-reversing dynamo; (b, c) Polarity records for reversing dynamos. Reversal frequency increases with increasing piles thickness. From Amit and Olson (2015).

0-300Ma Geomagnetic Polarity Time Scale (GPTS) revealed that a decrease in CMB heat flux relative to present-day of $\sim$30% can account for the Cretaceous Normal Polarity and Kiaman Reversed Polarity Superchrons, whereas the hyper-reversing periods in the Jurassic require a CMB heat flux equal to or higher than present-day. Possible links between GPTS transitions, large igneous provinces (LIPs), and the two lower mantle superplumes were explored. Lower mantle superplumes growth and collapse induced GPTS transitions by increasing and decreasing CMB heat flux, respectively. Age clusters of major LIPs postdate transitions from hyper-reversing to superchron geodynamo states by 30-60Myr, suggesting that superchron onset may be contemporaneous with LIP-forming instabilities produced during collapses of lower mantle superplumes.

We also tackled the problem from the mantle side. In Choblet et al. (2016) we presented numerical models of mantle dynamics forced by plate velocities history in the last 450 Ma. The lower mantle rheology and the thickness of a dense basal layer systematically vary and several initial procedures were

considered for each case. The resulting evolution of the CMB heat flux was analyzed in terms of criteria known to promote or inhibit reversals in numerical dynamos. Our results show that most models present a rather dynamic lower mantle with the emergence of two thermochemical piles dating only from about 200 Ma but a small minority of models present stationary piles over the last 450 Myr. At present, the composition field obtained in our models is found to correlate better with tomography than the temperature field. In addition, the CMB heat flux pattern slightly differs from the average temperature field in the 100-km thick mantle layer above it. The evolution of the mean CMB heat flux or of the amplitude of heterogeneities seldom presents the expected correlation with the evolution of the paleomagnetic reversal frequency suggesting these effects cannot explain the observations. In contrast, our analysis favors either "inertial control" on the geodynamo associated to polar cooling (Olson and Amit, 2014) or break of Taylor columns in the outer core as sources of increased reversal frequency (Fig. 3.16). Overall, the most likely candidates among our mantle dynamics models involve a viscosity increase in the mantle equal or smaller than 30: models with a discontinuous viscosity increase at the transition zone tend to agree better at present with observations of seismic tomography, but models with a gradual increase provide better correlation coefficients with some criteria proposed to affect reversal frequency.

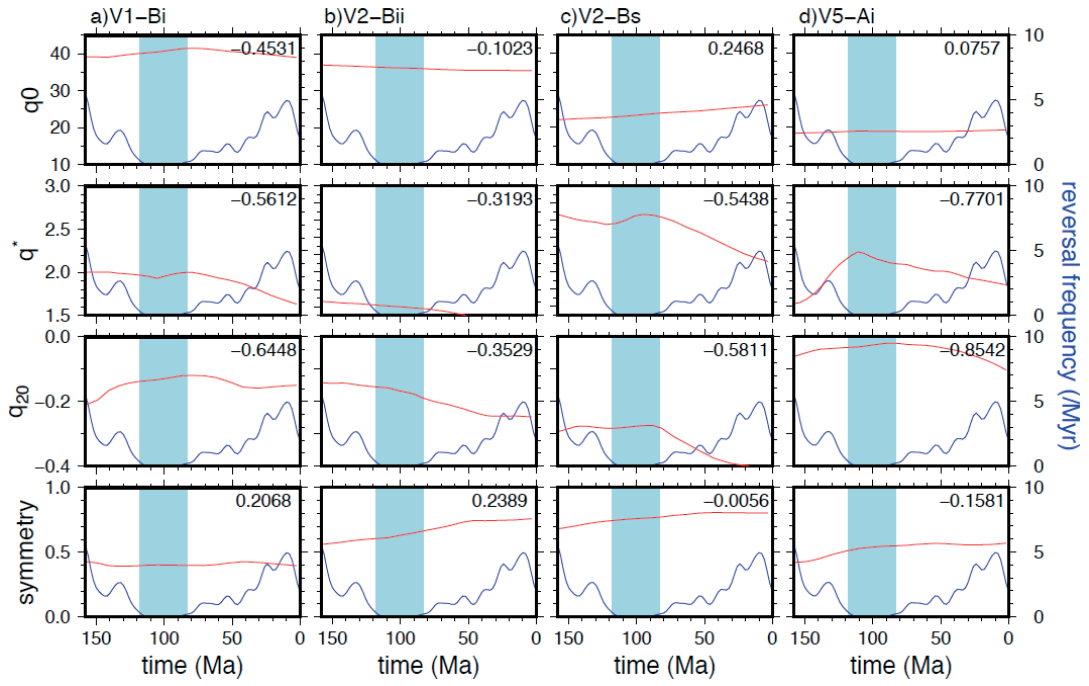

Figure 3.16: Time evolution of criteria on CMB heat flux (red) compared to the reversal frequency (blue) in the case of four selected numerical mantle convection models (a-d). The number in each panel (right upper corner) denotes the correlation coefficient between the two curves. The light blue rectangle denotes the Cretaceous Normal Superchron (CNS). From Choblet et al. (2016).

3.2.3 Martian hemispheric dichotomy

The hemispheric dichotomy in the crustal magnetic field intensity on Mars may also be a consequence of mantle control on the past dynamo of the planet. In Amit et al. (2011a) we used numerical dynamos driven by purely volumetric internal heating with imposed degree-1 heat flux heterogeneities to study mantle control on the past dynamo of Mars. We quantified both south-north and east-west magnetic field dichotomies from time-average properties that were calculated according to two different end member crust formation scenarios. Our results indicated that a moderate heat flux anomaly may have been sufficient for obtaining the observed dichotomy. Because of the excitation of a strong equatorial upwelling in the dynamo, the efficiency of a mantle heterogeneity centered at the geographical pole in producing a south-north dichotomy is much higher than that of an heterogeneity centered at the equator in producing an east-west dichotomy. These results argue against a significant True Polar Wander event with major planet re-orientation after the cessation of the dynamo

In the same topic of the Martian hemispheric magnetic dichotomy, in Monteux et al. (2015) we modeled the effects of a giant impact on the Martian magnetic field by imposing an impact induced thermal heterogeneity, and the subsequent heat flux heterogeneity, on the Martian CMB. The CMB heat flux lateral variations as well as the reduction in the mean CMB heat flux were determined by the size and geographic location of the impactor. A polar impactor led to a north-south hemispheric magnetic dichotomy that is stronger than an east-west dichotomy created by an equatorial impactor. The amplitude of the hemispheric magnetic dichotomy was mostly controlled by the horizontal Rayleigh number Ra_h which represents the vigor of the convection driven by the lateral variations of the CMB heat flux. We showed that, for a given Ra_h, an impact induced CMB heat flux heterogeneity is more efficient than a synthetic degree-1 CMB heat flux heterogeneity in generating strong hemispheric magnetic dichotomies (Fig. 3.17). Large Ra_h values were needed to get a dichotomy as strong as the observed one, favoring a reversing paleo-dynamo for Mars. Our results imply that an impactor radius of 1000 km could have recorded the magnetic dichotomy observed in the Martian crustal field only if very rapid post-impact magma cooling took place.

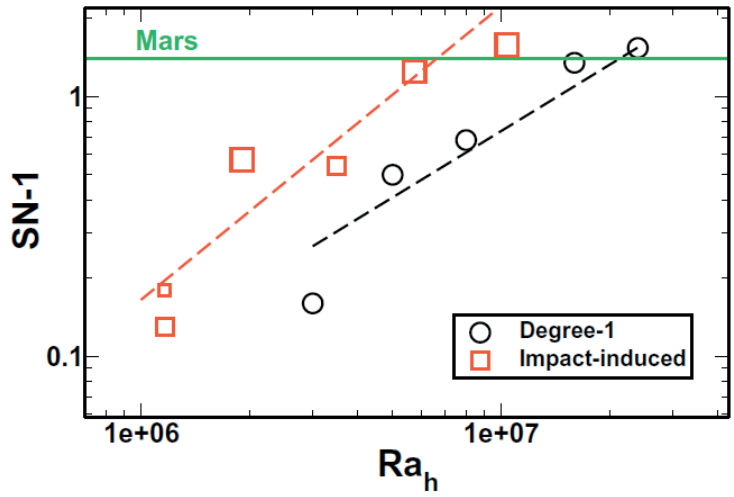

Figure 3.17: South-north dichotomy of the magnetic field intensity on Mars' surface as a function of the horizontal Rayleigh number. The black circles are the values obtained for the synthetic Y_1^0 CMB heat flux patterns. The red squares are the values obtained in cases of polar impact driven CMB heat flux patterns. The size of the red symbols increases with the size of the impactor. The corresponding power law fits are plotted with dashed lines. The green horizontal line represents the Martian value of south-north dichotomy from Amit et al. (2011a) based on observations of the Martian crustal magnetic field. For a given horizontal Rayleigh number the dynamo models with impact driven CMB heat flux produce larger south-north dichotomy than the dynamo models with degree-1 CMB heat flux. From Monteux et al. (2015).

Chapter 4

Perspectives

My future research perspectives are mostly a natural continuation of my work in recent years. Here I therefore tried to maintain as close as possible thematic division as in chapter 3. Notable new research avenues include dynamical origins of magnetic jerks (section 4.1.3 in collaboration with Katia Pinheiro, ON, Brazil) and fluid dynamics in sub-oceans of icy satellites (section 4.3 in collaboration with Gabriel Tobie, LPG). In addition, in modeling persistent dynamo features I have been so far focusing on the Earth (section 3.2.1) and Mars (section 3.2.3), while in the future I will model the persistent features of Mercury's field (section 4.2.1 in collaboration with Gaël Choblet and other co-authors). These future research perspectives are summarized below.

4.1 Rapid Core dynamics

4.1.1 A new method to infer the core flow from the geomagnetic secular variation

A possible culprit of core flow inversions from the geomagnetic SV is that theoretical assumptions may affect the solutions more than the data itself. We will design a new core flow inversion method based on minimization of field-aligned flow. The minimization of field-aligned flow is not motivated by the absence of such a flow in the core; On the contrary, our numerical dynamo models clearly show that the flow has a significant field-aligned component (Peña et al., 2016). The reason for the minimization of field-aligned flow is that it does not produce any SV and as such it is not constrained by the data. In addition, the method relies on consideration of advection and stretching solutions separately. This study is part of the Ph.D. work of Diego Peña under my supervision. In this work I will collaborate with Diego Peña and Katia Pinheiro (ON, Rio de Janeiro, Brazil), Filipe Terra-Nova (LPG) and Peter Olson.

4.1.2 More inferences from the geomagnetic secular variation

It has been argued that the SV timescales of the geomagnetic field vary as $1/\ell$ (where ℓ is the spherical harmonic degree), except for the dipole. We will investigate the validity of these scaling laws for sub-families of the geomagnetic field and SV spectra. Preliminary results using spectra from geomagnetic field models and numerical dynamo simulations reveal that the SV timescales decomposed into symmetric and asymmetric parts also vary as $1/\ell$, again except for the dipole. The asymmetric/symmetric SV timescales are persistently larger/smaller than the total, respectively. The symmetric dipole SV timescale in recent years and in long-term time-averages from numerical dynamos is below the extrapolated $1/\ell$ curve, whereas before $\sim$1965 the geomagnetic dipole tilt was rather steady and the symmetric dipole SV timescale exceeded the extrapolated $1/\ell$ curve. We hypothesize that the period of nearly steady geomagnetic dipole tilt between 1810-1965 was anomalous for the geodynamo. Overall, the deviation of the dipole SV timescales from the $1/\ell$ curves may indicate that magnetic diffusion contributes to the dipole SV more than it does for higher degrees. This study is part of the Master work of Maélie Coutelier in LPG under my supervision. In this work I will collaborate with Maélie Coutelier (LPG) and Uli Christensen (Max-Planck, Göttingen, Germany).

We will extend the work of Peña et al. (2016) to study magnetic field stretching at mid-shell of numerical dynamos. Because at depth the radial flow is non-zero, the radial magnetic induction equation there contains two additional terms involving radial advection of radial field and tangential shear of toroidal field. We will analyze and compare these four inductive SV contributions to the radial field at depth: tangential and radial advection of radial field, tangential stretching of radial field and tangential shear of toroidal field. Special foicus will be given to deep roots of intense NFPs on the CMB. This study is the second part of the Ph.D. work of Diego Peña in ON (Rio de Janeiro, Brazil) under my supervision. In this work I will collaborate with Diego Peña and Katia Pinheiro (On, Rio de Janeiro, Brazil).

4.1.3 Dynamical origins of magnetic jerks

Geomagnetic jerks are the shortest temporal variations of the core magnetic field registered by observatories and satellites. Neither the physical mechanism producing such abrupt changes nor their observed characteristics at the Earth's surface are well understood and remain as outstanding issues in geomagnetism. We will use synthetic core flow models to solve the radial magnetic induction equation in order to reproduce geomagnetic jerk characteristics. We will examine the dependence of magnetic jerk occurrence times and their characteristics on each type of flow. We will apply a polynomial fit in order to characterize and compare jerk occurrence times and amplitudes those from observatory data. Preliminary results demonstrate even steady flow models may generate secular acceleration changes of sign and reproduce

important characteristics of geomagnetic jerks, such as non-simultaneous behaviour, non-global pattern, spatial variability of amplitudes for each SV component and stronger jerks in the r component (Fig. 4.1). However, our synthetic models reproduce too weak amplitudes compared to geomagnetic data. The missing ingredients that may reproduce stronger and sharper magnetic jerks may include time-dependent flow models, small scale field features and mantle filtering effects. In this work I will collaborate with Katia Pinheiro (ON, Rio de Janeiro, Brazil) and Filipe Terra-Nova (LPG).

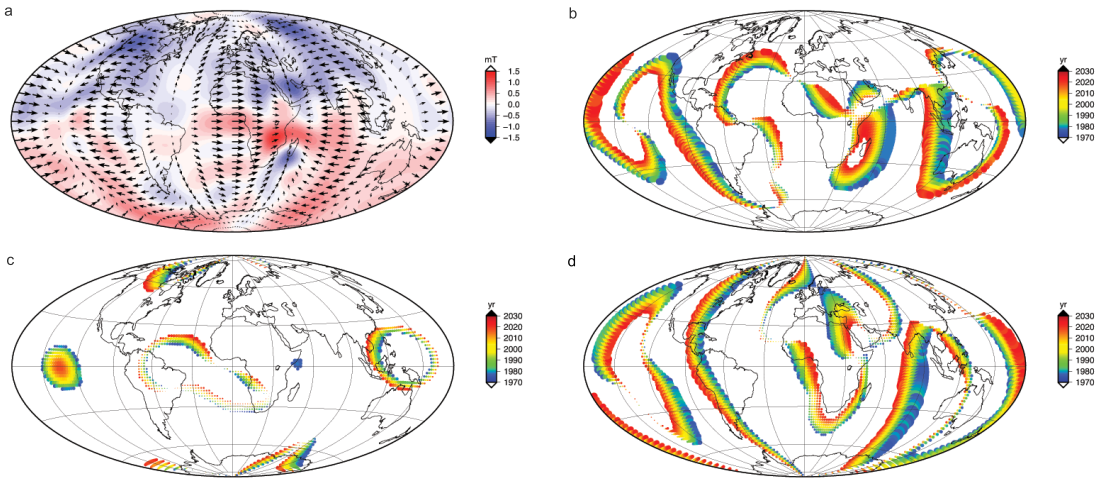

Figure 4.1: (a) Synthetic toroidal flow model $\mathcal{P}_2^{2s}$ (arrows) and resulting radial magnetic field (colors) for a snapshot 30 years after the simulation started. (b-d) Magnetic jerks occurrence times (color) and amplitudes (sizes of circles) in the radial, co-latitudinal and longitudinal components, respectively. From Pinheiro et al. (in preparation).

4.2 Mantle control on planetary dynamos

4.2.1 Mantle control on the South Atlantic Anomaly

It is under debate whether the present-day location of the South Atlantic Anomaly (SAA) in Brazil is a transient or steady feature prescribed by lower mantle heterogeneity. We will run a set of numerical dynamo simulations with heterogeneous CMB heat flux inferred from lower mantle seismic tomography models (Masters et al., 2000) to determine the persistent location of the minimum intensity at Earth's surface. Results will be compared among a variety of control parameters, in particular the Rayleigh number (representing the strength of convection) and the amplitude of CMB heat flux heterogeneity. Preliminary results show agreement between preferred longitudes of minimum surface intensity in dynamo models and in geomagnetic field models spanning decadal to millenial timescales (Fig. 4.2). In this work I will collaborate with Filipe Terra-Nova and Gaël Choblet (LPG).

4.2.2 Mantle control on Mercury's dynamo

We will attempt to explain the enigmatic morphology of Mercury's field using mantle control. Cao et al. (2014) found that combining CMB heat flux patterns that involve equatorial cooling (e.g. $-Y_2^0$) and a global volumetric heating induces a hemispheric convective mode. The resulting magnetic field is also hemispheric, as observed by the MESSENGER mission (Anderson et al., 2012). However, Cao et al. (2014) could not justify the presence of such thermal heterogeneity at the lower mantle of Mercury. We will show that a CMB heat flux pattern with dominant equatorial heating (though more complex than a single harmonic) may arise from tidal heating models of Mercury's mantle. This pattern will be imposed as a boundary condition on numerical dynamos with similar convection style and parameters as in Cao et al. (2014) to reproduce the observed field hemisphericity using a realistic CMB heat flux model. Other aspects of Mercury's field, in particular its axisymmetry and low intensity, will also be investigated. In this work I will collaborate with Gaël Choblet, Gabriel Tobie, Benoit Langlais and Erwan Thébault (LPG), Joana Oliveira (IPGP) and Marie Běhounková and Ondřej Čadek (Charles University, Prague, Czech Republic).

4.3 Fluid dynamics in sub-oceans of icy satellites

We will use numerical models of rotating convection in thin spherical shell to simulate the dynamics in sub-oceans of icy satellites. We will focus on the heat flux across the two boundaries which may affect the dynamics in the envelopes above and below. Preliminary results show that at the boundaries either equatorial cooling (Fig. 4.3) or polar cooling prevail, deepending on the role of inertia in the models (Soderlund et al., 2014). Stronger inertial effects give weaker time-average heat flux heterogeneities with a transition to polar cooling beyond a critical Rossby number. In this work I will collaborate with Gabriel Tobie (LPG).

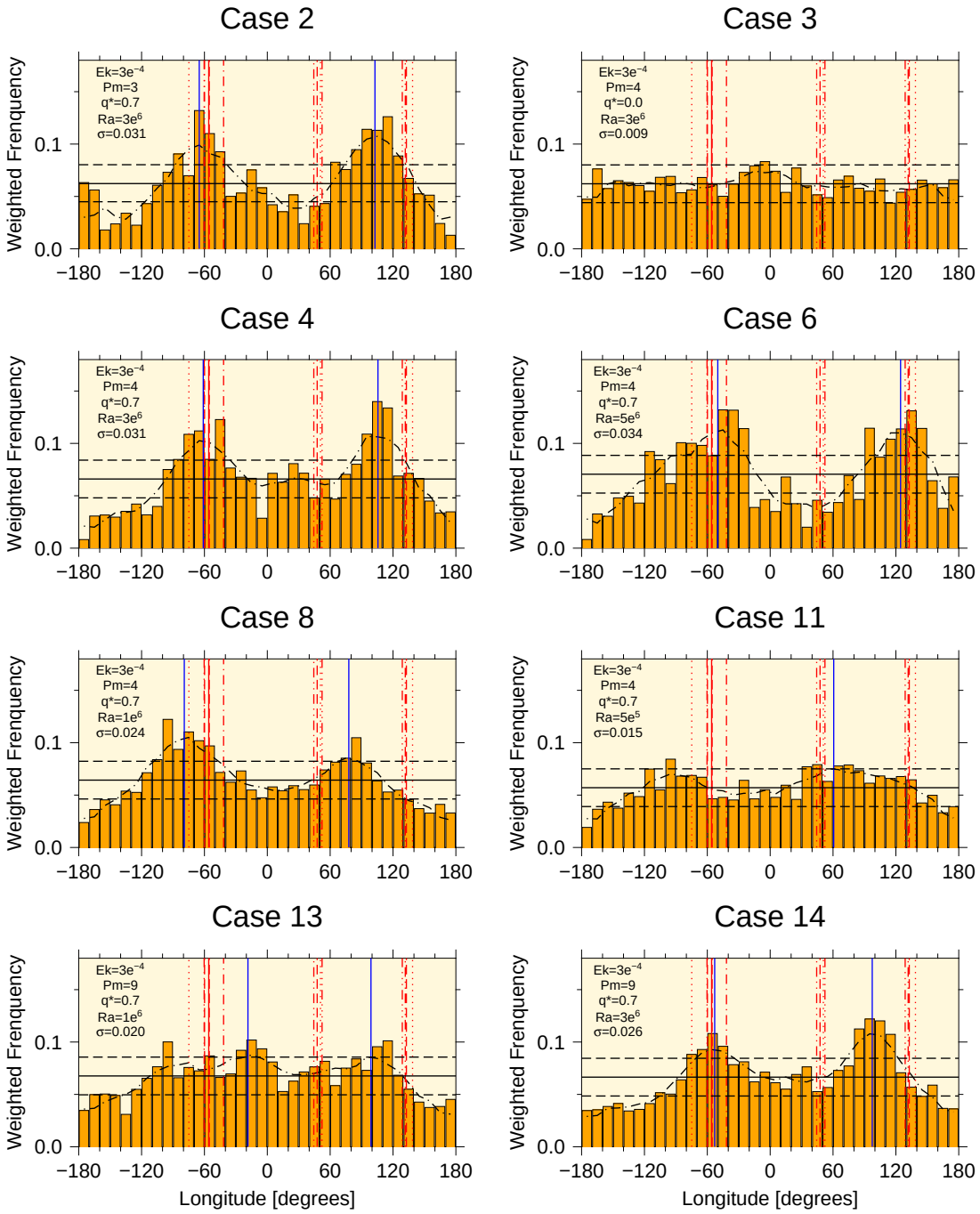

Figure 4.2: Frequency of surface intensity minimum in longitude bins in a set of numerical dynamos. The control parameters of each model are given in the upper left of each subplot. Also given the height of the peaks σ with respect to the mean which represents the strength of the heterogeneous boundary effect. Case 3 (top right) is with homogeneous boundary conditions and serves as a reference for the level of spatial heterogeneity due to finite run time. Horizontal solid lines and horizontal dahsed lines are the mean and ± 2 standard deviations from case 3. A peak above ± 2 standard deviations is considered statistically significant. Vertical blue lines denote persistent surface minima in the dynamo models. Vertical red lines denote persistent surface minima in various modern (Finlay et al., 2015), historical (Jackson et al., 2000) and archeomagnetic (Korte et al., 2009; Korte and Constable, 2011; Licht et al., 2013; Nilsson et al., 2014) field models, with each linestyle denoting another model.

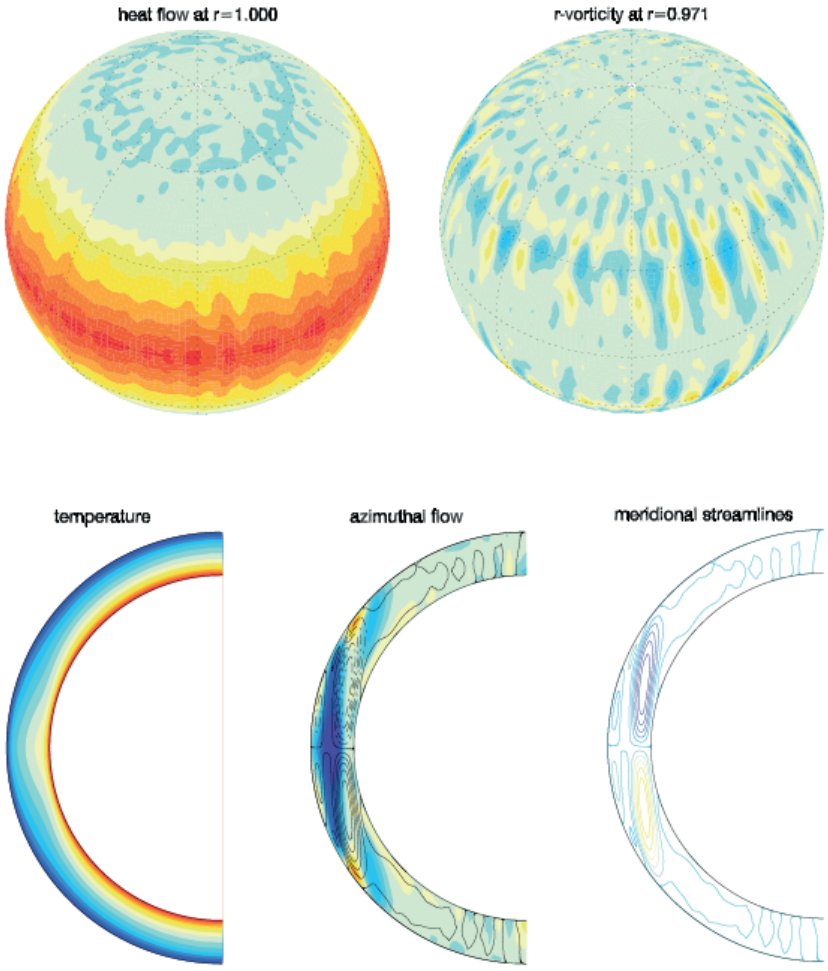

Figure 4.3: Images from a long-term time-average of a rotating-convection simulation. A thin shell with a ratio of inner to outer radii of 0.8 is employed. The control parameters are the Ekman number $E = 10^{-3}$, the Rayleigh number $Ra = 2 \cdot 105$ and the Prandtl number $Pr = 1$. Top: Heat flux across the outer boundary (left) and radial vorticity just below the Ekman boundary layer (right); Bottom: Zonal profiles of temperature (left), azimuthal flow (middle) and meridional flow (right). Solid/red contours denote anti-clockwise circulation, dashed/blue contours denote clockwise circulation. From Amit and Tobie (in preparation).

Bibliography

Alexandrescu, M., Gilbert, D., Hulot, G., LeMouël, J. L., Saracco, G., 1996. Worldwide wavelet analysis of geomagnetic jerks. J. Geophys. Res. (B10), 21975–21994.

Anderson, B. J., Johnson, C. L., Korth, H., Purucker, M. E., Winslow, R. M., Slavin, J. A., Solomon, S. C., McNutt, R. L., Raines, J. M., Zurbuchen, T. H., 2012. The global magnetic field of Mercury from MESSENGER orbital observations. Science 333, 1859–1862.

Aubert, J., 2005. Steady zonal flows in spherical shell fluid dynamos. J. Fluid Mech. 542, 53–67.

Aubert, J., Finlay, C. C., Fournier, F., 2013. Bottom-up control of geomagnetic secular variation by the Earth's inner core. Nature 502, 219–223.

Aurnou, J., Andreadis, S., Zhu, L., Olson, P., 2003. Experiments on convection in Earth's core tangent cylinder. Earth Planet. Sci. Lett. 212, 119–134.

Bloxham, J., Jackson, A., 1991. Fluid flow near the surface of the Earth's outer core. Rev. Geophys. 29, 97–120.

Cao, H., Aurnou, J. M., Wicht, J., Dietrich, W., Soderlund, K. M., Russell, C. T., 2014. A dynamo explanation for Mercury's anomalous magnetic field. Geophys. Res. Lett. 41, doi:10.1002/2014GL060196.

Christensen, U., Aubert, J., 2006. Scaling properties of convection-driven dynamos in rotating spherical shells and application to planetary magnetic fields. Geophys. J. Int. 166, 97–114.

Christensen, U., Olson, P., Glatzmaier, G., 1998. A dynamo model interpretation of geomagnetic field structures. Geophys. Res. Lett. 25, 1565–1568.

Christensen, U., Tilgner, A., 2004. Power requirement of the geodynamo from ohmic losses in numerical and laboratory dynamos. Nature 439, 169–171.

Christensen, U., Wardinsky, I., Lesur, V., 2012. Timescales of geomagnetic secular acceleration in satellite field models and geodynamo models. Geophys. J. Int. 190, 243–254.

Chulliat, A., Hulot, G., Newitt, L. R., 2010. Magnetic flux expulsion from the core as a possible cause of the unusually large acceleration of the North magnetic pole during the 1990s. J. Geophys. Res. 115, B07101, doi:10.1029/2009JB007143.

Chulliat, A., Olsen, N., 2010. Observation of magnetic diffusion in the Earth's outer core from Magsat, Orsted and CHAMP data. J. Geophys. Res. 115, doi:10.1029/2009JB006994.

Finlay, C., Olsen, N., Tøffner-Clausen, L., 2015. DTU candidate field models for IGRF-12 and the CHAOS-5 geomagnetic field model. Earth Planets Space 67:114.

Finlay, C. C., Aubert, J., Gillet, N., 2016. Gyre-driven decay of Earth's magnetic dipole. Nature Commun. 7, 10422.

Gillet, N., Jault, D., Finlay, C. C., 2015. Planetary gyre, time-dependent eddies, torsional waves and equatorial jets at the Earth's core surface. J. Geophys. Res. 120, 3991–4013.

Gillet, N., Pais, M. A., Jault, D., 2009. Ensemble inversion of time-dependent core flow models. Geochem. Geophys. Geosyst. 10, Q06004.

Gillet, N., Schaeffer, N., Jault, D., 2011. Rationale and geophysical evidence for quasi-geostrophic dynamics within the Earth's core. Phys. Earth Planet. Inter. 187, 380–390.

Glatzmaier, G., Coe, R., Hongre, L., Roberts, P., 1999. The role of the earth's mantle in controlling the frequency of geomagnetic reversals. Nature 401, 885–890.

Gubbins, D., 2003. Thermal core-mantle interactions: theory and observations. In: Dehant, V., Creager, K., Karato, S., Zatman, S. (Eds.), *Earth's Core: dynamics, structure and rotation*. AGU Geodynamics Series American Geophysical Union.

Gubbins, D., Sreenivasan, B., Mound, J., Rost, S., 2011. Melting of the Earth's inner core. Nature 473, 361–363.

Gubbins, D., Willis, P., Sreenivasan, B., 2007. Correlation of Earth's magnetic field with lower mantle thermal and seismic structure. Phys. Earth Planet. Inter. 162, 256–260.

Holme, R., 2007. Large-scale flow in the core. In: Olson, P. (Ed.), *Treatise on Geophysics*. Vol. 8. Elsevier Science.

Holme, R., Olsen, N., 2006. Core surface flow modelling from high-resolution secular variation. Geophys. J. Int. 166, 518–528.

Hulot, G., Eymin, C., Langlais, B., Mandea, M., Olsen, N., 2002. Small-scale structure of the geodynamo inferred from oersted and magsat satellite data. Nature 416, 620–623.

Jackson, A., Jonkers, A., Walker, M., 2000. Four centuries of geomagnetic secular variation from historical records. Phil. Trans. R. Soc. Lond. A358, 957–990.

Kelly, P., Gubbins, D., 1997. The geomagnetic field over the past 5 million years. Geophys. J. Int. 128, 315–330.

Konôpková, Z., McWilliams, R. S., Gómez-Pérez, N., Goncharov, A. F., 2016. Direct measurement of thermal conductivity in solid iron at planetary core conditions. Nature 534, 99–101.

Korte, M., Constable, C., 2011. Improving geomagnetic field reconstructions for 0-3 ka. Phys. Earth Planet. Inter. 3–4, 247–259.

Korte, M., Donadini, F., Constable, C., 2009. The geomagnetic field for 0-3ka: 2. a new series of time-varying global models. J. Geophys. Res. 10, Q06008, doi:10.1029/2008GC002297.

Kutzner, C., Christensen, U., 2004. Simulated geomagnetic reversals and preferred virtual geomagnetic pole paths. Geophys. J. Int. 157, 1105–1118.

LeMouël, J.-L., 1984. Outer core geostrophic flow and secular variation of Earth's magnetic field. Nature 311, 734–735.

Lhuillier, F., Fournier, A., Hulot, G., Aubert, J., 2011. The geomagnetic secular variation timescale in observations and numerical dynamo models. Geophys. Res. Lett. 38, L09306, doi:10.1029/2011GL047356.

Licht, A., Hulot, G., Gallet, Y., Thébault, E., 2013. Ensembles of low degree archeomagnetic field models for the past three millennia. Phys. Earth Planet. Inter. 224, 38–67.

Masters, G., Laske, G., Bolton, H., Dziewonski, A., 2000. The relative behavior of shear velocity, bulk sound velocity, and compressional velocity in the mantle: Implications for chemical and thermal structure. In: Karato, S., Forte, A., Liebermann, R., Masters, G., Stixrude, L. (Eds.), *Earths deep interior*. Vol. 117. AGU monograph, Washington D.C.

Merrill, R., McElhinny, M., McFadden, P., 1998. *The Magnetic Field of the Earth: Paleomagnetism, the Core, and the Deep Mantle*. Academic Press, San Diego, California, USA.

Moffatt, H., 1978. *Magnetic Field Generation in Electrically Conducting Fluids*. Cambridge University Press, Cambridge, U.K.

Nilsson, A., Holme, R., Korte, M., Suttie, N., Hill, M., 2014. Reconstructing holocene geomagnetic field variation: new methods, models and implications. Geophys. J. Int. 198, 229–248.

Olsen, N., Lüehr, H., Finlay, C. C., Sabaka, T. J., Michaelis, I., Rauberg, J., Tøffner-Clausen, L., 2014. The CHAOS-4 geomagnetic field model. Geophys. J. Int. 197, 815–827.

Olson, P., Aurnou, J., 1999. A polar vortex in the Earth's core. Nature 402, 170–173.

Olson, P., Christensen, U., 2002. The time averaged magnetic field in numerical dynamos with nonuniform boundary heat flow. Geophys. J. Int. 151, 809–823.

Olson, P., Christensen, U., Glatzmaier, G., 1999. Numerical modeling of the geodynamo: Mechanisms of field generation and equilibration. J. Geophys. Res. 104, 10383–10404.

Olson, P., Coe, R. S., Driscoll, P. E., Glatzmaier, G. A., Roberts, P. H., 2010. Geodynamo reversal frequency and heterogeneous core-mantle boundary heat flow. Phys. Earth Planet. Inter. 180, 66–79.

Olson, P., Deguen, R., 2012. Lopsided inner core growth and eccentricity of the geomagnetic dipole. Nature Geosci. 5(8), 565–569.

Olson, P., Deguen, R., Hinnov, L. A., Zhong, S., 2013. Controls on geomagnetic reversals and core evolution by mantle convection in the Phanerozoic. Phys. Earth Planet. Inter. 214, 87–103.

Olson, P., Sumita, I., Aurnou, J., 2002. Diffusive magnetic images of upwelling patterns in the core. J. Geophys. Res. 107, doi:10.1029/2001jb000384.

Pais, M. A., Jault, D., 2008. Quasi-geostrophic flows responsible for the secular variation of the Earth's magnetic field. Geophys. J. Int., doi:10.1111/j.1365–246X.2008.03741.x.

Pozzo, M., Davies, C., Gubbins, D., Alfè, D., 2012. Thermal and electrical conductivity of iron at Earth's core conditions. Nature 485, 355–358.

Roberts, P., Scott, S., 1965. On analysis of the secular variation, 1, a hydromagnetic constraint: Theory. J. Geomagn. Geoelectr. 17, 137–151.

Soderlund, K. M., Schmidt, B. E., Wicht, J., Blankenship, D. D., 2014. Ocean-driven heating of Europa's icy shell at low latitudes. Nature Geosci. 7, 16–19.

Stanley, S., 2010. A dynamo model for axisymmetrizing Saturn's magnetic field. Geophys. Res. Lett. 37, 5201.

Stanley, S., Elkins-Tanton, L., Zuber, M., Parmentier, E., 2008. Mars' paleomagnetic field as the result of a single-hemisphere dynamo. Science 321, 1822–1825.

Tanaka, S., Hamaguchi, H., 1997. Degree one heterogeneity and hemispherical variation of anisotropy in the inner core from PKP(BC)-PKP(DF) times. J. Geophys. Res. 102, 2925–2938.

Willis, P., Sreenivasan, B., Gubbins, D., 2007. Thermal core-mantle interaction: Exploring regimes for 'locked' dynamo action. Phys. Earth Planet. Inter. 165, 83–92.

Zhang, N., Zhong, S., 2011. Heat fluxes at the Earth's surface and core-mantle boundary since Pangea formation and their implications for the geomagnetic superchrons. Earth Planet. Sci. Lett. 306, 205–216.

Appendices - Reproduction of selected papers

Here I present five selected papers. Three papers are the outcome of my work with students (Huguet and Amit, 2012; Terra-Nova et al., 2015; Peña et al., 2016), one paper was written with a member of LPG (Amit and Choblet, 2012) and one paper resulted from a collaboration outside LPG (Amit and Olson, 2015). These five papers also span distinctive timescales which reflect my research work. Two papers deal with rapid core dynamics over decadal to centennial timescales (Huguet and Amit, 2012; Peña et al., 2016), one paper focuses on analysis of archeomagnetic field models on millennial timescales (Terra-Nova et al., 2015), one paper examines mantle control on the geodynamo corresponding to Millions of years (Amit and Choblet, 2012), and finally in Amit and Olson (2015) we proposed mantle control as an explanation to changes in paleomagnetic reversal frequency over timescales of hundreds of Millions of years.

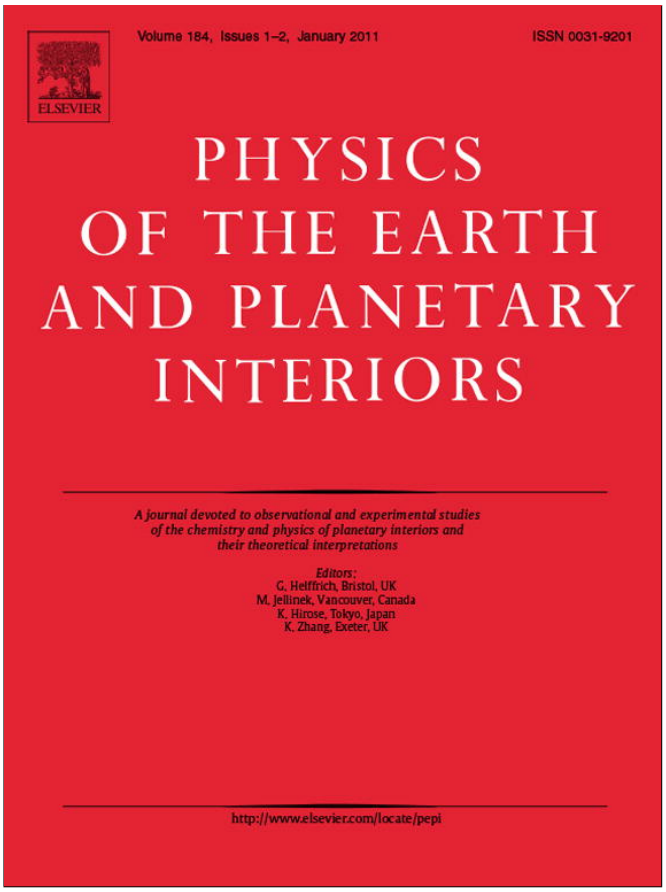

(This is a sample cover image for this issue. The actual cover is not yet available at this time.)

Physics of the Earth and Planetary Interiors 190-191 (2012) 34–43

Contents lists available at SciVerse ScienceDirect

Physics of the Earth and Planetary Interiors

journal homepage: www.elsevier.com/locate/pepi

Mantle-driven geodynamo features – Effects of compositional and narrow D″ anomalies

Hagay Amit *, Gaël Choblet

CNRS UMR 6112, Université de Nantes, Laboratoire de Planétologie et de Géodynamique, 2 rue de la Houssinière, Nantes F-44000, France

ARTICLE INFO

Article history:
Received 12 April 2011
Received in revised form 21 October 2011
Accepted 22 October 2011
Available online 2 November 2011
Edited by Keke Zhang

Keywords:
Geodynamo
Core flow
Geomagnetic field
Core–mantle boundary
Core–mantle thermal interactions
Lower mantle tomography
Thermal wind

ABSTRACT

Lower mantle heterogeneity could cause deviations from axial symmetry in geodynamo properties. Global tomography models are commonly used to infer the pattern of core–mantle boundary heat flux via a linear relation that corresponds to a purely thermal interpretation of lower mantle seismic anomalies, ignoring both non-thermal origins and non-resolved small scales. Here we study the possible impact on the geodynamo of narrow thermal anomalies in the base of the mantle, originating from either compositional heterogeneity or sharp margins of large-scale features. A heat flux boundary condition composed of a large-scale pattern and narrow ridges separating the large-scale positive and negative features is imposed on numerical dynamos. We find that hot ridges located to the west of a positive large-scale core–mantle boundary heat flux anomaly produce a time-average narrow elongated upwelling, a flow barrier at the top of the core and intensified low-latitudes magnetic flux patches. When the ridge is located to the east of a positive core–mantle boundary heat flux anomaly, the associated upwelling is weaker and the homogeneous dynamo westward drift leaks, precluding persistent intense low-latitudes magnetic flux patches. These signatures of the core–mantle boundary heat flux ridge are evident in the north–south component of the thermal wind balance. Based on the pattern of lower mantle seismic tomography (Masters et al., 2000), we hypothesize that hot narrow thermal ridges below central Asia and the Indian Ocean and below the American Pacific coast produce time-average fluid upwelling and a barrier for azimuthal flow at the top of the core. East of these ridges, below east Asia and Oceania and below the Americas, time-average intense geomagnetic flux patches are expected.

1. Introduction

The geomagnetic field is generated by the motion of an electrically-conductive fluid in Earth's liquid metallic outer core in a process known as the geodynamo. The dynamics in the core may be affected by the heterogeneous lower mantle (e.g. Gubbins, 2003). The signature of mantle control on the geodynamo is expected to be detectable over very long periods (Bloxham, 2002; Olson and Christensen, 2002; Aubert et al., 2008), possibly over intermediate timescales comparable to the period of available geomagnetic field observations (Aubert et al., 2007; Amit et al., 2008), and perhaps even on a snapshot (Gubbins et al., 2007; Willis et al., 2007). Several studies of mantle control on the geodynamo have used the pattern of lower mantle seismic shear velocity anomalies (e.g. Masters et al., 2000) as proxy to core–mantle boundary (CMB) heat flux anomalies, which was imposed as outer boundary condition on numerical dynamo simulations. These studies mainly focused on the role of the mantle in fixing the preferential longitudes of time-average high-latitude intense magnetic flux patches (Olson and Christensen, 2002; Aubert et al., 2008) and on characterizing the time-dependence of these robust features (Bloxham, 2002; Amit et al., 2010). It was found that the tangent cylinder (imaginary cylinder parallel to the rotation axis and tangential to the inner-core) acts as a flow barrier, so surface flow convergence at its latitude collects magnetic field lines to produce the high-latitude intense flux patches. The longitudes of these features are determined by the mantle thermal heterogeneity, though the relation between the CMB heat flux pattern and the locations of the patches is not trivial (Olson and Christensen, 2002; Aubert et al., 2007; Takahashi et al., 2008).

Less attention was given to the dynamics at low-latitudes where intense geomagnetic flux patches are observed in the historical field over the past four centuries (Jackson et al., 2000) and in recent high quality models derived from satellite data (e.g. Olsen and Mandea, 2008). In particular, the impact of lower mantle heterogeneity on the geodynamo at low-latitudes has not been investigated. Coincidently, low-latitudes seem to be regions where both theory and numerical simulations face difficulties. Theoretical assumptions employed in core flow inversions from geomagnetic secular variation are often based on dynamics of rapidly rotating

* Corresponding author.
E-mail address: Hagay.Amit@univ-nantes.fr (H. Amit).

0031-9201/$ - see front matter © 2011 Elsevier B.V. All rights reserved.
doi:10.1016/j.pepi.2011.10.005

fluid systems, including tangential geostrophy (e.g. LeMouël, 1984; Jackson, 1997; Hulot et al., 2002; Holme and Olsen, 2006), helical flow (Amit and Olson, 2004) and quasi-geostrophy (Pais and Jault, 2008). These assumptions are bound to break on approaching the equator (see e.g. Fig. 2 of Amit et al., 2007) where Coriolis force vanishes. Numerical dynamos often produce high-latitude intense flux patches (e.g. Christensen et al., 1998), but models exhibiting intense low-latitude patches are limited to a narrow regime of parameter space (Christensen et al., 2010). Instead, in this paper we further examine the impact of CMB heat flux heterogeneity on core dynamics, focusing on low-latitudes.

Two major shortcomings are known to bias the interpretation of seismic shear velocity v_s of the lowermost mantle obtained by global tomographic studies in terms of CMB heat flux patterns. First, non-thermal effects are likely to contribute to anomalous v_s in the D″ layer. Two broad anomalies of low v_s often considered as denser regions (e.g. Trampert et al., 2004) termed Large Low Shear Velocity Provinces (LLSVPs) cover a large fraction of the CMB (for a review see Garnero and McNamara, 2008). Geodynamical models (Tackley, 2002; McNamara and Zhong, 2005) show that compositional anomalies can play a major role in mantle dynamics, and may lead to the formation of such dense thermo-chemical piles corresponding to the geometry of LLSVPs. Another possible non-thermal source of anomalous v_s is an exothermic phase transition of deep mantle Perovskite to post-Perovskite structure that could affect deep mantle dynamics (Nakagawa and Tackley, 2006), especially if post-Perovskite is significantly less viscous than Perovskite (Cizkova et al., 2010; Nakagawa and Tackley, 2011) as suggested by diffusion rates computed using first-principle methods (Ammann et al., 2010). Nakagawa and Tackley (2008) showed that in such a framework, the mapping between v_s anomalies and CMB heat flux is more complex than the linear relation usually assumed. Based on results from their 3D spherical mantle convection simulations, Amit and Choblet (2009) constructed models of CMB heat flux accounting for both thermal and post-Perovskite lower mantle anomalies. These CMB heat flux models were imposed on numerical dynamos as outer boundary conditions. Amit and Choblet (2009) demonstrated that accounting for the effects of post-Perovskite phase transition may improve the agreement between the time-average dynamo models patterns and geodynamo related observations. Although the effect of mantle material with an intrinsically denser composition is also included in the models of Nakagawa and Tackley (2008), accounting for compositional anomalies in the mapping between v_s anomalies and CMB heat flux anomalies is non-unique and thus more difficult to implement.

A second caveat of the tomographic models is their low spatial resolution which excludes short wavelength features (e.g. Ritsema et al., 2007). Finer scale local studies of the D″ region indicate that the margins of the LLSVPs could be sharp (Ni et al., 2002; To et al., 2005; Wang and Wen, 2007) possibly as a result of the low viscosity of post-Perovskite (Nakagawa and Tackley, 2011). Similarly, the detection of Ultra Low Velocity Zones (ULVZs) – thin lenses of low seismic velocities observed in several regions above the CMB (e.g. Thorne and Garnero, 2004), require specific seismic studies. Due to the apparently larger reduction in v_s within ULVZs compared to the reduction in seismic compressional velocity v_p, ULVZs have often been associated with the presence of partial melts. Recent work showed that a solid-state iron-enriched composition is a viable alternative interpretation for ULVZs (Wicks et al., 2010). Whether or not partial melts are involved, dynamical models indicate that ULVZs likely correspond to the hottest regions of LLSVPs (e.g. McNamara et al., 2010). The locations of such regions are predominantly reported to lie on the edges of the LLSVPs, for example at the margins of the Pacific (Rost et al., 2005), although some localized exceptions are possible (McNamara et al., 2010; Rost et al., 2010). Considering the case of a purely thermal (plume cluster) model for lower mantle dynamics, Bull et al. (2009) also identified thin hot narrow regions on the edges of the LLSVPs, as well as thermal ridges at the centers of hot regions, although the latter in a less pronounced manner.

Altogether, these inferences pertain to the re-appraisal of the mapping from global tomography to CMB heat flux models. Bull et al. (2009) indicate for example that two end-member models for the lower mantle dynamics that differ significantly in terms of temperature fields above the CMB, when used to compute synthetic tomographic images, correlate equally well with a tomographic model in terms of power spectrum. High temperature (low heat flux) ridge-like features which appear in both models cannot be observed in global tomographic studies. In this context, we study the combined effect of large-scale thermal features as inferred from global tomography models and narrower thermal ridges. For intuitive understanding, we construct CMB heat flux patterns with a Y_2^2 structure (the dominant mode in global tomography models) superimposed by hot ridges separating the large-scale structures. We note that these idealized ridges are oriented in the north–south direction, which is shown in the following to affect the particular morphology of the resulting time-average geodynamo properties. We impose these patterns as outer boundary heat flux on numerical dynamos. We compare the reference tomographic Y_2^2 heat flux dynamo models (denoted 'G') with the Y_2^2+ ridges heat flux dynamo models (denoted 'GR'). We study the effect of the thermal ridges on the dynamics in the simulations.

To our best knowledge, numerical dynamo simulations with narrow ridge-like features imposed as outer boundary heat flux patterns have not been performed so far. However, laboratory experiments of rotating convection with such localized heaters were conducted (Sumita and Olson, 1999, 2002). These experiments found global locking of convection for very large heat flux anomalies. One heater produces a radially spiraling front from the CMB to the inner-core boundary separating cold and warm fluids, but the effect of several heaters is more local. The mantle-driven core flow inferred from these experiments could explain observations of the weak geomagnetic secular variation in the Pacific hemisphere and the hemispherical dichotomy in the upper inner-core seismic properties (Sumita and Olson, 1999, 2002).

Our numerical dynamo models differ from the laboratory experiments described above in several aspects. First, the experiments were conducted with a non-magnetic fluid, while our models solve the full MHD equations for dynamo action in a spherical shell. Second, the experiments imposed a local ridge over an otherwise homogeneous sphere, while we superimpose ridges on a large-scale Y_2^2 heat flux pattern. Third, the experiments used a strong heat flux anomaly that resulted in global convection locking, while we use a moderate heat flux anomaly that mildly modulates the convection but leaves the flow strongly time-dependent. In this moderate heat flux anomalies regime that we consider, the impact of the mantle on core dynamics is best seen in long-term time-averages at the top of the shell (e.g. Olson and Christensen, 2002; Aubert et al., 2008; Amit and Choblet, 2009). Finally, the heater in the experiments mimics cold localized mantle provinces, whereas our ridges represent warm mantle material located on the margins of large-scale cold and warm mantle structures.

The paper is outlined as follows. In Section 2 we describe the construction of the CMB heat flux patterns that account for thermal ridges at the margins of the LLSVPs, and we introduce the numerical dynamo models. In Section 3 we present results of the dynamo models, highlighting the impact of the thermal boundary ridges on the dynamics at the top of the shell. Our main findings, including some possible geophysical implications, are discussed in Section 4.

2. Methodology

We use 3D self-consistent numerical dynamos in a spherical shell. We implement the simulation MAGIC (Wicht, 2002), originally coded by Gary Glatzmaier. The control parameters are the heat flux based (modified) Rayleigh number $Ra = \alpha g_0 q_0 D^4/k\kappa\nu$, the Ekman number $E = \nu/\Omega D^2$, the Prandtl number $Pr = \nu/\kappa$, the magnetic Prandtl number $Pm = \nu/\lambda$ and a heat flux anomaly amplitude $q^* = (q_{max} - q_{min})/2q_0$, where α is thermal expansion coefficient, g_0 gravity on the outer boundary, q_0 mean heat flux across the outer boundary, D shell thickness, k thermal conductivity, κ thermal diffusivity, ν kinematic viscosity, Ω rotation rate and λ magnetic diffusivity. The inner to outer radii ratio is 0.35. The boundary conditions are rigid for the velocity and insulating for the magnetic field. The inner boundary has fixed buoyancy, and the outer boundary has a prescribed heat flux pattern. The grid includes 41 radial, 192 longitudinal and 96 latitudinal points, and in spectral space the fields were expanded up to degree and order 64. For more details on the method and governing equations see Olson and Christensen (2002).

We seek intuitive understanding of core dynamics governed by mantle heterogeneities of thermal and compositional origins with distinctive length scales. The dominant mode in lower mantle tomography models (Masters et al., 2000) is represented by a Y_2^2 pattern, classically interpreted as the largest scale temperature anomaly. Such a pattern was imposed by many authors as heat flux on the outer boundary of their numerical dynamo models (e.g. Bloxham, 2002; Olson and Christensen, 2002; Aubert et al., 2007; Sreenivasan, 2009). In our idealized study, we use the Y_2^2 pattern as a reference case. We model shorter wavelength structures by superimposing on the Y_2^2 pattern low heat flux ridges at the four margins of hot and cold large-scale structures. The ridges are modeled using a Gaussian geometry. A very thin Gaussian causes strong Gibbs effects when transformed to spherical harmonics as required by the pseudo-spectral method of the numerical dynamo code, whereas a very thick Gaussian smears the background Y_2^2 structure. We found that a 20° ridge width is an adequate compromise. We set the amplitude of the ridges to be equal to that of the hot Y_2^2 features.

Fig. 1 displays a scatter plot of the idealized long wavelength shear wave velocity anomaly and the prescribed CMB heat flux anomaly which includes the narrow ridges. As indicated above, these ridges may account not only for the possible effect of thermo-chemical convection in the lowermost mantle but also for non-resolved spatial features in the global tomography models. For this reason, this plot does not strictly illustrate a mapping between the heat flux and the actual seismic velocity (as in the results presented by Nakagawa and Tackley, 2008), but rather shows the mapping between the heat flux and the observed δv_s in large-scale tomographic models. Nevertheless, the multiple values of heat flux corresponding to a single value of δv_s identified by these authors as a result of the presence of dense thermo-chemical piles is reproduced in our idealized mapping where ridges are superimposed on the long wavelength structure. As in Nakagawa and Tackley (2008), this non-uniqueness is mostly associated to negative δv_s. In addition, our choice of ridge amplitude, in which the minimal heat flux is obtained both for the most negative δv_s and for zero seismic anomaly where the ridges are assumed to reside, is consistent with the mapping of Nakagawa and Tackley (2008) that is guided by estimates of lower mantle material properties.

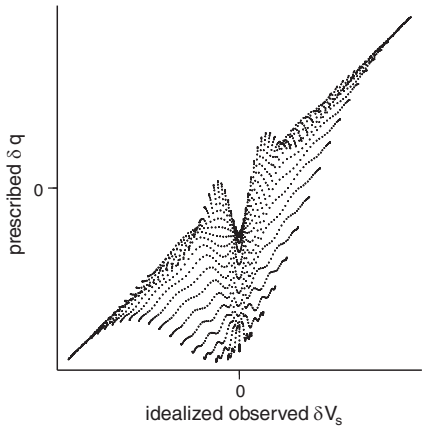

Fig. 1. Scatter plot of the prescribed CMB heat flux anomaly (Y_2^2 + ridges) as a function of the idealized description of shear wave velocity anomaly from global tomography (Y_2^2).

We use moderate heat flux anomalies $q^* < 1$. To emphasize the possible boundary signature, we consider models with relatively low Ra values. In the models with a lower Ra, a larger Pm number was used in order to maintain a large magnetic Reynolds number Rm for time-dependent chaotic dynamo action. The instantaneous surface magnetic fields have some morphological features that resemble the geomagnetic field, most notably the dominance of the axial dipole and high-latitude intense normal magnetic flux patches, but the field does not reverse. The instantaneous flow is dominated by strongly time-dependent columnar convection. Long simulations over about 5–10 magnetic diffusion times were performed for adequate time-averaging. The control and output parameters are summarized in Table 1.

To study the dynamical signature of the boundary thermal ridges, we analyze the curled force balance (following e.g. Aubert, 2005; Aubert et al., 2007; Sreenivasan, 2009), which can be written in non-dimensional form as

$$E\left(\frac{\partial\vec{\omega}}{\partial t} + \nabla\times(\vec{u}\cdot\nabla\vec{u}) - \nabla^2\vec{\omega}\right) - 2\frac{\partial\vec{u}}{\partial z} = \frac{Ra}{r_o}\nabla\times T\hat{r} + \frac{1}{Pm}\nabla\times((\nabla\times\vec{B})\times\vec{B}) \quad (1)$$

where $\vec{u}$ is velocity, $\vec{B}$ is magnetic field, T is co-density (representing buoyancy), $\vec{\omega} = \nabla\times\vec{u}$ is vorticity, z is axial cylindrical coordinate pointing in the direction of the rotation axis, r_o is outer core radius, $\hat{r}$ is a unit vector of the radial spherical coordinate r, and t is time. The terms in (1) from left to right represent the rate of change of vorticity, the curled inertial, viscous, Coriolis, buoyancy and Lorentz forces. We examine the leading terms in (1), in particular the validity of the approximated form of (1) for rapidly rotating flows termed the thermal wind balance (e.g. Pedlosky, 1987)

$$-2\frac{\partial\vec{u}}{\partial z} = \frac{Ra}{r_o}\nabla\times T\hat{r} \quad (2)$$

Table 1
Numerical dynamo models. For all cases $E = 3\times10^{-4}$ and $Pr = 1$. The magnetic Reynolds number Rm is calculated based on the kinetic energy in the volume of the shell.

Case	Pattern	q^*	Ra	Pm	Rm
G	Y_2^2	0.5	10^6	3	124
GR	Y_2^2 + ridges	0.5	10^6	3	125
G2	Y_2^2	0.5	5×10^5	4	103
GR2	Y_2^2 + ridges	0.5	5×10^5	4	104
GR2q	Y_2^2 + ridges	0.8	5×10^5	4	107
GR2p	Y_2^2 + ridges	0.5	5×10^5	7	176

'G' denotes 'Global', 'GR' denotes 'Global + Ridges', '2' denotes lower Ra cases, 'q' denotes larger q^*, 'p' denotes larger Pm.

The thermal wind equation relates the tangential gradient of buoyancy with the axial derivative of the velocity vector. The longitudinal ϕ- and the co-latitudinal θ-components of (2) are respectively (Amit et al., 2008)

$$-2\left(\cos\theta\frac{\partial u_\phi}{\partial r}-\frac{1}{r}\sin\theta\frac{\partial u_\phi}{\partial\theta}\right)=-\frac{Ra}{r_o}\frac{1}{r}\frac{\partial T}{\partial\theta} \tag{3}$$

$$-2\left(\cos\theta\frac{\partial u_\theta}{\partial r}-\frac{1}{r}\sin\theta\frac{\partial u_\theta}{\partial\theta}\right)=\frac{Ra}{r_o}\frac{1}{r\sin\theta}\frac{\partial T}{\partial\phi} \tag{4}$$

At low-latitudes, the first term on the left hand side of (3) and (4) is secondary. The curled Coriolis force at low-latitudes is associated with differential rotation (in the ϕ-component) or meridional divergence (in the θ-component).

3. Results

Fig. 2 shows the time-average upwelling at the top of the free stream just below the Ekman boundary layer and the time-average radial magnetic field on the outer boundary for case G with an imposed Y_2^2 heat flux (see Table 1) that represents the largest scale feature of lower mantle seismic tomography models. Fig. 3 shows the same images for case GR with the same control parameters but with an imposed Y_2^2+ ridges heat flux pattern that in addition accounts for structures of possible thermo-chemical origin that are typically non-resolved in the global tomography models. In these two cases the averaging periods exceed eight magnetic diffusion times.

The strongest downwellings occur at the edge of the tangent cylinder (Figs. 2b and 3b) where fluid convergence concentrates the most intense magnetic flux on the outer boundary (Figs. 2c and 3c). This tangent cylinder effect is a robust feature of numerical dynamos with homogeneous boundary conditions (e.g. Olson et al., 1999). The time-average longitudes of the strongest high-latitude intense magnetic flux patches are related to the longitudes of the positive heat flux anomalies (which correspond to cold outer core fluid). Because the ridges are hot, their impact on the locations of the high-latitude flux patches is negligible.

In contrast, the ridges may play an important role in the dynamics at low-latitudes. With a Y_2^2 heat flux pattern, low-latitudes are divided into two regions of downwellings and two regions of upwellings (each region occupying 90° longitude), with symmetric upwelling/downwelling (Fig. 2b). When the heat flux pattern includes ridges, the downwellings are more intense, and north–south elongated upwellings are formed below the ridges (Fig. 3b).

The global time-average magnetic field maps (Figs. 2c and 3c) are saturated by the high-latitude belts of intense flux. To appreciate the impact of the ridges on the magnetic field, we zoom into low-latitude regions. Fig. 4 presents a close-up of the velocity and magnetic field on the center of Fig. 3 (i.e. center of a ridge). The poloidal flow dominates in this region, as the fluid diverges from the hot ridge. Stronger field appears east of the ridge where cold fluid downwelling concentrates magnetic flux. Note that in these time-average images, the low-latitudes magnetic field structures are reversed with respect to the prevailing dipole polarity.

Interestingly, the dynamics is different when comparing ridges with a positive heat flux anomaly to the east or to the west. In Fig. 5 we zoom into a ridge with a positive heat flux anomaly to its west. The upwelling associated with this ridge is broken at the equator, and hot fluid may leak to the western side. In this region westward toroidal flow dominates. Moreover, the magnetic field exhibits patches of comparable intensity on both sides of the ridge. This ridge is thus less efficient in separating the large-scale cold and hot regions than the ridge shown in Fig. 4 with a positive heat flux anomaly to its east.

Competing effects of boundary-driven convection and the homogeneous background circulation co-exist in the dynamo models. The strength of boundary-driven convection is controlled by the imposed heat flux heterogeneity q^*, whereas the vigor of the background circulation is governed by the Rayleigh number Ra. One way to emphasize the boundary-driven dynamics is to reduce the strength of convection by using smaller Ra values (e.g. Sreenivasan, 2009). In cases G2 and GR2 we reduce Ra to about 2.5 times the critical value for the onset of non-magnetic convection. Even in this relatively low value, convection is still chaotic and strongly time-dependent with significant morphological differences between one snapshot to another. We identify in case GR2 the same dynamical features as in case GR. In particular, a clear time-average north–south elongated upwelling pattern appears below ridges with a positive heat flux anomaly to their east, acting as a flow barrier, whereas the ridge signature is weaker where the positive heat flux anomaly is to their west.

The time averaging relatively smears low-latitude magnetic field structures, which are generally more mobile than the high-latitude intense flux patches (Finlay and Amit, 2011). The signature of the

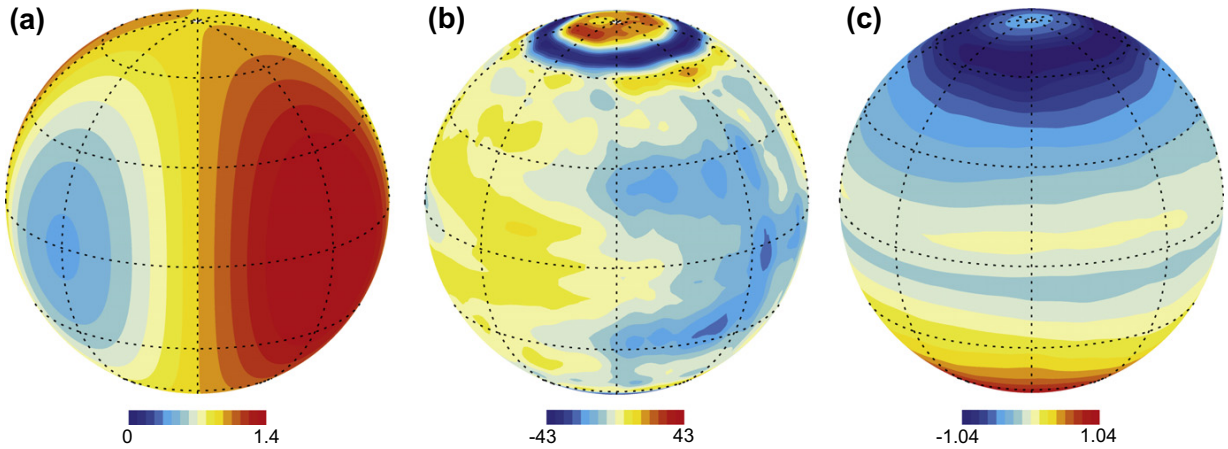

Fig. 2. Images of case G: (a) Imposed outer boundary heat flux normalized by the mean heat flux. (b) Time-average upwelling at the top of the free stream just below the Ekman boundary layer. (c) Time-average radial magnetic field on the outer boundary. The upwelling is given in units of v/D^2. The radial magnetic field is given in units of $\sqrt{\rho\mu_0\lambda\Omega}$, where ρ is the fluid density and μ_0 the permeability of free space.

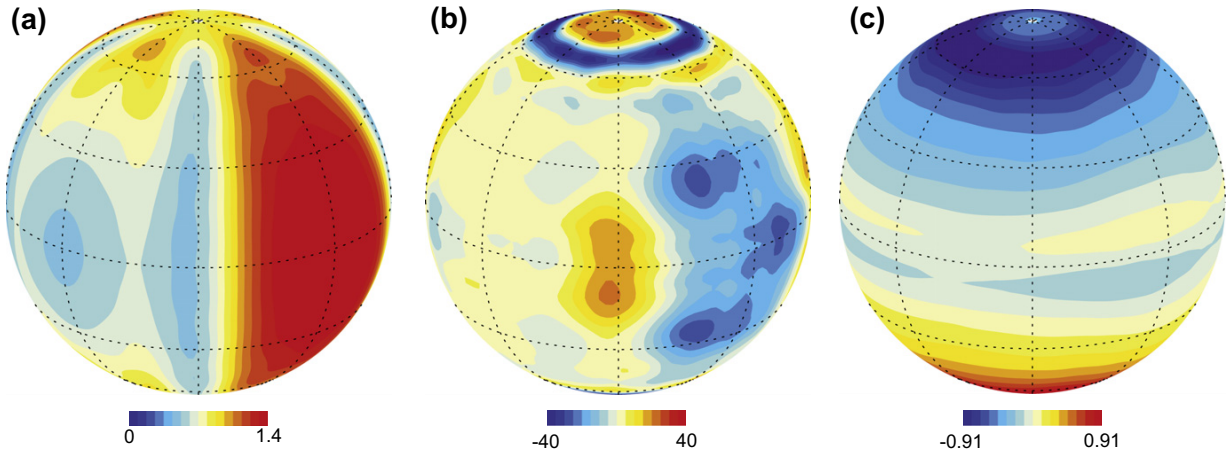

Fig. 3. As in Fig. 2 for case GR.

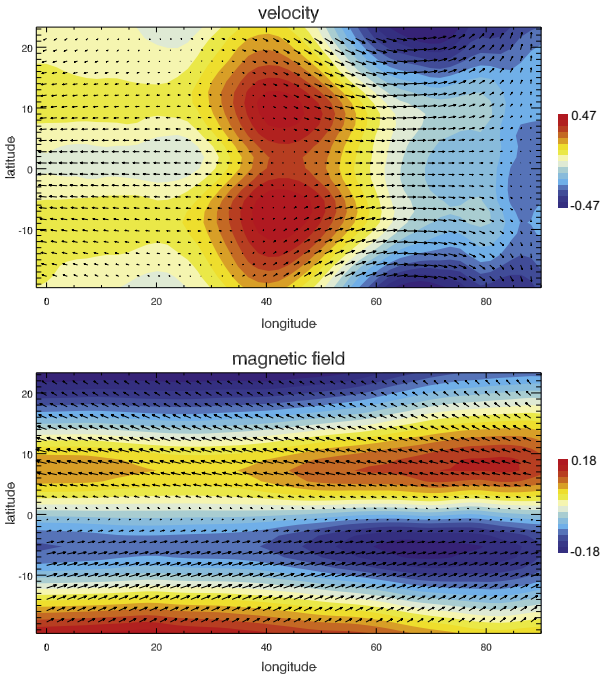

Fig. 4. Zoom into a ridge at low-latitudes of the time-average of case GR, with a positive heat flux anomaly to the east (where Fig. 3 is centered). Velocity at the top of the free stream is shown in the top panel, magnetic field in the bottom panel. Radial components are in colors, tangential components in arrows. The velocity is given in units of v/D. The magnetic field is given in units of $\sqrt{\rho\mu_0\lambda\Omega}$.

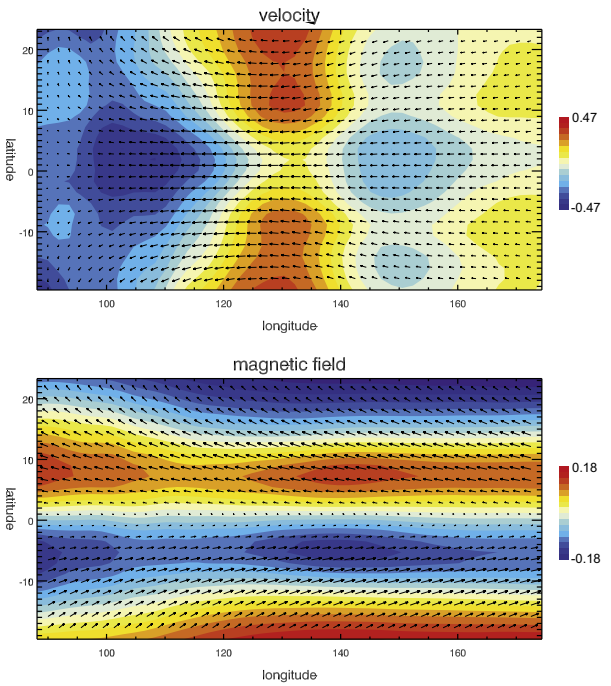

Fig. 5. As in Fig. 4 for a ridge with a positive heat flux anomaly to the west. Ranges are the same as in Fig. 4.

low-latitude structures is therefore more visible in snapshots than in time-averages. In general, the flux patches at low-latitudes are relatively more intense in the cases that include ridges than in the Y_2^2 cases. Lowering the Ra number yields a stronger boundary effect with relatively more intense low-latitudes magnetic flux patches. Increasing the boundary heterogeneity q^* (case GR2q) may affect both high- and low-latitudes. Fig. 6 shows an example of the radial magnetic field from case GR2. Note the intense normal polarity low-latitudes magnetic flux patches below 135°E in the northern hemisphere and 20°E in the southern hemisphere, and the intense low-latitudes reversed flux patch below 160°W in the northern hemisphere.

The dynamical signature of the boundary thermal ridges can clearly be seen in the curled force balance (1). In general, thermal wind (2) prevails in the dynamo models. Fig. 7 shows the balance between the curled Coriolis and buoyancy forces, the two dominant terms in the two tangential thermal wind components (3) and (4) at the top of the shell (just below the thermal boundary layer) for case G. The curled Lorentz force contributions are secondary and are more notable in the equatorial region where some meridional shear can be seen in the Coriolis terms. The curled inertial and viscous forces are negligible. In these time-average plots, the spatial distribution of the curled buoyancy forces reflects well the thermal heterogeneity of the imposed Y_2^2 CMB heat flux pattern.

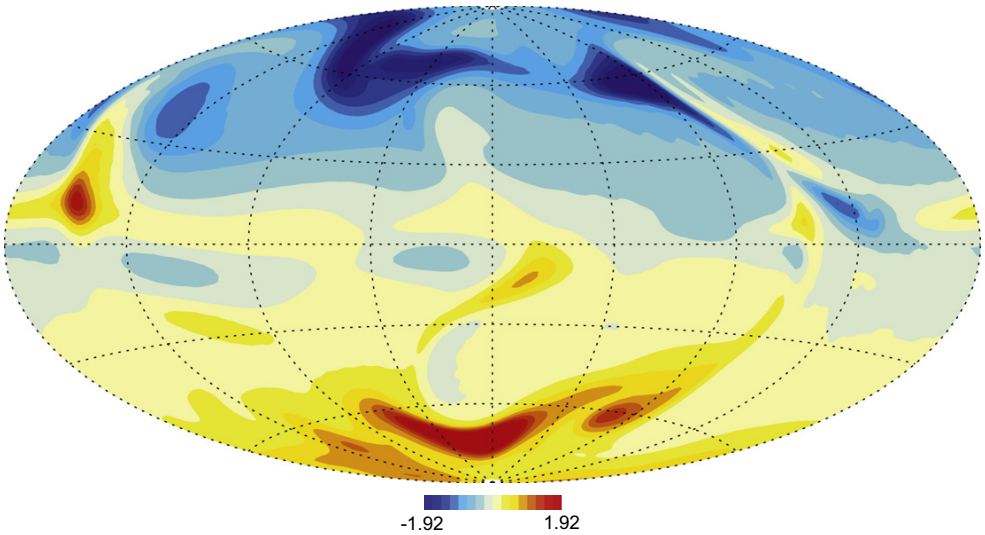

Fig. 6. The radial magnetic field on the CMB in a snapshot of case GR2. The field is given in units of $\sqrt{\rho\mu_0\lambda\Omega}$.

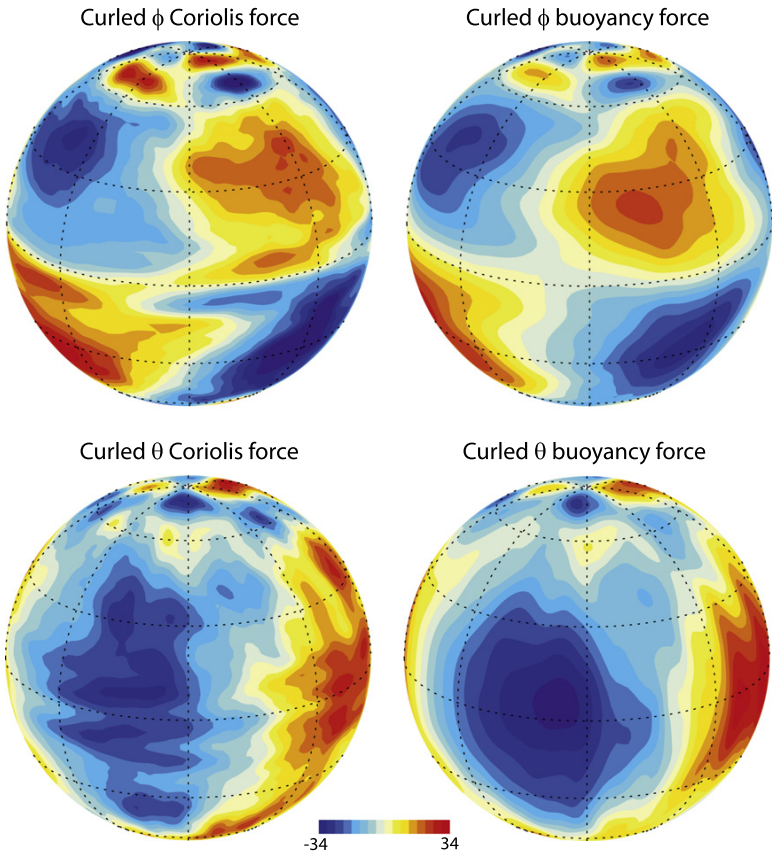

Fig. 7. Curled forces for the time-average of case G: Coriolis (left), buoyancy (right); Longitudinal (top) and co-latitudinal (bottom) components. Contour intervals are identical for all subplots. The images are centered at $\phi = 45^{\circ}$ E, a boundary between positive (to the east) and negative (to the west) large-scale heat flux structures in the Y_2^2 pattern. All curled forces are given in units of v^2/D^4.

The thermal wind balance holds in the time-average of case GR as well (Fig. 8). Several results are worth noting here. First, because in our idealized heat flux models the ridge is elongated in the north–south direction, it contains a significant gradient in the ϕ direction, and therefore the ridge signature in the thermal wind balance appears only in the θ-component. Second, the longitude

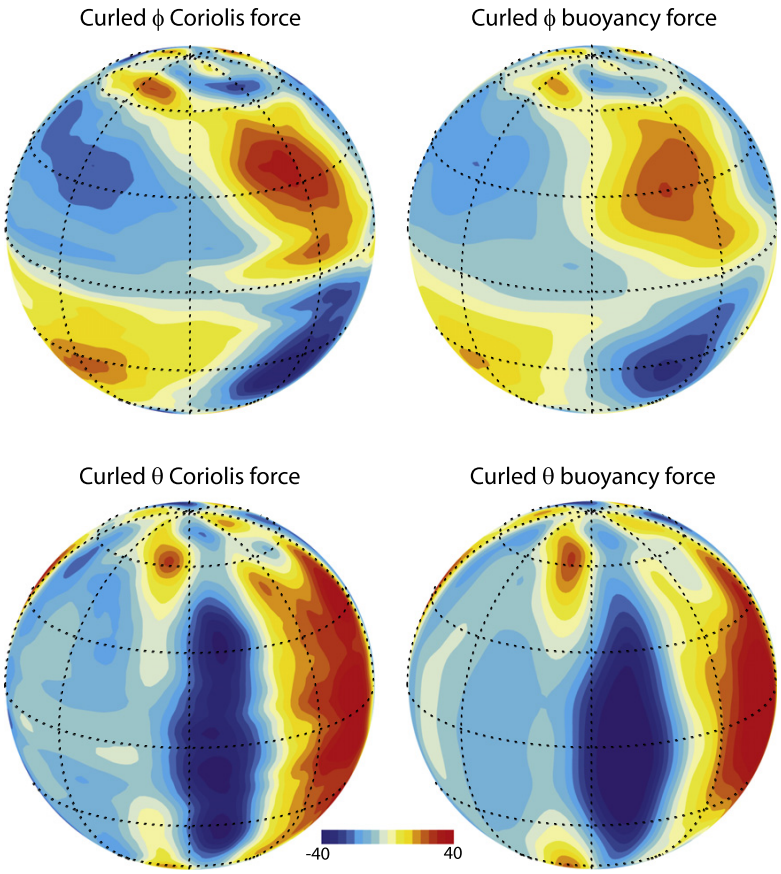

Fig. 8. As in Fig. 7 for the time-average of case GR. Contour intervals are identical for all subplots. The images are centered at $\phi = 45^{\circ}$E where a hot thermal ridge separates positive (to the east) and negative (to the west) large-scale heat flux structures in the $Y_2^2 +$ ridges pattern.

of the ridge-induced thermal wind is shifted to the east. Finally, the ridge signature is absent at $\phi = 135^{\circ}$E where the positive heat flux is to the west (Fig. 9). The same balances of curled forces are also found in the larger boundary anomaly case GR2q and in the larger *Pm* (and consequently larger *Rm*) case GR2p (not shown).

The thermal wind balance can also be identified in snapshots. Fig. 10 shows the upwelling, radial magnetic field, and the θ-component of the curled forces for a snapshot of case GR2. The Lorentz curled force is again mostly localized in the equatorial region. Smaller deviations from thermal wind stem from the curled inertial force primarily near intense downwellings, away from the broad and mild upwelling associated with the boundary ridge. Increasing *Ra* results in stronger inertial contributions, although in cases G and GR these are still secondary with respect to the dominant Coriolis and buoyancy terms.

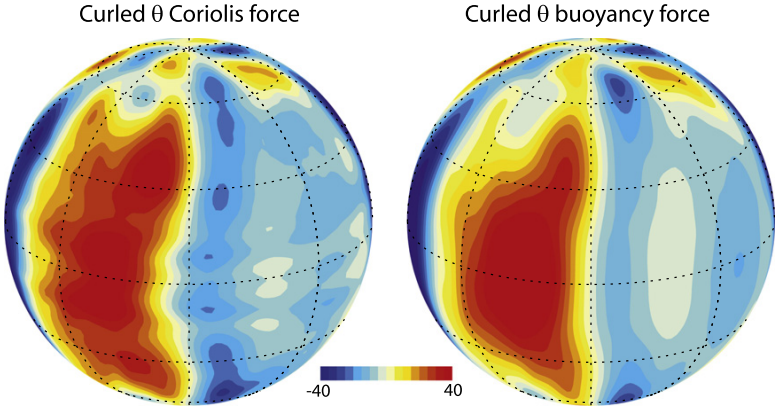

Fig. 9. As in Fig. 8, but this time the images are centered at $\phi = 135^{\circ}$E where a hot thermal ridge separates positive (to the west) and negative (to the east) large-scale heat flux structures. Color intervals are the same as in Fig. 8. Only the θ-components are displayed.

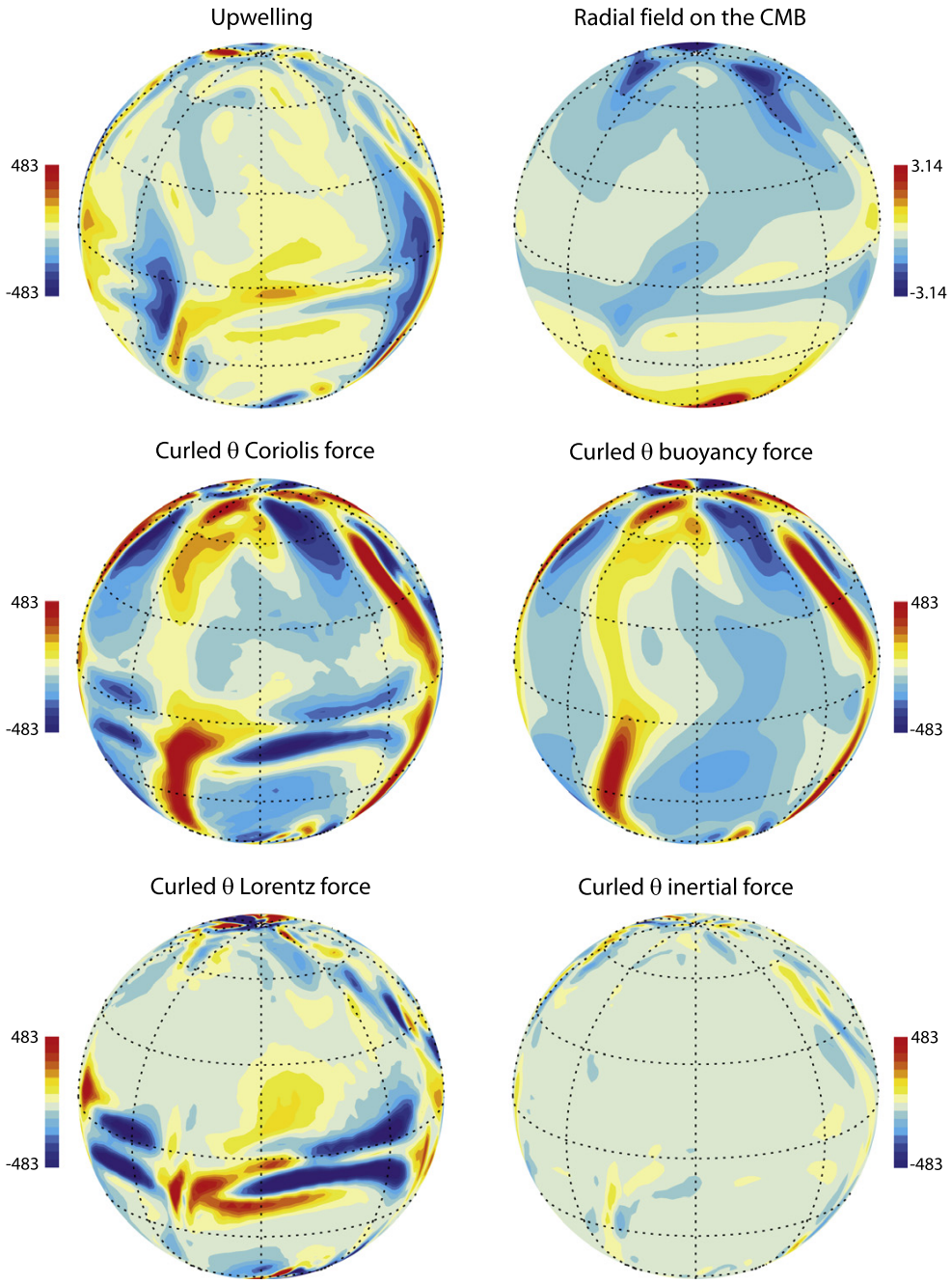

Fig. 10. A snapshot from case GR. Top: Upwelling just below the thermal boundary layer (left) and radial field on the outer boundary (right); Middle: The θ-component of the Coriolis (left) and buoyancy (right) curled forces; Bottom: The θ-component of the Lorentz (left) and inertial (right) curled forces. All images are centered at longitude $\phi = 45^{\circ}$ E. The upwelling is given in units of ν/D^2. The radial magnetic field is given in units of $\sqrt{\rho\mu_0\lambda\Omega}$. All curled forces are given in units of ν^2/D^4.

4. Discussion

The differences between the G and GR cases are rather straightforward. The symmetry in the Y_2^2 pattern is preserved in the time-average flow and magnetic field of the G cases, whereas the symmetry breaking of the hot ridge is expressed in the GR models in the form of an elongated time-average north–south upwelling structure below the ridge that separates an intensified downwelling from a weak upwelling. Less trivial is the difference between regions where a positive heat flux anomaly is east or west of the ridge. When a positive heat flux anomaly is east of the ridge, the upwelling associated with the ridge acts as a flow barrier, poloidal flow governs, and strong downwelling to the east concentrates stronger field there. In contrast, when a positive heat flux anomaly is west of the ridge, the ridge upwelling is less continuous, and both convection and magnetic field are comparably active on either side of the ridge.

The reason for the difference between the dynamics at the two ridge locations is related to the combined effect of time-average homogeneous dynamo zonal flow and the steady boundary-driven

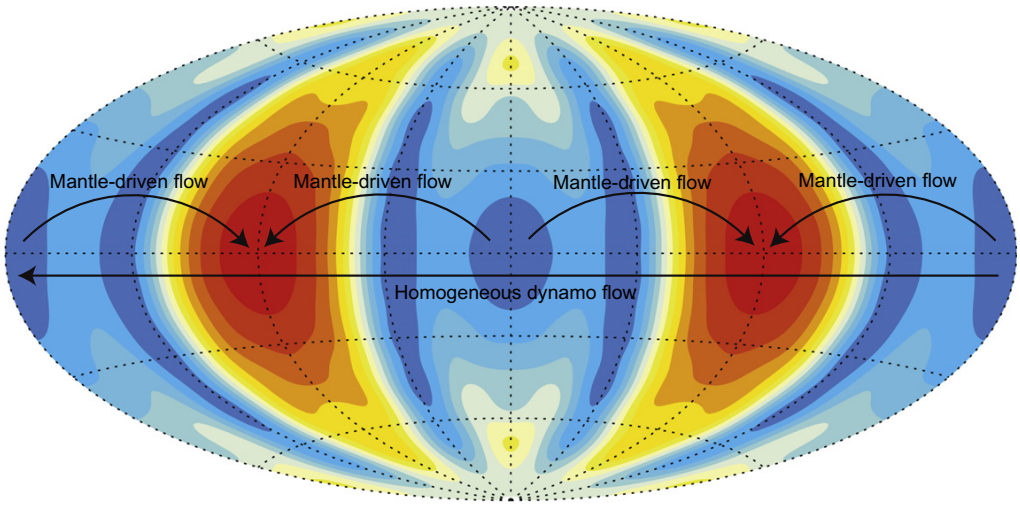

Fig. 11. The heat flux pattern imposed on the CMB in the cases with thermal ridges, and a schematic illustration of the steady flow at the top of the core. Straight arrow indicates westward flow in the background homogeneous dynamo, arc arrows indicate flow driven by thermal boundary heterogeneity. The image is centered at longitude $\phi = 0^{\circ}$. The two flows counteract each other on the ridge at longitude 45°E, but add up on the ridge at longitude 45°W.

flow. To demonstrate this point, consider the schematic illustration in Fig. 11. A dynamo model without boundary heterogeneity produces a time-average surface westward flow (straight arrow in Fig. 11) at low- and mid-latitudes (Aubert, 2005). The boundary-driven thermal flow (arc arrows in Fig. 11) is in general directed from hot to cold regions (Gubbins, 2003). In the context of our study, when cold material is east of the ridge (as in longitude 45°E), the two flows counteract, and the ridge acts as a flow barrier separating the two regions. In contrast, when cold material is west of the ridge (as in longitude 45°W), both flows are westward, the upwelling associated with the ridge is broken by the flow, and the separation is less effective.

The thermal wind balance in numerical dynamos was demonstrated in previous studies. Aubert (2005) displayed thermal wind equilibrium in zonal averages of numerical dynamos with homogeneous thermal boundary conditions. Boundary-driven thermal winds in numerical dynamos with heterogeneous boundary conditions were shown in time-averages, meridional sections or averages along axial cylinders (Aubert et al., 2007; Sreenivasan, 2009; Wicht and Christensen, 2010). Here we demonstrate that thermal wind holds on spherical surfaces at the top of the shell in both time-averages and snapshots. The time-average patterns of Coriolis and buoyancy curled forces in case G clearly reflect the Y_2^2 heterogeneity (Fig. 7). Substituting $T \propto \sin^2\theta\cos 2\phi$ (the real part of Y_2^2) into Eqs. (3) and (4) indeed recovers the $-\sin 2\theta\cos 2\phi$ pattern of the ϕ-component of the curled Coriolis and buoyancy forces and the $-\sin^2\theta\sin 2\phi$ pattern of their θ-component (Fig. 7). Because the ridge is elongated in the north–south direction, its signature is best seen in the θ-component (which involves $\partial T/\partial\phi$, see Eq. (4)) of case GR (Fig. 8). The azimuthal shift of the time-average Coriolis and buoyancy curled forces with respect to the location of the CMB heat flux ridge is probably related to the azimuthal shift in the time-average flow and field structures identified in previous studies of numerical dynamos with inhomogeneous outer boundary heat flux (Olson and Christensen, 2002; Aubert et al., 2007; Takahashi et al., 2008). The origin of the azimuthal shift in these dynamo properties is not clear. Aubert et al. (2007) argued that the shift is related to thermal advection effects and it is expected to diminish in the well-mixed conditions of Earth's core.

As with the north–south elongated upwelling, the ridge signature in the time-average θ-component of the thermal wind balance is seen when the positive heat flux anomaly is to the east (Fig. 8), but not when it is located to the west (Fig. 9). This further confirms our finding that the ridges are most influential on core dynamics when the positive heat flux anomaly is to the east. In these low-latitudes regions the azimuthal buoyancy gradient is balanced by meridional divergence of the fluid (second term on the left hand side of Eq. (4)).

A deviation from thermal wind is provided at low-latitudes by the curled Lorentz force (Fig. 10). Pais et al. (2004) argued that the radial curled Lorentz force is expected to become significant at low-latitudes. We find that the curled inertial force provides another deviation from thermal wind associated with small scales near transitory convective columns. This inertial effect is more pronounced in the larger *Ra* cases where turbulence becomes more important (Wicht and Christensen, 2010). The dynamics seems weakly sensitive to mild changes in either the heat flux heterogeneity amplitude or the magnetic Reynolds number.

Based on our findings and a global tomography model, we can now make some predictions concerning the locations at the top of Earth's outer core where persistent flow and field features may appear. The pattern of seismic shear velocity anomalies at the lowermost mantle in the global tomography model of Masters et al. (2000) would suggest that, if they exist, hot narrow thermal ridges would be located below central Asia and the Indian Ocean and below the American Pacific coast. In these meridional strips we predict (in a statistical sense) fluid upwelling at the top of the core and a barrier of azimuthal flow. At the western sides of the large-scale positive heat flux anomalies, below east Asia and Oceania and below the Americas, persistent intense low-latitudes geomagnetic flux patches are expected to form. Indeed it was argued based on paleomagnetic data (Laj et al., 1991; Hoffman, 1996; Love, 1998; Merrill and McFadden, 1999) and numerical dynamos with tomographic boundary conditions (Coe et al., 2000; Kutzner and Christensen, 2004) that during geomagnetic reversals the dipole axis tends to follow these two longitudes. The historical geomagnetic field shows one intense flux patch in the southern hemisphere branching all the way to the equator below Indonesia, where intense low-latitudes flux patches have been forming and subsequently migrating westward (Jackson et al., 2000), either by azimuthal advection or possibly due to a wave propagation (Finlay and Jackson, 2003).

In summary, the oversimplified linear relation between lower mantle seismic anomalies and CMB heat flux pattern employed

in most dynamo models ignores both non-thermal contributions and non-resolved small-scales of lower mantle heterogeneity and may therefore bias the recovery of mantle-driven geodynamo features. Amit and Choblet (2009) argued that accounting for lower mantle post-Perovskite anomalies in CMB heat flux models may improve the recovery of several observations representing time-average geodynamo features. Here we demonstrate that in addition, accounting for narrow lower mantle thermal anomalies of possible thermo-chemical origin could affect core dynamics at low-latitudes. Better understanding of the physical processes in the lowermost mantle and improved interpretation of the lateral seismic anomalies in terms of CMB heat flux heterogeneity may provide more accurate constraints on core dynamics and the geomagnetic field.

Acknowledgments

H.A. and G.C. were supported by a grant from the Agence Nationale de la Recherche (Project ANR-08-JCJC-0126-01). H.A. thanks Johannes Wicht for his help with the implementation of the MAGIC code. We thank two anonymous reviewers for their constructive reviews.

References

Amit, H., Aubert, J., Hulot, G., 2010. Stationary, oscillating or drifting mantle-driven geomagnetic flux patches? J. Geophys. Res. 115, B07108. doi:10.1029/2009JB006542.

Amit, H., Aubert, J., Hulot, G., Olson, P., 2008. A simple model for mantle-driven flow at the top of Earth's core. Earth Planets Space 60, 845–854.

Amit, H., Choblet, G., 2009. Mantle-driven geodynamo features – effects of post-perovskite phase transition. Earth Planets Space 61, 1255–1268.

Amit, H., Olson, P., 2004. Helical core flow from geomagnetic secular variation. Phys. Earth Planet. Inter. 147, 1–25.

Amit, H., Olson, P., Christensen, U., 2007. Tests of core flow imaging methods with numerical dynamos. Geophys. J. Int. 168, 27–39.

Ammann, M., Brodholt, J., Wookey, J., Dobson, D., 2010. First-principles constraints on diffusion in lower-mantle minerals and a weak D layer. Nature 465, 462–465.

Aubert, J., 2005. Steady zonal flows in spherical shell fluid dynamos. J. Fluid Mech. 542, 53–67.

Aubert, J., Amit, H., Hulot, G., 2007. Detecting thermal boundary control in surface flows from numerical dynamos. Phys. Earth Planet. Inter. 160, 143–156.

Aubert, J., Amit, H., Hulot, G., Olson, P., 2008. Thermo-chemical wind flows couple Earth's inner core growth to mantle heterogeneity. Nature 454, 758–761.

Bloxham, J., 2002. Time-independent and time-dependent behaviour of high-latitude flux bundles at the core–mantle boundary. Geophys. Res. Lett. 29. doi:10.1029/2001gl014543.

Bull, A., McNamara, A., Ritsema, J., 2009. Synthetic tomography of plume clusters and thermochemical piles. Earth Planet. Sci. Lett. 278, 152–162.

Christensen, U., Aubert, J., Hulot, G., 2010. Conditions for Earth-like geodynamo models. Earth Planet. Sci. Lett. 296, 487–496.

Christensen, U., Olson, P., Glatzmaier, G., 1998. A dynamo model interpretation of geomagnetic field structures. Geophys. Res. Lett. 25, 1565–1568.

Cizkova, H., Cadek, O., Matyska, C., Yuen, D., 2010. Implications of post-perovskite properties for core–mantle dynamics. Phys. Earth Planet. Inter. 180, 235–243.

Coe, R.S., Hongre, L., Glatzmaier, G.A., 2000. An examination of simulated geomagnetic reversals from a palaeomagnetic perspective. Philos. Trans. R. Soc. Lond. 358, 1141–1170.

Finlay, C., Amit, H., 2011. On the flow magnitude and field-flow alignment at Earth's core surface. Geophys. J. Int. 186, 175–192.

Finlay, C., Jackson, A., 2003. Equatorially dominated magnetic field change at the surface of Earth's core. Science 300, 2084–2086.

Garnero, E., McNamara, A., 2008. Structure and dynamics of Earth's lower mantle. Science 320, 626–628.

Gubbins, D., 2003. Thermal core–mantle interactions: theory and observations. In: Dehant, V., Creager, K., Karato, S., Zatman, S. (Eds.), Earth's Core: dynamics, structure and rotation. AGU Geodynamics Series American Geophysical Union.

Gubbins, D., Willis, P., Sreenivasan, B., 2007. Correlation of Earth's magnetic field with lower mantle thermal and seismic structure. Phys. Earth Planet. Inter. 162, 256–260.

Hoffman, K.A., 1996. Transitional paleomagnetic field behavior: preferred paths or patches? Surv. Geophys. 17, 207–211.

Holme, R., Olsen, N., 2006. Core surface flow modelling from high-resolution secular variation. Geophys. J. Int. 166, 518–528.

Hulot, G., Eymin, C., Langlais, B., Mandea, M., Olsen, N., 2002. Small-scale structure of the geodynamo inferred from Oersted and Magsat satellite data. Nature 416, 620–623.

Jackson, A., 1997. Time-dependency of tangentially geostrophic core surface motions. Phys. Earth Planet. Inter. 103, 293–311.

Jackson, A., Jonkers, A., Walker, M., 2000. Four centuries of geomagnetic secular variation from historical records. Philos. Trans. R. Soc. Lond. A358, 957–990.

Kutzner, C., Christensen, U., 2004. Simulated geomagnetic reversals and preferred virtual geomagnetic pole paths. Geophys. J. Int. 157, 1105–1118.

Laj, C., Mazaud, A., Weeks, R., Fuller, M., Herrero-Bevera, E., 1991. Geomagnetic reversal paths. Nature 351, 447.

LeMouël, J.-L., 1984. Outer core geostrophic flow and secular variation of Earth's magnetic field. Nature 311, 734–735.

Love, J.J. 1998. Paleomagnetic volcanic data and geometric regularity of reversals and excursions 103, 12435–12452.

Masters, G., Laske, G., Bolton, H., Dziewonski, A., 2000. The relative behavior of shear velocity, bulk sound velocity, and compressional velocity in the mantle: implications for chemical and thermal structure. In: Karato, S., Forte, A., Liebermann, R., Masters, G., Stixrude, L. (Eds.), Earths Deep Interior, vol. 117. AGU Monograph, Washington DC.

McNamara, A., Garnero, E., Rost, S., 2010. Tracking deep mantle reservoirs with ultra-low velocity zones. Earth Planet. Sci. Lett. 299, 1–9.

McNamara, A., Zhong, S., 2005. Thermochemical structures beneath Africa and the Pacific Ocean. Nature 437, 1136–1139.

Merrill, R.T., McFadden, P.L., 1999. Geomagnetic Polarity Transitions 37, 201–226.

Nakagawa, T., Tackley, P., 2006. Three-dimensional structures and dynamics in the deep mantle: effects of post-perovskite phase change and deep mantle layering. Geophys. Res. Lett. 33, L12S11.

Nakagawa, T., Tackley, P., 2008. Lateral variations in CMB heat flux and deep mantle seismic velocity caused by a thermal–chemical-phase boundary layer in 3D spherical convection. Earth Planet. Sci. Lett. 271, 348–358.

Nakagawa, T., Tackley, P., 2011. Effects of low-viscosity post-perovskite on thermo-chemical mantle convection in a 3-d spherical shell. Geophys. Res. Lett. 38, L04309. doi:10.1029/2010GL046494.

Ni, S., Tan, E., Gurnis, M., Helmberger, D., 2002. Sharp sides to the African superplume. Science 296, 1850–1852.

Olsen, N., Mandea, M., 2008. Rapidly changing flows in the Earth's core. Nat. Geosci. 1, 390–394.

Olson, P., Christensen, U., 2002. The time averaged magnetic field in numerical dynamos with nonuniform boundary heat flow. Geophys. J. Int. 151, 809–823.

Olson, P., Christensen, U., Glatzmaier, G., 1999. Numerical modeling of the geodynamo: mechanisms of field generation and equilibration. J. Geophys. Res. 104, 10383–110404.

Pais, M., Oliveira, O., Nogueira, F., 2004. Nonuniqueness of inverted core–mantle boundary flows and deviations from tangential geostrophy. J. Geophys. Res. 109, B08105.

Pais, M.A., Jault, D., 2008. Quasi-geostrophic flows responsible for the secular variation of the Earth's magnetic field. Geophys. J. Int. 173, 421–443.

Pedlosky, J., 1987. Geophysical Fluid Dynamics. Springer-Verlag, New York, USA.

Ritsema, J., McNamara, A., Bull, A., 2007. Tomographic filtering of geodynamic models: implications for model interpretation and large-scale mantle structure. J. Geophys. Res. 112, B01303.

Rost, S., Garnero, E., Thorne, M., Hutko, A., 2010. On the absence of an ultralow-velocity zone in the north Pacific. J. Geophys. Res. 115, B04312.

Rost, S., Garnero, E., Williams, Q., Manga, M., 2005. Seismological constraints on a possible plume root at the core–mantle boundary. Nature 435, 666–669.

Sreenivasan, B., 2009. On dynamo action produced by boundary thermal coupling. Phys. Earth Planet. Inter. 177, 130–138.

Sumita, I., Olson, P., 1999. A laboratory model for convection in Earth's core driven by a thermally heterogeneous mantle. Science 286, 1547–1549.

Sumita, I., Olson, P., 2002. Rotating thermal convection experiments in a hemispherical shell with heterogeneous boundary heat flux: implications for the Earth's core. J. Geophys. Res. 107, 2169.

Tackley, P., 2002. The strong heterogeneity caused by deep mantle layering. Geophys. Geochem. Geosyst. 3. doi:10.1029/2001GC000167.

Takahashi, F., Tsunakawa, H., Matsushima, M., Mochizuki, N., Honkura, Y., 2008. Effects of thermally heterogeneous structure in the lowermost mantle on the geomagnetic field strength. Earth Planet. Sci. Lett. 272, 738–746.

Thorne, M., Garnero, E., 2004. Inferences on ultralow-velocity zone structure from a global analysis of SPdKS waves. J. Geophys. Res. 109, B08301.

To, A., Romanowicz, B., Capdeville, Y., Takeuchi, N., 2005. 3D effects of sharp boundaries at the borders of the African and Pacific superplumes: observation and modeling. Earth Planet. Sci. Lett. 233, 137–153.

Trampert, J., Deschamps, F., Resovsky, J., Yuen, D., 2004. Probabilistic tomography maps chemical heterogeneities throughout the lower mantle. Science 306, 853–856.

Wang, Y., Wen, L., 2007. Geometry and P and S velocity structure of the African Anomaly. J. Geophys. Res. 112, B05313.

Wicht, J., 2002. Inner-core conductivity in numerical dynamo simulations. Phys. Earth Planet. Inter. 132, 281–302.

Wicht, J., Christensen, U., 2010. Torsional oscillations in dynamo simulations. Geophys. J. Int. 181, 1367–1380.

Wicks, J., Jackson, J., Sturhahn, W., 2010. Very low sound velocities in iron-rich (Mg, Fe)O: implications for the core–mantle boundary region. Geophys. Res. Lett. 37. doi:10.1029/2010GL043689.

Willis, P., Sreenivasan, B., Gubbins, D., 2007. Thermal core–mantle interaction: exploring regimes for 'locked' dynamo action. Phys. Earth Planet. Inter. 165, 83–92.

Geophysical Journal International

Geophys. J. Int. (2012) **190,** 856–870 doi: 10.1111/j.1365-246X.2012.05542.x

Magnetic energy transfer at the top of the Earth's core

Ludovic Huguet* and Hagay Amit

CNRS UMR 6112, Université de Nantes, Laboratoire de Planétologie et de Géodynamique, 2 rue de la Houssinière, Nantes, F-44000, France.
E-mail: Hagay.Amit@univ-nantes.fr

Accepted 2012 May 8. Received 2012 May 7; in original form 2011 July 15

SUMMARY

We introduce a formalism to track magnetic energy transfer between spherical harmonic degrees due to the interaction of fluid flow and radial magnetic field at the top of the Earth's core. Large-scale synthetic single harmonic flows are characterized by a fixed difference between harmonics participating in the transfer. Large-scale toroidal flows result in more local energy transfer than small-scale poloidal flows. Axisymmetric poloidal flows are most efficient in producing energy transfer and dipole changes. The azimuthal phase relation between the field and the flow may play a major role in the energy transfer. Geomagnetic energy transfer induced by core flow models exhibit a striking transfer spectrum pattern of alternating extrema suggestive of energy cascade, but the detailed transfer spectrum matrix reveals rich behaviour with both local Kolmogorov-like transfer and non-local transfer, the latter about twice larger. The transfer spectrum reverses from even maxima and odd minima between 1840 and 1910 to odd maxima and even minima between 1955 and 1990. The transfer spectrum matrix shows geomagnetic energy cascade from low to high degrees as well as non-local transfer from the dipole directly to higher degrees, explaining the simultaneous dipole decrease and non-dipole increase during the historical period.

Key words: Dynamo: theories and simulations; Geomagnetic induction; Magnetic field; Rapid time variations; Core, outer core and inner core.

1 INTRODUCTION

The geomagnetic field is generated by convection-driven flow of an electrically conducting fluid at the Earth's outer core. Measurements of the geomagnetic field and its secular variation (SV) may provide vital constraints on core dynamics. Geomagnetic field models based on surface observatories and recent satellite data (Jackson *et al.* 2000; Olsen & Mandea 2008) show that the radial field at the core–mantle boundary (CMB) is dominated by an axial dipole component. Since the advent of geomagnetic measurements about 170 yr ago, the geomagnetic dipole intensity has been rapidly decreasing (Olson & Amit 2006). The rate of dipole decrease has been varying significantly with time (Fig. 1).

Efforts to unravel the kinematic mechanisms responsible for the current dipole decrease focused mostly on a local-spatial approach. Gubbins (1987) used the integral form of the axial dipole $m_z \propto \int_S B_r \cos\theta dS$ (where B_r is the radial geomagnetic field on the CMB, θ is co-latitude and dS is a surface increment of the CMB) to identify CMB regions that provide positive/negative contributions to the axial dipole. He argued that the growth and intensification of reversed flux patches, especially below the southern Atlantic, are responsible for most of the dipole decrease. Emergence of reversed flux patches on the CMB and their deep core upwellings origin have been identified in many numerical dynamos as triggers to dipole collapse and subsequent polarity reversals (Wicht & Olson 2004; Takahashi *et al.* 2007; Aubert *et al.* 2008; Olson *et al.* 2009). Following Moffatt (1978), Olson & Amit (2006) derived an integral equation for mapping advective and diffusive contributions to axial dipole SV. They found that the combined effects of growth of reversed flux by magnetic diffusion, poleward advection of reversed flux and equatorward advection of normal flux by the flow, have worked in unison to decrease the dipole. Liu & Olson (2009) proposed a power law for the dipole decrease rate as a function of the magnetic Reynolds number.

Alternatively, dipole changes can be studied via a spectral approach. Degree–time plots obtained from numerical dynamo models show that during reversals the peak of poloidal magnetic field energy on the outer boundary moves progressively from the dipole to higher degrees, which is suggestive of a forward magnetic energy cascade (Olson *et al.* 2009; Amit & Olson 2010). Gissinger *et al.* (2010) argued that reversals in their low magnetic Prandtl number forced magnetohydrodynamic (MHD) simulations can be approximated by a simple set of differential equations representing energy exchange between the dipole and the quadrupole. Amit & Olson (2010) designed a spectral approach for studying dipole SV, and more generally, temporal variations in the Mauersberger–Lowes geomagnetic spectrum. They manipulated the radial magnetic induction equation to an equation for the SV of the Mauersberger–Lowes

*Now at: LGL, Laboratoire de Géologie de Lyon, CNRS, Université Lyon 1, ENS-Lyon, Géode, 2 rue Raphaël Dubois, 69622 Villeurbanne, France.

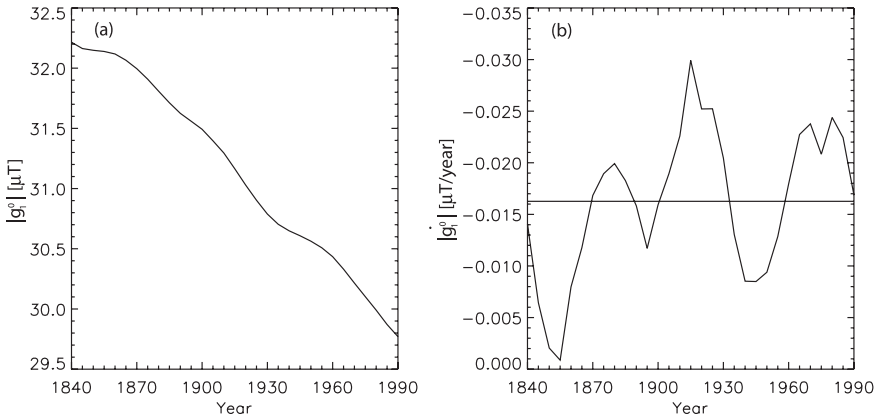

Figure 1. Absolute geomagnetic axial dipole Gauss coefficient $|g_1^0|$ in μT (a) and its SV $|\dot{g}_1^0|$ in μT yr^{-1} (b) based on the historical field model *gufm1* of Jackson *et al.* (2000) for the period 1840–1990. The horizontal line in (b) denotes the time-average axial dipole decrease rate.

spectrum. Motivated by classical turbulence theory, they assumed that magnetic energy is transferred locally between neighbouring spherical harmonic degrees. Their spectral transfer rates showed a persistent inverse energy cascade in the quadrupole family and a time-dependent forward energy cascade in the dipole family, consistent with the observed simultaneous dipole decrease and non-dipole increase during the historical era.

The local transfer assumption adopted by Amit & Olson (2010) is supported by non-magnetic and MHD turbulence theory and simulations. According to the classical turbulence theory of Kolmogorov, energy cascades between similar size eddies without major jumps between distinctive length scales (Kolmogorov 1941; Batchelor 1953; Frisch 1995). The energy at a certain degree is statistically decoupled from any large-scale energy source and is determined solely by the rate of energy transfer across the inertial range (Moffatt 1978). Numerical simulations of the time evolution of kinetic and magnetic energy and helicity (Pouquet *et al.* 1976) and helical kinematic dynamos (Mininni 2007) show that magnetic energy is progressively excited at larger scales as time increases, thus intensifying the large-scale field by inverse cascade of magnetic helicity. Numerical MHD simulations of turbulence find both local Kolmogorov-like and non-local transfers (Yousef *et al.* 2007; Mininni 2011). Forced MHD turbulence simulations show local magnetic energy transfer (Alexakis *et al.* 2005a; Carati *et al.* 2006). Local magnetic energy transfer was found to be associated with energy cascade by magnetic field advection, whereas non-local transfer was found to be associated with energy injected from the large scales directly into the small scales by magnetic field stretching induced by the poloidal flow (Alexakis *et al.* 2007). Amit & Olson (2010) argued that because the core flow is dominantly toroidal (see Finlay & Amit 2011, and references therein), local transfer is expected to dominate geomagnetic induction at the top of the core. Mininni (2011) summarized based on turbulence MHD simulations that the transfer of magnetic energy from one degree to another seems dominantly local, whereas non-local effects are more dominant in the transfer from kinetic to magnetic energy that generates the dynamo.

How important is the role of classical 3-D isotropic, homogeneous turbulence in the geodynamo? According to the very small estimates of the Rossby number in the Earth's core (Olsen & Mandea 2008), turbulence is expected to be negligible compared to rotational effects. However, estimates of the local Rossby number that rely on eddy size rather than system length scale suggest that turbulence in the Earth's core is nearly as important as rotation, and that inertial effects may play an important role in polarity reversals (Christensen & Aubert 2006; Olson & Christensen 2006). Alternatively, it is possible that boundary layer control rather than force balance determines the competition between turbulence and rotation. King *et al.* (2009) argued based on experiments and numerical simulations that the relation between the Ekman and thermal boundary layer thicknesses dictates whether the flow will be organized in equatorially symmetric columns or in random 3-D structures. According to their scaling laws, the Earth's core is not far from the transition between the rapidly rotating regime to the turbulent regime.

Direct evidence for turbulence in the core is difficult to obtain. The geomagnetic field reversals time-series can be fitted by a log-normal distribution that is suggestive of 'multiplicative noise' in the geodynamo due to a turbulent α-effect (Ryan & Sarson 2007). King *et al.* (2009) illustrated that deviations from equatorial symmetry may suggest the presence of turbulence in a rapidly rotating system. Some core flow models inferred from inversions of geomagnetic SV show persistent deviations from equatorial symmetry, most notably westward drift in mid-latitudes of the southern hemisphere without a northern counterpart (Jackson 1997; Pais & Hulot 2000; Amit & Olson 2006; Holme & Olsen 2006). Quasi-geostrophic core flow models which assume equatorial symmetry were found capable of explaining the SV (Pais & Jault 2008; Gillet *et al.* 2009, 2011). The core flow models of Schaeffer & Pais (2011) obtained without imposing equatorial symmetry contain 66–84 per cent (depending on the length scale) symmetric kinetic energy, that is, the flow is about half way between purely symmetric to equally symmetric/antisymmetric. Deviations from equatorial symmetry might also arise from the impact of the lower mantle heterogeneity on the geodynamo (Aubert *et al.* 2007; Gubbins *et al.* 2007), though possibly only on long timescales (Olson & Christensen 2002). The symmetry level of the flow in the Earth's core is still under debate.

In this paper, we introduce a formalism to track magnetic energy transfer between different spherical harmonic degrees in the Mauersberger–Lowes spectrum, which can be useful in identifying Kolmogorov-like turbulence signature at the top of the core. We forward solve the radial frozen-flux magnetic induction equation for a given flow and radial field models. The SV is transformed to Gauss coefficients, and in conjunction with the field Gauss

coefficients, the energy transfer between each pair of spherical harmonics within the observed spectrum is calculated. We apply our formalism to synthetic flows for intuitive physical understanding, and to core flow models inferred from the geomagnetic SV for geophysical interpretation. Our approach allows to test the local transfer assumption of Amit & Olson (2010) and to examine the possibility that the current geomagnetic dipole decrease is caused by a forward magnetic energy cascade. Furthermore, our method sheds light on the overall variability of the large-scale geomagnetic field spectrum during the historical period.

For given flow and field models, admissible magnetic energy transfers are constrained by the selection rules of the Gaunt and Elsasser integrals (Elsasser 1946). These rules dictate whether a certain flow is capable of converting toroidal magnetic field to poloidal and vice versa, and are therefore fundamental to kinematic dynamo theory (Bullard & Gellman 1954). Kahle *et al.* (1967) used the Gaunt and Elsasser integrals to invert for the flow at the top of the core from geomagnetic field and SV models. Whaler (1986) used the triangle rule to relate the maximum spherical harmonic degree of the flow with the sum of maximum degrees of the field and its SV. For our purposes, the selection rules are used to verify the validity of the energy transfers generated by synthetic flows.

Assessing energy transfer from the interaction between the core field and flow is obviously prone to errors due to uncertainties in these models. The historical field model *gufm1* of Jackson *et al.* (2000) might suffer from problems of insufficient data coverage and poor data quality. In general, geomagnetic field models constructed from observations are not constrained to obey the MHD equations and energy conservation is not implicit. Much more severe is the case of core flow models inferred from the geomagnetic SV, which are prone to numerous theoretical and practical sources of errors (Holme 2007). Any inference concerning the behaviour of the geomagnetic energy transfer during the historical period should therefore be taken with caution.

In addition, our analysis ignores the contribution of magnetic diffusion to the temporal changes of the geomagnetic energy spectrum. Magnetic diffusion SV is expected to be a localized phenomenon (Amit & Christensen 2008), so its impact on the large-scale spectrum is arguably secondary. Based on free decay formalisms using fundamental modes, magnetic diffusion was found to be generally negligible (Amit & Olson 2010). Nevertheless, the contribution of magnetic diffusion to the temporal changes of the geomagnetic spectrum is unknown.

The paper is outlined as follows. In Section 2 we describe our formalism, method, error estimates and graphical visualization of the results. Our energy transfer solutions for synthetic and core flow models are given in Section 3. We discuss our main findings in Section 4.

2 THEORY AND METHOD

The Mauersberger–Lowes spectrum at the CMB is one of the primary outputs of the dynamo process in the core (Dormy *et al.* 2000). The magnetic field spectrum R_n at the CMB can be expressed as a function of spherical harmonic degree n in terms of the Gauss coefficients of the core field as (Lowes 1974)

$$R_n = (n+1)\left(\frac{a}{c}\right)^{2n+4}\sum_{m=0}^{n}\left(\left(g_n^m\right)^2+\left(h_n^m\right)^2\right), \tag{1}$$

where a is the Earth's radius, c is the radius of the core and g_n^m and h_n^m are the Gauss coefficients of the core field at spherical harmonic degree and order n and m, respectively. The total magnetic energy is given by

$$\langle B_r^2\rangle = \sum_{n}^{n_{\max}}\frac{n+1}{2n+1}R_n, \tag{2}$$

where B_r is the radial magnetic field on the CMB, $n_{\max}$ is the truncation level, and $\langle\rangle$ denotes CMB surface average. Similar to (1), the definition of the SV spectrum at the CMB is given by (Alldredge 1984; McLeod 1996; Voorhies 2004)

$$S_n = (n+1)\left(\frac{a}{c}\right)^{2n+4}\sum_{m=0}^{n}\left(\left(\dot{g}_n^m\right)^2+\left(\dot{h}_n^m\right)^2\right), \tag{3}$$

where the dots denote time derivatives. Using (1), the temporal variation of the field spectrum is written as (Cain *et al.* 1989)

$$\dot{R}_n = 2(n+1)\left(\frac{a}{c}\right)^{2n+4}\sum_{m=0}^{n}\left(g_n^m\dot{g}_n^m+h_n^m\dot{h}_n^m\right). \tag{4}$$

From (2), the temporal variation of the total magnetic energy is

$$\frac{\partial}{\partial t}\left\langle B_r^2\right\rangle = \sum_{n}^{n_{\max}}\frac{n+1}{2n+1}\dot{R}_n. \tag{5}$$

Note that $\dot{R}_n$ has units of $\mu\mathrm{T}^2\ \mathrm{yr}^{-1}$, whereas S_n has units of $\mu\mathrm{T}^2\ \mathrm{yr}^{-2}$. Moreover, S_n is positive by definition, whereas $\dot{R}_n$ may acquire both signs. While R_n and S_n define the energy at each spherical harmonic degree of the field and SV, respectively, $\dot{R}_n$ is the rate of change of the energy at each degree.

Fig. 2 shows the three spectra for three arbitrary snapshots from the geomagnetic field and SV model *gufm1* of Jackson *et al.* (2000). From hereafter, we shall consider the field model up to degree

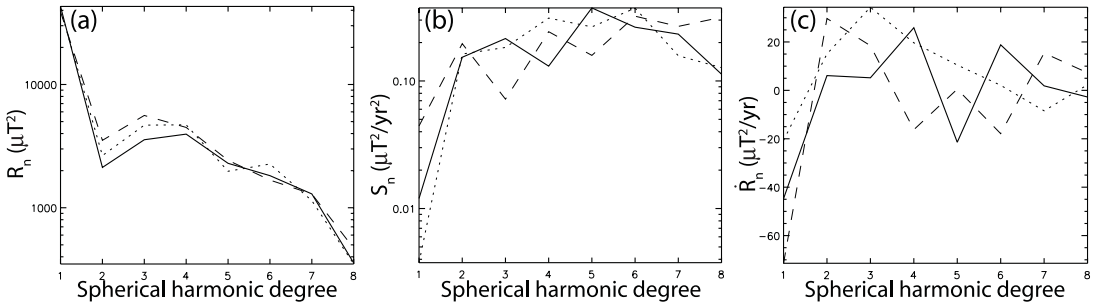

Figure 2. Three arbitrary snapshots (solid: 1900, dotted: 1940, dashed: 1980) of geomagnetic spectra from *gufm1* (Jackson *et al.* 2000) as a function of spherical harmonic degree: (a) R_n in $\mu\mathrm{T}^2$ in log-scale; (b) S_n in $\mu\mathrm{T}^2\ \mathrm{yr}^{-2}$ in log-scale; (c) $\dot{R}_n$ in $\mu\mathrm{T}^2\ \mathrm{yr}^{-1}$ in linear scale.

$n_{\max} = 8$ to avoid biases due to variations in data quality and spatial resolution with time (Holme *et al.* 2011). Fig. 2(a) demonstrates the well-known dipole-dominated geomagnetic field spectrum with decreasing power towards higher harmonics. The SV spectrum in Fig. 2(b), in contrast, is increasing with n, so the dipole SV contains less energy than the SV in the higher harmonics. The rate of change of the dipole energy $\dot{R}_1$ is negative (Fig. 2c), reflecting the historical decrease in dipole intensity (Gubbins 1987; Olson & Amit 2006). Interestingly, although the energy in the dipole change is smaller than in the higher harmonics, that is, $S_1 < S_{n\neq 1}$, the rate of change of the dipole energy is in most periods the largest, that is, $|\dot{R}_1| > |\dot{R}_{n\neq 1}|$. In most cases $\dot{R}_{n\neq 1}$ are positive, representing the non-dipole increase that accompanies the historical dipole decrease (Amit & Olson 2010).

For incompressible flow, the radial component of the induction equation just below the CMB where the radial velocity vanishes is

$$\dot{B}_r + \vec{u_h} \cdot \nabla B_r + B_r \nabla_h \cdot \vec{u_h} = \eta \hat{r} \cdot \nabla^2 \vec{B}, \tag{6}$$

where $\dot{B}_r$ is the time derivative of the radial magnetic field on the CMB, $\vec{u_h}$ is the free stream tangential fluid velocity vector at the top of the core, η is the magnetic diffusivity of the outer core, $\hat{r}$ is the radial unit vector and $\vec{B}$ is the magnetic field vector. The subscript h denotes the direction tangent to the spherical CMB surface: $\nabla_h = \nabla - \frac{\partial}{\partial r}$.

Assuming that magnetic diffusion is negligible with respect to magnetic field advection by the flow (Roberts & Scott 1965), (6) becomes

$$\dot{B}_r = -(\vec{u_h} \cdot \nabla B_r + B_r \nabla_h \cdot \vec{u_h}). \tag{7}$$

Amit & Olson (2010) have shown that the radial magnetic induction equation can be recasted to a time-evolution equation for the magnetic energy spectrum. In the frozen-flux limit, their eq. (8) is simply

$$\dot{R}_n = T_n, \tag{8}$$

where T_n is the transfer spectrum representing magnetic energy transfer induced by the flow.

The tangential fluid velocity at the top of the core can generally be written as

$$\vec{u_h} = \nabla \times \mathcal{T}\hat{r} + \nabla_h \mathcal{P}, \tag{9}$$

where $\mathcal{T}$ and $\mathcal{P}$ are toroidal and poloidal flow potentials, respectively. The tangential flow components are then given by

$$u_\phi = -\frac{1}{r}\frac{\partial \mathcal{T}}{\partial \theta} + \frac{1}{r\sin\theta}\frac{\partial \mathcal{P}}{\partial \phi}, \tag{10}$$

$$u_\theta = \frac{1}{r\sin\theta}\frac{\partial \mathcal{T}}{\partial \phi} + \frac{1}{r}\frac{\partial \mathcal{P}}{\partial \theta}, \tag{11}$$

where r, θ, ϕ are the radial, co-latitude and longitude spherical coordinates. Eq. (7) can be written in terms of $\mathcal{T}$ and $\mathcal{P}$ as

$$\dot{B}_r = -\left[\frac{1}{r^2\sin\theta}\left(\frac{\partial \mathcal{T}}{\partial \phi}\frac{\partial B_r}{\partial \theta} - \frac{\partial \mathcal{T}}{\partial \theta}\frac{\partial B_r}{\partial \phi}\right) + \frac{1}{r^2}\left(\frac{\partial \mathcal{P}}{\partial \theta}\frac{\partial B_r}{\partial \theta} + \frac{1}{\sin^2\theta}\frac{\partial \mathcal{P}}{\partial \phi}\frac{\partial B_r}{\partial \phi}\right) + B_r \nabla_h^2 \mathcal{P}\right]. \tag{12}$$

We consider two types of flows. First, synthetic flows are constructed from single spherical harmonics as $\mathcal{T} = A\mathcal{T}_n^{mc}$ or $\mathcal{T} = A\mathcal{T}_n^{ms}$, where A is the flow amplitude, $\mathcal{T}_n^m$ is the associated Legendre polynomial and the superscripts c and s denote $\cos m\phi$ and $\sin m\phi$, respectively. The same nomenclature applies for the poloidal potential, $\mathcal{P} = A\mathcal{P}_n^{mc}$ or $\mathcal{P} = A\mathcal{P}_n^{ms}$. In all cases, we tune A so that the maximum flow is arbitrarily set to 10 km yr^{-1}, allowing comparison between the efficiency of different synthetic flows to generate T_n. We use the field at 1980 from the historical model *gufm1* (Fig. 3) for comparing the behaviour of energy transfer produced by different synthetic flows.

Secondly, frozen-flux core flow models inferred from inversions of geomagnetic SV data are investigated. We use the helical core flow model of Amit & Olson (2004), which assumes a linear relation between the tangential flow divergence $\nabla_h \cdot \vec{u_h}$ and the radial vorticity ζ at the top of the free stream

$$\nabla_h \cdot \vec{u_h} = \mp k\zeta, \tag{13}$$

where the minus/plus signs apply in the northern/southern hemispheres, respectively, and k is a constant. We choose flow models obtained with $k = 0.15$ that was found to optimize the agreement with the observed length of day variation record (Amit & Olson 2006). As described in Amit & Olson (2004), the toroidal and poloidal flow potentials were computed from a set of advection–diffusion equations based on (12) and (13) and solved on a regular spherical grid. Single epoch flows between 1840 and 1990 in 5 yr intervals were inverted based on the historical geomagnetic SV model from *gufm1*. Here, the field models of the respective periods are used. We note that the local numerical scheme used to infer the core flow models does not impose any spectral constraint (Amit & Olson 2004).

To calculate magnetic energy transfer from one degree to another, we track the interactions between each spherical harmonic degree n' of the radial field with the full flow $\vec{u_h}$. The total radial field on

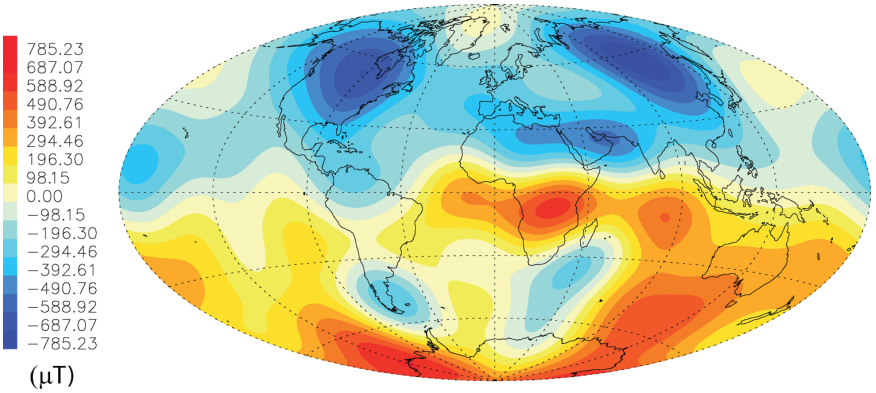

Figure 3. The radial geomagnetic field on the CMB in μT in 1980 from *gufm1* (Jackson *et al.* 2000) truncated at spherical harmonic degree $n_{\max} = 8$.

the CMB is given in terms of the Gauss coefficients by

$$B_r = \sum_{n=1}^{n_{\max}} \sum_{m=0}^{n} \left(\frac{a}{c}\right)^{n+2} (n+1)\, P_n^m(\cos\theta) \left(g_n^m \cos m\phi + h_n^m \sin m\phi\right), \tag{14}$$

where P_n^m are the Schmidt semi-normalized Legendre polynomials. We calculate the contribution to $\dot{B}_r$ from the advection of the radial field of degree n' $B_r^{n'}$ by the flow $\vec{u_h}$ using the frozen-flux radial magnetic induction eq. (12). Note that this interaction in general may contain all spherical harmonics. We then apply a spectral transform to obtain the SV Gauss coefficients $\dot{g}_n^m$ and $\dot{h}_n^m$, and in conjunction with the field Gauss coefficients g_n^m and h_n^m we compute the energy transfer based on (4) and (8). We denote as $T_{n'\to n}$ the energy change of degree n due to the interaction of the degree n' field $B_r^{n'}$ with the total flow $\vec{u_h}$. The net energy transfer between degrees p and n is the matrix component

$$T_{pn} = T_{p\to n} - T_{n\to p}, \tag{15}$$

where $p < n$. The physical meaning of (15) is that energy may be transferred from degree p to degree n and vice versa, and the net balance is the difference between the two transfers. If T_{pn} is positive net energy is transferred from the lower degree p to the higher degree n, whereas if T_{pn} is negative net energy is transferred from the higher degree n to the lower degree p. The matrix T_{pn} therefore contains only the terms above the main diagonal, because the terms below the main diagonal are folded into the net transfer, and the main diagonal itself represents energy transfer within a degree (e.g. from the axial to the equatorial dipole). Local transfer is represented by the diagonal just above the main diagonal in T_{pn} (i.e. $n = p+1$). To assess the role of non-local transfer, we calculate the ratio of absolute local to non-local transfers

$$L = \frac{\sum_{n'=1}^{n_{\max}-1} |T_{n'n'+1}|}{\sum_{p'=1}^{n_{\max}-2} \sum_{n'=p'+2}^{n_{\max}} |T_{p'n'}|}. \tag{16}$$

We repeat these calculations for all degrees from $n = 1$ to $n_{\max}$. Apart from the matrix T_{pn}, we also calculate the integrated magnetic energy change by advection for each degree strictly due to transfer within the observed spectrum $n_{\max} \geq n \geq 1$, from hereafter denoted by $T_n(\mathbb{N}_1^{\max})$, as

$$T_n\left(\mathbb{N}_1^{\max}\right) = \sum_{n'=1}^{n-1} T_{n'n} - \sum_{n'=n+1}^{n_{\max}} T_{nn'}. \tag{17}$$

Finally, we also compute the overall change following (4) by calculating the SV from the interaction of the full field B_r with the full flow, from hereafter denoted by $T_n(\mathbb{N}_1^{\max} \to \mathbb{N}_1)$, that is, energy transfer from the observed spectrum $\mathbb{N}_1^{\max}$ to the entire spectrum $\mathbb{N}_1$. Note that the latter includes energy leaking from $n \leq n_{\max}$ to $n > n_{\max}$, whereas T_{pn} and $T_n(\mathbb{N}_1^{\max})$ contain strictly energy transfers within $n \leq n_{\max}$.

For all forward calculations of the radial frozen-flux magnetic induction equation we use a spatial grid step of 5°. The spectral transforms are performed until degree and order 10, but we consider only degrees $n = 1$–8 from which the core field model was constructed. To test the precision of our numerical scheme, we first consider two simple synthetic flows. In case 1 (see Table 1), solid body rotation with respect to the rotation axis $\mathcal{T}_1^0$ uniformly advects the field to the west. The SV contains azimuthal phase variations only, so the power in each degree is unchanged. This can easily be demonstrated analytically. For example, substituting $\mathcal{T} = A\mathcal{T}_1^0$ and a dipole field into (12) gives

$$\dot{B}_r = -\left(\frac{2A}{c^2}\right)\left(\frac{a}{c}\right)^3 \left(-g_1^1 \sin\theta \sin\phi + h_1^1 \sin\theta \cos\phi\right). \tag{18}$$

Table 1. Summary of synthetic flows. Horizontal line spaces separate tests, symmetric flows and antisymmetric flows. The integrated dipole energy change by advective transfers within the observed spectrum is $T_1(\mathbb{N}_1^8)$, and the rms absolute integrated change induced by the flow within the observed spectrum based on (5) is $\sum_1^8 \frac{n+1}{2n+1} |T_n(\mathbb{N}_1^8)|$, both in $\mu\mathrm{T}^2\,\mathrm{yr}^{-1}$. The difference between harmonics participating in the dominant transfers is Δn.

Case	Synthetic flow	$T_1\left(\mathbb{N}_1^8\right)$	$\sum_1^8 \frac{n+1}{2n+1} \lvert T_n\left(\mathbb{N}_1^8\right)\rvert$	Δn
1	$\mathcal{T}_1^0$	0.0006	0.015	0
2	$\mathcal{T}_1^{1c}$	1.54	3.85	0
3	$\mathcal{P}_2^0$	204.40	426.75	2
4	$\mathcal{T}_2^{1c}$	83.76	210.82	1
5	$\mathcal{P}_2^{2c}$	155.60	312.28	2
6	$\mathcal{P}_2^{2s}$	34.51	179.97	2
7	$\mathcal{T}_5^{4c}$	27.26	128.20	2–4
8	$\mathcal{P}_1^0$	−88.50	366.04	1
9	$\mathcal{T}_2^0$	22.07	136.85	1

Identifying the spherical harmonics in (18) indicates that the SV in this case is comprised of equatorial dipole changes only: $\dot{g}_1^1 = -\frac{A}{c^2} h_1^1$, $\dot{h}_1^1 = \frac{A}{c^2} g_1^1$, and therefore (4) and (8) give $T_1 = 4(\frac{a}{c})^6 (g_1^1 \dot{g}_1^1 + h_1^1 \dot{h}_1^1) = 0$. In words, energy has exchanged hands strictly between g_1^1 and h_1^1 without involving other harmonics, and the overall dipole energy is unchanged. The same type of magnetic energy exchange appears in case 2 where $\mathcal{T} = A\mathcal{T}_1^{1c}$. In this case, solid body rotation about an axis in the equatorial plane results in uniform meridional advection and energy transfer from g_1^0 to h_1^1. As in case 1, no energy transfer between different degrees occurs. These expected results can be directly obtained from the selection rules of Bullard & Gellman (1954) that restrict the interaction of a $\mathcal{T}_1^0$ flow and a poloidal magnetic field to either a change of phase in the poloidal field or to a conversion to a toroidal field (see their fig. 3c).

The known solutions in cases 1 and 2 allow testing the accuracy of our numerical scheme. In these cases the matrix components T_{np} representing the net energy transfer, the total change for each degree strictly due to energy transfer within the observed spectrum $T_n(\mathbb{N}_1^8)$ and the overall change including energy leaking from the observed spectrum to degrees beyond $n_{\max} = 8$ denoted by $T_n(\mathbb{N}_1^8 \to \mathbb{N}_1)$ are expected to be zero, so non-zero values in these quantities are numerical errors. Compared with a reference value, given in case 2 by the contribution of the term $g_1^0 \dot{g}_1^0$ to T_n, the maximum numerical error in case 2 is ∼2.2 per cent. In case 1, where the reference value is the contribution of the $g_1^1 \dot{g}_1^1$ term, the maximum numerical error is 0.2 per cent. The relative error in case 2 is larger than in case 1 because the large g_1^0 term participates in the SV in case 2 but not in case 1. Overall, simulating a zero $\dot{R}_n$ is most stringent, and is likely to yield the largest relative numerical errors. The maximal ∼2 per cent error reported here should therefore be considered as an upper bound relative error estimate.

3 RESULTS

3.1 Synthetic flows

We begin by analysing the magnetic energy transfer due to the interaction of simple synthetic single harmonic flows with the geomagnetic field. As stated earlier, we use for all synthetic flow cases the geomagnetic field model *gufm1* of Jackson *et al.* (2000) for the year 1980 expanded until spherical harmonic degree $n_{\max} = 8$. We

focus on flows symmetric to the equator that are often considered more geophysical due to the dominance of rotational effects in the Earth's core. In addition, we consider some antisymmetric flows that are suggested by some core flow models inferred from inversions of the geomagnetic SV. We note that for the synthetic flows the sign of the circulation is arbitrary; A change of sign for the flow would result in a change of sign for all components of the matrix T_{pn}, so that if flow $\mathcal{T}_n^m$ yields dipole decrease, flow $-\mathcal{T}_n^m$ would yield dipole increase. A summary of the synthetic flows and some statistics of the results are given in Table 1.

While the differential rotation in case 1 may be important for the dynamo generation, such a flow does not yield any poloidal energy transfer at the top of the core. The next equatorially symmetric toroidal flow is $\mathcal{T}_2^{1c}$ (case 4). This flow is comprised of two pairs of vortices, a cyclone and an anticyclone, in each hemisphere. The meridional flow, which is the sole component that may cause axial dipole changes (Olson & Amit 2006), is equatorward in $\phi = 90^\circ$W and poleward in $\phi = 90^\circ$E. The main SV structures are related to the meridional advection of the two intense high-latitude geomagnetic flux patches in the northern hemisphere (Fig. 4a), which are in-phase with the flow. The reduction of the axial dipole by the southward advection of the north American patch is balanced by the dipole strengthening due to the northward advection of the Siberian patch. In the southern hemisphere, the two normal flux patches yield little SV due to the weak meridional field gradient associated with the patch below the Indian Ocean and the off-phase relation with the flow of the patch below the Pacific. However, the equatorward advection of the reversed flux patch below Patagonia (Fig. 4a) results in a net dipole increase (Fig. 4c).

Our spectral transfer analysis of case 4 indicates that practically all the dipole increase is due to net energy transfer from the quadrupole (Fig. 4b), which is simultaneously decreasing (Fig. 4c). This transfer between degrees 1 and 2 can be demonstrated analytically. Substituting an axial dipole field and the $\mathcal{T}_2^{1c}$ flow into (12) gives

$$\dot{B}_r = -\frac{2A}{c^2}\left(\frac{a}{c}\right)^3 g_1^0 \cos\theta \sin\theta \sin\phi. \tag{19}$$

The coefficient $\dot{h}_2^1$ arises from (19). Because $h_2^1 < 0$ and $\dot{h}_2^1 = -\frac{2\sqrt{3}A}{9c^2}(\frac{a}{c})^{-1} g_1^0 > 0$, the term $h_2^1 \dot{h}_2^1$ provides a significant negative contribution to $T_{1\to 2}$. In addition, substituting an h_2^1 field and the $\mathcal{T}_2^{1c}$ flow into (12) gives

$$\dot{B}_r = \frac{6\sqrt{3}A}{5c^2}\left(\frac{a}{c}\right)^4 h_2^1 \left(5\cos^3\theta - 3\cos\theta + \frac{1}{2}\cos\theta\right). \tag{20}$$

The first two terms on the right-hand side of (20) are identified with the axial octupole SV. The last term on the right-hand side of (20) gives the coefficient $\dot{g}_1^0$. Because $g_1^0 < 0$ and $\dot{g}_1^0 = \frac{3\sqrt{3}A}{10c^2}(\frac{a}{c})h_2^1 < 0$,

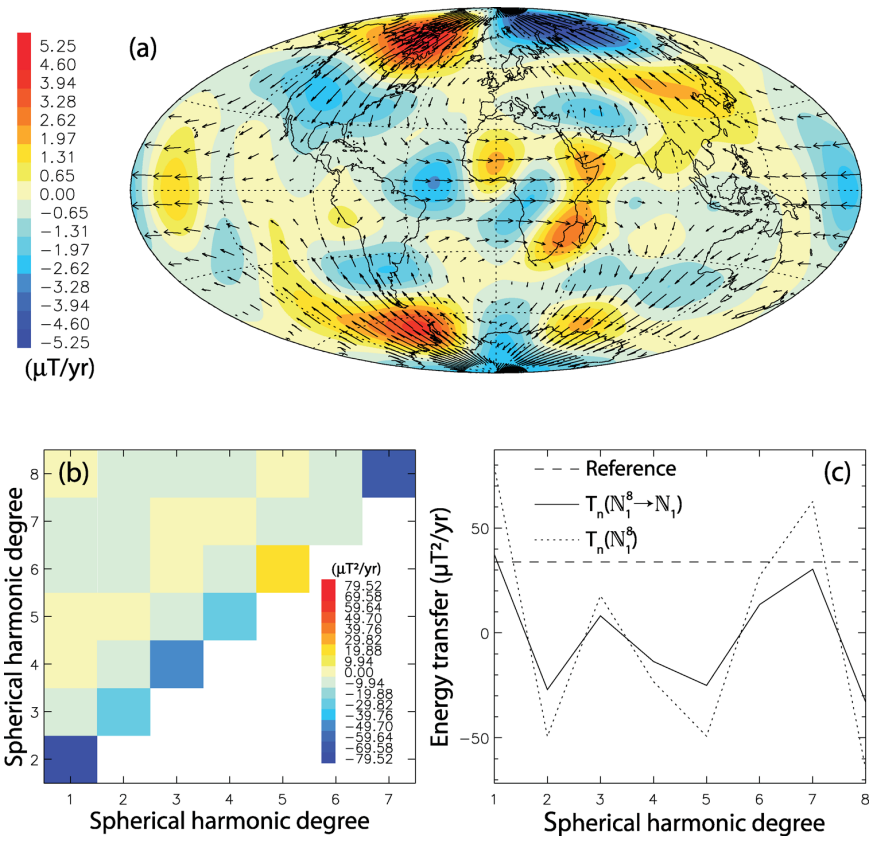

Figure 4. Case 4: (a) SV in μT yr^{-1} with superimposed arrows for the synthetic flow; (b) matrix components T_{np} in μT^2 yr^{-1}; (c) total change within the observed spectrum $T_n(\mathbb{N}_1^8)$ (dotted) and total change including energy leaking beyond $T_n(\mathbb{N}_1^8 \to \mathbb{N}_1)$ (solid), both in μT^2 yr^{-1}. The reference horizontal dashed line in (c) is the contribution of the term $g_1^0 \dot{g}_1^0$ to T_1.

the term $g_1^0 \dot{g}_1^0$ provides a significant positive contribution to $T_{2\to1}$. Both contributions, the negative $h_2^1 \dot{h}_2^1$ to $T_{1\to2}$ and the positive $g_1^0 \dot{g}_1^0$ to $T_{2\to1}$, add up to a negative T_{12} corresponding to a net energy transfer from the quadrupole to the dipole (Fig. 4b), to a dipole increase and to a quadrupole decrease (Fig. 4c).

Overall, the magnetic energy transfer is dominantly local in this case, that is, the difference between the degrees involved in the transfers is $\Delta n = 1$ (Table 1). An inverse energy cascade is seen continuously throughout almost the entire spectrum, except for forward cascade from $n = 5$ to $n = 6$. In all degrees, however, the transfer is always local between neighbouring harmonics. Moreover, the integrated energy transfer within the observed spectrum $T_n(\mathbb{N}_1^8)$ and the total advective change $T_n(\mathbb{N}_1^8 \to \mathbb{N}_1)$ are well correlated (Fig. 4c), so the energy leaking out of the observed spectrum plays a secondary role in the large-scale kinematics.

The largest scale symmetric flows that generate kinematic dynamos were found based on linear combinations of $\mathcal{T}_1^0$, $\mathcal{P}_2^0$, $\mathcal{P}_2^{2c}$ and $\mathcal{P}_2^{2s}$ (Kumar & Roberts 1975; Gubbins *et al.* 2000a,b). The poloidal flow $\mathcal{P}_2^{2c}$ of case 5 is comprised of two equatorial sources and two equatorial sinks, with saddles in the poles. The meridional flow at 90°E and 90°W (the longitudes of the equatorial sources) advects the two northern hemisphere high-latitude intense flux patches poleward (see the two large positive SV structures in Fig. 5a), thus strengthening the axial dipole (Fig. 5c). This dipole increase is due to energy transfer from degree 3 (Fig. 5b). Substituting an axial dipole field and the $\mathcal{P}_2^{2c}$ flow into (12) gives

$$\dot{B}_r = \frac{20A}{c^2}\left(\frac{a}{c}\right)^3 g_1^0 \sin^2\theta \cos\theta \cos 2\phi \qquad (21)$$

demonstrating that the SV due to such a field–flow interaction indeed results in a strong degree 3 coefficient $\dot{g}_3^2$. Changing the phase of the flow may be important. The $\mathcal{P}_2^{2s}$ flow is off-phase with the northern hemisphere normal flux patches resulting in bipolar SV structures due to westward drift that does not affect the axial dipole. In the southern hemisphere the distance between the two normal flux patches is such that one patch is advected poleward while the other is advected equatorward, resulting in a weak net dipole change (Table 1). In both cases 5 and 6, the energy transfer is strictly between harmonics differing by $\Delta n = 2$, in agreement with the selection rules of the Gaunt and Elsasser integrals (see fig. 5c of Bullard & Gellman 1954). In case 5, the largest net energy transfer is from $n = 3$ to the dipole (Figs 5b and c); In case 6, the energy is transported forward from degrees 3, 4 and 5 to degrees 5, 6 and 7, respectively, resulting in a minimum in T_3 and a maximum in T_7 (not shown). Also note that in both cases the dipole increases when accounting for energy transfer strictly within the observed spectrum, but the dipole change is much smaller when including the energy escaping from the observed spectrum to higher degrees.

To investigate the impact of small scales on the magnetic energy transfer, we consider case 7 with a toroidal $\mathcal{T}_5^{4c}$ flow. The resulting SV is characterized by somewhat smaller scales than in the previous cases (Fig. 6a). More importantly, the transfer is less local, and the difference between the harmonics involved in the transfer is not

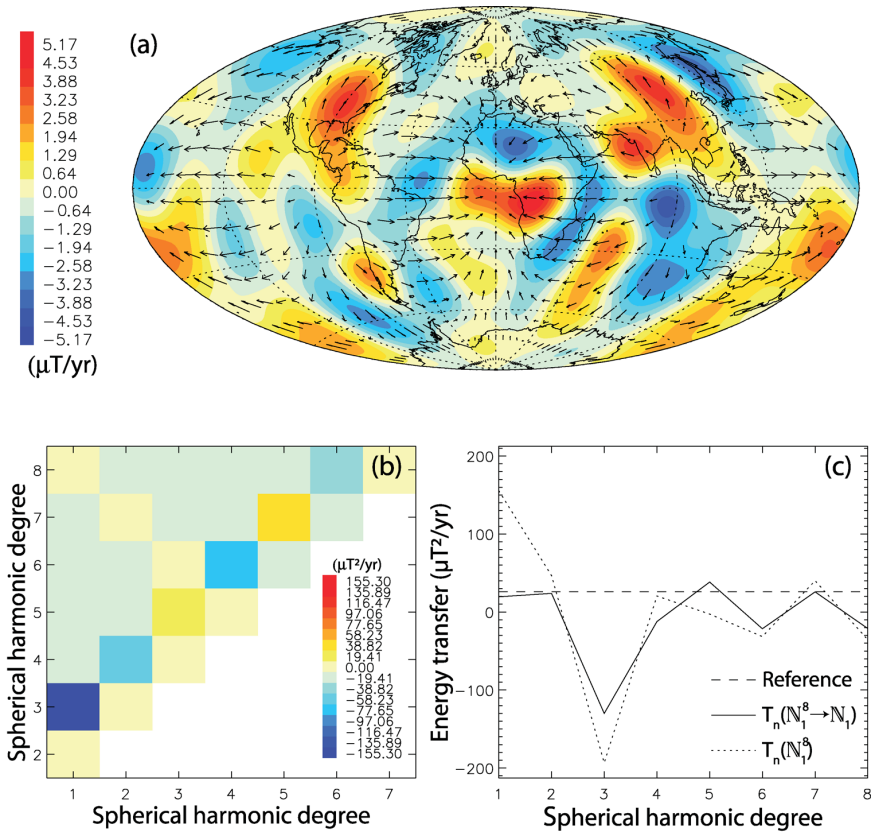

Figure 5. As in Fig. 4 for case 5.

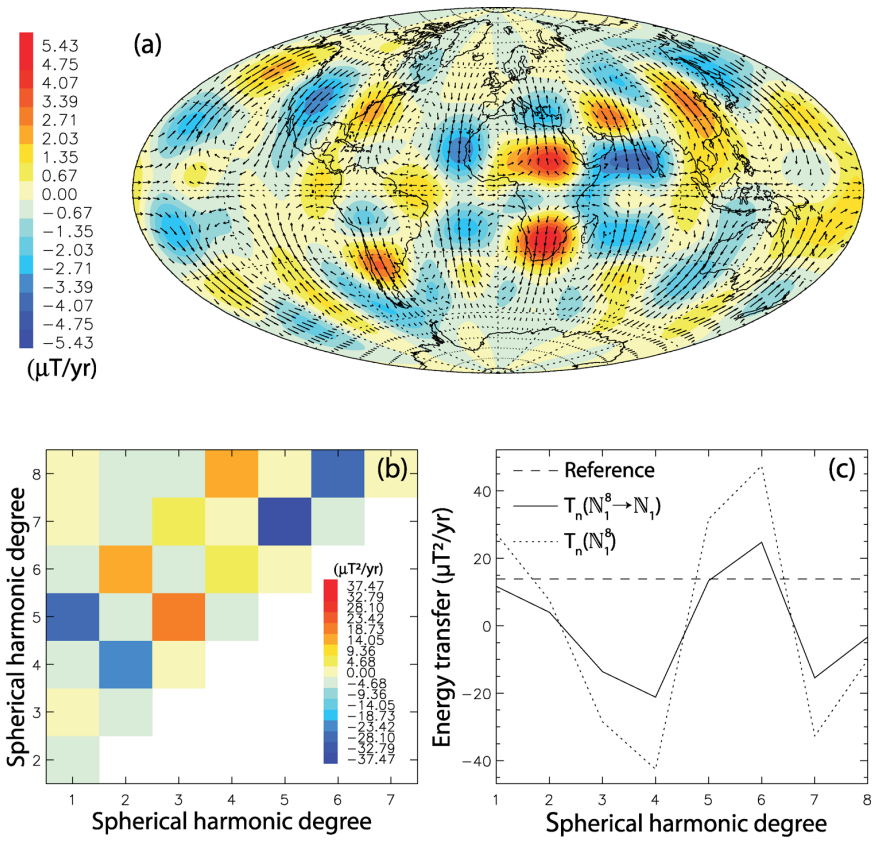

Figure 6. As in Fig. 4 for case 7.

fixed, ranging $\Delta n = 2$–4. The most significant energy transfer is from $n = 7$ to $n = 5$ (Fig. 6b), resulting in a minimum in T_7 (Fig. 6c).

We also examine two antisymmetric flows, one toroidal and one poloidal (see Table 1). The poloidal flow $\mathcal{P}_1^0$ of case 8 is all northward from a south pole source to a north pole sink. The transfer is purely local (Table 1), as prescribed by the selection rules that permit either poloidal-to-poloidal magnetic energy transfer between neighbouring degrees or poloidal-to-toroidal within the same degree (see fig. 4 of Bullard & Gellman 1954). The toroidal flow $\mathcal{T}_2^0$ (case 9) is zonal with a north–south shear, so that the motion is eastward/westward in the northern/southern hemispheres, respectively. In such a purely zonal motion, dipole changes are excluded to the equatorial component (Amit & Olson 2008). The energy transfer in this case is local, that is, between neighbouring harmonics (Fig. 7b). An inverse magnetic energy cascade appears from degree $n = 4$ to the dipole and from degree $n = 7$ to $n = 5$, with the exception of a forward transfer from degree $n = 4$ to $n = 5$, resulting in a minimum in T_4 (Fig. 7c).

3.2 Core flows

We now implement our formalism to calculate the geomagnetic energy transfer induced by core flow models. As stated earlier, we use the purely helical core flow model of Amit & Olson (2004) obtained from inversions of geomagnetic SV from *gufm1* (Jackson *et al.* 2000) in 5-yr intervals during the period 1840–1990. In addition to the two integrated quantities, one of magnetic energy transfer strictly within the observed spectrum $T_n(\mathbb{N}_1^8)$, and the other of magnetic energy transfer from the observed to the entire spectrum $T_n(\mathbb{N}_1^8 \rightarrow \mathbb{N}_1)$, we also consider the observed change $\dot{R}_n$ calculated based on the geomagnetic field and SV Gauss coefficients (red solid line in Fig. 8). The observed $\dot{R}_n$ differs from T_n because the latter is affected by the SV misfit of the core flow models. In addition, magnetic diffusion is likely to affect $\dot{R}_n$ (Holme & Olsen 2006; Holme 2007; Amit & Christensen 2008). In contrast, it is possible that inverted core flows cannot mimic magnetic diffusion (Holme 2007), and unmodelled diffusive effects are absorbed by the SV misfit (Rau *et al.* 2000). If this is indeed the case, our calculated transfer spectrum T_n may indeed represent the transport of energy by the flow.

Fig. 8 shows the temporal evolution of the three quantities for each spherical harmonic degree. Overall, the three quantities follow similar trends, suggesting that the geomagnetic energy leakage outside the observed spectrum, the energy change due to interactions of small-scale flow with large-scale field and of small-scale field with large-scale flow, the SV misfit of the core flow models and the impact of magnetic diffusion on the shape of the geomagnetic field spectrum, are all secondary in the interpretation of the geomagnetic energy transfer. The largest discrepancies among the three curves seem to appear in the dipole term. In addition, the dipole change curve contains higher frequencies than the higher harmonics, highlighting the challenging task of investigating dipole

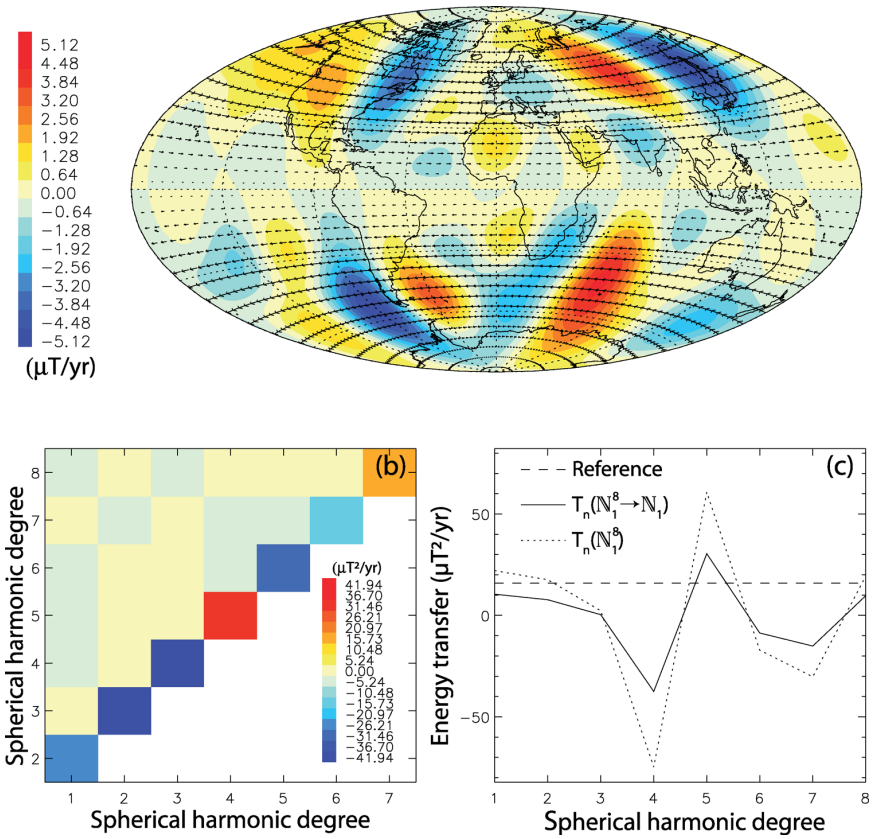

Figure 7. As in Fig. 4 for case 9. The reference horizontal dashed line in (c) is the contribution of the term $h_1^1 \dot{h}_1^1$ to T_1.

variability. The quadrupole energy rate of change is the smallest in magnitude. Higher harmonics often display relatively long periods of either steady or linear trends, possibly due to the stronger temporal regularization of higher degrees in *gufm1*.

As shown in the movie *TransferGeomag.gif* and reported in Table 2, a pattern of alternating minima/maxima is a robust feature of the transfer spectra T_n induced by the core flows. The period 1840–1910 is characterized by even maxima and odd minima T_n, whereas the period 1955–1990 is reversed with odd maxima and even minima. The intermediate period is transitory with a relatively smooth T_n pattern. Overall, the analysis of the core flows is much more complex than in the synthetic flows. Energy transfer occurs both locally and between non-neighbouring degrees. The ratio of local to non-local transfers is about ∼0.5 (Table 2). Cascades are not continuous through long parts of the spectrum, but instead energy transfer in one direction is often interrupted by opposite direction of transport between neighbouring degrees. Most strikingly, rapid variations in T_{pn} from one snapshot to another provide evidence for the strong time-dependence of core dynamics on short timescales.

Kolmogorov-like turbulent behaviour may arise in a statistical sense (Moffatt 1978), so it is worth-while examining the time-average energy transfer. Following Amit & Olson (2010), we search for time-averages of intervals that may highlight some trends in the behaviour of the energy transfer. Figs 9–11 show three time-averages of intervals characterized by different T_n trends (see Fig. 8 and Table 2). In the time-average of the period 1840–1910, even maxima and odd minima dominate T_n at intermediate degrees (Fig. 9b). The lowest diagonal ($\Delta n = 1$) is mostly negative (Fig. 9a), that is, an inverse cascade transfers geomagnetic energy from high to low neighbouring degrees. The left column, in contrast, is characterized by positive structures, representing forward non-local transfer from the dipole mainly to degrees $n = 3$–4 and $n = 6$ (Fig. 9a) that results in the two peaks of T_4 and T_6 (Fig. 9b).

In 1915–1950, both the lowest diagonal and the left column contain significant positive structures, so energy cascades forward through neighbouring degrees, but also energy is transferred from the dipole to higher degrees $n = 3$ and 5. The spectral region in between the lowest diagonal and left column contains some negative values, mostly due to energy transfer from $n = 5$ to $n = 2$–3 (Fig. 10a). Overall, the forward energy transfer in both the lowest diagonal and the left column yield simultaneous dipole decrease and non-dipole increase at this interval (Figs 10b and 8).

In the interval 1955–1990, the upper part of the transfer matrix is dominantly positive, the intermediate is mostly negative and the lower is once again positive (Fig. 11a). Geomagnetic energy is transported from most of the spectrum to the high degrees, especially to $n = 7$. Energy leaves from intermediate degrees $n = 4$–6 to the rest of the spectrum. Dipole energy is transferred to degrees 2–3. The total transfer contains maxima in odd degrees and minima in even degrees (Fig. 11b).

Finally, we wish to relate the spectral analysis with its origin in physical space. Holme *et al.* (2011) demonstrated that field

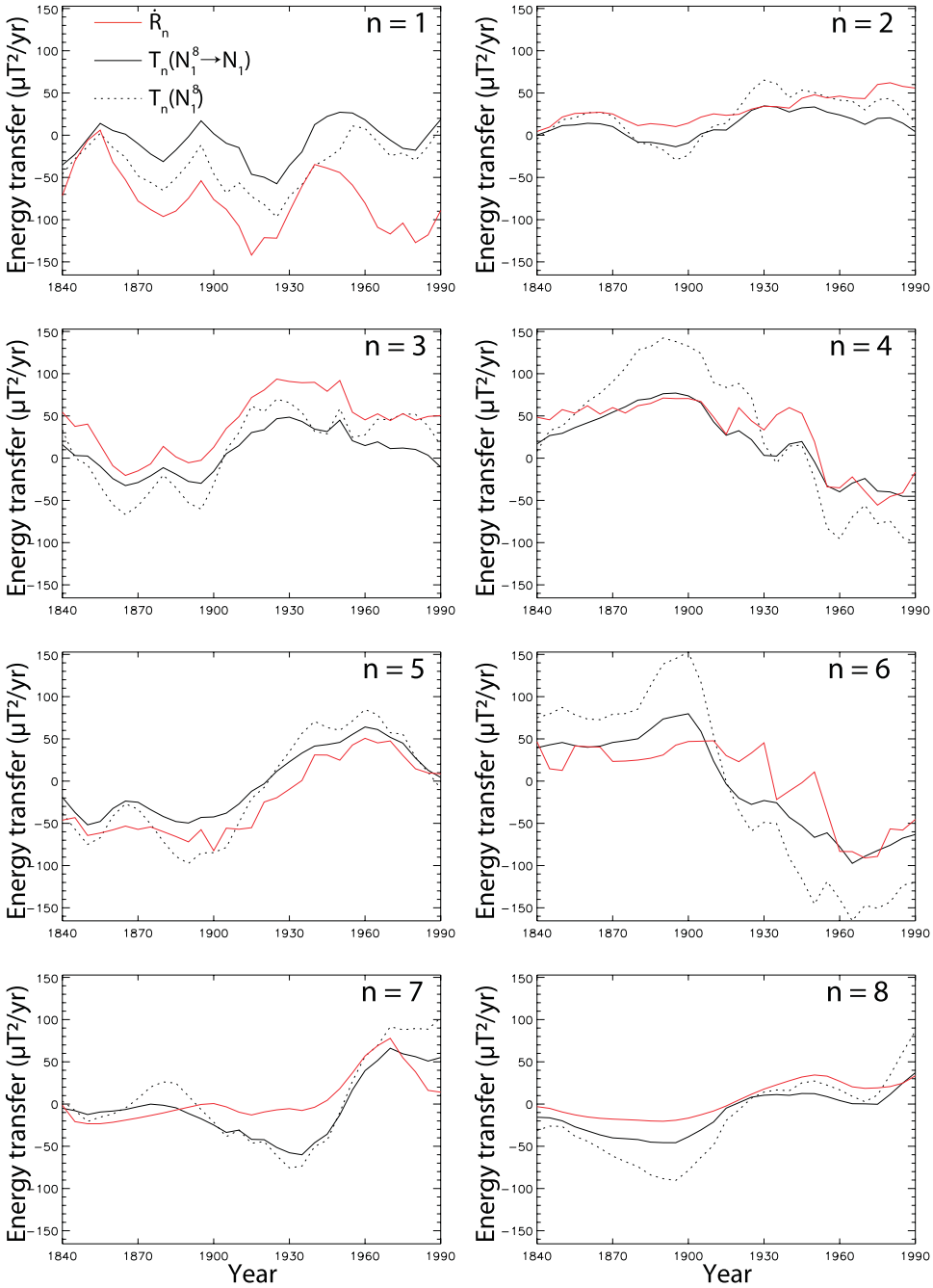

Figure 8. Total geomagnetic energy transfers $T_n(\mathbb{N}_1^8)$ (dotted black) and $T_n(\mathbb{N}_1^8 \rightarrow \mathbb{N}_1)$ (solid black), and the observed change $\dot{R}_n$ (red), for each spherical harmonic degree as a function of time for the historical period 1840–1990.

concentration in one hemisphere (eastern or western) corresponds to a spectrum dominated by even harmonics. The geomagnetic SV exhibits strong hemispheric dichotomy between the active Atlantic and the quite Pacific, which is thought to originate in thermal core–mantle coupling (Christensen & Olson 2003; Gubbins 2003). The product of B_r and SV, which is relevant for $\dot{R}_n$ (4), has roughly the same hemispheric asymmetry, but with an opposite sign (because g_1^0 is negative). This is evident in the coincidence between minima of S_n and maxima of $\dot{R}_n$ and vice versa (Figs 2b and c). The alternating even/odd peaks of T_n are therefore partially related to the Atlantic/Pacific SV dichotomy. However, the strong temporal evolution of T_n seen in Figs 9–11 indicates that thermal core–mantle coupling alone cannot explain the observed spectral variations.

Table 2. Summary of core flows in 5-yr intervals for the period 1840–1990. The integrated dipole energy change by transfers within the observed spectrum is $T_1(\mathbb{N}_1^8)$, and the rms absolute integrated change within the observed spectrum based on (5) is $\sum_1^8 \frac{n+1}{2n+1}|T_n(\mathbb{N}_1^8)|$, both in $\mu\mathrm{T}^2\,\mathrm{yr}^{-1}$. Even maxima and odd minima in $T_n(\mathbb{N}_1^8)$ are denoted by 'Even/odd', odd maxima and even minima are denoted by 'Odd/even', and '–' marks a relatively smooth pattern. The ratio of local to non-local transfers L (16) is also given. Horizontal line spaces separate the different Max/Min periods. The statistics of the total and partial time-averages are given at the bottom.

Year	$T_1\left(\mathbb{N}_1^8\right)$	$\sum_1^8 \frac{n+1}{2n+1}\lvert T_n\left(\mathbb{N}_1^8\right)\rvert$	Max/Min	L
1840	−46.01	136.34	Even/odd	0.52
1845	−27.85	132.19	Even/odd	0.39
1850	−13.45	158.36	Even/odd	0.47
1855	2.23	169.08	Even/odd	0.52
1860	−14.65	186.25	Even/odd	0.52
1865	−26.02	198.51	Even/odd	0.50
1870	−48.15	225.36	Even/odd	0.48
1875	−55.94	240.64	Even/odd	0.46
1880	−65.47	269.47	Even/odd	0.50
1885	−50.93	300.89	Even/odd	0.53
1890	−33.99	322.07	Even/odd	0.55
1895	−11.48	312.35	Even/odd	0.55
1900	−45.57	317.63	Even/odd	0.45
1905	−68.51	281.67	Even/odd	0.34
1910	−56.29	209.10	Even/odd	0.25
1915	−72.41	185.10	–	0.32
1920	−82.05	204.77	–	0.30
1925	−97.04	252.99	–	0.39
1930	−72.24	227.27	–	0.43
1935	−58.48	215.80	–	0.55
1940	−35.87	199.43	–	0.70
1945	−27.58	208.49	–	0.68
1950	−16.92	219.63	Odd/even	0.70
1955	11.03	223.50	Odd/even	0.52
1960	8.01	259.52	Odd/even	0.37
1965	−8.15	268.37	Odd/even	0.39
1970	−24.35	251.92	Odd/even	0.47
1975	−20.92	276.11	Odd/even	0.29
1980	−29.85	275.40	Odd/even	0.30
1985	−13.05	253.39	Odd/even	0.43
1990	9.65	249.02	Odd/even	0.38
1840–1990	−35.24	81.82	–	0.46
1840–1910	−37.47	210.62	Even/odd	0.47
1915–1950	−57.82	202.69	–	0.51
1955–1990	−8.45	251.17	Odd/even	0.39

4 DISCUSSION

The analysis of the energy transfer in the synthetic flows shows that most energy transfers align on one diagonal, so the difference between dominant harmonics participating in the transfer Δn is nearly constant. Flows $\mathcal{T}_2^m$ and $\mathcal{P}_1^m$ are local, that is, energy is being transferred strictly between neighbouring harmonics and T_{pn} is dominated by the lower diagonal (see $\Delta n = 1$ in Table 1). Poloidal symmetric flows $\mathcal{P}_2^m$ that were found efficient in generating dynamo action (Kumar & Roberts 1975; Gubbins *et al.* 2000a,b) are characterized by $\Delta n = 2$. Similar energy transfer was found in the analysis of the magnetic spectrum of a numerical dynamo model (Olson *et al.* 2009). The magnetic energy transfers obtained by these low degree synthetic flows are in agreement with the selection rules of the Gaunt and Elsasser integrals (Bullard & Gellman 1954), thus confirming the sensibility of our mathematical formulation and numerical scheme. The small-scale flow $\mathcal{T}_5^{4c}$ shows deviations from a constant Δn and includes transfers between 2–4 degrees differences. Overall, the transfer induced by large-scale toroidal flows is more local than that generated by small-scale poloidal flows, in agreement with studies of MHD turbulence simulations that attributed local transfer to magnetic field advection and non-local effects to magnetic field stretching (Alexakis *et al.* 2007). Some single harmonic synthetic flows show magnetic energy cascade over most of the observed spectrum (Fig. 4).

Of the nine synthetic flows studied here, the two axisymmetric poloidal flows seem to be the most efficient in producing energy transfer in general and dipole changes in particular (Table 1). The $\mathcal{P}_2^0$ flow (case 3) has an equatorial source and polar sinks, so magnetic flux is advected from low- to high-latitudes and thus strengthening the axial dipole. Note that by simply changing the sign of the flow the opposite effect, in this case dipole decrease, is obtained. A Y_2^0 CMB heat flux heterogeneity was found to be very efficient in terms of increasing (or decreasing, depending on the sign) reversal frequency by attracting magnetic flux to the equatorial region and hence initiating dipole polarity transitions (Glatzmaier *et al.* 1999; Kutzner & Christensen 2004; Olson *et al.* 2010). Our results therefore support the importance of the $\mathcal{P}_2^0$ flow in obtaining rapid dipole changes. The axisymmetric poloidal $\mathcal{P}_1^0$ flow is perpendicular to the equator, an unlikely feature in a rapidly rotating system as the Earth's core, so it is not geophysically relevant. This flow does not change the dipole dramatically, but the energy transfer of other degrees is large.

The phase of the flow may be very important for the energy transfer. Flows $\mathcal{P}_2^{2c}$ and $\mathcal{P}_2^{2s}$ interact differently with the present geomagnetic field, resulting in remarkably different energy transfers. Flow $\mathcal{P}_2^{2c}$ is in-phase with the field in the northern hemisphere, advecting the two northern hemisphere high-latitude intense flux patches poleward and thus strengthening the axial dipole (Fig. 5c) and causing overall strong energy transfers (Table 1). In contrast, flow $\mathcal{P}_2^{2s}$ interacts with the southern hemisphere flux patches, but one patch is advected poleward while the other is advected equatorward, resulting in a weak dipole change and weaker energy transfers (Table 1). A CMB heat flux pattern of Y_2^2 was found to be inefficient in reversing the dipole (Olson *et al.* 2010), perhaps because in a dynamically self-consistent system the vortices tend to correlate with magnetic flux patches and thus minimize the advection of these high-latitude features (Amit *et al.* 2010; Finlay & Amit 2011).

While toroidal flows seem less efficient than poloidal flows in inducing energy transfers, we recall that for comparison purposes all synthetic flows were set with identical amplitudes. In the Earth's core, most studies suggest that toroidal flows are much stronger than poloidal flows, possibly by about an order of magnitude (Finlay & Amit 2011). Differences of about a factor of 2–3 between the more efficient poloidal flows to the less efficient toroidal flows (Table 1) are physically insightful, but in the geophysical context these differences could thus be overshadowed by the much larger amplitude toroidal flows in the Earth's core.

Alternating minima/maxima of T_n is characteristic of turbulent magnetic energy cascades (Alexakis *et al.* 2005b). Evidence for magnetic energy cascade is suggestive in the temporal variations of the geomagnetic energy spectrum (Voorhies 2004), in particular in the form of moving peaks of successive R_n structures with time (Amit & Olson 2010). Our detailed inspection of the energy transfer between pairs of harmonics T_{pn} shows a more complex behaviour. The magnetic energy cascade in case 4 indeed contains a pattern of alternating minima/maxima of T_n (Fig. 4). However, while such a

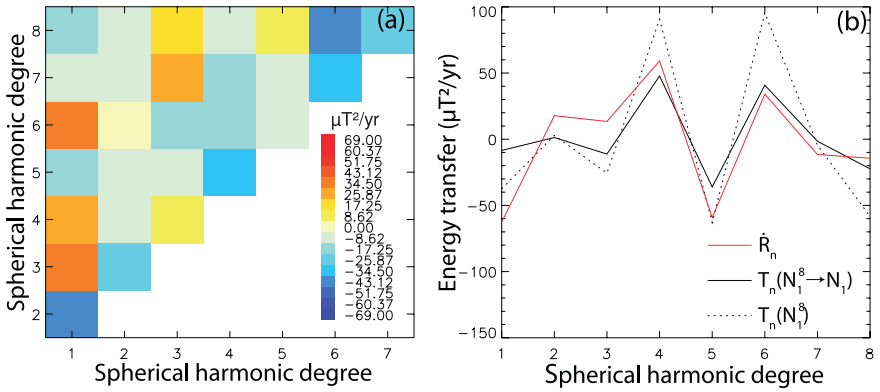

Figure 9. Geomagnetic energy transfer matrix T_{pn}, the two total energy transfers $T_n(\mathbb{N}_1^8)$ (dotted black) and $T_n(\mathbb{N}_1^8 \rightarrow \mathbb{N}_1)$ (solid black), and the observed $\dot{R}_n$ (red), all in $\mu T^2\ yr^{-1}$, for the time-average of the interval 1840–1910.

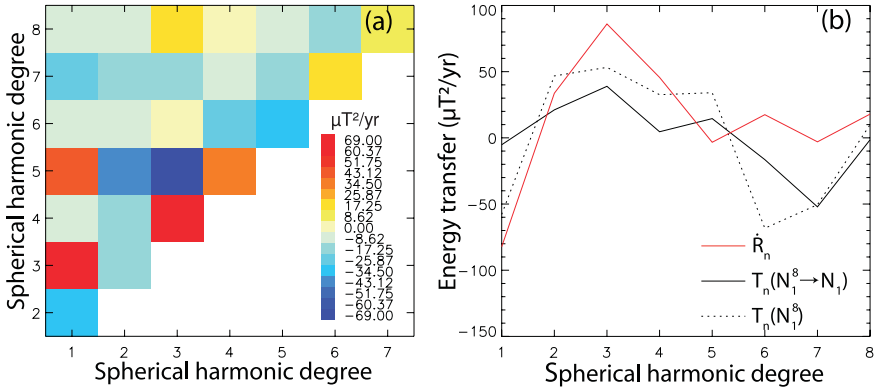

Figure 10. As in Fig. 9 for the time-average of the interval 1915–1950.

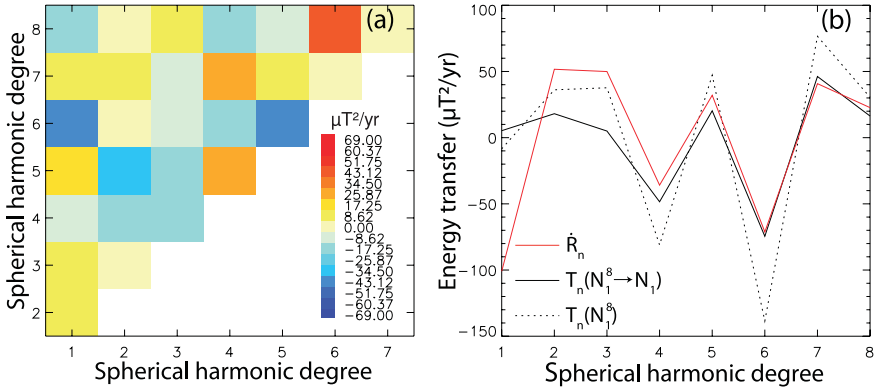

Figure 11. As in Fig. 9 for the time-average of the interval 1955–1990.

pattern of alternating minima/maxima of T_n dominates most of the core flows, the energy transfer T_{pn} is not exclusively local. In the period 1840–1910 (Fig. 9a), an inverse cascade transfers energy from high to low degrees, but in addition non-local energy transfer occurs from the dipole to higher degrees. These opposing trends result in a relatively slow dipole decrease (see minimum in Fig. 1b during this period). Energy transfer from the dipole induces maxima of T_4 and T_6, while inverse energy cascade from $n = 5$ to $n = 4$ gives a minimum at $n = 5$, thus resulting in the even maxima and odd minima T_n pattern (Fig. 9b). In the period 1955–1990 (Fig. 11a) this T_n pattern has reversed. Magnetic energy is transferred from intermediate degrees $4 - 6$ to lower and higher degrees, yielding maxima in T_5 and T_7 and minima in T_4 and T_6 (Fig. 11b). In between, a short transition period between 1915 and 1950 is characterized by a relatively smooth T_n spectrum (Fig. 10b). This transition period exhibits a forward energy cascade and non-local energy transfer from the dipole to higher degrees (Fig. 10a), giving the fastest dipole decrease (Figs 1b and 8).

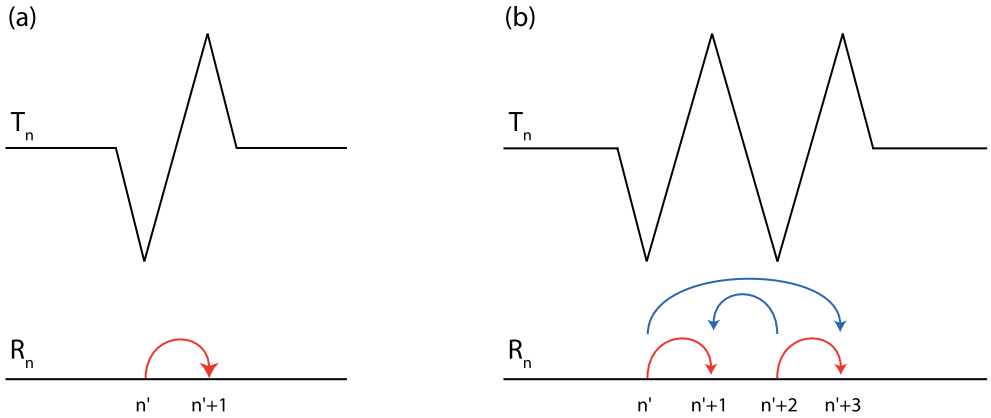

Figure 12. Schematic illustrations of alternating extrema in the transfer spectrum T_n (top) and some possible interpretations in terms of the transfer of magnetic energy spectrum R_n (bottom). (a) One pair of minimum/maximum T_n is likely to indicate local forward energy transfer. (b) Two pairs of minima/maxima T_n may be interpreted as either local forward energy cascade (red) or a more complex combination of non-local forward and local inverse transfers (blue).

The above-mentioned analysis shows that some caution is required when interpreting alternating minima/maxima T_n as an energy cascade. Indeed, when one pair of minimum/maximum appears, the most likely scenario is local transfer (see Fig. 12a following fig. 1 of Mininni 2011). However, multiple minima/maxima T_n, as typically found in the transfer spectra induced by the core flows (Figs 9 and 11), may arise due to either local or non-local transfers. In that case the solution is non-unique (Amit & Olson 2010). Consider the example in Fig. 12b where the T_n pattern contains minima in degrees n' and $n'+2$ and maxima in degrees $n'+1$ and $n'+3$. The cascade scenario would suggest forward energy transfer from n' to $n'+1$ and from $n'+2$ to $n'+3$. However, alternative scenarios are also possible, for example, non-local forward transfer from n' to $n'+3$ and local inverse transfer from $n'+2$ to $n'+1$. Tracking the transfer between each pair of degrees using the T_{pn} matrix reveals the actual paths of energy. Our T_{pn} solutions obtained from the core flows show a rich behaviour with both local Kolmogorov-like and non-local transfers.

Tracking magnetic energy transfer may shed light on the kinematics of the historical geomagnetic dipole moment decrease. Fig. 8 shows that dipole SV differs from temporal variations of higher harmonics in the larger differences among the $T_n(\mathbb{N}_1^8)$, $T_n(\mathbb{N}_1^8 \rightarrow \mathbb{N}_1)$ and $\dot{R}_n$ curves. This suggests that magnetic diffusion may play a more important role in the dipole evolution (Holme & Olsen 2006). The growth of reversed flux patches on the CMB by radial magnetic diffusion (Chulliat & Olsen 2010) has indeed been interpreted as a major cause for the dipole decrease (Gubbins 1987; Olson & Amit 2006). Dipole SV is sometimes underestimated by core flow inversions (Jackson 1997), possibly because the inversions cannot mimic the effects of magnetic diffusion SV (Whaler & Davis 1997; Holme 2007). The increasing difference between T_1 and $\dot{R}_1$ in the past several decades (Fig. 8) may suggest that dipole decrease by core flow has recently been relatively slow, and alternatively an increase in the rate of magnetic flux expulsion took place. The smaller differences among the three curves for the higher harmonics provide confidence in the overall interpretation of the energy transfer.

Amit & Olson (2010) argued that forward cascade with strong time-variability in the dipole family may explain the axial dipole decrease, while a much steadier inverse cascade governs the quadrupole family. However, their calculations rely on a local transfer assumption, which we find only partially valid. Our analysis shows that the direction of energy cascade may vary, but non-local energy transfer from the dipole to higher degrees seems more persistent. Integration over the entire observed spectrum shows that the contribution of non-local transfer is typically twice larger than that of local transfer (Table 2). Based on these findings, explaining the temporal changes in the geomagnetic spectrum by a strictly local energy transfer seems unsatisfactory.

The time-average for the entire period 1840–1990 resembles the time-average over the transitory interval 1915–1950 (Fig. 10) with both forward energy cascade from low to high degrees and non-local energy transfer from the dipole to higher degrees. The reversing trends of alternating extrema, from even maxima and odd minima between 1840 and 1910 (Fig. 9) to odd maxima and even minima between 1955 and 1990 (Fig. 11), cancel each other in the time-average of the entire period 1840–1990. It is unknown how long the first phase persisted prior to 1840. It is possible that currently the geodynamo is at the beginning of a long period of odd maxima and even minima T_n with relatively small contributions of core flow to the geomagnetic dipole decrease.

ACKNOWLEDGMENTS

HA thanks Coerte Voorhies for encouraging to test the local transfer assumption. We thank Peter Olson, Benoit Langlais, Gaël Choblet and Thierry Alboussière for insightful discussions. We are grateful to Bruce Buffett and an anonymous reviewer for constructive comments that significantly improved the paper. This study was supported by the Centre National d'Etudes Spatiales (CNES).

REFERENCES

Alexakis, A., Mininni, P. & Pouquet, A., 2005a. Imprint of large-scale flows on turbulence, *Phys. Rev. Lett.,* **93,** 264503, doi:10.1103/PhysRevLett.95.264503.

Alexakis, A., Mininni, P. & Pouquet, A., 2005b. Shell to shell energy transfer in MHD. I. steady state turbulence, *Phys. Rev. E.,* **72,** 046301, doi:10.1103/PhysRevE.72.046301.

Alexakis, A., Mininni, P. & Pouquet, A., 2007. Turbulent cascades, transfer, and scale interactions in magnetohydrodynamics, *New J. Phys.,* **9,** 1–20.

Alldredge, L., 1984. Harmonics required in main field and secular variation models, *J. Geomagn. Geoelectr.,* **36,** 63–72.

Amit, H. & Christensen, U., 2008. Accounting for magnetic diffusion in core flow inversions from geomagnetic secular variation, *Geophys. J. Int.,* **175,** 913–924.

Amit, H. & Olson, P., 2004. Helical core flow from geomagnetic secular variation, *Phys. Earth planet. Inter.,* **147,** 1–25.

Amit, H. & Olson, P., 2006. Time-average and time-dependent parts of core flow, *Phys. Earth planet. Inter.,* **155,** 120–139.

Amit, H. & Olson, P., 2008. Geomagnetic dipole tilt changes induced by core flow, *Phys. Earth planet. Inter.,* **166,** 226–238.

Amit, H. & Olson, P., 2010. A dynamo cascade interpretation of the geomagnetic dipole decrease, *Geophys. J. Int.,* **181,** 1411–1427.

Amit, H., Aubert, J. & Hulot, G., 2010. Stationary, oscillating or drifting mantle-driven geomagnetic flux patches? *J. geophys. Res.,* **115,** B07108, doi:10.1029/2009JB006542.

Aubert, J., Amit, H. & Hulot, G., 2007. Detecting thermal boundary control in surface flows from numerical dynamos, *Phys. Earth planet. Inter.,* **160,** 143–156.

Aubert, J., Aurnou, J. & Wicht, J., 2008. The magnetic structure of convection-driven numerical dynamos, *Geophys. J. Int.,* **172,** 945–956.

Batchelor, G., 1953. *The Theory of Homogeneous Turbulence,* Cambridge University Press, Cambridge, UK.

Bullard, E. & Gellman, H., 1954. Homogeneous dynamos and terrestrial magnetism, *Phil. Trans. R. Soc. A.,* **247,** 213–278.

Cain, J., Wang, Z., Schmitz, D. & Meyer, J., 1989. The geomagnetic spectrum for 1989 and core-crustal separation, *Geophys. J.,* **97,** 443–447.

Carati, D., Debliquy, O., Knaepen, B., Teaca, B. & Verma, M., 2006. Energy transfers in forced MHD turbulence, *J. Turb.,* **7,** 1–12.

Christensen, U. & Aubert, J., 2006. Scaling properties of convection-driven dynamos in rotating spherical shells and application to planetary magnetic fields, *Geophys. J. Int.,* **166,** 97–114.

Christensen, U. & Olson, P., 2003. Secular variation in numerical geodynamo models with lateral variations of boundary heat flow, *Phys. Earth planet. Inter.,* **138,** 39–54.

Chulliat, A. & Olsen, N., 2010. Observation of magnetic diffusion in the Earth's outer core from Magsat, ørsted and CHAMP data, *J. geophys. Res.,* **115,** doi:10.1029/2009JB006994.

Dormy, E., Valet, J.-P. & Courtillot, V., 2000. Numerical models of the geodynamo and observational constraints. *Geochem. Geophys. Geosyst.,* **1**(10), 1037, doi:10.1029/2000GC000062.

Elsasser, W., 1946. Induction effects in terrestrial magnetism part I. Theory, *Phys. Rev.,* **69,** 106–116.

Finlay, C. & Amit, H., 2011. On flow magnitude and field-flow alignment at Earth's core surface, *Geophys. J. Int.,* **186,** 175–192.

Frisch, U., 1995. *Turbulence: The Legacy of A.N. Kolmogorov*. Cambridge University Press, Cambridge.

Gillet, N., Pais, M. & Jault, D., 2009. Ensemble inversion of time-dependent core flow models, *Geochem. Geophys. Geosyst.,* **10,** Q06004, doi:10.1029/2008GC002290.

Gillet, N., Schaeffer, N. & Jault, D., 2011. Rationale and geophysical evidence for quasi-geostrophic rapid dynamics within the Earth's outer core, *Phys. Earth planet. Inter.,* **187,** 380–390.

Gissinger, C., Dormy, E. & Fauve, S., 2010. Morphology of field reversals in turbulent dynamos, *Europhys. Lett.,* **90,** 49001, doi:10.1209/0295-5075/90/49001.

Glatzmaier, G., Coe, R., Hongre, L. & Roberts, P., 1999. The role of the earth's mantle in controlling the frequency of geomagnetic reversals, *Nature,* **401,** 885–890.

Gubbins, D., 1987. Mechanism for geomagnetic polarity reversals, *Nature,* **326,** 167–169.

Gubbins, D., 2003. Thermal core-mantle interactions: theory and observations, in *Earth's Core: Dynamics, Structure and Rotation*. eds Dehant, V., Creager, K., Karato, S. & Zatman, S., American Geophysical Union, Washington, DC.

Gubbins, D., Barber, C., Gibbons, S. & Love, J., 2000a. Kinematic dynamo action in a sphere: I effects of differential rotation and meridional circulation on solutions with axial dipole symmetry, *Proc. R. Soc. Lond. A,* **456,** 1333–1353.

Gubbins, D., Barber, C., Gibbons, S. & Love, J., 2000b. Kinematic dynamo action in a sphere: II symmetry selection, *Proc. R. Soc. Lond. A,* **456,** 1669–1683.

Gubbins, D., Willis, P. & Sreenivasan, B., 2007. Correlation of Earth's magnetic field with lower mantle thermal and seismic structure, *Phys. Earth planet. Inter.,* **162,** 256–260.

Holme, R., 2007. Large-scale flow in the core, in *Treatise on Geophysics*. Vol. 8, ed. Olson, P., Elsevier Science, London.

Holme, R. & Olsen, N., 2006. Core surface flow modelling from high-resolution secular variation, *Geophys. J. Int.,* **166,** 518–528.

Holme, R., Olsen, N. & Bairstow, F., 2011. Mapping geomagnetic secular variation at the core mantle boundary, *Geophys. J. Int.,* **186,** 521–528.

Jackson, A., 1997. Time-dependency of tangentially geostrophic core surface motions, *Phys. Earth planet. Inter.,* **103,** 293–311.

Jackson, A., Jonkers, A. & Walker, M., 2000. Four centuries of geomagnetic secular variation from historical records, *Phil. Trans. R. Soc. Lond. A,* **358,** 957–990.

Kahle, A., Vestine, E. & Ball, R., 1967. Estimated surface motions at the core surface, *J. geophys. Res.,* **72,** 1095–1108.

King, E., Stellmach, S., Noir, J., Hansen, U. & Aurnou, J., 2009. Boundary layer control of rotating convection systems, *Nature,* **457,** 301–304.

Kolmogorov, A. N., 1941. The local structure of turbulence in incompressible viscous fluid for very large Reynolds numbers, *Proc. USSR Acad. Sci.,* **30,** 299–303.

Kumar, S. & Roberts, P., 1975. A three-dimensional kinematic dynamo, *Proc. R. Soc. Lond. A,* **344,** 235–258.

Kutzner, C. & Christensen, U., 2004. Simulated geomagnetic reversals and preferred virtual geomagnetic pole paths, *Geophys. J. Int.,* **157,** 1105–1118.

Liu, L. & Olson, P., 2009. Geomagnetic dipole moment collapse by convective mixing in the core, *Geophys. Res. Lett.,* **36,** L10305, doi:10.1029/2009GL038130.

Lowes, F., 1974. Spatial power spectrum of the main geomagnetic field, *Geophys. J. R. astr. Soc.,* **36,** 717–730.

McLeod, M., 1996. Spatial and temporal power spectra of the geomagnetic field, *J. geophys. Res.,* **101,** 2745–2764.

Mininni, P., 2007. Inverse cascades and α effect at a low magnetic Prandtl number, *Phys. Rev. E.,* **76,** 026316, doi:10.1103/PhysRevE.76.026316.

Mininni, P., 2011. Scale interactions in magnetohydrodynamic turbulence, *Ann. Rev. Fluid Mech.,* **43,** 377–397.

Moffatt, H., 1978. *Magnetic Field Generation in Electrically Conducting Fluids*. Cambridge University Press, Cambridge.

Olsen, N. & Mandea, M., 2008. Rapidly changing flows in the Earth's core, *Nature Geosci.,* **1,** 390–394.

Olson, P. & Amit, H., 2006. Changes in earth's dipole, *Naturwissenschaften,* **93,** 519–542.

Olson, P. & Christensen, U., 2002. The time averaged magnetic field in numerical dynamos with nonuniform boundary heat flow, *Geophys. J. Int.,* **151,** 809–823.

Olson, P. & Christensen, U., 2006. Dipole moment scaling for convection-driven planetary dynamos, *Earth planet. Sci. Lett.,* **250,** 561–571.

Olson, P., Driscoll, P. & Amit, H., 2009. Dipole collapse and reversal precursors in a numerical dynamo, *Phys. Earth planet. Inter.,* **173,** 121–140.

Olson, P., Coe, R., Driscoll, P., Glatzmaier, G. & Roberts, P., 2010. Geodynamo reversal frequency and heterogeneous core-mantle boundary heat flow, *Phys. Earth planet. Inter.,* **180,** 66–79.

Pais, A. & Hulot, G., 2000. Length of day decade variations, torsional oscillations and inner core superrotation: evidence from recovered core surface zonal flows, *Earth planet. Sci. Lett.,* **118,** 291–316.

Pais, M.A. & Jault, D., 2008. Quasi-geostrophic flows responsible for the secular variation of the Earth's magnetic field, *Geophys. J. Int.,* **173,** 421–443, doi:10.1111/j.1365-246X.2008.03741.x.

Pouquet, A., Frisch, U. & Léeorat, J., 1976. Strong MHD helical turbulence and the nonlinear dynamo effect, *J. Fluid Mech.,* **77,** 321–354.

Rau, S., Christensen, U., Jackson, A. & Wicht, J., 2000. Core flow inversion tested with numerical dynamo models, *Geophys. J. Int.,* **141,** 485–497.

Roberts, P. & Scott, S., 1965. On analysis of the secular variation, 1, a hydromagnetic constraint: theory, *J. Geomagn. Geoelectr.,* **17,** 137–151.

Ryan, D. & Sarson, G., 2007. Are geomagnetic field reversals controlled by turbulence within the Earth's core? *Geophys. Res. Lett.,* **34,** L02307, doi:10.1029/2006GL028291.

Schaeffer, N. & Pais, M., 2011. On symmetry and anisotropy of Earth-core flows, *Geophys. Res. Lett.,* **38,** L10309, doi:10.1029/2011GL046888.

Takahashi, F., Matsushima, M. & Honkura, Y., 2007. A numerical study on magnetic polarity transition in an MHD dynamo model, *Earth Planets Space,* **59,** 665–673.

Voorhies, C., 2004. Narrow-scale flow and a weak field by the top of Earth's core: evidence from Orsted, Magsat, and secular variation, *J. geophys. Res.,* **109,** doi:10.1029/2003JB002833.

Whaler, K., 1986. Geomagnetic evidence for fluid upwelling at the core-mantle boundary, *Geophys. J. R. astr. Soc.,* **86,** 563–588.

Whaler, K. & Davis, R., 1997. Probing the Earth's core with geomagnetism, in *Earth's Deep Interior,* ed. Crossley, D., Gordon and Breach, Amsterdam.

Wicht, J. & Olson, P., 2004. A detailed study of the polarity reversal mechanism in a numerical dynamo model, *Geochem. Geophys. Geosyst.,* **5,** doi:10.1029/2003GC000602.

Yousef, T., Rincon, F. & Schekochihin, A., 2007. Exact scaling laws and the local structure of isotropic magnetohydrodynamic turbulence, *J. Fluid Mech.,* **575,** 111–120.

Earth and Planetary Science Letters 414 (2015) 68–76

Contents lists available at ScienceDirect

Earth and Planetary Science Letters

www.elsevier.com/locate/epsl

Lower mantle superplume growth excites geomagnetic reversals

Hagay Amit [a,*], Peter Olson [b]

[a] CNRS UMR 6112, Université de Nantes, Laboratoire de Planétologie et de Géodynamique, 2 rue de la Houssinière, Nantes, F-44000, France
[b] Department of Earth and Planetary Sciences, Johns Hopkins University, Baltimore, MD 21218, USA

ARTICLE INFO

Article history:
Received 1 September 2014
Received in revised form 5 January 2015
Accepted 11 January 2015
Available online xxxx
Editor: Y. Ricard

Keywords:
geodynamo
polarity reversals
core convection
core–mantle boundary
D″ layer
superplumes

ABSTRACT

Seismic images of the lower mantle reveal two large-scale, low shear wave velocity provinces beneath Africa and the Pacific that are variously interpreted as superplumes, plume clusters or piles of dense mantle material associated with the D″ layer. Here we show that time variations in the height of these structures produce variations in heat flux across the core–mantle boundary that can control the rate at which geomagnetic polarity reversals occur. Superplume growth increases the mean core–mantle boundary heat flux and its lateral heterogeneity, thereby stimulating polarity reversals, whereas superplume collapse decreases the mean core–mantle boundary heat flux and its lateral heterogeneity, inhibiting polarity reversals. Our results suggest that the long, stable polarity geomagnetic superchrons such as occurred in the Cretaceous, Permian, and earlier in the geologic record were initiated and terminated by the collapse and growth of lower mantle superplumes, respectively.

1. Introduction

Paleomagnetic data records extreme variability in the rate at which the geomagnetic field has reversed its polarity, from hyper-reversing periods in which the geomagnetic field reversed as often as every 40 thousand years, to superchrons in which the polarity remained stable for 40 million years (e.g. Merrill et al., 1998; Gradstein et al., 2012). There is little doubt that some of this variability is intrinsically random, and arises from the stochastic nature of the dynamo process (Ryan and Sarson, 2007; Wicht et al., 2009). However, the reversal record over the whole of Phanerozoic time is far from random (Olson et al., 2014). Its non-random behavior includes the approximately 200 million years repeat time for superchrons as well as their approximately 40 million years durations (Fig. 1). Both of these far exceed any known timescale of the fluid dynamics intrinsic to the outer core, but they are commensurate with timescales inferred for the variability of mantle dynamics, specifically, the overturn timescale of mantle convection and the development times of deep mantle plumes, respectively. Although mantle dynamics has been widely implicated in controlling geomagnetic reversal frequency (Glatzmaier et al., 1999; Kutzner and Christensen, 2004; Driscoll and Olson, 2009b, 2011; Olson et al., 2010, 2013; Pétrélis et al., 2011; Zhang and Zhong, 2011; Biggin et al., 2012; Olson and Amit, 2014), the precise connection remains enigmatic.

Answers to the puzzle of paleomagnetic reversal variations and their relation to mantle convection history can be found in the structure and dynamical behavior of the D″ layer at the base of the lower mantle. The pattern of seismic heterogeneity in the D″ layer that defines the large low shear velocity provinces (e.g. Garnero and McNamara, 2008), which is dominated in the present-day mantle by a spherical harmonic degree 2 (Dziewonski et al., 2010), has been variously interpreted as the long-lived root structure of two mantle superplumes (Romanowicz and Gung, 2002; Torsvik et al., 2010), plume clusters (Schubert et al., 2004; Bull et al., 2009) or dense chemical piles lying just above the core–mantle boundary (CMB) (Tackley, 2002; McNamara and Zhong, 2005; Tan and Gurnis, 2007). In this paper we make no distinction between these alternatives, using the terms *piles* and *superplumes* interchangeably for the two large seismic structures located in the lowermost mantle beneath Africa and the central Pacific.

How might lower mantle piles influence the long-term behavior of the geodynamo? The most obvious way is by controlling the heat loss from the core, which in turn controls the energy available to drive the geodynamo and its reversals. Models of the general circulation of the mantle (Zhang and Zhong, 2011; Olson et al., 2013) and inferences based on the interpretation of D″ structure (e.g. Masters et al., 2000) indicate that the CMB heat flux below the two piles is lower than the mean for the CMB as a whole, and likewise, the CMB heat flux is higher than the mean in regions where the piles are absent. In mantle general circulation

* Corresponding author.
E-mail address: Hagay.Amit@univ-nantes.fr (H. Amit).

http://dx.doi.org/10.1016/j.epsl.2015.01.013
0012-821X/

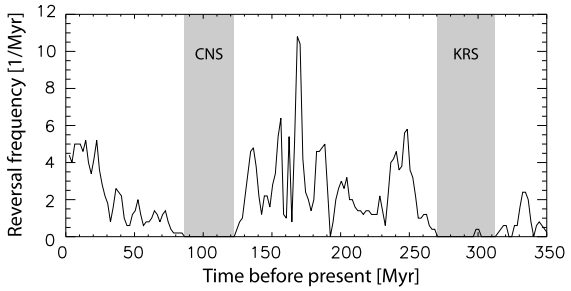

Fig. 1. Average paleomagnetic reversal frequency for 0–350 Ma based on the geomagnetic polarity time scale of Gradstein et al. (2012). The Cretaceous Normal Polarity Superchron (CNS) and Kiaman Reverse Polarity Superchron (KRS) are shaded. The bin size is 5 Myrs and the bin step is 2 Myrs.

models, this variation is a consequence of the flow pattern, which advects dense D″ material into piles beneath upwellings, reducing core heat flux there, and advects dense D″ material from beneath downwellings, increasing the core heat flux at those locations.

If the locations of the two main piles have remained relatively fixed (Burke et al., 2008; Dziewonski et al., 2010; Burke, 2011), the heat flux from the core could still have fluctuated if the heights of the piles changed with time. Figs. 2a and b illustrate how time variability in core heat flux might be produced this way. In the fully collapsed state the dense D″ layer has uniform thickness, and assuming the heat flux across this layer is by conduction, the CMB heat flux is laterally homogeneous. As the piles grow, the increase in the thermal gradient where the D″ layer is thinned exceeds the decrease in the thermal gradient where it is thickened, so that the mean heat flux from the core increases, along with its lateral variation. Assuming that the volume of the D″ layer is conserved and that the temperature difference between the CMB and the top of the D″ layer remains unchanged, growth and collapse of the piles yield large fluctuations in the mean CMB heat flux and its lateral variation, both of which affect the geodynamo and its reversals. Fig. 2c shows that this same argument applies to growth and collapse of a single pile, as has been argued was the case during the assembly of Pangaea (Zhang et al., 2010).

Numerical dynamo simulations show that when the convection in the outer core is stronger the probability for a reversal is larger (Christensen and Aubert, 2006; Olson and Christensen, 2006; Aubert et al., 2009; Driscoll and Olson, 2009b), so that increasing mean CMB heat flux increases reversal frequency (Driscoll and Olson, 2009a, 2011). In numerical dynamos with heterogeneous CMB heat flux patterns, increasing amplitude of boundary heterogeneity usually increases reversal frequency (Kutzner and Christensen, 2004; Olson et al., 2010; Heimpel and Evans, 2013), in particular for the present day tomographic heterogeneity (Olson and Amit, 2014). Another factor that may affect reversal frequency evident in specific zonal patterns is the amount of equatorial vs. polar heat flux (Glatzmaier et al., 1999; Kutzner and Christensen, 2004; Olson et al., 2010), but this effect depends on the dynamo internal control parameters in a non-trivial way. Close to the onset of reversals increased equatorial heat flux may increase reversal frequency, whereas far from the onset increased equatorial heat flux decreases reversal frequency (see geographic vs. inertial controls in Olson and Amit, 2014). Finally, increased equatorial symmetry in the CMB heat flux pattern may stabilize the dipole (Pétrélis et al., 2009, 2011).

Relating the observed variations in the paleomagnetic reversal frequency to the history of the mantle turns out to be a challenging task. Zhang and Zhong (2011) imposed plate tectonics reconstruction as a mechanical boundary condition on mantle convection simulations. Olson et al. (2013) used the time-dependent CMB heat flux model of Zhang and Zhong (2011) as a thermal outer boundary condition on a numerical dynamo simulation in an attempt to reproduce the paleomagnetic reversal frequency. The immediate problem is that during the Cretaceous Normal Superchron (CNS) plates speeds are relatively high (e.g. Lithgow-Bertelloni and Richards, 1998), the corresponding mantle convection vigor and mean CMB heat flux are stronger than average (Zhang and Zhong, 2011), and the predicted core convection and reversal frequency are therefore also higher than usual (Olson et al., 2013), in striking contradiction to the paleomagnetic observation. In contrast, Olson et al. (2013) recovered well the KRS superchron, because in their mantle convection model the D″ piles were (partially) collapsed at that time and the CMB heat flux was weaker than average, behaviors which support our model.

Olson and Amit (2014) demonstrated that reversal frequency varies linearly with a non-dimensional number which they termed the heterogeneity-corrected local Rossby number. This number combines the conventional local Rossby number and the amplitude of the CMB heterogeneity. Although the validity of this linear relation was demonstrated in a rather narrow range of parameter space and it is plausible that it would fail at more realistic conditions these results can be applied qualitatively within the context of a particular set of dynamo parameters. Since it has been shown that it is difficult to explain the variations in reversal frequency by the mean CMB heat flux alone, it could be that the time-dependent amplitude of heterogeneity may help explaining this observation. Finally, possible changes in the CMB heat flux pattern, in particular equatorial vs. polar contributions, should also be considered.

In this paper we develop a simple model of D″ piles that relates the mean CMB heat flux and the amplitude of its lateral heterogeneity to the D″ piles height. We impose the resulting CMB heat

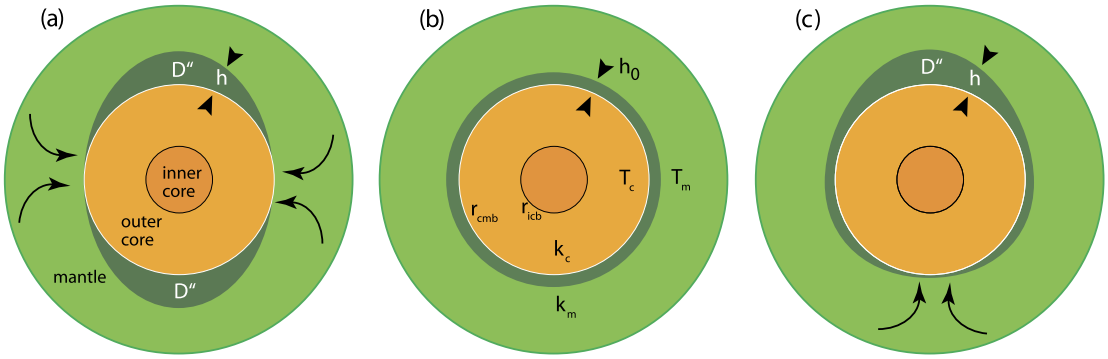

Fig. 2. Schematic illustration of D″ structure. (a) Equatorial section illustrating the dual lower mantle pile configuration with variable height h; (b) Same section illustrating fully collapsed piles configuration, where h_0 is the layer thickness in the collapsed configuration; (c) As in (a) for the single pile configuration. Arrows in (a) and (c) indicate mantle downwellings above regions of thin D″ layer.

Table 1
Non-dimensional mean CMB heat flux q_0^* and heterogeneity amplitude δq^* as functions of non-dimensional piles height amplitude H^* (11). The maximum allowed value H^*_{max} (6) is also given. Expressions are given for the lowest two zonal spherical harmonics planforms. Note that the magnitude of the dual pile planform is different than its conventional value due to (5).

Pile configuration	$f(\phi,\theta)$	q_0^*	δq^*	H^*_{max}
Rotated Y_1^0/single	$\cos\theta$	$\frac{1}{2H^*}\ln\frac{1+H^*}{1-H^*}$	$\frac{H^*}{1-H^{*2}}$	1
Rotated Y_2^0/dual	$\frac{2}{3}(3\cos^2\theta-1)$	$\sqrt{\frac{3}{2H^*(3-2H^*)}}\tan^{-1}(\sqrt{\frac{6H^*}{3-2H^*}})$	$\frac{H^*}{1+\frac{2}{3}H^*-\frac{8}{9}H^{*2}}$	$\frac{3}{2}$

flux as an outer boundary condition on numerical dynamo simulations to establish quantitatively the connection between the height of the D″ piles and the dynamo reversal frequency. We show that lower mantle piles growth can switch the dynamo from non-reversing (superchron) to reversing dynamo states, and conversely, piles collapse can lead to superchron conditions in the core.

2. D″ pile model

Fig. 2 illustrates our D″ pile model in the fully developed and fully collapsed states. The D″ layer thickness h can be generally written as the sum of two parts, a mean thickness h_0 and a spatially varying deviation h':

$$h = h_0 + h' \tag{1}$$

The average of h' over the CMB spherical surface is by definition zero. We conserve the total volume of the D″ layer, i.e., we assume that h_0 is constant with time. The deviation h' is represented as

$$h' = Hf(\phi,\theta) \tag{2}$$

where H is a time-dependent amplitude and $f(\phi,\theta)$ is a planform function representing the spatial heterogeneity, with ϕ and θ being longitude and co-latitude spherical coordinates measured with respect to the symmetry axis of the piles. The amplitude H varies on the long timescale of mantle dynamics (tens of Myr overturn), which is much longer than the overturn time in the core (centuries), so that the core is assumed to be in thermal and magnetohydrodynamical equilibrium with H at every epoch. This separation of timescales between core and mantle overturn times allows us to model the dynamo response at each epoch assuming that H is fixed over that epoch.

If the pile height is non-dimensionalized as $H^* = H/h_0$, the non-dimensional form of (1) becomes

$$h^* = 1 + H^* f(\phi,\theta) \tag{3}$$

The non-dimensional pile height H^* may be generally defined by half the difference between the extremes of h^* (in analogy to the definition of non-dimensional heat flux, e.g. Olson and Christensen, 2002):

$$H^* = \frac{h^*_{max} - h^*_{min}}{2} \tag{4}$$

This constrains the magnitude of the planform function to satisfy

$$\frac{f_{max} - f_{min}}{2} = 1 \tag{5}$$

Finally, to ensure that h^* remains positive over the entire CMB, the pile height is limited by

$$H^* < \frac{1}{|f_{min}|} \equiv H^*_{max} \tag{6}$$

Because the D″ layer is assumed to be in conductive equilibrium with the lower mantle and the outer core, the CMB heat flux obeys Fourier's law:

$$q = k_m \frac{\Delta T}{h} \tag{7}$$

where k_m is lower mantle thermal conductivity and $\Delta T = T_c - T_m$ is the temperature difference across the D″ layer. As in (1), the CMB heat flux is written as the sum of two parts, a mean part q_0 plus a spatially varying heterogeneity q':

$$q = q_0 + q' \tag{8}$$

Combining (1)–(8) gives

$$q_0 + q' = \frac{k_m \Delta T}{h_0 + Hf(\phi,\theta)} \tag{9}$$

Note that both q_0 and q' in (9) are time-dependent. We now define a non-dimensional CMB heat flux $q^* = q/Q$, where $Q = k_m \Delta T/h_0$ corresponds to the CMB heat flux in the fully collapsed pile state (see Fig. 2b). The non-dimensional form of (9) is then

$$q_0^* + q'^* = \frac{1}{1 + H^* f(\phi,\theta)} \tag{10}$$

with the mean non-dimensional heat flux defined as

$$q_0^* = \frac{1}{4\pi}\int_S \frac{1}{1 + H^* f(\phi,\theta)} \sin\theta d\phi d\theta \tag{11}$$

where S denotes a spherical integration. This integral depends on the specific spatial form of $f(\phi,\theta)$; analytical solutions to the lowest two zonal spherical harmonics are given in Table 1 and shown in Fig. 3a. Spherical harmonic Y_1^0 corresponds to the single pile or plume configuration; Y_2^0 corresponds to the dual pile or plume configuration.

The amplitude of the CMB heat flux heterogeneity can be defined in terms of its peak-to-peak difference as (Olson and Christensen, 2002)

$$\delta q = \frac{q_{max} - q_{min}}{2} \tag{12}$$

Normalized by the heat flux scale Q, (12) becomes

$$\delta q^* = \frac{q_{max} - q_{min}}{2Q} \tag{13}$$

Considering the D″ model (10), the non-dimensional amplitude of the CMB heat flux heterogeneity (13) also varies from one pile configuration to another; analytical solutions to the single and dual pile configurations are given in Table 1 and shown in Fig. 3b. Note that as with q_0^* (Fig. 3a), for both configurations the δq^* curves approach infinity as H^* approaches H^*_{max}. Also note the larger q_0^* and δq^* values for the single pile configuration, for a given H^*, compared to the dual pile configuration.

3. Dynamo reversals driven by lower mantle piles

To demonstrate how the growth of lower mantle piles can excite magnetic reversals, we impose the CMB heat flux boundary conditions from the previous section on the outer boundary of low resolution numerical dynamos that include compositional forcing

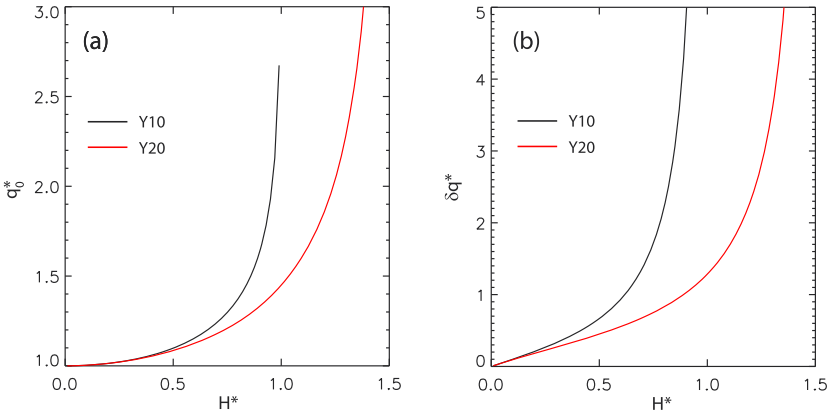

Fig. 3. (a) Non-dimensional mean CMB heat flux q_0^* vs. non-dimensional piles height H^*; (b) Non-dimensional CMB heat flux heterogeneity amplitude δq^* vs. non-dimensional piles height H^*. The curves are based on the analytical solutions given in Table 1. Single pile configurations are in black, dual pile configurations are in red. Both configurations are restricted to the range $H^*_{max} > H^* > 0$ (see (6) and Table 1). (For interpretation of the references to color in this figure legend, the reader is referred to the web version of this article.)

due to inner core growth. We make use of the co-density formulation (Braginsky and Roberts, 1995) in which $C = \rho(\alpha T + \beta\chi)$ where ρ is mean density, T is temperature, χ is the light element concentration (mixing ratio) in the outer core, and α and β are their respective expansivities. For the non-dimensional governing equations see e.g. Christensen and Aubert (2006). Control parameters for these dynamos include the Ekman number E, the Prandtl number Pr and the magnetic Prandtl number Pm defined respectively by

$$E = \frac{\nu}{\Omega D^2}, \qquad Pr = \frac{\nu}{\kappa}, \qquad Pm = \frac{\nu}{\eta} \tag{14}$$

where ν is kinematic viscosity, Ω is the angular velocity of rotation, D is the outer core shell thickness, κ is the diffusivity of the co-density and η is magnetic diffusivity. Buoyancy is parameterized in terms of the Rayleigh number Ra, which can be defined for thermochemical dynamos as (Olson, 2007)

$$Ra = \frac{\beta g D^5 \dot{\chi}}{\kappa \nu^2} \tag{15}$$

where g is gravity at the CMB and $\dot{\chi}$ is the time rate of change of the light element concentration (mixing ratio) in the outer core due to inner core growth. Here we have used D and D^2/ν to scale length and time, respectively, and $\rho\beta D^2\dot{\chi}/\nu$ to scale co-density. The final internal control parameter is ϵ, the sink (or source) term that appears in the co-density transport equation (Christensen and Wicht, 2007), which models the combined effects of the rate of mixing of light elements in the outer core, secular cooling of the outer core, curvature of the core adiabat, and radioactive heat sources; Here we use $\epsilon = -1$, corresponding to a volumetric sink that absorbs all the buoyancy flux that enters the outer core through the inner core boundary, appropriate for convection that is primarily compositionally-driven.

The thermal and compositional boundary conditions for the numerical dynamo models are expressed in terms of the non-dimensional co-density, C^*. At the ICB we set $C^* = 1$, assuming uniform temperature and composition there. At the CMB we impose a heat flux pattern consistent with our piles models. Fig. 4 shows maps of CMB heat flux corresponding to single and dual piles configurations. Fig. 4a shows a map of the CMB heat flux with a pattern of lateral heterogeneity based on the model of lower mantle seismic heterogeneity by Dziewonski et al. (2010). This map has a mean heat flux of $q_0 = 100$ mW/m^2, close to the adiabatic heat flux in the outer core for an assumed thermal

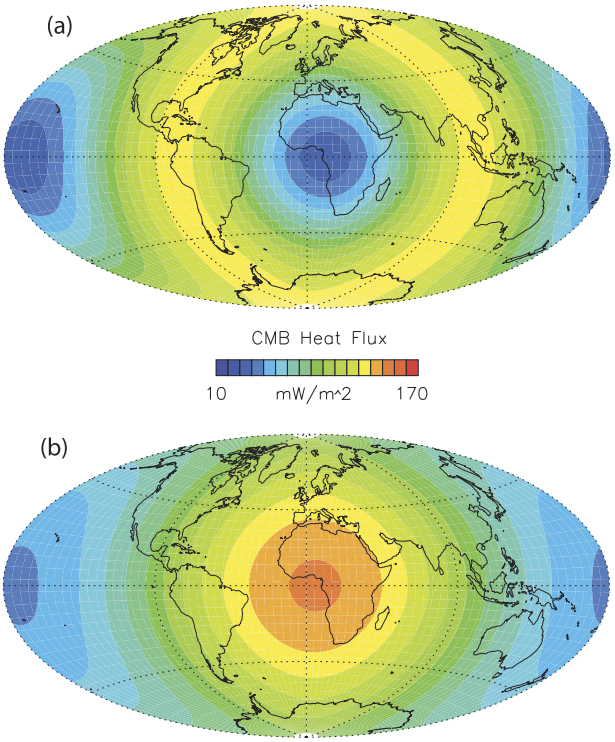

Fig. 4. CMB heat flux patterns in the dual (a) and single (b) superplume configurations. The same 100 mW/m^2 mean heat flux applies to both cases. The peak-to-peak variation is 60 and 100 mW/m^2 in (a) and (b), respectively.

conductivity of $k_c = 130$ W/m/K, and a lateral heterogeneity amplitude of $\delta q = 30$ mW/m^2. Its heterogeneity pattern, which is a close approximation to our dual pile model f, was generated using the following three spherical harmonics measured in longitude and co-latitude coordinates: Y_2^0, Y_2^2 and Y_1^1, with amplitudes in relative proportions of $10:10:1$, respectively. For comparison, Fig. 4b shows a map of the CMB heat flux pattern for a single pile configuration. This map has the same mean heat flux of $q_0 = 100$ mW/m^2 but the heterogeneity amplitude is $\delta q = 50$ mW/m^2.

In order to use CMB heat flux patterns like those shown in Fig. 4 as outer boundary conditions in our numerical dynamo models, two steps are necessary. First, the adiabatic CMB heat flux q_{ad}

Table 2
Dynamo models setup and main results for models with $E = 6 \cdot 10^{-3}$ and dual pile configuration (top), $E = 1 \cdot 10^{-3}$ and dual pile configuration (middle) and $E = 6 \cdot 10^{-3}$ and single pile configuration (bottom). For variables definitions see main text.

H^*	$2\delta q^*$	q_0/Q	q_0 [W/m^2]	q_0/q_{ad}	q^*_{0c}	$\sigma(q^*_{0c})$	Ra	τ_d	Dipole	N	ω_{sh}
10^{-5}	10^{-5}	1	0.05	0.5	−0.03	10^{-7}	$0.6 \cdot 10^5$	16	1.15 ± 0.05	0	na
0.61	0.57	1.13	0.06	0.57	−0.02	0.008	$0.7 \cdot 10^5$	16	1.2 ± 0.1	0	na
0.86	0.94	1.29	0.06	0.65	−0.02	0.01	$0.8 \cdot 10^5$	16	0.9 ± 0.2	0	na
1.0	1.29	1.45	0.07	0.72	−0.01	0.01	$0.9 \cdot 10^5$	80	0.7 ± 0.2	0	na
1.10	1.67	1.61	0.08	0.81	−0.01	0.02	10^5	70	0.65 ± 0.22	0	na
1.18	2.15	1.80	0.09	0.90	−0.003	0.02	$1.1 \cdot 10^5$	225	0.60 ± 0.23	0	na
1.21	2.39	1.89	0.09	0.95	−0.002	0.02	$1.15 \cdot 10^5$	150	0.50 ± 0.24	1	na
1.24	2.69	2.00	0.10	1.0	0	0.02	$1.2 \cdot 10^5$	510	0.43 ± 0.23	21	0.44
1.26	2.94	2.09	0.10	1.04	0.001	0.02	$1.25 \cdot 10^5$	240	0.45 ± 0.24	18	0.34
1.28	3.22	2.18	0.11	1.09	0.002	0.02	$1.3 \cdot 10^5$	220	0.44 ± 0.25	23	0.27
1.30	3.56	2.29	0.11	1.14	0.004	0.02	$1.4 \cdot 10^5$	218	0.47 ± 0.24	25	0.25
1.32	3.98	2.42	0.12	1.21	0.005	0.02	$1.5 \cdot 10^5$	335	0.34 ± 0.26	59	0.24
1.34	4.43	2.60	0.13	1.30	0.007	0.03	$1.6 \cdot 10^5$	310	0.32 ± 0.23	65	0.24
1.18	2.15	1.80	0.09	0.90	−0.003	0.011	$14 \cdot 10^5$	65	1.0 ± 0.13	0	na
1.3	3.56	2.29	0.11	1.14	0.004	−0.013	$18 \cdot 10^5$	65	0.44 ± 0.28	4	0.48
0.705	1.47	1.25	0.06	0.64	−0.02	0.02	$0.75 \cdot 10^5$	80	1.04 ± 0.18	0	na
0.854	3.15	1.49	0.07	0.74	−0.01	0.03	$0.9 \cdot 10^5$	167	0.72 ± 0.18	0	na
0.9175	5.80	1.71	0.09	0.86	−0.005	0.05	$1.0 \cdot 10^5$	165	0.63 ± 0.18	0	na
0.9375	7.74	1.83	0.09	0.92	−0.003	0.06	$1.1 \cdot 10^5$	250	0.30 ± 0.18	20	0.35
0.9575	11.51	2.00	0.10	1.00	$-6 \cdot 10^7$	0.09	$1.2 \cdot 10^5$	250	0.25 ± 0.12	34	0.30
0.97	16.41	2.16	0.11	1.08	0.002	0.11	$1.3 \cdot 10^5$	242	0.16 ± 0.09	44	0.19
0.98	24.75	2.34	0.12	1.17	0.004	0.16	$1.4 \cdot 10^5$	222	0.14 ± 0.08	53	0.17
0.985	33.08	2.48	0.12	1.24	0.006	0.20	$1.5 \cdot 10^5$	140	0.17 ± 0.11	39	0.22
0.985	33.08	2.48	0.12	1.24	0.006	0.20	$1.6 \cdot 10^5$	120	0.17 ± 0.11	44	0.24

must be subtracted from the mean heat flux, since the dynamo model makes the Boussinesq approximation in which the adiabatic gradient is already removed. Second, the laterally varying residual CMB heat flux $q - q_{ad}$ must be converted to non-dimensional co-density. Because we assume the dynamo is dominated by compositional convection, an appropriate non-dimensional scaling factor for the heat flux is $Q_c = \alpha\nu\ q_0/\beta k_c D\dot{\chi}$ (the subscript 'c' denotes 'core' as opposed to the scaling factor Q on the mantle side). The non-dimensional mean CMB co-density flux for the dynamo model then becomes

$$\frac{\partial C^*_0}{\partial r^*} = -q^*_{0c} = -Q_c\left(1 - \frac{q_{ad}}{q_0}\right) \tag{16}$$

and the non-dimensional amplitude of the CMB co-density heterogeneity for the dynamo models becomes

$$\delta\left(\frac{\partial C^*}{\partial r^*}\right) = -\delta q^*_c = -Q_c\frac{\delta q}{q_0}. \tag{17}$$

Table 2 summarizes the parameters used in the numerical dynamo simulations as well as some main results. In these models we have assumed that $q_{ad} = 2Q$ at $H^* = 1.24$, and furthermore, that a Rayleigh number $Ra = 1.2 \cdot 10^5$ corresponds to adiabatic CMB conditions $q_0 = q_{ad}$, so that $q^* = q^*_{0c} = 0$ at this Ra-value. Changes in q^*_{0c} relative to this reference state are then obtained from the dual pile curve for q^*_0 in Fig. 3a scaled according to (16). Likewise, changes in δq^*_c relative to the reference state $\delta q^*_{ad} = 2.69$ are obtained from the dual pile curve for δq^* in Fig. 3b scaled according to (17). Lastly, the relative changes in Ra are calculated assuming that Q_c remains constant in the outer core, so that Ra increases in proportion to q_0. We set $E = 6 \cdot 10^{-3}$, $Pr = 1$ and $Pm = 20$ in these cases.

Several reasons compel us to use dynamo models with these parameters. First, they lie within the parameter space identified by Christensen et al. (2010) as being Earth-like in terms of their magnetic field morphology. Second, they exhibit polarity reversals that are separated by stable polarity chrons in which the field is dominated by an axial dipole component. Third, the time-average reversal frequency in these dynamos changes systematically with the control parameters E and Ra, and with the boundary heterogeneity amplitude (Olson and Amit, 2014). Finally, the large E-value allows computing long time series, thereby registering enough reversals to construct meaningful statistics. There are of course drawbacks to our approach, perhaps the gravest being that these dynamos are very far from Earth-like status in terms of some individual control parameters, in particular, E and Pm. For this reason, we choose to focus attention on their qualitative behavior: Whether they reverse at all as well as the conditions under which they reverse frequently. In addition, we also include a couple of dynamo cases at $E = 1 \cdot 10^{-3}$ that show qualitative agreement.

Fig. 5 shows maps of the radial magnetic field on the outer boundary in the piles dynamos. Time-average maps were constructed by considering $+B_r$ during normal polarities and $-B_r$ during reversed polarities. Low H^* non-reversing dynamos yield radial field morphology with a clear signature of the CMB heat flux heterogeneity, in particular on time-average. This is evident by the two intense flux patches at each hemisphere in Fig. 5b that appear at about the same longitudes as the positive heat flux anomalies in the dual pile pattern (Fig. 4a). Although at a snapshot the correlation with the CMB heat flux pattern may be substantially inferior, there is a statistical preference for these intense flux patches to be aligned with the mantle heterogeneity (Olson and Christensen, 2002). Note that in the snapshot shown here (Fig. 5a) the equatorial symmetry and the order 2 dominance are preserved, although the patches are somewhat shifted in longitude with respect to the CMB heat flux pattern. Increasing Ra and H^* gives reversing dynamos with smaller scale more time-dependent fields (Fig. 5c) in which the mantle signature is less evident, probably requiring longer simulation times for statistical convergence. Nevertheless, the order 2 signature can still be identified in the time-average map of the larger Ra and H^* dual pile dynamo (Fig. 5d). Likewise, an order 1 signature characterizes the single pile dynamo (Fig. 5f), although it is surprisingly shifted by about 180° from the corresponding positive anomaly in the CMB heat flux pattern (Fig. 4b) due to strong westward drift driven by this particular boundary condition.

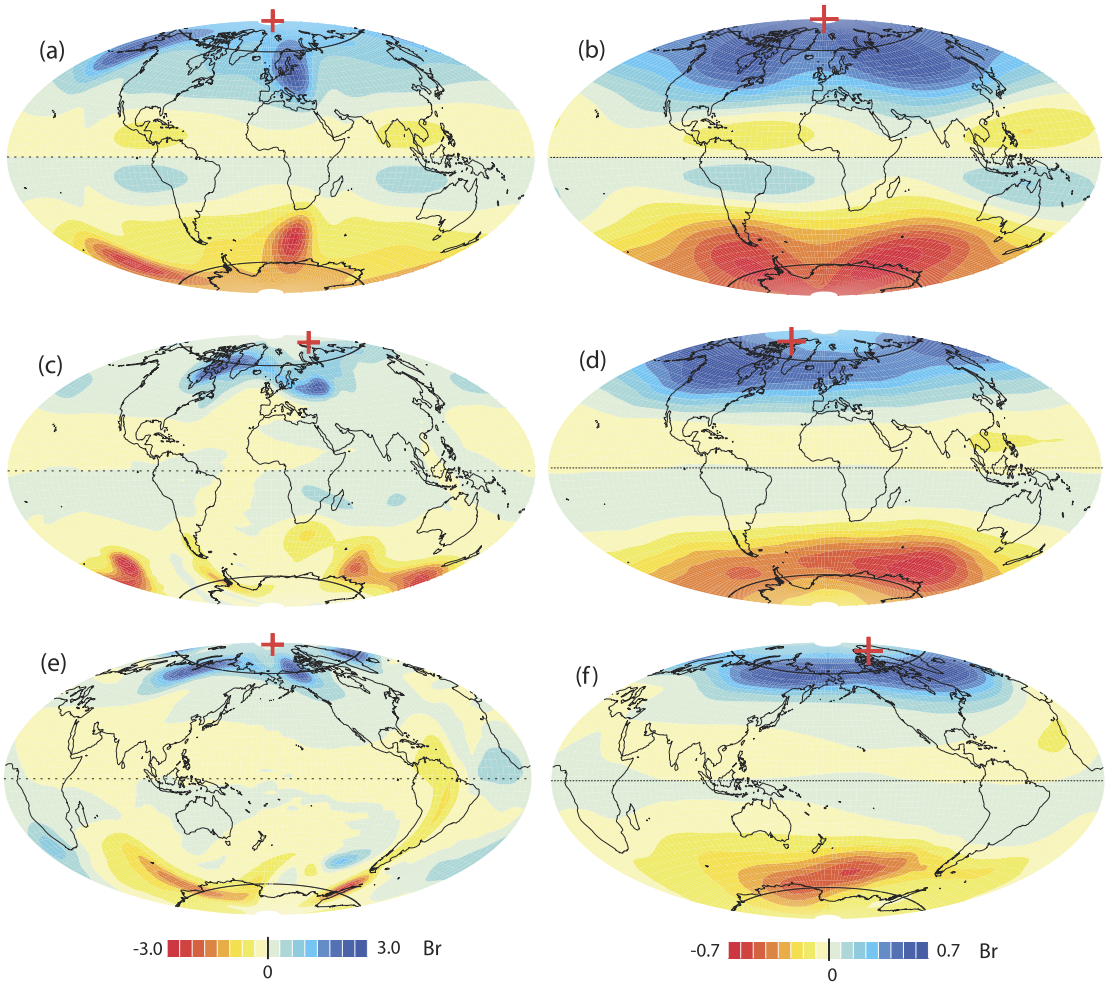

Fig. 5. Snapshot and time-average maps of the radial magnetic field on the CMB from the piles dynamos. Left column are snapshots, right column are time-averages. The radial magnetic field is given in non-dimensional (Elsasser number) units. Red crosses indicate geomagnetic dipole axis positions. Black lines denote the latitudes of the tangent cylinder. (a, b) Dual piles non-reversing dynamo with $H^* = 1$ and $Ra = 0.9 \cdot 10^5$; (c, d) Dual piles reversing dynamo with $H^* = 1.28$ and $Ra = 1.3 \cdot 10^5$; (e, f) Single pile reversing dynamo with $H^* = 0.96$ and $Ra = 1.2 \cdot 10^5$. Note that the dual pile dynamos are centered at 0° longitude, whereas the single pile dynamo is centered at 180° longitude. (For interpretation of the references to color in this figure legend, the reader is referred to the web version of this article.)

Fig. 6 illustrates the dependence of the reversal frequency on the pile height as well as the irregularity of the chron durations. Pile dynamos with low H^* values exhibit very small dipole tilt oscillations (Fig. 6a), i.e. no apparent tendency to reverse. This state corresponds to superchron conditions in our models. Increasing H^* gives chaotic aperiodic reversals with strongly variable and irregular chron durations (Fig. 6b). A further increase in H^* leads to a stochastic hyper-reversing dynamo (Fig. 6c).

Fig. 7 shows the non-dimensional reversal frequency $N^* = N/\tau_d$ as functions of H^* and q_0^* for the first set of dual pile dynamos (Table 2, top). The error bars correspond to $\sqrt{N}/\tau_d$, consistent with Poisson distribution (Lhuillier et al., 2013). Reversal onset occurs near $H^* = 1.2$ and $q_0^* = 1.9$, and the reversal frequency increases approximately linearly beyond onset. The present-day (0–5 Ma) reversal rate of about 4 per million years corresponds to $N^* \simeq 0.2$, assuming $\tau_d = 50$ kyr. By extrapolation, $N^* = 0.2$ occurs near $H^* = 1.35$ and $q_0^* = 2.55$ in Figs. 7a and b, respectively. Accordingly, there is a fairly small window separating the pile height that would produce magnetic superchrons and the pile height that would produce frequent, and even hyper-frequent reversals. The associated increase in CMB heat flux is also relatively moderate, and amounts to a change of only ∼35% between these two dynamo states. The parameter ω_{sh} in Table 2 is the Sherman statistic for each reversal sequence. Random reversal sequences produce $\omega_{sh} \simeq 1/e$, whereas periodic and clustered reversal sequences have larger and smaller ω_{sh}-values, respectively (Olson et al., 2014).

To test these results, we also ran dual pile dynamos at $E = 1 \cdot 10^{-3}$ and larger Ra with the CMB heterogeneity parameters listed in the second set in Table 2 (middle). These dynamos have substantially greater flow velocities (magnetic Reynolds numbers above 400, as opposed to ∼150 for the first set cases) as well as smaller length scales, requiring substantially more numerical resolution and hence far longer running times, so that their reversal statistics are too meager to quantify reliably. Nevertheless, the results are qualitatively consistent with those of the first set and Fig. 7 in that increasing pile height transitions the dynamo from non-reversing to reversing behavior.

We have made a parallel series of calculations for single pile dynamos at $E = 6 \cdot 10^{-3}$ (for control parameters and summary results see the third set in Table 2 bottom). Fig. 8 shows the variation in non-dimensional reversal frequency vs. non-dimensional pile height and non-dimensional mean CMB heat flux for these cases. Note that the Rayleigh number for reversal onset in the single pile

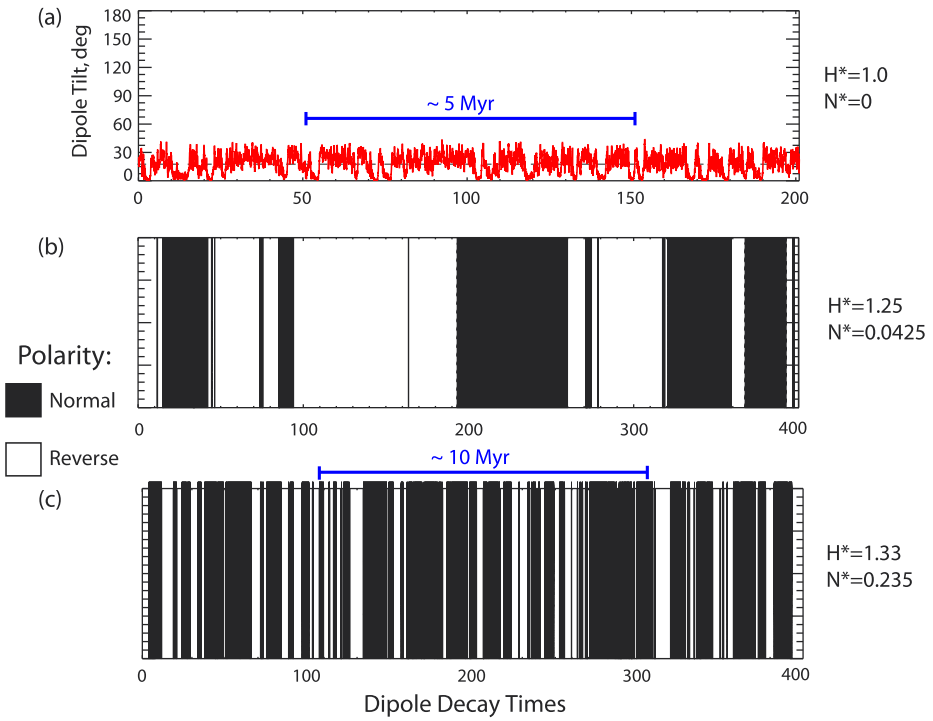

Fig. 6. Magnetic polarity timeseries in the dual pile dynamos with increasing H^*. Time is given in units of dipole decay time. (a) Dipole tilt timeseries (red) and its average (dashed black) in a non-reversing dynamo; (b, c) Polarity records for reversing dynamos. (For interpretation of the references to color in this figure legend, the reader is referred to the web version of this article.)

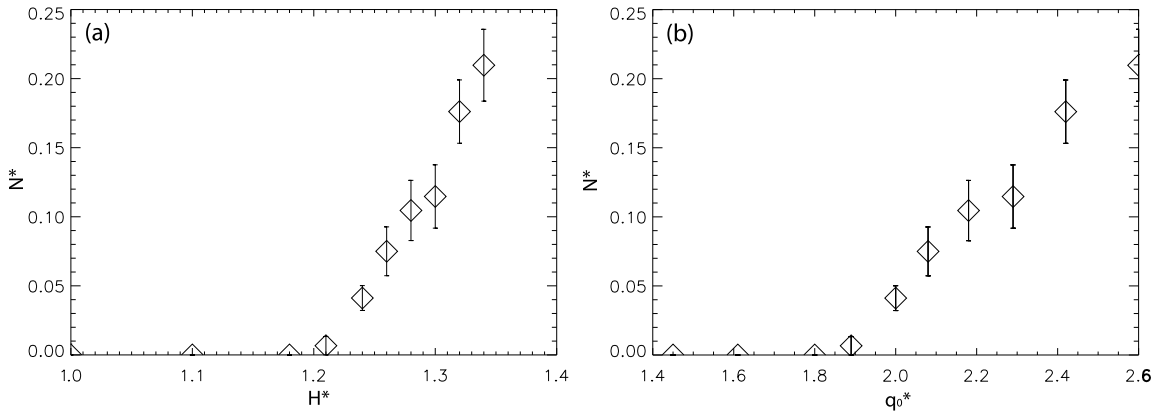

Fig. 7. Non-dimensional reversal frequency vs. non-dimensional piles height (a) and vs. non-dimensional mean CMB heat flux (b) in the set of dual pile (rotated Y_2^0) dynamo models.

dynamos in Table 2 bottom differs somewhat from the Rayleigh number for reversal onset in the dual pile dynamos in Table 2 top, and beyond onset their reversal frequencies differ somewhat. Even so, in qualitative terms the same behavior is found for these single pile cases as for the dual piles cases in Fig. 7. Specifically, the non-reversing state transitions to a reversing state at some critical value of H^* (or alternatively, q_0^*) and beyond this onset the rate of reversals increases rapidly, especially in terms of H^*. For both single and dual pile configurations the reversal frequency increases nearly linearly with H^*, but in terms of mean heat flux reversal frequency increases like $\sqrt{q_0^*}$. These trends are consistent with the non-linear relationship between q_0^* and H^* shown in Fig. 3a. In summary, the implications of pile growth and collapse are practically the same regardless of whether one pile or two piles are involved.

4. Discussion

Clearly our D″ pile model is very simplified. It is probable that complex dynamical scenarios in the lowermost mantle yield much more complex CMB heat flux patterns (e.g. Lay et al., 2008). For example, post-perovskite phase transition may cause spread piles with sharp edges and regions of enhanced CMB heat flux (Nakagawa and Tackley, 2011), thus distorting the idealized linear mapping between seismic and thermal anomalies at the D″ layer (Nakagawa and Tackley, 2008). Accounting for post-perovskite in the construction of CMB heat flux models may affect the morphology of persistent dynamo features (Amit and Choblet, 2009). Obtaining a more realistic CMB heat flux pattern from a refined D″ pile model is worth-while, but it is beyond the scope of this study.

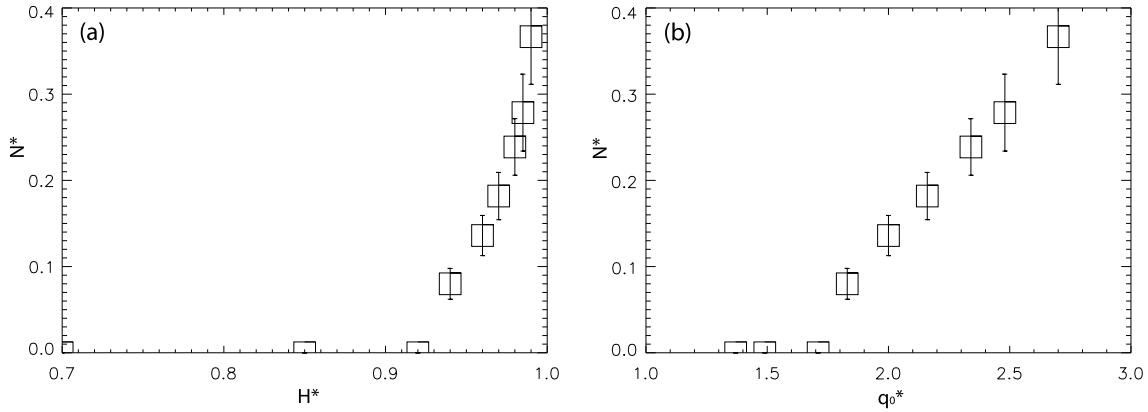

Fig. 8. As in Fig. 7 for the set of single pile (rotated Y_1^0) dynamo models.

Although our D″ pile model is highly simplified and the reversing numerical dynamo models are very large-scale, some useful insights may be drawn. Assuming that the D″ layer volume and the temperature difference across the D″ are both conserved in time, we have shown theoretically that the mean CMB heat flux rapidly increases as D″ chemical piles grow (Fig. 3a). The amplitude of the CMB heat flux heterogeneity δq^* also increases with growing piles (Fig. 3b). Reversals in numerical dynamo models with heterogeneous CMB heat flux are more frequent when the mean is increased, and in the tomographic case also when the amplitude of the lateral heterogeneity is increased (Olson et al., 2010; Heimpel and Evans, 2013; Olson and Amit, 2014). It was not clear a priori whether the CMB heat flux pattern of the dual pile structure would enhance or suppress reversals, especially since it contains a significant zonal component that may work either way (Olson and Amit, 2014). Our numerical dynamo models show that these two effects work in unison to increase reversal frequency with growing piles.

The longevity of the dual pile structure in the lower mantle remains controversial. Volcanic hotspot reconstructions (Torsvik et al., 2006) point to the existence of two superplumes far back into the Paleozoic, whereas mantle global circulation models predict a single superplume during Pangaea assembly prior to 330 Ma (Zhang et al., 2010) and superchron conditions in the core during the transition (Olson et al., 2013). Our D″ model predicts that geomagnetic reversals are stimulated by piles growth in either configuration.

Most tomographic heat flux patterns are dominated by the Y_2^2 spherical harmonic. The rotated Y_2^0 pattern used in our study also contains a significant Y_2^2 component, but in addition a $+Y_2^0$ contribution appears (Fig. 4a). This polar cooling may have a substantial effect on reversal frequency. Previous studies found that polar cooling stabilizes the dynamo and may yield superchrons (Glatzmaier et al., 1999; Kutzner and Christensen, 2004). Olson and Amit (2014) argued that close to the onset of reversals polar cooling indeed inhibits reversals, but farther from the onset the opposite effect occurs and polar cooling increases reversal frequency. These special effects of zonal heterogeneity in the CMB heat flux pattern motivate further inspection of the rotated Y_2^0 pattern and its impact on reversal frequency.

An exact quantitative comparison between our results to those obtained by tomographic dynamos (e.g. Olson and Amit, 2014) is difficult, because in previous studies the mean CMB heat flux and the heterogeneity amplitude are two independent parameters, whereas in our D″ pile model both quantities are controlled by the piles height. Based on the linear fits obtained by Olson and Amit (2014) with tomographic patterns, an increase of ∼10% in the mean CMB heat flux (corresponding to an increase of ∼5% in the local Rossby number) with an arbitrary reference reversal frequency of $N^* = 0.1$ would give an increase of ∼25% in the reversal frequency. In contrast, with our D″ pile model the same increase of ∼10% in the mean CMB heat flux with a reference $N^* = 0.1$ results in an increase of ∼70% in the reversal frequency (Fig. 7b). It is likely that the reason for this much larger increase in reversal frequency with our D″ pile model is that the heterogeneity amplitude increases together with the mean CMB heat flux (Fig. 3).

Our results are qualitatively consistent with predictions from previous dynamo reversal studies (Kutzner and Christensen, 2004; Olson et al., 2010; Driscoll and Olson, 2011; Olson and Amit, 2014). Intense outer core convection, high CMB heat flux and fully developed lower mantle piles correspond to times with frequent polarity reversals, whereas superchrons correspond to times with weaker core convection, lower CMB heat flux and reduced piles height. In particular, the onset and termination of the CNS and KRS superchrons (Fig. 1) may mark piles partial collapse and growth stages, respectively. The modulation of piles height and subsequent CMB heat flux needed to explain the observed variability in paleomagnetic reversal frequency is modest; The increase in piles height that is needed to go from non-reversing superchron conditions $N^* = 0$ during the CNS to present-day rapidly reversing conditions of $N^* = 0.2$ is ∼13%, and the corresponding increase in mean CMB heat flux is ∼35%. Such changes are only slightly larger than those found in mantle general circulation models (Zhang and Zhong, 2011; Nakagawa and Tackley, 2013; Olson et al., 2013), although the fluctuations in CMB heat flux predicted by the latter models are in many cases not closely in phase with the reversal frequency variations during this time interval.

There is independent observational support for Cenozoic superplume growth, based on the uplift history of the African continent and the origin of the African Superswell on the nearby ocean floor (Nyblade and Robinson, 1994). The timing of the uplift of Africa (Bond, 1978) coincides with the trend of increasing geomagnetic reversal frequency in the Cenozoic C-sequence, as our model predicts. Geodynamic considerations (Lithgow-Bertelloni and Silver, 1998) indicate that the African Superswell is supported by a mantle upwelling, and mantle reconstructions indicate that this upwelling has strengthened over the past 80 Myr through growth of the lower mantle African superplume (Conrad and Gurnis, 2003). It has been proposed that Cenozoic tectonic uplift has aridified East Africa, driving climate change and forcing early hominid evolution in that region (Sepulchre et al., 2006). Likewise, it has been suggested that superplume growth terminated the KRS, leading to formation of the Siberian Traps and contributing to the Permian mass extinction (Courtillot and Olson, 2007). Through such inter-

actions, superplumes in the deep mantle may impact the climate system as well as the geodynamo.

Acknowledgements

P.O. was supported by Frontiers in Earth System Dynamics grant EAR-1135382 from the National Science Foundation. We thank two anonymous reviewers for their constructive reviews. We are grateful to U. Christensen for helpful discussions.

References

Amit, H., Choblet, G., 2009. Mantle-driven geodynamo features – effects of post-perovskite phase transition. Earth Planets Space 61, 1255–1268.
Aubert, J., Labrosse, S., Poitou, C., 2009. Modelling the paleo-evolution of the geodynamo. Geophys. J. Int. 179, 1414–1428.
Biggin, A.J., Steinberger, B., Aubert, J., Suttie, N., Holme, R., Torsvik, T.H., van der Meer, D.G., van Hinsbergen, D.J.J., 2012. Possible links between long-term geomagnetic variations and whole-mantle convection processes. Nat. Geosci. 5, 526–533.
Bond, G., 1978. Evidence for late Tertiary uplift of Africa relative to North America, South America, Australia and Europe. J. Geol. 86, 47–65.
Braginsky, S.I., Roberts, P.H., 1995. Equations governing convection in Earth's core and the geodynamo. Geophys. Astrophys. Fluid Dyn. 79, 1–97.
Bull, A., McNamara, A., Ritsema, J., 2009. Synthetic tomography of plume clusters and thermochemical piles. Earth Planet. Sci. Lett. 278, 152–162.
Burke, K., 2011. Plate tectonics, the Wilson cycle, and mantle plumes: geodynamics from the top. Annu. Rev. Earth Planet. Sci. 39, 1–29.
Burke, K., Steinberger, B., Torsvik, T.H., Smethhurst, M.A., 2008. Plume generation zones at the margins of large low shear velocity provinces on the core–mantle boundary. Earth Planet. Sci. Lett. 265, 49–60.
Christensen, U., Aubert, J., 2006. Scaling properties of convection-driven dynamos in rotating spherical shells and application to planetary magnetic fields. Geophys. J. Int. 166, 97–114.
Christensen, U., Aubert, J., Hulot, G., 2010. Conditions for Earth-like geodynamo models. Earth Planet. Sci. Lett. 296, 487–496.
Christensen, U., Wicht, J., 2007. Numerical dynamo simulations. In: Olson, P. (Ed.), Treatise on Geophysics, vol. 8. Elsevier Science.
Conrad, C., Gurnis, M., 2003. Seismic tomography, surface uplift, and the breakup of Gondwanaland: integrating mantle convection backwards in time. Geochem. Geophys. Geosyst. 4. http://dx.doi.org/10.1029/2001GC000299.
Courtillot, V., Olson, P., 2007. Mantle plumes link magnetic superchrons to Phanerozoic mass depletion events. Earth Planet. Sci. Lett. 260, 495–504.
Driscoll, P.E., Olson, P.L., 2009a. Effects of buoyancy and rotation on the polarity reversal frequency of gravitationally-driven numerical dynamos. Geophys. J. Int. 178, 1337–1350.
Driscoll, P.E., Olson, P.L., 2009b. Polarity reversals in geodynamo models with core evolution. Earth Planet. Sci. Lett. 282 (1–4), 24–33.
Driscoll, P.E., Olson, P.L., 2011. Superchron cycles driven by variable core heat flow. Geophys. Res. Lett. 38 (9), L09304.
Dziewonski, A.M., Lekic, V., Romanowicz, B.A., 2010. Mantle anchor structure: an argument for bottom up tectonics. Earth Planet. Sci. Lett. 299, 69–79.
Garnero, E., McNamara, A., 2008. Structure and dynamics of Earth's lower mantle. Science 320, 626–628.
Glatzmaier, G., Coe, R., Hongre, L., Roberts, P., 1999. The role of the Earth's mantle in controlling the frequency of geomagnetic reversals. Nature 401, 885–890.
Gradstein, F., Ogg, J., Schmitz, M., Ogg, G., 2012. The Geologic Time Scale 2012. Elsevier Science, Amsterdam.
Heimpel, M.H., Evans, M.E., 2013. Testing the geomagnetic dipole and reversing dynamo models over Earth's cooling history. Phys. Earth Planet. Inter. 224, 124–131.
Kutzner, C., Christensen, U.R., 2004. Simulated geomagnetic reversals and preferred virtual geomagnetic pole paths. Geophys. J. Int. 157, 1105–1118.
Lay, T., Herlund, J., Buffett, B.A., 2008. Core–mantle boundary heat flow. Nat. Geosci. 1, 25–32.
Lhuillier, F., Hulot, G., Gallet, Y., 2013. Statistical properties of reversals and chrons in numerical dynamos and implications for the geodynamo. Phys. Earth Planet. Inter. 220, 19–36.
Lithgow-Bertelloni, C., Richards, M.A., 1998. Dynamics of Cenozoic and mesozoic plate motion. Rev. Geophys. 36, 27–78.
Lithgow-Bertelloni, C., Silver, P.G., 1998. Dynamic topography, plate driving forces and the African superswell. Nature 395, 269–272.
Masters, G., Laske, G., Bolton, H., Dziewonski, A., 2000. The relative behavior of shear velocity, bulk sound velocity, and compressional velocity in the mantle: implications for chemical and thermal structure. In: Karato, S., Forte, A., Liebermann, R., Masters, G., Stixrude, L. (Eds.), Earths Deep Interior. In: AGU Monograph, vol. 117. American Geophysical Union, Washington, DC.
McNamara, A., Zhong, S., 2005. Thermochemical structures beneath Africa and the Pacific Ocean. Nature 437, 1136–1139.
Merrill, R.T., McElhinny, M.W., McFadden, P.L., 1998. The Magnetic Field of the Earth: Paleomagnetism, the Core, and the Deep Mantle. Academic Press, San Diego, California, USA.
Nakagawa, T., Tackley, P.J., 2008. Lateral variations in CMB heat flux and deep mantle seismic velocity caused by a thermal-chemical-phase boundary layer in 3D spherical convection. Earth Planet. Sci. Lett. 271, 348–358.
Nakagawa, T., Tackley, P.J., 2011. Effects of low-viscosity post-perovskite on thermo-chemical mantle convection in a 3-D spherical shell. Geophys. Res. Lett. 38, L04309.
Nakagawa, T., Tackley, P.J., 2013. Implications of high core thermal conductivity on Earth's coupled mantle and core evolution. Geophys. Res. Lett. 40, 2652–2656.
Nyblade, A.A., Robinson, S.W., 1994. The African superswell. Geophys. Res. Lett. 21. http://dx.doi.org/10.1029/94GL00631.
Olson, P., 2007. Gravitational dynamos and the low frequency geomagnetic secular variation. Proc. Natl. Acad. Sci. 104, 20159–20166.
Olson, P., Amit, H., 2014. Magnetic reversal frequency scaling in dynamos with thermochemical convection. Phys. Earth Planet. Inter. 229, 122–133.
Olson, P., Christensen, U., 2002. The time averaged magnetic field in numerical dynamos with nonuniform boundary heat flow. Geophys. J. Int. 151, 809–823.
Olson, P., Christensen, U., 2006. Dipole moment scaling for convection-driven planetary dynamos. Earth Planet. Sci. Lett. 250, 561–571.
Olson, P., Coe, R.S., Driscoll, P.E., Glatzmaier, G.A., Roberts, P.H., 2010. Geodynamo reversal frequency and heterogeneous core–mantle boundary heat flow. Phys. Earth Planet. Inter. 180, 66–79.
Olson, P., Deguen, R., Hinnov, L.A., Zhong, S., 2013. Controls on geomagnetic reversals and core evolution by mantle convection in the Phanerozoic. Phys. Earth Planet. Inter. 214, 87–103.
Olson, P., Hinnov, L.A., Driscoll, P.E., 2014. Nonrandom geomagnetic reversal times and geodynamo evolution. Earth Planet. Sci. Lett. 388, 9–17.
Pétrélis, F., Besse, J., Valet, J.P., 2011. Plate tectonics may control geomagnetic reversal frequency. Geophys. Res. Lett. 38, L19303.
Pétrélis, F., Fauve, S., Dormy, E., Valet, J.P., 2009. Simple mechanism for reversals of Earth's magnetic field. Phys. Rev. Lett. 102, 144503.
Romanowicz, B., Gung, Y., 2002. Superplumes from the core–mantle boundary to the lithosphere: implications for heat flux. Science 296, 513–516.
Ryan, D.A., Sarson, G.R., 2007. Are geomagnetic field reversals controlled by turbulence within the Earth's core? Geophys. Res. Lett. 34, L02307. http://dx.doi.org/10.1029/2006GL028291.
Schubert, G., Masters, G., Olson, P., Tackley, P., 2004. Superplumes or plume clusters? Phys. Earth Planet. Inter. 146, 147–162.
Sepulchre, P., Ramstein, G., Fluteau, F., Schuster, M., Tiercelin, J.-J., Brunet, M., 2006. Tectonic uplift and Eastern Africa aridification. Science 313, 1419–1423.
Tackley, P., 2002. The strong heterogeneity caused by deep mantle layering. Geochem. Geophys. Geosyst. 3. http://dx.doi.org/10.1029/2001GC000167.
Tan, E., Gurnis, M., 2007. Compressible thermochemical convection and application to lower mantle structures. J. Geophys. Res. 112. http://dx.doi.org/10.1029/2006JB004505.
Torsvik, T.H., Burke, K., Steinberger, B., Webb, S.J., Ashwel, L.D., 2010. Diamonds sampled by plumes from the core–mantle boundary. Nature 466, 352–355.
Torsvik, T.H., Smethhurst, M.A., Burke, K., Steinberger, B., 2006. Large igneous provinces generated from the margins of the large low-velocity provinces in the deep mantle. Geophys. J. Int. 167, 1447–1460.
Wicht, J., Stellmach, S., Harder, H., 2009. Numerical models of the geodynamo: from fundamental Cartesian models to 3D simulations of field reversals. In: Glassmeier, H., Soffel, H., Negendank, J. (Eds.), Geomagnetic Field Variations – Space–time Structure, Processes, and Effects on System Earth. Springer, Berlin.
Zhang, N., Zhong, S., 2011. Heat fluxes at the Earth's surface and core–mantle boundary since Pangea formation and their implications for the geomagnetic superchrons. Earth Planet. Sci. Lett. 306, 205–216.
Zhang, N., Zhong, S.J., Leng, W., Li, Z.X., 2010. A model for the evolution of the Earth's mantle structure since the early Paleozoic. J. Geophys. Res. 115, B06401.

AGU PUBLICATIONS

JGR

Journal of Geophysical Research: Solid Earth

RESEARCH ARTICLE

10.1002/2014JB011742

Key Points:
- Most RFPs exhibit westward drift and almost all migrate to higher latitudes
- Advection and diffusion of RFPs explain the historical decrease in the ADM
- Spherical harmonic degrees 4 and above strongly affect the existence of the RFPs

Correspondence to:
F. Terra-Nova,
filipe.terranova@iag.usp.br

Citation:
Terra-Nova, F., H. Amit, G. A. Hartmann, and R. I. F. Trindade (2015), The time dependence of reversed archeomagnetic flux patches, *J. Geophys. Res. Solid Earth*, *120*, 691–704, doi:10.1002/2014JB011742.

Received 5 NOV 2014
Accepted 14 JAN 2015
Accepted article online 20 JAN 2015
Published online 18 FEB 2015

The time dependence of reversed archeomagnetic flux patches

Filipe Terra-Nova[1,2], Hagay Amit[2], Gelvam A. Hartmann[1,3], and Ricardo I. F. Trindade[1]

[1]Departamento de Geofísica, Instituto de Astronomia, Geofísica e Ciências Atmosféricas, Universidade de São Paulo, São Paulo, Brazil, [2]CNRS, Université de Nantes, Nantes Atlantiques Universités, UMR CNRS 6112, Laboratoire de Planétologie et de Géodynamique, Nantes, France, [3]Observatório Nacional, Rio de Janeiro, Brazil

Abstract Archeomagnetic field models may provide important insights to the geodynamo. Here we investigate the existence and mobility of reversed flux patches (RFPs) in an archeomagnetic field model. We introduce topological algorithms to define, identify, and track RFPs. In addition, we explore the relations between RFPs and dipole changes and apply robustness tests to the RFPs. In contrast to previous definitions, patches that reside on the geographic equator are adequately identified based on our RFPs definition. Most RFPs exhibit a westward drift and migrate toward higher latitudes. Undulations of the magnetic equator and RFPs oppose the axial dipole moment (ADM). Filtered models show a tracking behavior similar to the nonfiltered model, and surprisingly new RFPs occasionally emerge. The advection and diffusion of RFPs have worked in unison to yield the decrease of the ADM at recent times. The absence of RFPs in the period 550–1440 A.D. is related to a low in intermediate degrees of the geomagnetic power spectrum. We thus hypothesize that the RFPs are strongly dependent on intermediate spherical harmonic degrees 4 and above.

1. Introduction

The geomagnetic field is generated by convective motions of an electrically conducting fluid in the Earth's outer core. This field is observed directly since about 1590 A.D. by ships, observatories, and more recently at space by satellites [e.g., *Jackson et al.*, 2000; *Jonkers et al.*, 2003; *Hulot et al.*, 2010]. For periods preceding direct magnetic measurements, analysis of archeological and geological materials (indirect observations) provide vital information about the field. At first order, these two kinds of observations show that the field is dominated by an axial dipole. However, some nondipole features are also present, particularly in regions at the core-mantle boundary (CMB) where the polarity is opposite to that of the axial dipole (the so-called reversed flux patches, from hereafter RFPs). Expansion and intensification of these RFPs over at least the past century seem to contribute to the historical decrease in the intensity of the dipole moment [*Gubbins*, 1987].

Changes in the dipole are intrinsically related to the flow patterns of the fluid at the top of the outer core, especially to core flow features near RFPs [*Olson and Amit*, 2006; *Amit and Olson*, 2008]. Most of the radial field at the CMB is negative in the Northern Hemisphere and positive in the Southern Hemisphere. A normal flux patch has the same sign as its hemisphere, whereas an RFP has the opposite sign to its hemisphere. The most intense RFPs over the past decades are observed below the southern Atlantic hemisphere [e.g., *Jackson et al.*, 2000; *Olsen et al.*, 2010]. Direct measurements of the geomagnetic dipole intensity reveal a sustained rapid decrease since 1840 A.D. [*Gubbins*, 1987; *Bloxham and Jackson*, 1992; *Jackson et al.*, 2000; *Gubbins et al.*, 2006; *Olson and Amit*, 2006; *Finlay*, 2008]. Dipole secular variation (SV) contributes substantially to the observed field variation at Earth's surface, in particular, the steady decrease in dipole intensity over historical times. Therefore, understanding the dipole SV is crucial to understanding and perhaps predicting how the field evolves. However, it is worth noting that at its source, the CMB, dipole SV constitutes a very small part of the total SV: The SV spectrum is "blue," i.e., its power increases with harmonic degree (smaller scales).

The geomagnetic dipole intensity has been investigated using maps of the spatial contributions to the axial dipole [*Gubbins*, 1987; *Gubbins et al.*, 2006]. The temporal variability in the integrated contribution of reversed flux to the axial dipole balances its total change [*Olson and Amit*, 2006], emphasizing the role of RFPs in the decrease of dipole intensity over the historical era. However, the role of RFPs in dipole changes over millennial timescales has not yet been explored.

Journal of Geophysical Research: Solid Earth 10.1002/2014JB011742

Previous analyses of archeomagnetic field models were mostly carried out on the kinematics of high-latitude intense normal polarity flux patches. These patches were found to be mobile with alternating eastward-westward drifts [*Dumberry and Finlay*, 2007; *Wardinski and Korte*, 2008; *Korte and Holme*, 2010]. *Amit et al.* [2010] designed an algorithm for identification and tracking of intense flux patches in numerical dynamos. *Amit et al.* [2011] applied a similar algorithm for intense archeomagnetic flux patches. They found more westward drift in the Southern Hemisphere than in the Northern Hemisphere, which may indicate the impact of core-mantle thermal coupling on the geodynamo. None of these studies identified and tracked reversed archeomagnetic flux patches.

Based on theoretical arguments and numerical dynamo models, high-latitude intense normal polarity flux patches and RFPs are thought to reflect distinctive dynamical mechanisms. Rapid rotation effects in the outer core yield a flow barrier and surface convergence at the latitudes of the inner core tangent cylinder [*Aurnou et al.*, 2003]. In an α^2 dynamo, columns of fluid that are nearly invariant in the direction of the rotation axis [*Busse*, 1970] intersect the CMB at these tangent cylinder latitudes [*Olson et al.*, 1999]. Downwelling associated with columnar cyclones [*Olson et al.*, 2002; *Amit et al.*, 2007] concentrate magnetic flux to produce the high-latitude intense patches [*Olson and Christensen*, 2002]. The mobility of these robust field structures may be linked to the motion of the vortices [*Amit et al.*, 2010], so their longevity may therefore maintain the axial dipole dominance. In contrast, low- and middle-latitude RFPs could be related to the expulsion of toroidal magnetic field by deep upwelling and radial diffusion below the CMB [*Bloxham*, 1986]. If persistent, such local processes may eventually lead to a global polarity reversal [*Aubert et al.*, 2008]. These distinctive dynamo processes motivate examining the time dependence of RFPs, to compliment previous studies that described the mobility of high-latitude intense normal polarity flux patches [*Dumberry and Finlay*, 2007; *Wardinski and Korte*, 2008; *Amit et al.*, 2011].

In this paper we introduce topological algorithms to define, identify, and track RFPs. We use the CALS3k.4b archeomagnetic field model constructed for the past three millenia [*Korte and Constable*, 2011]. We explore the relation between RFPs temporal evolution and dipole changes. The robustness of the archeomagnetic RFPs is tested to assess the reliability of the identification and tracking results.

2. Methods

2.1. Identification and Tracking

The reversed flux patches (RFPs) identification method at each snapshot comprises four steps. First, the magnetic equator is identified. Second, each grid point is associated with a magnetic hemisphere. Third, peaks of RFPs are identified. Finally, an intensity criterion is invoked to filter out weak insignificant RFPs.

RFPs on the CMB are commonly defined as positive/negative radial field structures in the Northern/Southern Hemispheres [e.g., *Olson and Amit*, 2006]. This definition might be problematic. For example, a patch residing on the geographic equator is considered partly normal partly reversed. We therefore seek a more appropriate definition. In this paper, we use the magnetic equator to define the polarity at each grid point. We coded an algorithm to map the magnetic equator. At a given longitude on the CMB, the magnetic equator is defined as the point where the radial geomagnetic field B_r changes sign. To distinguish between sign changes associated with the magnetic equator or with an RFP, the algorithm searches first a longitude where there is just one point of change in the sign of B_r. This point is guaranteed to be the magnetic equator. From this initial location of magnetic equator, the algorithm selects the closest point on the neighbor longitude which has a change in sign of B_r.

After mapping the magnetic equator we define the magnetic hemispheres. Every grid point north/south of the magnetic equator is assigned to its respective magnetic hemisphere. A difficulty arises at some longitudes where the magnetic equator appears more than once. An algorithm marches from colatitude 0° to 180°, assigning the northernmost point to the northern magnetic hemisphere. Then, after every crossing of the magnetic equator, the next point is assigned to the opposite hemisphere.

Once each point on the CMB is associated with a magnetic hemisphere and a polarity (normal or reversed), the next step is to identify the peaks of RFPs. For this purpose we coded an algorithm to determine field maxima and minima of flux patches at the CMB. The algorithm searches the maxima and minima of the radial field by comparison with neighboring cells. A grid point is considered to be a maximum/minimum if it has higher/lower value than its eight neighboring cells. Maximum or minimum values indicate the coordinates (colatitude and longitude) of the peak of the RFPs at the CMB.

Journal of Geophysical Research: Solid Earth 10.1002/2014JB011742

For the final identification step we imposed a criterion of threshold intensity to avoid interpreting insignificantly weak extreme points. For every snapshot, only RFPs with peak values larger than half the most intense RFP of the same snapshot were considered. Obviously, only snapshots with more than one RFP were affected by this criterion.

To track RFPs in time, we coded an algorithm that calculates the distance of each RFP to all RFPs in the next snapshot. The spherical distance is calculated along a great circle. A critical distance was set based on typical large-scale core flow values from geomagnetic secular variation inversions. In the core flow model of *Amit and Olson* [2006], the maximum of time-averaged flow plus 1 standard deviation is about 70 km/yr. We used this value multiplied by the time step between snapshots of 10 years to obtain the critical distance for tracking. A pair of RFPs at two successive snapshots which has a spherical distance lower than this critical value is denoted as the same RFP. If an RFP in the new snapshot is farther from all previous snapshot's RFPs than the critical distance, it is denoted as a new RFP.

2.2. Dipole Changes

We took advantage of the above definitions to map local contributions to the axial dipole moment (ADM), and we investigated the temporal behavior of these contributions. The axial component of the magnetic dipole moment (m_z) is defined as follows [*Moffatt*, 1978; *Gubbins*, 1987; *Gubbins et al.*, 2006; *Olson and Amit*, 2006]:

$$m_z = \frac{4\pi a^3}{\mu_0} g_1^0 = \frac{3r_o}{2\mu_0} \int_S B_r \cos\theta \mathrm{d}S \tag{1}$$

where a is the radius of the Earth, $\mu_0 = 4\pi \times 10^7$ Hm^{-1} is the free space magnetic permeability, g_1^0 is the axial dipole Gauss coefficient, r_o is the radius of the core, B_r is the radial component of the magnetic field on the CMB, θ is colatitude and dS denotes a CMB surface increment. The integrand $B_r \cos\theta$ represents the spatial distribution of local contributions to the ADM. Thus, mapping $B_r \cos\theta$ allows imaging local contributions to the ADM.

We associate different types of $B_r \cos\theta$ structures to different ADM contributions as:

$$m_z = m_{n+} + m_{n-} + m_{r+} + m_{r-} \tag{2}$$

where the subscripts n and r denote contributions from regions of normal and reversed flux respectively, m_{n+} represents reinforcing contributions (mostly from high-latitude flux patches), m_{n-} corresponds to opposite contributions (totally from magnetic equator undulations), m_{r+} represents reinforcing contributions and m_{r-} denotes opposite contributions. Note that m_{r+} contributions appear when an RFP is localized at least partly between the magnetic equator and the geographic equator.

2.3. Robustness Tests

Uncertainties in archeomagnetic field models will produce erroneous results concerning the existence and mobility of RFPs. Robustness tests are clearly required. Two tests were performed, one using the power spectrum, the other using low-pass-filtered fields.

The Mauersberger-Lowes spectrum at the CMB is one of the primary outputs of the dynamo process in the core [*Dormy et al.*, 2000]. The magnetic field spectrum R_n at the CMB can be expressed as a function of spherical harmonic degree n in terms of the Gauss coefficients of the core field as [*Lowes*, 1974]:

$$R_n = (n+1)\left(\frac{a}{r_o}\right)^{2n+4} \sum_{m=0}^{n} \left(g_n^m\right)^2 + \left(h_n^m\right)^2 \tag{3}$$

where n is degree, m is order, and the sets g_n^m and h_n^m are the Gauss coefficients. We compared the spectrum at periods without RFPs with the spectrum at periods with RFPs to test whether the absence of patches is due to low field resolution manifested by a steeper descending spectrum.

In the second test, we defined a low-pass filter $F(n)$ by

$$F(n) = \begin{cases} 1 & , \text{ if } n < n_0 \\ cos\left(\frac{n-n_0}{n_f-n_0} \cdot \frac{\pi}{2}\right) & , \text{ if } n \geq n_0 \end{cases} \tag{4}$$

where n_0 marks the beginning of the filtering and n_f marks the truncation. At $n = n_f$ the filter $F(n_f) = 0$, so the highest degree considered is $n_f - 1$. We examined the sensitivity of the identification and tracking

Journal of Geophysical Research: Solid Earth 10.1002/2014JB011742

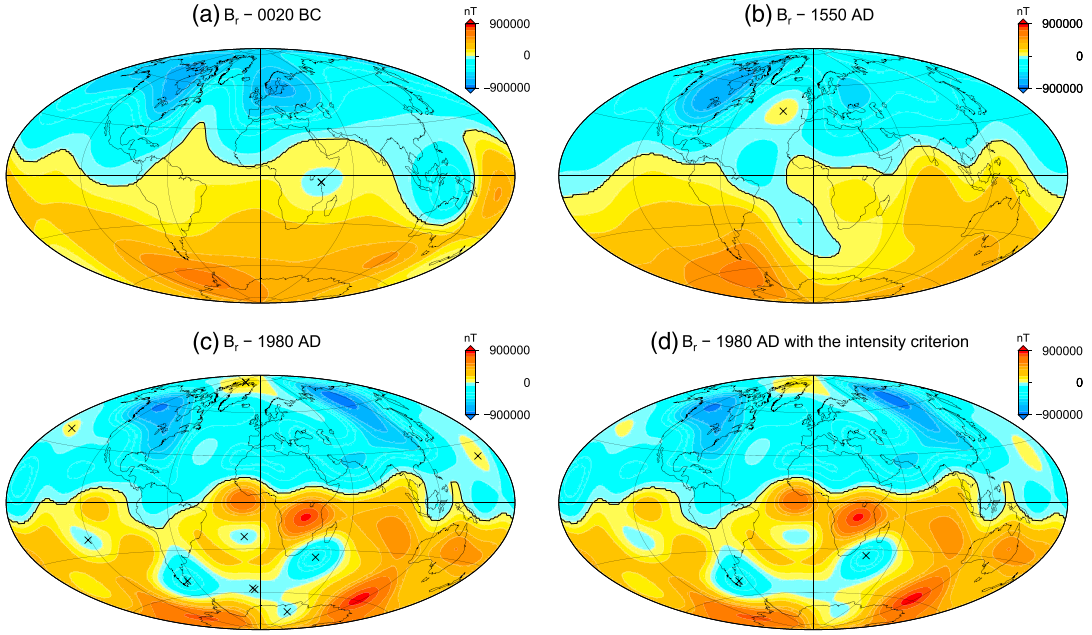

Figure 1. Radial geomagnetic field on the CMB at (a) 0020 B.C., (b) 1550 A.D., and (c) 1980 A.D. based on the CALS3k.4b archeomagnetic field model of [*Korte and Constable*, 2011]. The black line is the mapped magnetic equator, and the black X symbols are the peaks of the RFPs. (d) The RFPs identification for 1980 A.D. with the intensity criterion.

of RFPs to the small-scale field, which is most uncertain in the archeomagnetic field models, by comparing our results using the nonfiltered archeomagnetic field model with those obtained using different low-pass-filtered field models. Finally, we compare our results with the same analysis based on the historical field model GUFM1 [*Jackson et al.*, 2000] to further assess the robustness of the results from the archeomagnetic models.

3. Results

3.1. Identification and Tracking

We used the CALS3k.4b model of *Korte and Constable* [2011] for the interval 990 B.C. until 1990 A.D. This model was constructed from intensity and direction data acquired in archeological (potteries, bricks, etc.) and geological (basaltic flows and lake sediments) materials. In addition, this model is constrained by GUFM1 [*Jackson et al.*, 2000] from 1840 onward, the latter inverted from direct measurements from observatories and satellites. The database used in this model is an extension of the previous compilation of *Korte et al.* [2009]. Consequently, this model presents an improvement in the fit of the Gauss coefficients due to database updates. The model is expanded up to spherical harmonic degree 10 and the temporal resolution is 10 years. We used a regular grid on the CMB of 1° in longitude and latitude.

Figure 1 illustrates the performance of our identification algorithm using three snapshots of the radial archeomagnetic field model on the CMB. The magnetic equator is marked by a solid black line, and each identified RFP is marked by an X symbol (see Figure 1). Our algorithm for mapping the magnetic equator resolves well the magnetic hemispheres, defines local polarity, and correctly identifies RFPs that reside on the geographic equator. Therefore, RFPs are never considered partly normal partly reversed. Figure 1a shows an example of a successfully identified RFP that resides on the geographic equator below eastern Africa.

Figure 1b shows an example of an especially complicated case for the mapping of the magnetic equator. For some longitudes the magnetic equator is crossed 3 times (in other rare snapshots not shown here up to five such crossings occurred). In addition, the magnetic equator penetrates up to a relatively high latitude. Nevertheless, our algorithm correctly maps the magnetic equator. Although the field morphology of the snapshot in Figure 1b is somewhat extreme, in many snapshots of the studied period a significant deviation

Journal of Geophysical Research: Solid Earth 10.1002/2014JB011742

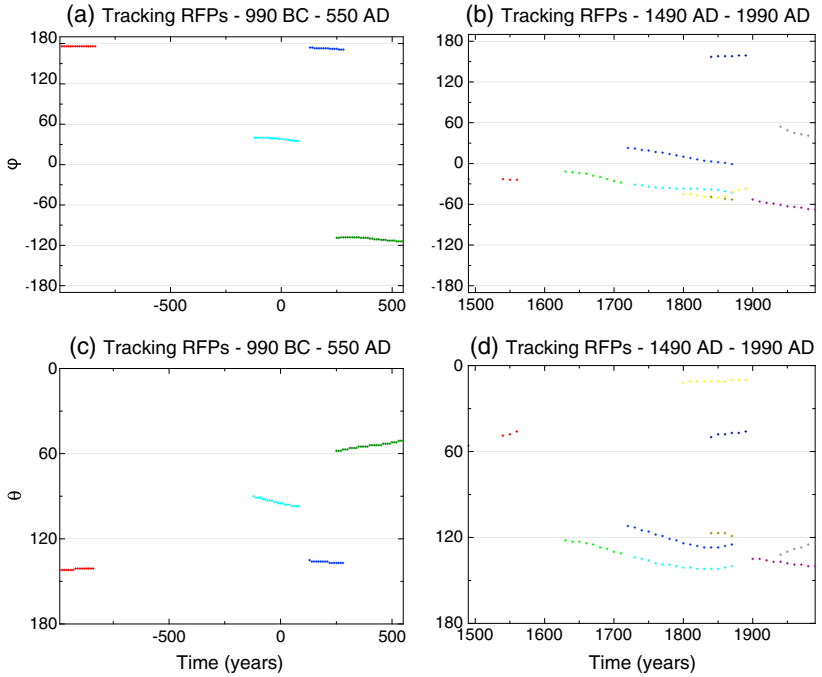

Figure 2. Temporal evolution of the (a, b) longitude, and (c, d) colatitude of peaks of intense RFPs in the model CALS3k.4b [*Korte and Constable*, 2011]. Figures 2a and 2c are from 990 B.C. to 550 A.D.; Figures 2b and 2d are from 1490 A.D. to 1990 A.D. The same colors are used for longitude and colatitude of a given RFP. Longitudes and colatitudes are given in degrees. All curves are dotted; In Figures 2a and 2c the dotted lines seem solid due to the large period covered.

of the magnetic equator from the geographic equator appears. The identification of magnetic hemispheres allowed the straightforward mapping of regions of reversed flux. Furthermore, deep intrusions of normal polarity field to the opposite hemisphere as a result of undulations of the magnetic equator were correctly interpreted as normal flux. This is exemplified by a large normal polarity intrusion south of the geographic equator but north of the magnetic equator that is correctly identified as a region of normal flux in Figure 1b.

Some RFPs are very weak, as evidenced in Figure 1c. Two of these peaks (at high latitudes of the southern Atlantic Ocean) are very close to each other. Accounting for these weak peaks might bias the tracking of RFPs. We therefore introduced in Figure 1d the intensity criterion (compare Figures 1c and 1d). Figure 1d contains two peaks of intense RFPs in the Southern Hemisphere. These two RFPs are part of a large area of reversed flux over the Atlantic Ocean, South America, and Antarctica.

The tracking of RFPs that pass the intensity criterion is separated into intervals with different RFPs activity. For all intervals, we tracked longitude and colatitude (Figure 2). The first interval is from 990 B.C. to 550 A.D. (Figures 2a and 2c) and the second from 1450 A.D. to 1990 A.D. (Figures 2b and 2d). No patches were observed between these two intervals, comprising the period 550 A.D.–1440 A.D. in Figure 2. From 990 B.C. to 550 A.D., four RFPs were identified and tracked. In this period, we found two nearly stationary RFPs (red and blue) and two with westward drift (green and cyan). The latter two RFPs exhibit motion toward higher latitudes. From 1450 A.D. to 1990 A.D. the field model is characterized by higher spatial resolution resulting in a much higher occurrence of RFPs. Most RFPs exhibit a westward drift, but some quasi-stationary RFPs are also observed. In addition, most RFPs migrate toward higher latitudes.

We quantified the statistical behavior of RFPs. Table 1 shows the average rate of azimuthal displacement per year for three types of motions: quasi-stationary, westward, and eastward. The critical azimuthal angular velocity distinguishing drift from quasi-stationary is the quarter of the weighted average of all RFPs, with the weighting being proportional to the lifetime of each RFP. We did not take the average minus 1 standard

Journal of Geophysical Research: Solid Earth 10.1002/2014JB011742

Table 1. Types of RFPs Azimuthal Motions and the Rate of Their Displacement per Year[a]

	Nonfiltered		f8/11		f5/11		f3/8	
	N_{RFPs}	Rate	N_{RFPs}	Rate	N_{RFPs}	Rate	N_{RFPs}	Rate
Quasi-stationary	2	−0.01	3	−0.01	4	−0.01	2	−0.02
Westward	9	−0.10	10	−0.09	8	−0.09	3	−0.17
Eastward	2	0.07	1	0.02	2	0.04	0	0

[a] N_{RFPs} is the number of RFPs. The f8/11, f5/11, and f3/8 are filtered models in spherical harmonic degrees between 8 and 11, 5 and 11, and 3 and 8, respectively. Each rate is given in °/*yr*. Quarter of the average of rate is the critical value to distinguish quasi-stationary and drifting features.

deviation because the distribution of RFPs azimuthal angular velocity turns out to be non-Gaussian. RFPs that have angular velocity higher than this critical value are considered drifting. Table 1 indicates that the RFPs exhibit more a westward drift than other kind of azimuthal motions. Quasi-stationary motion occurs much less and the number of RFPs with eastward drift is the lowest. Finally, the rate of westward drift is significantly larger than the rate of eastward drift.

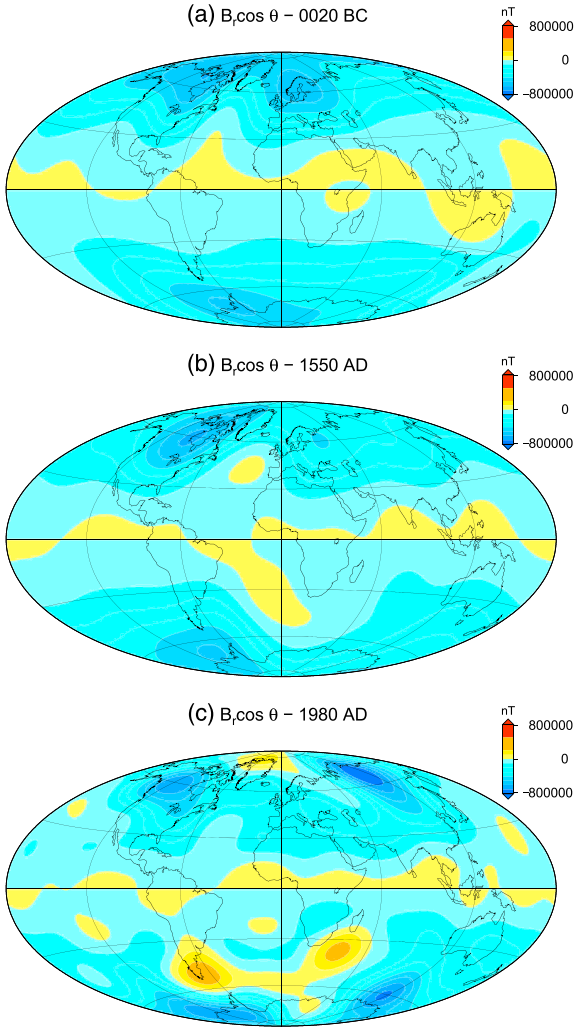

Figure 3. Local contributions to the ADM $B_r \cos\theta$ at (a) 0020 B.C., (b) 1550 A.D., and (c) 1980 A.D.

3.2. Dipole Changes

Spatial contributions (by normal or reversed flux) to the ADM were mapped using the integrand of equation (1), $B_r \cos\theta$. Positive values denote opposite contributions to ADM, while negative values denote reinforcing contributions. Figure 3 shows local contributions to the ADM in the same years as in Figure 1. High-latitude intense normal flux patches provide the most important reinforcing contributions to the ADM. Midlatitude RFPs constitute the most significant opposite contributions to the ADM.

The mathematical definition of ADM contributions considers the geographic equator. Consequently, in Figure 3a below eastern Africa contributions from one RFP (Figure 1a) are partly reinforcing partly opposite. Another type of opposite contribution to the ADM corresponds to areas of magnetic equator undulations. This can be seen for example in Figure 3b below the southern Atlantic Ocean, where normal flux associated with deep magnetic equator intrusion (Figure 1b) yields an opposing contribution to the ADM. In Figure 3c there are two regions of significant opposite contribution for the ADM, one below Patagonia and the other below South Africa. These structures correspond to intense RFPs on the CMB (see Figure 1d).

Journal of Geophysical Research: Solid Earth 10.1002/2014JB011742

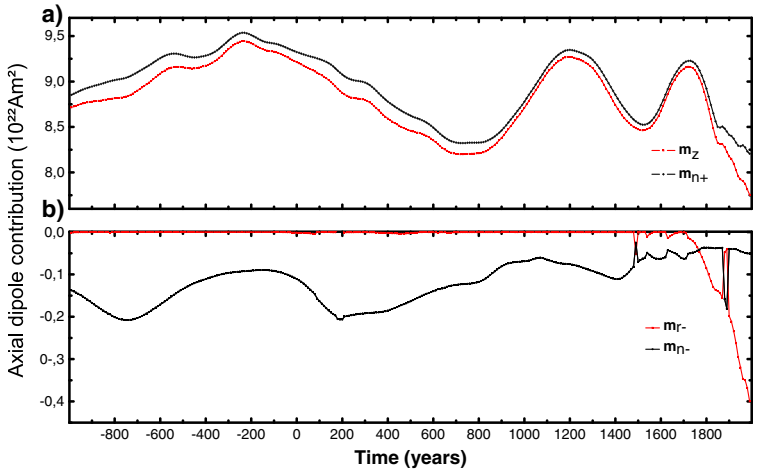

Figure 4. Time dependence of ADM and its different contributions. Values of (a) total m_z and m_{n+} and (b) m_{r-} and m_{n-}. All ADM contributions are expressed in 10^{22} A m^2. Note the difference in scales between Figures 4a and 4b.

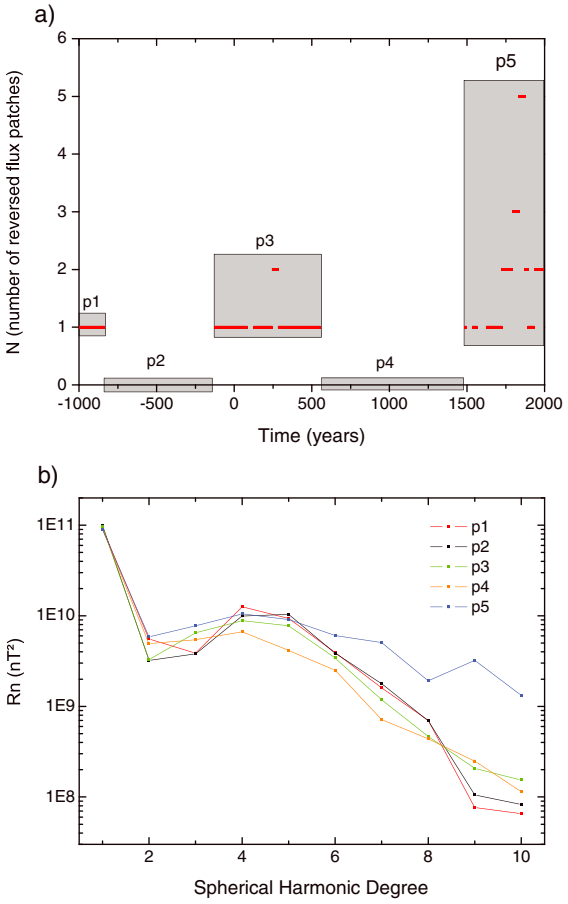

Figure 5. (a) Number of RFPs as a function of time. The five grey rectangles separate five periods. (b) Time-average power spectra for each period in (a).

Figure 4 shows the total ADM (m_z) and its contributions (2), including reinforcing contributions by normal flux (m_{n+}), opposite contributions by normal flux due to magnetic equator undulations (m_{n-}), and opposite contributions by reversed flux (m_{r-}). The reinforcing contributions by reversed flux (m_{r+}) were found to be negligible. The absolute values of m_z and m_{n+} (Figure 4a) are much higher than those of m_{r-} and m_{n-} (Figure 4b), but the temporal variations of the latter contributions are not negligible. From 990 B.C. until about 1800 A.D. the trend of ADM changes is dominantly controlled by high-latitude normal patches. The ADM changes in this period show no correlation with m_{n-} changes. However, the small differences between m_{n+} and m_z are associated with changes in m_{n-}. In 1730 A.D. we detect the most recent local maximum (in absolute value) of m_z and m_{n+} with 9.14×10^{22} A m^2 and 9.23×10^{22} A m^2, respectively (Figure 4a). In 1990 A.D. the corresponding values decreased to 7.75×10^{22} A m^2 and 8.19×10^{22} A m^2, respectively.

Between 990 B.C. and 1760 A.D. RFPs have little impact on ADM changes and m_{r-} is negligible (Figure 4b). The

Journal of Geophysical Research: Solid Earth 10.1002/2014JB011742

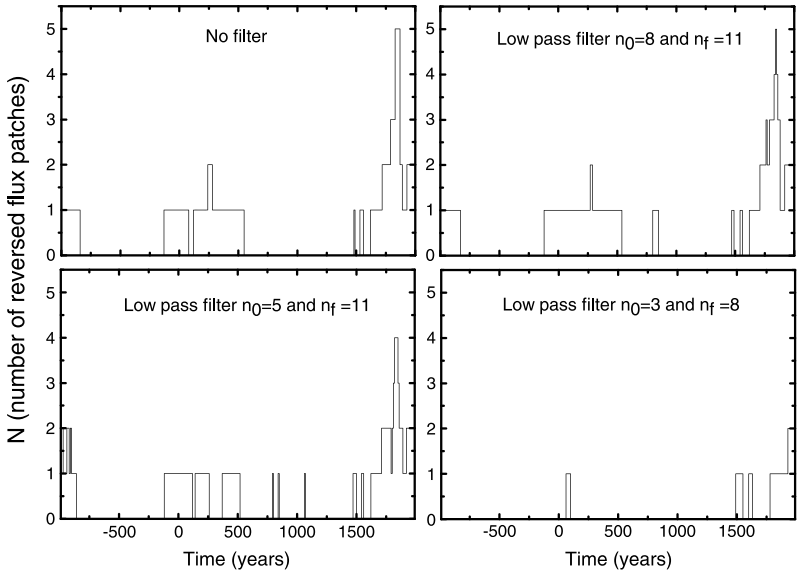

Figure 6. Number of RFPs as a function of time in the filtered field models.

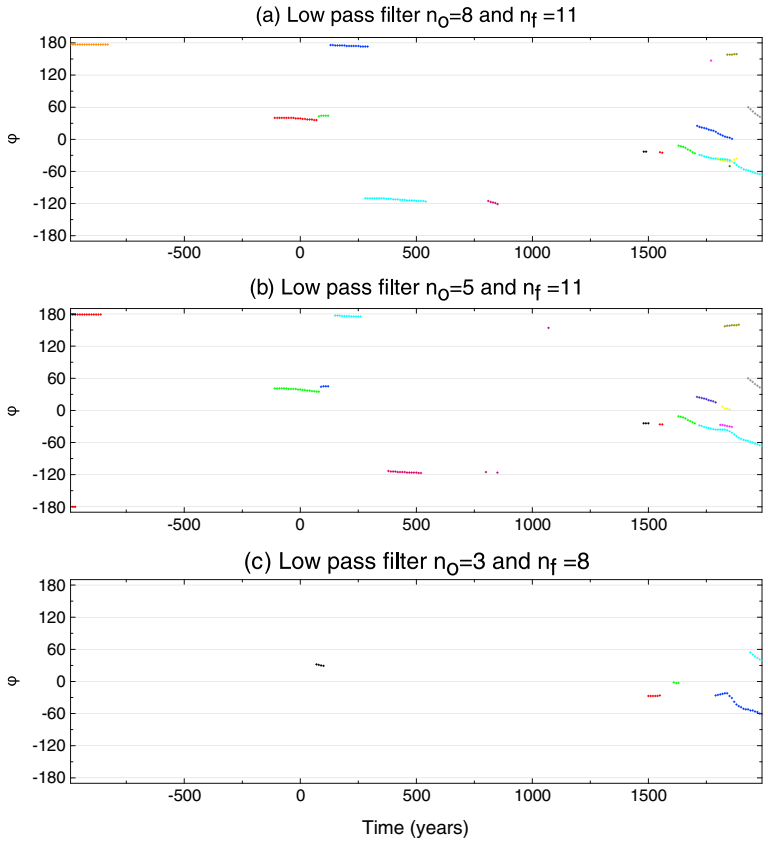

Figure 7. As in Figures 2a and 2b for the filtered field models.

Journal of Geophysical Research: Solid Earth 10.1002/2014JB011742

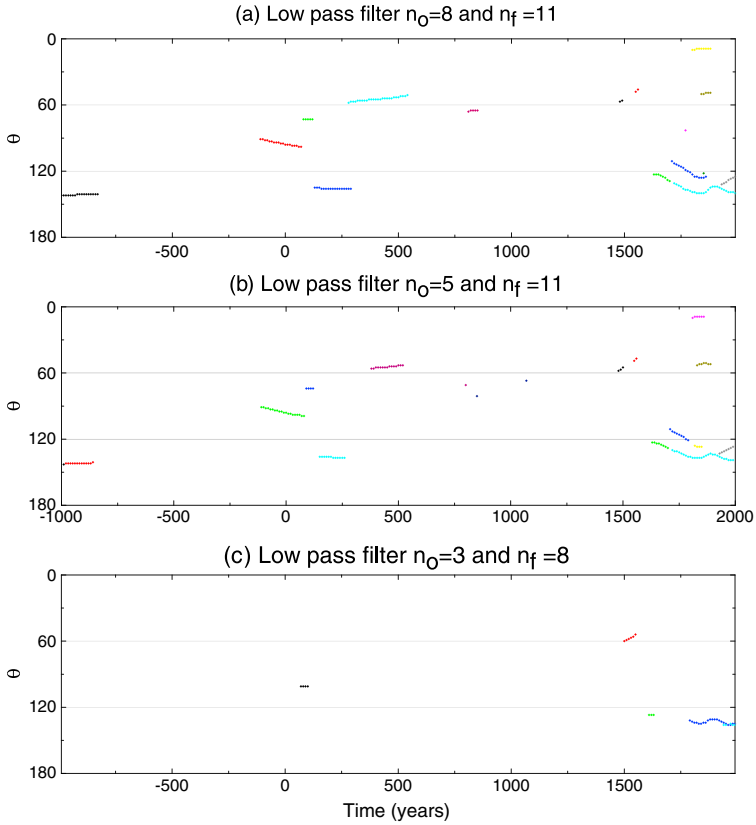

Figure 8. As in Figures 2c and 2d for the filtered field models.

values of m_{n-} are nonnegligible. However, changes of trend and absolute values of m_{n-} are an order of magnitude too low to play a major role in the ADM changes during this period (compare scales between Figures 4a and 4b). The influence of RFPs started to be higher than the influence of magnetic undulations from ~1770 A.D. with increasing trend until 1990 A.D. The m_{r-} absolute value was 0.40 × 10^{22} A m^2 in 1990 A.D., about 5% of the total ADM in this year. While this absolute value of m_{r-} may seem low, the difference between the total ADM change m_z and the normal flux reinforcing contributions m_{n+} increases from 1790 to 1990 A.D. (Figure 4b) mostly due to the increase in the amplitude of the opposite contributions by m_{r-}.

3.3. Robustness Tests

Figure 5a shows the number of identified RFPs as a function of time. Five periods of time were considered: p1 (990 B.C.–840 B.C.), p2 (830 B.C.–140 B.C.), p3 (130 B.C.–550 A.D.), p4 (560 A.D.–1480 A.D.), and p5 (1490 A.D.–1990 A.D.). In periods p1, p3, and p5 RFPs were found, with p5 having the highest number of RFPs. In periods p2 and p4 no RFPs were found. Figure 5b shows time-averaged power spectra of the intervals identified in Figure 5a. The power spectra exhibit comparable values up to spherical harmonic degree 4. The spectrum in period p4 decreases faster than the others between spherical harmonic degrees 4 and 8. Note that p4 represents almost 1000 years of absence of RFPs. The most recent period p5 has higher values for almost all spherical harmonic degrees. The earlier periods p1, p2, and p3 have a strong decrease of R_n starting in degree 6, and the periods p1 and p2 have the lowest power spectrum values for degrees 9 and 10. Note that the absence of RFPs in period p2 is not reflected in its power spectrum compared to periods p1 and p3.

Next we used low pass filters with three different wave number bands to study the sensitivity of RFPs to uncertain small scales of the field model. The filters are n_o = 8 and n_f = 11 (denoted f8/11), n_o = 5 and

Journal of Geophysical Research: Solid Earth 10.1002/2014JB011742

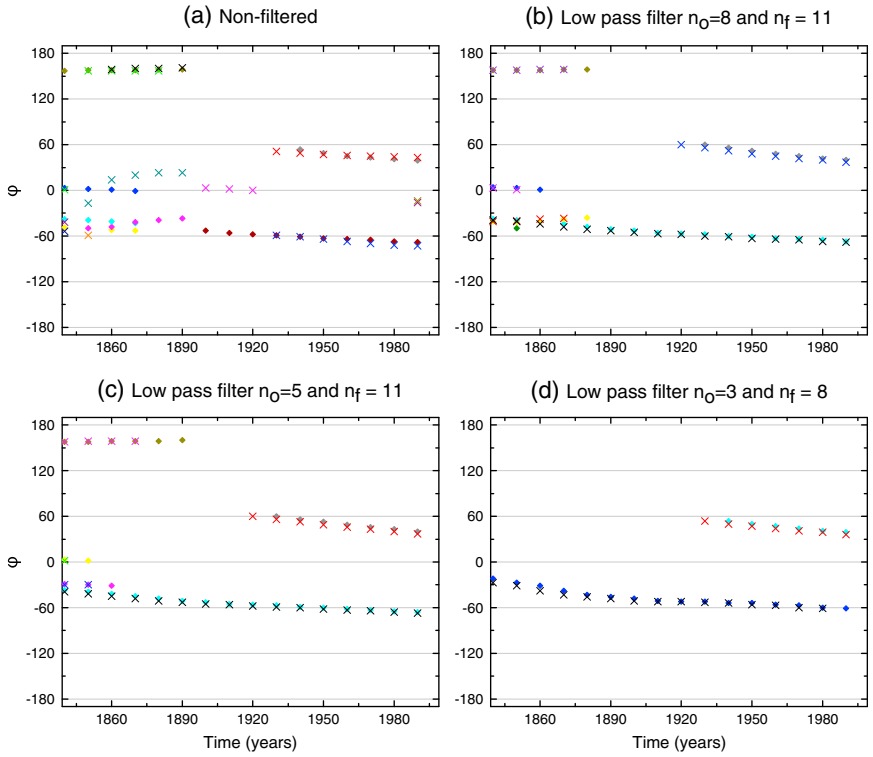

Figure 9. As in Figures 2a and 2b for the period 1840–1990 A.D. for the filtered field models of GUFM1 and CALS3k.4b. Crosses/diamonds represent RFPs of GUFM1/CALS3k.4b respectively.

$n_f = 11$ (denoted f5/11), and $n_o = 3$ and $n_f = 8$ (denoted f3/8) (see (4)). Figure 6 shows that the number of patches per year in filtered models f8/11 and f5/11 was almost the same as that in the nonfiltered model. Filtered model f3/8 has much lower number of patches than the others in all periods. Surprisingly, some new RFPs emerged in models f8/11 or f5/11. Moreover, the total number of patches was even slightly higher in f8/11 than in the nonfiltered model. More specifically note that the large interval of absence of patches (560 A.D.–1480 A.D.) in the nonfiltered model is occasionally abrupt in the filtered models f8/11 and f5/11, even though this interval is characterized by low values of R_n for spherical harmonic degrees higher than 4 (Figure 5b).

We now address the question of how the filters could change the spatial behavior of the RFPs. For this purpose, we tracked in time the coordinates of the RFPs in the filtered models and we compared the results obtained by the different field models (Figures 7 and 8). Figures 2a, 2b, and 7a show similar results between the filtered model f8/11 and the nonfiltered model, with dominance of westward drift. In addition, some new RFPs are occasionally identified and others showed a larger lifetime than in the nonfiltered model. Figure 7b shows that the f5/11 filtered model is also characterized by westward drift and quasi-stationary behavior with most RFPs exhibiting a somewhat shorter lifetime. Figures 7c and 8c show the action of the strongest filter. The low number of RFPs strongly limits the robustness of characterizing their behavior in this model. Only five RFPs were tracked, three of them with westward drift and two were quasi-stationary (Table 1). The time dependence of the colatitude of the RFPs (Figures 2c, 2d, and 8) is rather similar in the nonfiltered, f8/11 and f5/11 models: Most RFPs migrate toward higher latitudes. The most prominent examples include a low-latitude RFP migrating southward between 120 B.C.–80 A.D., a high-latitude RFP moving northward between 210 A.D. and 550 A.D., and several midlatitude RFPs heading southward between 1630 A.D. and the present.

Journal of Geophysical Research: Solid Earth 10.1002/2014JB011742

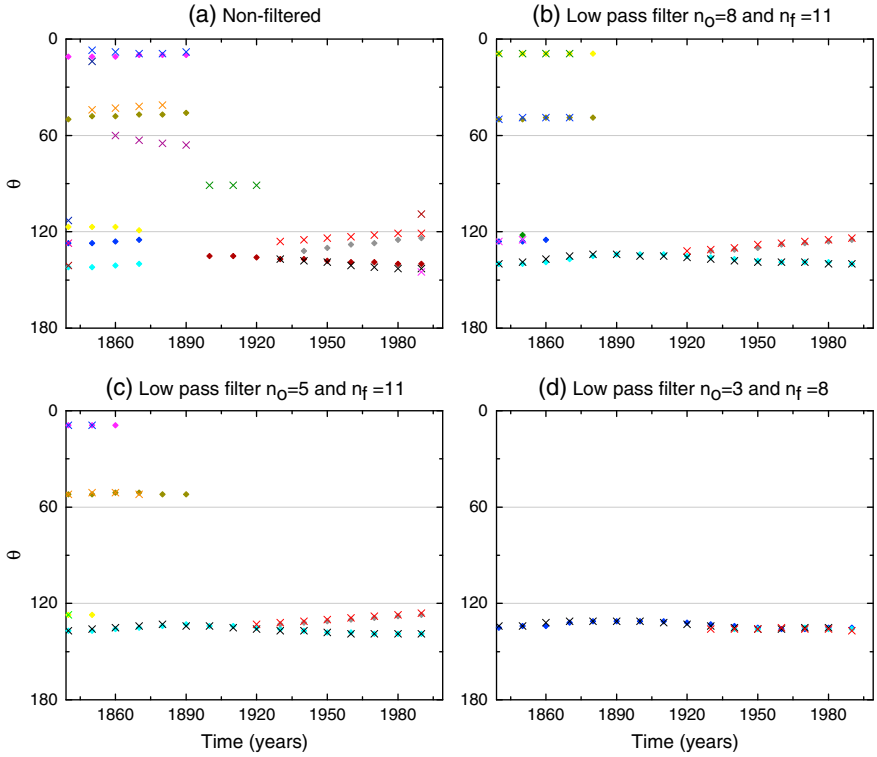

Figure 10. As in Figures 2c and 2d for the period 1840-1990 A.D. for the filtered field models of GUFM1 and CALS3k.4b. Crosses/diamonds represent RFPs of GUFM1/CALS3k.4b, respectively.

3.4. Comparison With the Historical Field

To further test the robustness of the archeomagnetic RFPs, we compare in Figures 9 and 10 results from CALS3k.4b and GUFM1 for the period 1840 to 1990 A.D. Overall, there is a very good agreement between the tracking in both field models. Stronger filters yield even more coincident RFP positions and motions between the two models. As with CALS3k.4b, most RFPs in GUFM1 and their filtered models exhibit westward drift and migrate toward higher latitudes, while some RFPs are characterized by a quasi-stationary behavior.

4. Discussion

Our definition of the local polarity based on the magnetic equator yielded accurate identification of reversed flux patches (RFPs). The intensity criterion filtered out weak RFPs and the velocity criterion connected adequate RFPs in successive snapshots, thus providing meaningful tracking results. Defined this way, RFPs could even be identified on the geographic equator.

One of the earliest and most prominent observations of geomagnetism was the westward drift of field structures [e.g., *Bullard et al.*, 1950; *Yukutake*, 1967; *Bloxham and Gubbins*, 1985; *Finlay and Jackson*, 2003]. Although the core flow is probably more complex, the zonal part of core flow models is often westward at low and middle latitudes, in particular, in the Southern Hemisphere [*Amit and Olson*, 2006]. The dynamical origin of this westward drift is still debated. Recently, it was argued that the westward drift is caused by the gravitational coupling between the inner core and the mantle [*Aubert*, 2013; *Aubert et al.*, 2013]. We find that most RFPs exhibit westward drift. In Table 1, we quantify the azimuthal displacement rate of the RFPs. The westward drifting RFPs move in an average rate of −0.10°/yr, comparable to inferred zonal core flow motions [*Hulot et al.*, 2002; *Holme and Olsen*, 2006]. Tracking in filtered models showed slightly more quasi-stationary RFPs (although still westward drifting RFPs occur more), even though these RFPs have shorter lifetime. The azimuthal displacement rate of the RFPs changes mildly among the different

Journal of Geophysical Research: Solid Earth 10.1002/2014JB011742

filtered models, suggesting that the displacement of RFPs is not associated to the highest spherical harmonic degrees. In addition, most RFPs at both hemispheres migrated toward higher latitudes.

We identified different types of possible morphological contributions to the axial dipole moment (ADM) (see Figures 3 and 4). Magnetic equator undulations in early times explain the difference between total ADM and contributions of the intense high-latitude normal flux patches. At recent times, this difference is well explained by opposite contributions of RFPs. The reinforcing contributions of RFPs (which hypothetically may exist) were found negligible. Temporal changes in the intensity and latitude of high-latitude normal flux patches rule exclusively the trend of the ADM when the field is poorly represented in terms of reversed flux regions (likely associated to low resolution of the field model). Finally, RFPs expansion and intensification since 1870 A.D. to present is probably the kinematic signature of radial diffusion at the top of the outer core [*Gubbins*, 1987; *Olson and Amit*, 2006] which may indicate the presence of a thin magnetic boundary layer below the CMB [*Amit and Christensen*, 2008; *Chulliat and Olsen*, 2010].

Changes in the dipole field due to RFPs were only important after 1770 A.D., which is near when CALS3k.4b is constrained by GUFM1. It is likely that RFPs should contribute continually to the dipole field but that low data quality does not allow to resolve them in earlier times. The similar behavior of RFPs in CALS3k.4b and GUFM1 suggests that the spatiotemporal smoothness of the archeomagnetic field model does not prevent identification and tracking of RFPs, but its low resolution reduces the intensity of the RFPs and hence their contribution to the dipole.

Absence of RFPs in the period 550 A.D.–1440 A.D. is related to the low geomagnetic power spectrum in spherical harmonics $n = 4–8$, which is associated with fewer data, resulting in a stronger effect of regularization. However, between 830 B.C. and 140 B.C. the absence of RFPs does not seem to be associated with low geomagnetic power spectrum, because the neighboring periods p1 and p3 (which have similar power spectra as period p2) contain RFPs. The absence of RFPs in this period could therefore genuinely reflect different field morphology and possibly different core dynamics activity in this time interval. The geomagnetic power spectrum for the recent period (p5) is much stronger than that of earlier periods because of the much better coverage and quality of the recent data.

Periods with lower values of geomagnetic power spectrum at high spherical harmonic degree lead to larger-scale field that mask small-scale field structures. Morphologically, it implies that two neighboring regions of opposite flux would be smoothed to one region of the more intense flux. This effect creates undulations in the magnetic equator and obscures RFPs, which limits relating RFPs to ADM changes. Perhaps surprisingly, the filtered models f8/11 and f5/11 show comparable number and more continuous RFPs than in the nonfiltered model. This may be associated to the resolution effects. Another possibility is that two neighboring RFPs, with low intensity values that do not pass the intensity criterion, may merge to one strong RFP after filtering and thus pass the intensity criterion. Note that the large interval of absence of RFPs (560 A.D.–1480 A.D.) in the nonfiltered model is occasionally abrupt in the filtered models f8/11 and f5/11. In these models spherical harmonic degrees 4 and 5 are not filtered whereas higher spherical harmonic degrees 9 and 10 are strongly reduced. Moreover, period p1 has the lowest values of spherical harmonic degrees 9 and 10. These results indicate that spherical harmonic degrees $n = 4–8$ strongly affect RFPs in the archeomagnetic field model. Indeed, the f3/8 filtered model strongly affects intermediate spherical harmonic degrees $n = 4–8$ and contains very few RFPs. Furthermore, period p4 had the lowest values of spherical harmonic degrees $n = 4–8$ compared to the other periods and in this period RFPs are absent (see Figure 5b).

Robust tracking results common to the nonfiltered as well as filtered models may shed light on the kinematics of RFPs. RFPs in all field models exhibit either a westward drift or to a much lesser extent quasi-stationary behavior. In most cases the RFPs drift to higher latitudes, thus systematically weakening the prevailing dipole polarity.

5. Conclusions

Our algorithm allows defining, identifying, and tracking reversed flux patches (RFPs). Our main findings are the following:

1. Most RFPs exhibit westward drift.
2. More than 75% of RFPs migrate toward higher latitudes.

Journal of Geophysical Research: Solid Earth 10.1002/2014JB011742

3. In some periods (but not all) the absence of RFPs is due to the low resolution of the field model. Overall, the data are not sufficient to show that the RFPs have not been present at all times in the recent few millennia.
4. Filtered models and comparison with GUFM1 suggest that RFPs are prominent.
5. Spherical harmonic degrees 4 and above strongly affect the existence of the RFPs.

Lastly, we draw attention to the need for new archeomagnetic data to allow for better constrained field models, as well as filters to better select the data used as database to the models. These new models will allow to better identify and track field structures (e.g., RFPs), and consequently to improve the understanding of RFPs and their role in core dynamics on millennial timescales.

Acknowledgments
The field model data for this paper are available at EarthRef.org Digital Archive (ERDA). Data set name: Global archeomagnetic field models CALS3k.4 and CALS3k.4b. Data set link: http://earthref.org/ERDA/1142/. F. Terra-Nova and G. A. Hartmann acknowledge grants 2013/14629-8 and 2010/10754-4, São Paulo Research Foundation (FAPESP), respectively. We would like to thank the Laboratoire de Planétologie et de Géodynamique (LPGNantes/CRNS) and the Instituto de Astronomia, Geofísica e Ciências Atmosféricas (IAG/USP) for the institutional support. This study was partially performed during a 4 month visit of F. Terra-Nova in LPGNantes. We are grateful to Richard Holme and Mathieu Dumberry for their constructive comments that significantly improved the manuscript.

References

Amit, H., and U. Christensen (2008), Accounting for magnetic diffusion in core flow inversions from geomagnetic secular variation, *Geophys. J. Int.*, *175*, 913–924.
Amit, H., and P. Olson (2006), Time-average and time-dependent parts of core flow, *Phys. Earth Planet. Inter.*, *155*, 120–139.
Amit, H., and P. Olson (2008), Geomagnetic dipole tilt changes induced by core flow, *Phys. Earth Planet. Inter.*, *166*, 226–238.
Amit, H., P. Olson, and U. Christensen (2007), Tests of core flow imaging methods with numerical dynamos, *Geophys. J. Int.*, *168*, 27–39.
Amit, H., J. Aubert, and G. Hulot (2010), Stationary, oscillating or drifting mantle-driven geomagnetic flux patches, *J. Geophys. Res.*, *115*, B07108, doi:10.1029/2009JB006542.
Amit, H., M. Korte, J. Aubert, C. Constable, and G. Hulot (2011), The time-dependence of intense archeomagnetic flux patches, *J. Geophys. Res*, *116*, B12106, doi:10.1029/2011JB008538.
Aubert, J. (2013), Flow throughout the Earth's core inverted from gomagnetic observations and numerical dynamo models, *Geophys. J. Int.*, *192*, 537–556, doi:10.1093/gji/ggs051.
Aubert, J., H. Amit, G. Hulot, and P. Olson (2008), Thermo-chemical flows couple the Earth's inner core growth to mantle heterogeneity, *Nature*, *454*, 758–761.
Aubert, J., C. Finlay, and F. Fournier (2013), Bottom-up control of geomagnetic secular variation by the Earth's inner core, *Nature*, *502*, 219–223, doi:10.1038/nature12574.
Aurnou, J., S. Andreadis, L. Zhu, and P. Olson (2003), Experiments on convection in Earth's core tangent cylinder, *Earth Planet. Sci. Lett.*, *212*, 119–134.
Bloxham, J. (1986), The expulsion of magnetic flux from the Earth's core, *Geophys. J. R. Astron. Soc.*, *87*, 669–678.
Bloxham, J., and D. Gubbins (1985), The secular variation of the Earth's magnetic field, *Nature*, *325*, 511–513.
Bloxham, J., and A. Jackson (1992), Time-dependent mapping of the magnetic field at the core-mantle boundary, *J. Geophys. Res*, *97*, 19,537–19,563.
Bullard, E. C., C. Freedman, H. Gellman, and J. Nixon (1950), The westward drift of the Earth's magnetic field, *Philos. Trans. R. Soc. London, Ser. A*, *243*, 67–92.
Busse, F. (1970), Thermal instabilities in rapidly rotating systems, *J. Fluid Mech.*, *44*, 441–460.
Chulliat, A., and N. Olsen (2010), Observation of magnetic diffusion in the Earth's outer core from Magsat, Ørsted and CHAMP data, *J. Geophys. Res.*, *115*, B05105, doi:10.1029/2009JB006994.
Dormy, E., J. Valet, and V. Courtillot (2000), Numerical models of the geodynamo and observational constrains, *Geochem. Geophys. Geosyst.*, *1*, 1037, doi:10.1029/2000GC000062.
Dumberry, M., and C. Finlay (2007), Eastward and westward drift of the Earth's magnetic field for the last three millennia, *Earth Planet. Sci. Lett.*, *254*, 146–157.
Finlay, C. (2008), Historical variation of the geomagnetic axial dipole, *Phys. Earth Planet. Inter.*, *170*, 1–14.
Finlay, C., and A. Jackson (2003), Equatorially dominated magnetic field change at the surface of Earth's core, *Science*, *300*, 2084–2086.
Gubbins, D. (1987), Mechanism for geomagnetic polarity reversals, *Nature*, *326*, 167–169.
Gubbins, D., A. Jones, and C. Finlay (2006), Fall in Earth's magnetic field is erratic, *Science*, *312*, 900–902.
Holme, R., and N. Olsen (2006), Core surface flow modelling from high-resolution secular variation, *Geophys. J. Int.*, *166*, 518–528.
Hulot, G., C. Eymin, B. Langlais, M. Mandea, and N. Olsen (2002), Small-scale structure of the geodynamo inferred from Ørsted and Magsat satellite data, *Nature*, *416*, 620–623.
Hulot, G., C. Finlay, C. Constable, N. Olsen, and M. Mandea (2010), The magnetic field of planet Earth, *Space Sci. Rev.*, *152*, 159–222, doi:10.1007/s11214-010-9644-0.
Jackson, A., A. Jonkers, and M. Walker (2000), Four centuries of geomagnetic secular variation from historical records, *Philos. Trans. R. Soc. London, Ser. A*, *358*, 957–990.
Jonkers, A., A. Jackson, and A. Murray (2003), Four centuries of geomagnetic data from historical records, *Rev. Geophys.*, *41*(2), 1006, doi:10.1029/2002RG000115.
Korte, M., and C. Constable (2011), Improving geomagnetic field reconstructions for 0–3 ka, *Phys. Earth Planet. Inter.*, *188*(3–4), 247–259.
Korte, M., and R. Holme (2010), On the persistence of geomagnetic flux lobes in global field models, *Phys. Earth Planet. Inter.*, *182*, 179–186.
Korte, M., F. Donadini, and C. Constable (2009), The geomagnetic field for 0–3 ka: 2. A new series of time-varying global models, *J. Geophys. Res.*, *10*, Q06008, doi:10.1029/2008GC002297.
Lowes, F. (1974), Spatial power spectrum of the main magnetic field, *Geophys. J. R. Astron. Soc.*, *36*, 717–730.
Moffatt, H. (1978), *Magnetic Field Generation in Electrically Conducting Fluids*, Cambridge Univ. Press, Cambridge, U. K.
Olsen, N., H. Luehr, T. J. Sabaka, I. Michaelis, J. Rauberg, and L. Tøffner-Clausen (2010), CHAOS-4—A high-resolution geomagnetic field model derived from low-altitude CHAMP data, Abstract GP21A–0992 presented at 2010 AGU Fall Meeting.
Olson, P., and H. Amit (2006), Changes in Earth's dipole, *Naturwissenschaften*, *93*, 519–542.
Olson, P., and U. Christensen (2002), The time averaged magnetic field in numerical dynamos with nonuniform boundary heat flow, *Geophys. J. Int.*, *151*, 809–823.
Olson, P., U. Christensen, and G. Glatzmaier (1999), Numerical modeling of the geodynamo: Mechanisms of field generation and equilibration, *J. Geophys. Res.*, *104*, 10,383–11,0404.

Journal of Geophysical Research: Solid Earth 10.1002/2014JB011742

Olson, P., I. Sumita, and J. Aurnou (2002), Diffusive magnetic images of upwelling patterns in the core, *J. Geophys. Res.*, *107*(B12), 2348, doi:10.1029/2001JB000384.
Wardinski, I., and M. Korte (2008), The evolution of the core-surface flow over the last seven thousands years, *J. Geophys. Res.*, *113*, B05101, doi:10.1029/2007JB005024.
Yukutake, T. (1967), The westward drift of the Earth's magnetic field in historic times, *J. Geomagn. Geoelec.*, *19*, 93–96.

Peña *et al. Earth, Planets and Space* (2016) 68:78
DOI 10.1186/s40623-016-0453-x

Earth, Planets and Space

FULL PAPER Open Access

Magnetic field stretching at the top of the shell of numerical dynamos

Diego Peña[1*], Hagay Amit[2] and Katia J. Pinheiro[1,2]

Abstract

The process of magnetic field stretching transfers kinetic energy to magnetic energy and by that maintains dynamos against Ohmic dissipation. Stretching at the top of the outer core may play an important role at specific regions. High-latitude intense magnetic flux patches may be concentrated by flow convergence. Reversed flux patches may emerge due to expulsion of toroidal field advected to the core–mantle boundary by fluid upwelling. Here we analyze snapshots from self-consistent 3D numerical dynamos to unravel the nature of field–flow interactions that induces stretching secular variation at the top of the core. We find that stretching at the top of the shell has a significant influence on the secular variation despite the relatively weak poloidal flow. In addition, locally stretching is often more effective than advection in particular at regions of significant field-aligned flow. Magnetic flux patches are concentrated by fluid downwelling and dispersed by fluid upwelling. Stretching is more efficient than advection in intensifying magnetic flux patches. Both stretching and the poloidal flow mostly depend on the magnetic Prandtl number *Pm*. Decreasing *Pm* gives smaller poloidal flow but stronger stretching. Accounting for field–flow interactions in both the advection and stretching terms suggests that the magnetic Reynolds number overestimates the actual ratio of magnetic advection to diffusion by ∼50 %. Morphological resemblance between local stretching in our dynamo models and local observed geomagnetic secular variation may suggest the presence of stretching at the top of the Earth's core. Our results shed light on the kinematic origin of intense geomagnetic flux patches and may have implications to the convective state of the upper outer core.

Introduction

The geomagnetic field is generated by convective motions of an electrically conductive fluid in Earth's rapidly rotating liquid outer core. The field is measured by surface magnetic observatories and dedicated satellites. Geomagnetic measurements are inverted for spherical harmonic models which can be downward continued to the top of the region of field generation, i.e., the core–mantle boundary (CMB). Temporal changes in the geomagnetic field termed secular variation (SV) provide vital insight into the fluid dynamics and dynamo action at the top of the core. Indeed, geomagnetic field and SV models (e.g., Jackson et al. 2000; Olsen and Mandea 2008) have been used as constraints on numerical dynamo simulations (e.g., Christensen et al. 1998, 2010; Aubert et al. 2013) or to infer various aspects of Earth's core dynamics (e.g., Finlay and Jackson 2003), in particular the fluid flow just below the CMB (for a review, see Holme 2007).

According to dynamo theory, the SV is comprised of magnetic advection, stretching and diffusion. Magnetic field advection transfers magnetic energy from one degree to another, whereas magnetic field stretching transfers kinetic energy to magnetic energy and by that maintains dynamos against Ohmic dissipation (e.g., Moffatt 1978; Mininni 2011). Therefore, magnetic field stretching is responsible for dynamo action. Better understanding of the field–flow interactions that yield magnetic field stretching is therefore fundamental for dynamo theory. Of course dynamo action might not necessarily occur at the entire outer core. For example, the dynamo may be deep seated due to stable stratification at the top of core, as was argued for Mercury (Christensen 2006) and for the Earth (Pozzo et al. 2012; Gubbins and Davies 2013). Here, however, we focus on the CMB,

*Correspondence: dpena@on.br
[1] Geophysics Department, Observatório Nacional, CEP: 20921-400 Rio de Janeiro, Brazil
Full list of author information is available at the end of the article

for comparison with geomagnetic field and SV models inferred from observations.

Fluid dynamics systems are often characterized by non-dimensional numbers. These numbers give valuable physical intuition concerning the relative importance of different processes in the system, for example the dominant force acting on the fluid and the role of turbulence. However, calculations of dynamo-related non-dimensional numbers using typical scales and ignoring field–flow interactions might provide non-representative values. Finlay and Amit (2011) calculated various alternative magnetic Reynolds numbers *Rm* that took into account different length scales of core dynamics. They extrapolated SV spectra to obtain an advective length scale; inferences from numerical dynamos (Amit and Christensen 2008) and from expansion of reversed flux patches (Chulliat and Olsen 2010) were used to infer a diffusive length scale. Finlay and Amit (2011) focused on magnetic field advection and ignored magnetic field stretching. It is important to re-evaluate non-dimensional numbers in order to better understand core dynamics in light of field–flow interactions and accounting for magnetic stretching effects.

Global criteria for characterizing the observed geomagnetic field (Christensen et al. 2010) are practical because the field spectrum is decreasing with degree (most energy at largest scale, i.e., dipole). In contrast, the geomagnetic SV spectrum is increasing with degree, which is a problem for global characterization. Some SV features like westward drift (Finlay and Jackson 2003) or Pacific/Atlantic dichotomy (Christensen and Olson 2003) could be related to external forcings such as gravitational coupling between the inner core and the mantle (Aubert et al. 2013) or core–mantle thermal interactions (Holme et al. 2011) rather than core convection itself. Alternatively, geomagnetic SV may be locally studied. Robust geomagnetic field features such as intense normal and reversed flux patches have a particular signature on the SV. Local analysis of field–flow interactions may provide a detailed interpretation of the SV in the vicinity of these robust field features.

Stretching may play an important role in specific regions of the CMB, such as high-latitude intense geomagnetic flux patches. These robust non-axisymmetric features typically reside near the edge of the inner core tangent cylinder (Jackson et al. 2000), possibly due to flow convergence at these latitudes (Olson et al. 1999). In rapidly rotating numerical dynamo models surface convergence is correlated with columnar cyclones (Olson et al. 2002; Amit et al. 2007), so the flow near these patches has a large field-aligned component and produces little magnetic advection (Finlay and Amit 2011). Regardless of whether the locations of downwellings are directly related to a thermal mantle anomaly (Gubbins 2003) or to the chaotic time-dependent buoyancy at the top of the core, the kinematic relation between concentrated magnetic flux and fluid downwelling is expected from the stretching term in the radial magnetic induction equation.

Magnetic field stretching may also be the underlying mechanism for regions of weak field intensity at Earth's surface. Striking deviations of the geomagnetic field from axial dipolarity appear in the form of reversed flux patches, i.e., regions on the CMB where the sign of the radial field is opposite to that of the axial dipole field. In the past century, the most intense and extensive reversed flux patches have been growing and intensifying at the southern Atlantic of the CMB (e.g., Jackson et al. 2000; Olsen et al. 2014). At Earth's surface these structures are expressed as a notably low-intensity zone termed the South Atlantic Magnetic Anomaly (Hartmann and Pacca 2009). The field intensity at this region is at present decreasing at rates of up to 12 % over the past 30 years (Finlay et al. 2010), much faster than the decline of the geomagnetic dipole moment (Olson and Amit 2006; Finlay 2008). It has been proposed that reversed flux patches emerge due to expulsion of toroidal field (Bloxham 1986) which is transported to the CMB by fluid upwelling (e.g., Aubert et al. 2008a).

It is under debate whether any stretching effects prevail at the top of Earth's core. Seismic studies (Helffrich and Kaneshima 2010) and revised estimates of large core thermal conductivity from mineral physics calculations (Pozzo et al. 2012; Koker et al. 2012) suggest that the top of the core is stably stratified (Gubbins and Davies 2013). This may indicate that the flow just below the CMB is purely toroidal and no stretching SV is present there, although the radial flow may penetrate a stably stratified layer, e.g., if the convection columns are large enough (Takehiro and Lister 2001) or in the presence of certain waves (Buffett 2014). Low geomagnetic SV at special points where the radial field gradient is zero also supports stable stratification (Whaler 1980), but uncertainty in their exact locations renders such an interpretation questionable (Whaler and Holme 2007). In contrast, Zhang et al. (2015) claimed that the thermal conductivity is as low as previously estimated and thus the whole of the outer core convects. Regional interpretations of the geomagnetic SV also favor some local upwelling/downwelling (Olson and Aurnou 1999; Chulliat et al. 2010; Amit 2014).

Global core flow models inverted from the geomagnetic SV can be constructed with and without poloidal flow (Holme 2007). Based on various theoretical arguments, most models assume some relation between the toroidal and poloidal flows. In particular, quasi-geostrophic

models rely on poloidal flow to project CMB flows to the volume of the core (Pais and Jault 2008; Gillet et al. 2009). Lesur et al. (2015) inverted geomagnetic data simultaneously for the field and the core flow. When a purely toroidal flow was incorporated in the inversion the data could not be adequately fitted, in contradiction to upper core stratification. However, inclusion of weak poloidal flow was sufficient to explain the SV. Lesur et al. (2015) concluded that the upper core is weakly stratified.

In this paper, we analyze output from self-consistent 3D numerical dynamos to unravel the nature of field–flow interactions and the contribution of magnetic field stretching to the SV at the top of the spherical shell. Analytical and statistical tools are designed to quantify these kinematic processes. We zoom-in to specific regions on the outer boundary to explore the kinematic origins of intense normal and reversed magnetic flux patches. The dependence of the results on the dynamo control parameters is explored. The results are discussed in the context of geomagnetic field and SV models.

Methods

Numerical dynamo models

Fluid motions in Earth's outer core are governed by the magnetohydrodynamics equations: Navier–Stokes, magnetic induction, conservation of energy and mass (continuity for an incompressible fluid). In non-dimensional form these equations can be written (e.g., Olson et al. 1999) as follows:

$$E\left(\frac{\partial \vec{u}}{\partial t}+\vec{u}\cdot\nabla\vec{u}-\nabla^2\vec{u}\right)+2\hat{z}\times\vec{u}+\nabla P = Ra\frac{\vec{r}}{r_o}T+\frac{1}{Pm}\left(\nabla\times\vec{B}\right)\times\vec{B} \quad (1)$$

$$\frac{\partial \vec{B}}{\partial t}=\nabla\times(\vec{u}\times\vec{B})+\frac{1}{Pm}\nabla^2\vec{B} \quad (2)$$

$$\frac{\partial T}{\partial t}+\vec{u}\cdot\nabla T=\frac{1}{Pr}\nabla^2 T+\epsilon \quad (3)$$

$$\nabla\cdot\vec{u}=0 \quad (4)$$

$$\nabla\cdot\vec{B}=0 \quad (5)$$

where $\vec{u}$ is the fluid velocity, $\vec{B}$ is the magnetic field, T is temperature (or more generally co-density), t is time, $\hat{z}$ is a unit vector in the direction of the rotation axis, P is pressure, $\vec{r}$ is the position vector, r_o is the core radius, and ϵ is heat (or buoyancy) source or sink. The magnetic field changes in time [first term in (2)] due to its generation by the fluid flow [second term in (2)] and its destruction (or magnetic diffusion) due to the finite electrical conductivity of the outer core fluid [third term in (2)]. In return the flow varies in time [first term in (1)] due to all the forces acting on it, including the magnetic Lorentz force [last term in (1)].

Four non-dimensional parameters in (1)–(3) control the dynamo action. The heat flux Rayleigh number (Olson and Christensen 2002) represents the strength of buoyancy force driving the convection relative to retarding forces

$$Ra=\frac{\alpha g_o q_o D^4}{k\kappa\nu} \quad (6)$$

where α is thermal expansivity, g_o is gravitational acceleration on the outer boundary at radius r_o, q_o is the mean heat flux across the outer boundary, D is shell thickness, k is thermal conductivity, κ is thermal diffusivity, and ν is kinematic viscosity. The Ekman number represents the ratio of viscous and Coriolis forces

$$E=\frac{\nu}{\Omega D^2} \quad (7)$$

where Ω is the rotation rate. The Prandtl number is the ratio of kinematic viscosity to thermal diffusivity

$$Pr=\frac{\nu}{\kappa} \quad (8)$$

and the magnetic Prandtl number is the ratio of kinematic viscosity to magnetic diffusivity λ

$$Pm=\frac{\nu}{\lambda} \quad (9)$$

The condition for dynamo action is that the magnetic field generation term will sufficiently exceed the diffusion term in (2). The scaled ratio between these two terms is given by the magnetic Reynolds number

$$Rm=\frac{UD}{\lambda} \quad (10)$$

where U is a typical velocity scale.

Numerical dynamos provide self-consistent solutions to the full set of Eqs. (1)–(5) in a spherical shell (Christensen and Wicht 2007). We used the numerical implementation MagIC (Wicht 2002). Due to computational limitations, dynamo simulations use control parameters very far from Earth-like conditions, and therefore, relating the results to the real core conditions is challenging. Our chosen control parameters (Table 1) are even more moderate than what modern computers are capable of. The reason is that smaller E values produce such small-scale structures that the local relations between the field and the flow would become difficult to interpret. We

Table 1 Dynamo models control parameters

Model	*Ra*	*E*	*Pm*	*Rm*	r_e/r_o	$\bar{\delta\tau}$
1	2×10^5	1×10^{-3}	5	137	0.966	14.75
2	2×10^5	1×10^{-3}	10	255	0.966	11.9
3	4×10^5	1×10^{-3}	5	219	0.966	33.07
4	5×10^5	3×10^{-4}	3	82	0.983	22.51
5	1×10^6	3×10^{-4}	3	125	0.983	14.60
6	3×10^6	3×10^{-4}	3	234	0.983	78.98
7	1×10^7	1×10^{-4}	1.3	126	0.989	9.42
8	1×10^7	1×10^{-4}	2	218	0.989	5.50
9	3×10^7	1×10^{-4}	2	446	0.989	16.66

The Rayleigh number is *Ra*, the Ekman number is *E* and the magnetic Prandtl number is *Pm*. For all models we set the Prandtl number as $Pr = 1$. The magnetic Reynolds number *Rm* is calculated based on the total kinetic energy in the shell, r_e denotes the radial level at which the simulations were analyzed, and $\bar{\delta\tau}$ denotes the average time difference between successive snapshots in units of magnetic advection time

focus on dynamos in the non-reversing dipole-dominated regime (e.g., Kutzner and Christensen 2002; Christensen and Aubert 2006).

The shell geometry is identical to Earth's core with an inner to outer boundary radii ratio of 0.35. The inner and outer boundaries of the shell are set to be insulating and rigid. To simulate generic thermochemical convection (e.g., Aubert et al. 2008b), on the inner core boundary fixed co-density is set, on the outer boundary fixed heat flux is prescribed, and the source/sink term in (3) is set to $\epsilon = 0$. The number of radial grid points N_r is chosen to accommodate at least five grid points across the Ekman boundary layer. In our models, N_r varies from 49 for the larger $E = 1 \times 10^{-3}$ cases to 61 for the lower $E = 1 \times 10^{-4}$ cases. Horizontal resolution is also increased with decreasing Ekman number, from maximum degree and order $\ell_{\max} = 64$ for the $E = 1 \times 10^{-3}$ cases to $\ell_{\max} = 96$ for the $E = 1 \times 10^{-4}$ cases.

It is of particular interest to examine the radial component of the induction equation just below the outer boundary, because only the radial component of the geomagnetic field at the CMB is accessible from observations. The radial component of (2) at the top of the shell where the radial velocity vanishes is

$$\frac{\partial B_r}{\partial t} + \vec{u}_h \cdot \nabla B_r + B_r \nabla_h \cdot \vec{u}_h = \frac{1}{Pm}\left(\frac{1}{r_o^2}\frac{\partial^2}{\partial r^2}\left(r^2 B_r\right) + \nabla_h^2 B_r\right) \tag{11}$$

where B_r is the radial field, $\vec{u}_h$ is the 2D velocity vector tangent to the spherical surface, $\nabla_h = \nabla - \frac{\partial}{\partial r}$, and r is the radial coordinate. The first term in (11) is the SV, the second term represents magnetic field advection, the third term represents magnetic field stretching, and the term on the right-hand side denotes magnetic diffusion.

The frozen-flux theory (Roberts and Scott 1965) assumes that the majority of SV on short timescales and large length scales is produced by the advection and stretching action due to the velocity field rather than diffusion of the magnetic field. Based on the observed SV and inferences from mineral physics experiments Rm $\sim$ 500 in Earth's outer core (e.g., Bloxham and Jackson 1991), supporting the frozen-flux hypothesis. Under this assumption (11) simplifies to

$$\frac{\partial B_r}{\partial t} = -\vec{u}_h \cdot \nabla B_r - B_r \nabla_h \cdot \vec{u}_h \tag{12}$$

This equation is the common starting point for modeling the flow at the core surface (e.g., Holme 2007). It is termed the frozen-flux induction equation, because accordingly magnetic field lines are simply carried by the flow.

The radial magnetic field B_r and the tangential velocity $\vec{u}_h$ were taken at the top of the free stream (just below the Ekman boundary layer) to analyze the different terms of the radial induction equation. Note that in the dynamo models at the top of the free stream the radial velocity is more than an order of magnitude smaller than the tangential velocity hence (11) holds. In order to obtain statistics of the dynamical characteristics of the simulations, for each dynamo model ten snapshots were taken at arbitrary times enough separated so that their structures are non-correlated. Overall, 90 snapshots were globally analyzed, of which more than 350 zoom-ins to local regions of intense magnetic flux patches were selected.

Statistical measures

We calculate several statistical properties to analyze the results, including global and local RMS ratios ($\|X\|/\|Y\|$) and spatial correlations corr(X, Y) between X and Y. The RMS $\|X\|$ is obtained by integration of X over the

spherical surface at the top of the free stream. We compute the ratio of RMS stretching to RMS advection St/Ad as well as the ratio of RMS poloidal flow to RMS toroidal flow $\mathcal{P}/\mathcal{T}$. We also calculate the spatial correlation coefficient between tangential divergence $\delta_h \equiv \nabla_h \cdot \vec{u}_h$ and plus/minus radial vorticity $\omega_r \equiv \hat{r}\cdot\nabla \times \vec{u}$ (where $\hat{r}$ is the radial unit vector) in the Northern/Southern Hemisphere, respectively, termed helical flow by Amit and Olson (2004)

$$H_u = \begin{cases} \mathrm{corr}(\delta_h, -\omega_r) & \theta < \pi/2 \\ \mathrm{corr}(\delta_h, \omega_r) & \theta > \pi/2 \end{cases} \tag{13}$$

where θ is co-latitude. The correlation coefficient between the absolute radial field and downwelling is $\mathrm{corr}(|B_r|, \delta_h^-)$ with δ_h^- defined by

$$\delta_h^- = \begin{cases} \delta_h & \delta_h < 0 \\ 0 & \delta_h > 0 \end{cases} \tag{14}$$

Likewise, the correlation coefficient between absolute radial field and upwelling is $\mathrm{corr}(|B_r|, \delta_h^+)$ with δ_h^+ defined by

$$\delta_h^+ = \begin{cases} 0 & \delta_h < 0 \\ \delta_h & \delta_h > 0 \end{cases} \tag{15}$$

Local analyses are classified by polarity, i.e., normal or reversed, and by latitude. High latitudes are arbitrarily defined by patches that are centered at higher than 45° latitude. Classified this way, four types of patches are possible: normal polarity at high latitudes (HN), normal polarity at low latitudes (LN), reversed polarity at high latitudes (HR) and reversed polarity at low latitudes (LR). In addition, normalized integrated values allow evaluation of level of cancellation in a given region

$$\xi_f = \left| \frac{\int_S f \, \mathrm{d}S}{\int_S |f| \, \mathrm{d}S} \right| \tag{16}$$

where f is the studied quantity in a region S and $\mathrm{d}S = r^2 \sin\theta \mathrm{d}\phi \mathrm{d}\theta$ is a spherical surface increment. If all advection has the same sign in a region then $\xi_\mathrm{a} = 1$, whereas if the advection has alternating signs of equal amount then $\xi_\mathrm{a} = 0$. The same type of interpretation holds for the stretching efficiency ξ_s. In order to test whether the stretching intensifies or weakens the magnetic flux, the normalized integrated value of their product is evaluated:

$$\xi_\mathrm{e} = \frac{\int_S B_r^2 \nabla_h \cdot \vec{u}_h \, \mathrm{d}S}{\int_S |B_r^2 \nabla_h \cdot \vec{u}_h| \, \mathrm{d}S} \tag{17}$$

If the stretching SV and B_r have the same sign (i.e., field intensification by stretching) then $\xi_\mathrm{e} > 0$, whereas if $\xi_\mathrm{e} < 0$ then stretching has an opposite sign to B_r and it therefore locally weakens the field.

Next we estimate an effective magnetic Reynolds number that accounts for field–flow interactions. For the advective part, following Finlay and Amit (2011) we calculate the angle γ between the vectors $\vec{u}_h$ and $\nabla_h B_r$ so that $(\pi/2 - \gamma)$ is the angle between a B_r-contour and the core surface flow $\vec{u}_h$. The level of field-aligned flow is represented by

$$\cos\gamma = \frac{\vec{u}_h \cdot \nabla_h B_r}{|\vec{u}_h||\nabla_h B_r|} \tag{18}$$

If the field and the flow are perfectly aligned then $\gamma = \pi/2$ and advection is zero, whereas if the flow is perpendicular to B_r-contours then $\gamma = 0$ and advection efficiency is optimal. Accordingly, the effective advective magnetic Reynolds number Rm_a is then

$$Rm_\mathrm{a} = Rm \cdot \cos\gamma \tag{19}$$

The effective stretching magnetic Reynolds number Rm_s is simply

$$Rm_\mathrm{s} = Rm_\mathrm{a} \cdot \mathrm{St/Ad} \tag{20}$$

In order to combine Rm_a and Rm_s the correlation between the two SV contributions should be accounted for. We therefore compute the interaction between the two terms by

$$\xi_{Rm} = \frac{||\,\mathrm{Ad} + \mathrm{St}||}{||\mathrm{Ad}|| + ||\mathrm{St}||} \tag{21}$$

If St and Ad are correlated then $\xi_{Rm} = 1$. If St and Ad are non-correlated then $\xi_{Rm} = \sqrt{1+c^2}/(1+c)$ where c is their amplitude ratio. In this case a minimum of $\xi_{Rm} = \sqrt{2}/2$ is obtained for $c = 1$ (i.e., equal advection and stretching amplitudes). Finally, if St and Ad are anti-correlated then $\xi_{Rm} = |-1+c|/(1+c)$. In this case for $c = 1$ $\xi_{Rm} = 0$, i.e., advection and stretching cancel each other to yield zero inductive SV. The effective magnetic Reynolds number is then given by

$$Rm_\mathrm{e} = (Rm_\mathrm{a} + Rm_\mathrm{s})\xi_{Rm} \tag{22}$$

To get some intuition to the quantities $\cos\gamma$ and ξ_{Rm} we report their values for some large-scale synthetic cases. For the radial field, we use a dipole with present-day Earth-like tilt (Olsen et al. 2014) and for the flow we use large-scale degree-1 toroidal and poloidal flows (Table 2). Obviously for the toroidal flows stretching is zero and $\xi_{Rm} = 1$. Because the dipole field is dominantly axial, the most effective advection scenario (i.e., largest $\cos\gamma$) occurs when the flow is oriented north-south ($\mathcal{P}_1^0$). Overall the two quantities $\cos\gamma$ and ξ_{Rm} are clearly distinctive with either one larger for different cases.

Table 2 Field–flow interferences in synthetic cases

Flow	cos γ	ξ_{Rm}
$\mathcal{T}_1^0$	0.65	1.00
$\mathcal{T}_1^1$	0.64	1.00
$\mathcal{P}_1^0$	0.76	0.65
$\mathcal{P}_1^1$	0.61	0.74

$\mathcal{T}_1$ and $\mathcal{P}_1$ are large-scale degree-1 toroidal and poloidal synthetic flows. cos γ is the field–flow alignment factor and ξ_{Rm} is the advection/stretching interference factor

Finally, we examine the dependence of the statistical quantities on the non-dimensional control parameters of the dynamo models. Each quantity (St/Ad, $\mathcal{P}/\mathcal{T}$, H_u, etc.) may be expressed as a generic power law:

$$f = C \cdot E^a \cdot Ra^b \cdot Pm^c \tag{23}$$

where f is the statistical quantity and C, a, b, c are fitting coefficients. The relative misfit σ_r of the power law is given by

$$\sigma_r = \sqrt{\frac{\sum_{i=1}^{n}(f_i^{\mathrm{dyn}} - f_i)^2}{\sum_{i=1}^{n}(f_i^{\mathrm{dyn}})^2}} \tag{24}$$

where f^{dyn} is the statistical quantity obtained from the dynamo models and n is the number of dynamo models analyzed. Relative misfits larger than an arbitrary threshold value of 0.07 were considered inadequate, and in these cases, the fits were not interpreted.

The power law fits (23) obtained by the misfit minimization (24) are applied to time-average statistical quantities. The time-dependence is expressed by the standard deviation (Tables 3, 4). Note that the standard deviation was not used to assess the fits.

This paper contains many variables. While some are conventional, others were introduced to denote newly defined properties. For clarity we list in the "Appendix" all the variables used in this paper.

Results

Kinematics of intense magnetic flux patches

Figure 1 shows an arbitrary snapshot from dynamo model 4. As in all models considered in this study, the radial magnetic field on the outer boundary exhibits axial dipole dominance (Fig. 1a). The tangential divergence δ_h is highly correlated with the radial vorticity ω_r in the Southern Hemisphere and highly anti-correlated in the Northern Hemisphere (Fig. 1c, d). The toroidal flow dominates over the poloidal flow at the top of the free stream ($\mathcal{P}/\mathcal{T} < 1$). Nevertheless globally, the stretching contribution to the frozen-flux SV is larger than that of advection (Fig. 1e, f). Intense magnetic flux patches present positive and negative correlations with downwelling and upwelling structures, respectively. Because our dynamo models are dominated by the axial dipole, most of the intense flux patches are obviously of normal polarity at high latitudes (HN) and only a few are normal (LN) and reversed (LR) at low latitudes. The flux patches are rather large scale and are significantly more intense than their surroundings.

Figure 2 shows a typical intense high-latitude normal polarity (HN) magnetic flux patch (see upper polygon in Fig. 1a). This patch is located close to the center of an anti-clockwise vortex (Fig. 2a, c) that is highly correlated with a downwelling structure (Fig. 2d). The flow in this region is predominately toroidal. The main part of the flow is aligned with the B_r-contours (Fig. 2a), causing non-efficient advection (Fig. 2e). In contrast, the high correlation between the magnetic flux patch and the downwelling structure produces a strong stretching SV (Fig. 2f) that locally intensifies the magnetic field with an efficiency of $\xi_e = 0.94$. Consequently, the local stretching SV is remarkably twice larger than advective SV.

Another HN (lower polygon in Fig. 1a) is located west of a strong southward flow (Fig. 3a). This flow system produces an intense advective SV at the eastern part of the patch. In the western part, the flow and hence the advection are weak. Despite the relatively weak poloidal flow, the downwelling structure shown in Fig. 3d produces intense stretching SV (Fig. 3f). In this patch, the stretching SV is only slightly larger than advective SV, but it is still able to locally intensify the magnetic field with an efficiency of $\xi_e = 0.87$.

Overall we found three types of intense magnetic flux patches (out of the four possible types): Most of them are high-latitude normal polarity flux patches (HN), whereas a smaller number are low-latitude normal polarity (LN) and low-latitude reversed polarity (LR). Reversed flux patches at high latitudes (RH) are rare. The same holds for all the dynamo models examined here. From hereafter we therefore report local analyses of HN, LN and LR only.

Next we examine a dynamo model with a larger Ra, and otherwise all parameters unchanged (Table 1). Figure 4 shows an arbitrary snapshot from dynamo model 6. As in model 4, the radial magnetic field has the characteristic axial dipolar dominance and the flow is predominantly toroidal. The global correlation of radial vorticity and tangential divergence is again high. Intense magnetic flux patches are positively correlated with downwelling structures and negatively with upwelling structures. However, the field and flow features are smaller scale and advection is globally stronger than stretching.

Table 3 Global statistics

Model	St/Ad	$\mathcal{P}/\mathcal{T}$	H_u	corr($\lvert B_r\rvert, \delta_h^-$)	corr($\lvert B_r\rvert, \delta_h^+$)	HN	LN	LR
1	0.56 ± 0.04	0.43 ± 0.03	0.84 ± 0.04	0.30 ± 0.05	-0.11 ± 0.02	40	1	10
2	0.48 ± 0.06	0.47 ± 0.03	0.78 ± 0.03	0.27 ± 0.04	-0.08 ± 0.03	48	5	19
3	0.62 ± 0.15	0.41 ± 0.01	0.84 ± 0.01	0.31 ± 0.05	-0.08 ± 0.02	28	0	5
4	0.93 ± 0.15	0.40 ± 0.03	0.88 ± 0.03	0.37 ± 0.09	-0.15 ± 0.04	29	4	3
5	0.76 ± 0.10	0.39 ± 0.02	0.87 ± 0.02	0.30 ± 0.05	-0.14 ± 0.03	25	2	1
6	0.68 ± 0.10	0.41 ± 0.03	0.85 ± 0.02	0.37 ± 0.02	-0.13 ± 0.02	31	3	6
7	0.95 ± 0.12	0.33 ± 0.01	0.87 ± 0.01	0.29 ± 0.04	-0.15 ± 0.02	21	3	3
8	0.71 ± 0.08	0.34 ± 0.02	0.84 ± 0.03	0.28 ± 0.05	-0.13 ± 0.01	29	0	2
9	0.65 ± 0.05	0.36 ± 0.01	0.80 ± 0.02	0.42 ± 0.03	-0.13 ± 0.01	26	8	6

Dynamo models time-average and standard deviation values. St/Ad is stretching/advection RMS ratio, and $\mathcal{P}/\mathcal{T}$ is poloidal/toroidal flow RMS ratio. H_u is the helical flow correlation (13), corr($\lvert B_r\rvert, \delta_h^-$) and corr($\lvert B_r\rvert, \delta_h^+$) are the correlations between the absolute radial magnetic field and downwelling (14) and upwelling (15), respectively. Also, the number of analyzed magnetic flux patches of each type is given: high-latitude normal intense flux patches (HN), low-latitude normal intense flux patches (LN) and low-latitude reversed flux patches (LR)

Table 4 Local statistics

Model	Patch type	St/Ad	$\mathcal{P}/\mathcal{T}$	H_u	corr($\lvert B_r\rvert, \delta_h^-$)	corr($\lvert B_r\rvert, \delta_h^+$)	ξ_a	ξ_s	ξ_e
1	HN	0.69 ± 0.23	0.34 ± 0.05	0.91 ± 0.11	0.44 ± 0.19	-0.28 ± 0.08	0.44 ± 0.09	0.76 ± 0.09	0.92 ± 0.09
	LN	0.28 ± 0.00	0.60 ± 0.00	0.70 ± 0.00	0.38 ± 0.00	-0.34 ± 0.00	0.11 ± 0.00	0.31 ± 0.00	0.62 ± 0.00
	LR	0.48 ± 0.14	0.63 ± 0.11	0.79 ± 0.19	0.42 ± 0.17	-0.18 ± 0.13	0.07 ± 0.04	0.20 ± 0.06	0.68 ± 0.13
2	HN	0.55 ± 0.21	0.40 ± 0.07	0.83 ± 0.09	0.29 ± 0.19	-0.19 ± 0.09	0.28 ± 0.09	0.59 ± 0.18	0.77 ± 0.20
	LN	0.33 ± 0.10	0.59 ± 0.12	0.71 ± 0.23	0.43 ± 0.24	-0.17 ± 0.13	0.11 ± 0.06	0.38 ± 0.16	0.56 ± 0.22
	LR	0.43 ± 0.16	0.79 ± 0.14	0.59 ± 0.22	0.28 ± 0.22	-0.04 ± 0.19	0.11 ± 0.08	0.25 ± 0.13	0.62 ± 0.19
3	HN	0.60 ± 0.19	0.33 ± 0.05	0.91 ± 0.03	0.30 ± 0.18	-0.19 ± 0.11	0.24 ± 0.08	0.56 ± 0.16	0.87 ± 0.06
	LN	–	–	–	–	–	–	–	–
	LR	0.65 ± 0.27	0.61 ± 0.06	0.82 ± 0.09	0.60 ± 0.14	-0.20 ± 0.03	0.26 ± 0.08	0.52 ± 0.13	0.84 ± 0.09
4	HN	1.27 ± 0.51	0.32 ± 0.07	0.87 ± 0.20	0.71 ± 0.10	-0.39 ± 0.11	0.63 ± 0.13	0.61 ± 0.13	0.85 ± 0.09
	LN	1.10 ± 0.29	$0.39 \pm \pm 0.02$	0.91 ± 0.05	0.78 ± 0.03	-0.48 ± 0.08	0.58 ± 0.14	0.35 ± 0.09	0.57 ± 0.11
	LR	0.24 ± 0.01	0.69 ± 0.01	0.52 ± 0.06	-0.23 ± 0.06	0.14 ± 0.01	0.06 ± 0.00	0.28 ± 0.02	0.24 ± 0.01
5	HN	0.95 ± 0.30	0.32 ± 0.05	0.83 ± 0.14	0.54 ± 0.13	-0.35 ± 0.06	0.57 ± 0.14	0.75 ± 0.08	0.93 ± 0.04
	LN	0.43 ± 0.00	0.42 ± 0.00	0.91 ± 0.00	0.57 ± 0.00	-0.22 ± 0.00	0.47 ± 0.00	0.72 ± 0.00	0.94 ± 0.00
	LR	0.72 ± 0.00	0.86 ± 0.00	0.71 ± 0.00	0.49 ± 0.00	-0.23 ± 0.00	0.09 ± 0.00	0.16 ± 0.00	0.67 ± 0.00
6	HN	0.74 ± 0.15	0.34 ± 0.05	0.91 ± 0.04	0.40 ± 0.18	-0.27 ± 0.10	0.39 ± 0.07	0.69 ± 0.11	0.87 ± 0.10
	LN	0.69 ± 0.15	0.60 ± 0.07	0.91 ± 0.01	0.54 ± 0.18	-0.18 ± 0.00	0.12 ± 0.10	0.32 ± 0.26	0.82 ± 0.04
	LR	0.68 ± 0.13	0.73 ± 0.31	0.85 ± 0.06	0.54 ± 0.18	-0.19 ± 0.03	0.11 ± 0.06	0.17 ± 0.08	0.76 ± 0.09
7	HN	1.18 ± 0.28	0.28 ± 0.08	0.80 ± 0.15	0.54 ± 0.13	-0.30 ± 0.07	0.59 ± 0.09	0.62 ± 0.08	0.89 ± 0.06
	LN	0.81 ± 0.20	0.40 ± 0.01	0.91 ± 0.02	0.54 ± 0.16	-0.25 ± 0.12	0.55 ± 0.06	0.51 ± 0.05	0.74 ± 0.04
	LR	1.12 ± 0.12	0.58 ± 0.01	0.81 ± 0.04	0.48 ± 0.06	-0.09 ± 0.02	0.08 ± 0.06	0.04 ± 0.04	0.67 ± 0.05
8	HN	0.78 ± 0.20	0.27 ± 0.04	0.83 ± 0.12	0.45 ± 0.15	-0.30 ± 0.06	0.50 ± 0.12	0.68 ± 0.08	0.89 ± 0.06
	LN	–	–	–	–	–	–	–	–
	LR	0.93 ± 0.00	0.94 ± 0.00	0.60 ± 0.00	0.57 ± 0.00	-0.18 ± 0.00	0.14 ± 0.00	0.20 ± 0.00	0.63 ± 0.00
9	HN	0.68 ± 0.15	0.31 ± 0.06	0.81 ± 0.11	0.48 ± 0.18	-0.24 ± 0.07	0.32 ± 0.06	0.63 ± 0.07	0.84 ± 0.04
	LN	0.61 ± 0.13	0.45 ± 0.07	0.82 ± 0.04	0.51 ± 0.05	-0.23 ± 0.04	0.28 ± 0.05	0.54 ± 0.07	0.83 ± 0.02
	LR	0.85 ± 0.09	0.67 ± 0.17	0.70 ± 0.06	0.55 ± 0.19	-0.22 ± 0.07	0.20 ± 0.20	0.25 ± 0.25	0.88 ± 0.07
$\bar{x}$	HN	0.82	0.32	0.86	0.46	−0.28	0.44	0.65	0.90
	LN	0.61	0.49	0.84	0.53	−0.27	0.32	0.45	0.73
	LR	0.68	0.72	0.71	0.42	−0.13	0.13	0.23	0.66

Dynamo models time-average and standard deviation values for each patch type. RMS ratios, correlations and patch types are the same as in Table 3. ξ_a and ξ_s are the absolute normalized integrated values of advection and stretching SV, respectively, ξ_e is the normalized integrated value of the product of stretching SV and B_r. $\bar{x}$ denotes averages over all dynamo models

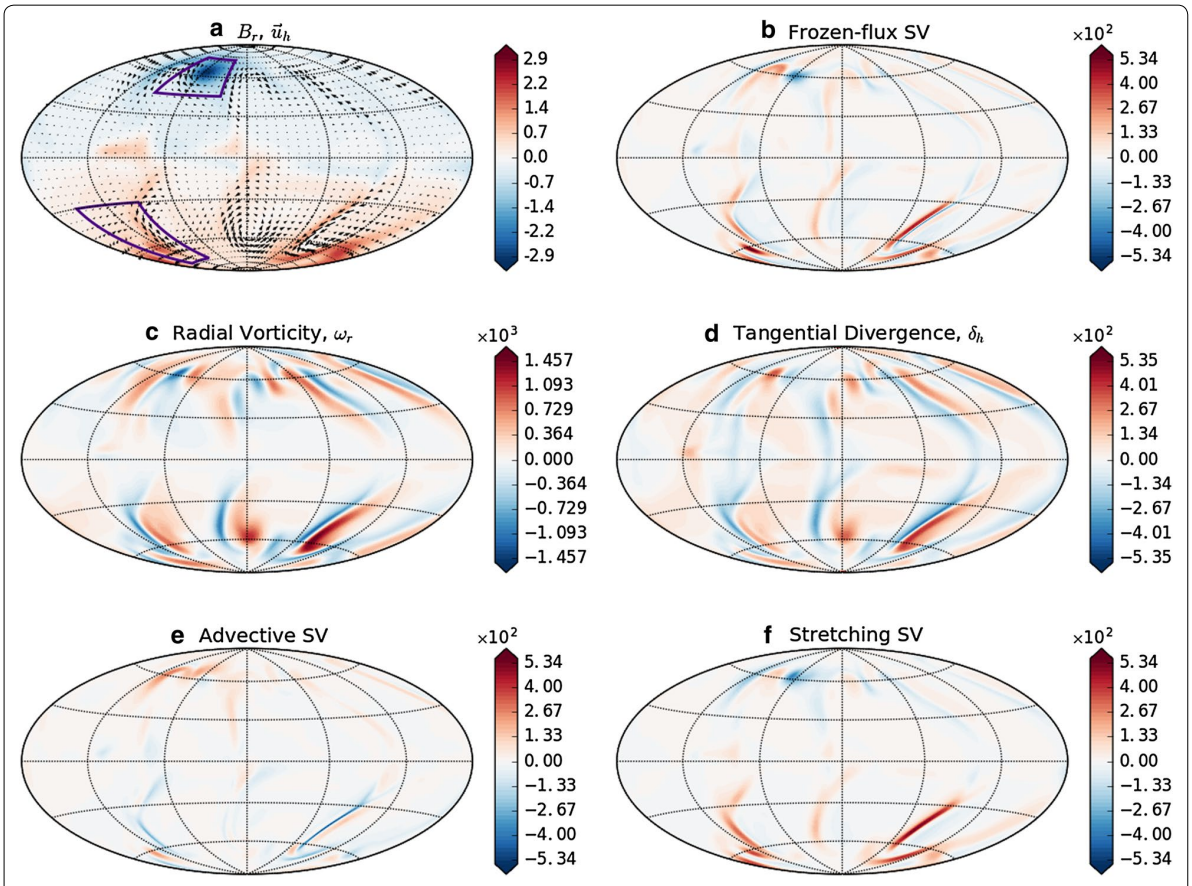

Fig. 1 Snapshot from dynamo model 4: **a** radial magnetic field B_r (*in colors*) and the tangential flow $\vec{u}_h$ (*black arrows*). The *upper* and *lower* polygons denote the zoom-in zones shown in Figs. 2 and 3, respectively. **b** The frozen-flux SV, **c** radial vorticity ω_r, **d** tangential divergence δ_h, **e** advective SV and **f** stretching SV. All plots are at a radial level just below the Ekman boundary layer (r_e in Table 1). All variables are non-dimensional. The global statistics for this snapshot are: St/Ad=1.18; $\mathcal{P}/\mathcal{T} = 0.36$; $H_u = 0.89$; $\mathrm{corr}(|B_r|, \delta_h^-) = 0.46$; $\mathrm{corr}(|B_r|, \delta_h^+) = -0.20$

Figure 5 shows an intense high-latitude normal polarity flux patch (lower polygon in Fig. 4a). This HN is at the center of a clockwise vortex correlated with a downwelling structure (Fig. 5c, d). A large part of the flow is field aligned, so advection is confined to a region close to the patch center (Fig. 5a, e). The interaction of the downwelling structure with the intense flux patch on the northern part produces a strong stretching structure (Fig. 5f), but some shift in the southern part leads to moderate St/Ad RMS ratio. The stretching and advective contributions to the SV are comparable despite the relatively weak poloidal flow.

Next we analyze an LR (upper polygon in Fig. 4a). The southward flow is roughly perpendicular to the B_r-contours (Fig. 6a), producing a strong advective SV (Fig. 6e). The downwelling structure in Fig. 6d is well correlated with this reversed flux patch, and hence the stretching structure shown in Fig. 6f also presents an important contribution to the SV. In contrast, stretching locally intensifies the magnetic field with a smaller efficiency than in the HN (Fig. 5). In addition, the poloidal flow is relatively larger than in HN.

Dynamo model 9 (Fig. 7) has lower E and larger Ra resulting in larger Rm (Table 1) and a more complex behavior. As in previous models, the flow is predominately toroidal and tangential divergence and radial vorticity correlation is high. However, the magnetic flux patches in this model are small scale and a larger number of them appear at low latitudes (Table 3). The main contribution to the SV is advective.

Figure 8 shows an HN (upper polygon in Fig. 7a) from dynamo model 9. This patch is at the center of an anti-clockwise vortex (Fig. 8a) related to a downwelling structure (Fig. 8d). Advection is effective at the peak

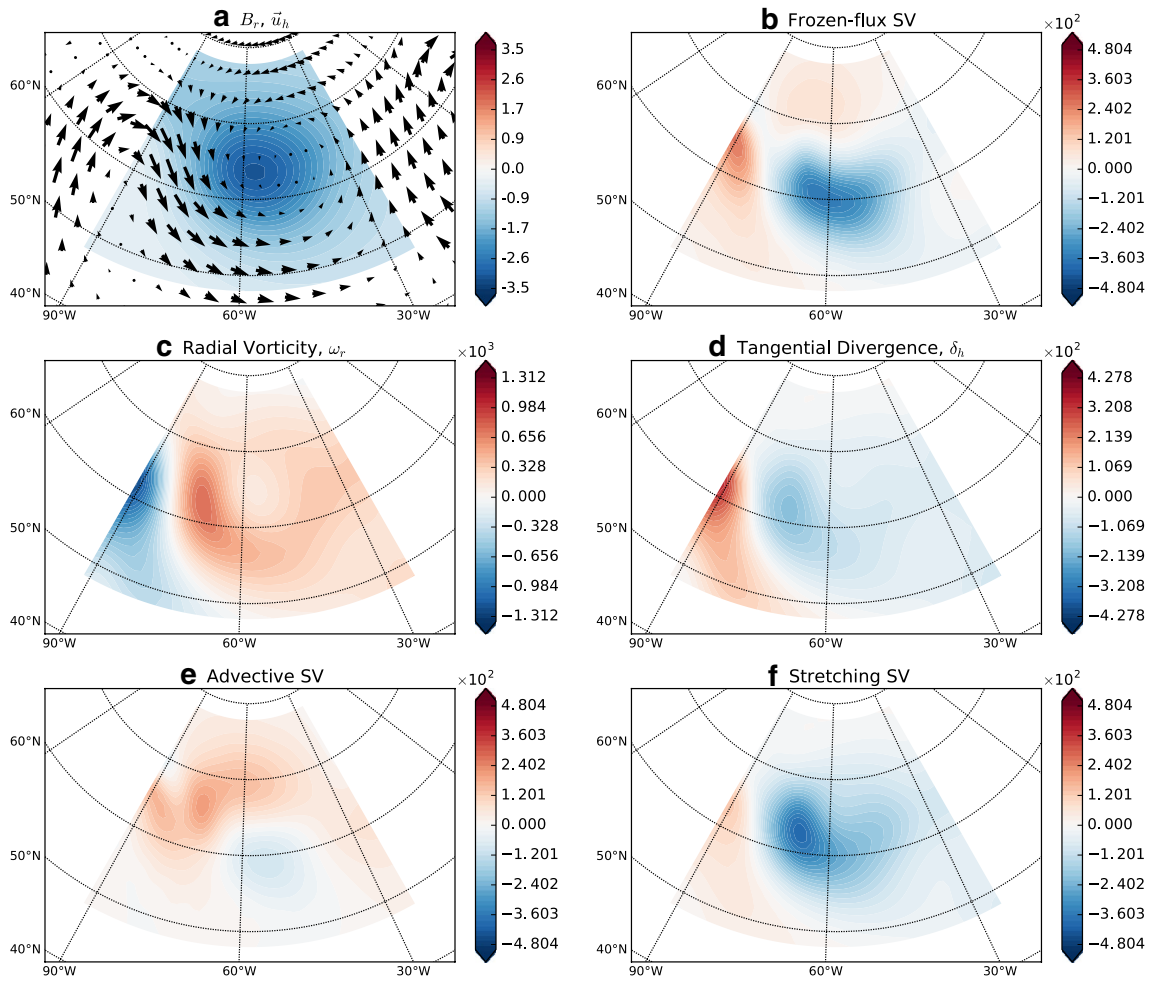

Fig. 2 Intense high-latitude normal polarity magnetic flux patch (HN) in dynamo model 4 (*upper polygon* in Fig. 1a). **a** Radial magnetic field B_r (*in colors*) and tangential velocity $\vec{u}_h$ (*black arrows*), **b** frozen-flux secular variation SV, **c** radial vorticity ω_r, **d** tangential divergence δ_h, **e** advective SV and **f** stretching SV. The local statistics for this patch are: St/Ad $= 2.01$; $\mathcal{P}/\mathcal{T} = 0.23$; $H_u = 0.97$; corr$(|B_r|, \delta_h^-) = 0.71$; corr$(|B_r|, \delta_h^+) = -0.36$; $\xi_a = 0.66$; $\xi_s = 0.80$; $\xi_e = 0.94$

of the patch (see Fig. 8e). In contrast, the downwelling structure exhibits a phase shift with the B_r patch resulting in a weak stretching (Fig. 8f) and thus an advective dominant SV.

In dynamo model 9 some intense normal polarity flux patches appear at low latitudes (LN). Figure 9 shows an LN (lower polygon in Fig. 7a). This patch is located west of an anti-clockwise vortex correlated with an upwelling structure (Fig. 9d). A large component of the flow is perpendicular to the B_r-contours and consequently, the advective SV efficiency is high. Stretching is less efficient due to the phase shift between the downwelling structure (Fig. 9d) and the intense flux patch. In this low-latitude intense flux patch, the stretching locally intensifies the magnetic field with an efficiency of $\xi_e = 0.88$.

Table 3 summarizes the global statistics of all snapshots from each dynamo simulation, while Table 4 summarizes the local statistics per patch type. In all models, both globally and for the patches, absolute magnetic flux is positively/negatively correlated with downwelling/upwelling, respectively. The best global correlation of absolute magnetic flux and downwelling is obtained in dynamo model 9 (Table 3). In dynamo model 4 for HN and LN the flux to downwelling correlations are highest, while LR has the best flux to downwelling correlation in dynamo model 3 (Table 4).

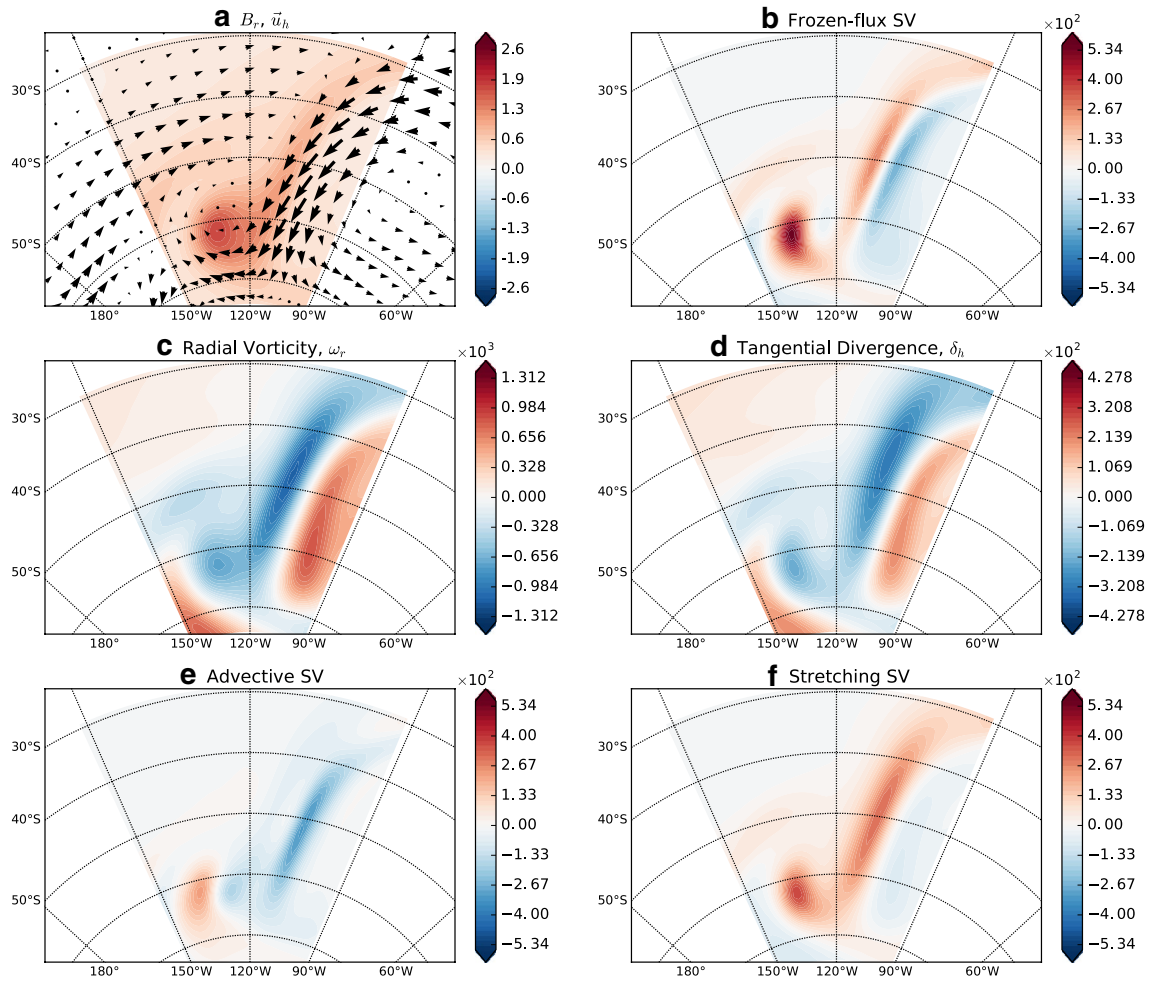

Fig. 3 As in Fig. 2 for another intense high-latitude normal polarity magnetic flux patch (HN) in dynamo model 4 (*lower polygon* in Fig. 1a). The statistics for this patch are: St/Ad = 1.23; $\mathcal{P}/\mathcal{T} = 0.28$; $H_u = 0.97$; corr($|B_r|, \delta_h^-$) = 0.74; corr($|B_r|, \delta_h^+$) = −0.47; $\xi_a = 0.67$; $\xi_s = 0.68$; $\xi_e = 0.87$

Parameters dependence

In order to examine more quantitatively the dependence of the statistical measures on the non-dimensional control parameters, we used a generic power law (23). The fitting parameters C, a, b and c were calculated using a conventional least-squared fit. Power law fits were applied for global and local measures.

The best fit for the global St/Ad ratio is given by

$$\mathrm{St/Ad} = 3.245 \cdot E^{-0.183} \cdot Ra^{-0.174} \cdot Pm^{-0.469} \tag{25}$$

with a relative misfit of $\sigma_r = 0.063$. In (25) the E and Ra powers are comparable, which motivates the following approximation:

$$\mathrm{St/Ad} \approx C \cdot (E \cdot Ra)^a \cdot Pm^c \tag{26}$$

The best fit of (26) is

$$\mathrm{St/Ad} \approx 3.508(E \cdot Ra)^{-0.172} \cdot Pm^{-0.482} \tag{27}$$

with $\sigma_r = 0.063$. Then (27) could be approximated in logarithmic scale as

$$\log(\mathrm{St/Ad}) \approx \log C - \frac{1}{6}\log(E\,Ra\,Pm^3) \tag{28}$$

Figure 10a confirms the similarity between the −0.152 slope of the fitted linear curve and the approximated power of $-\frac{1}{6}$ in (28). The parameter dependence of the global St/Ad is thus given by

$$\mathrm{St/Ad} \approx 2.996(E\,Ra\,Pm^3)^{-\frac{1}{6}} \tag{29}$$

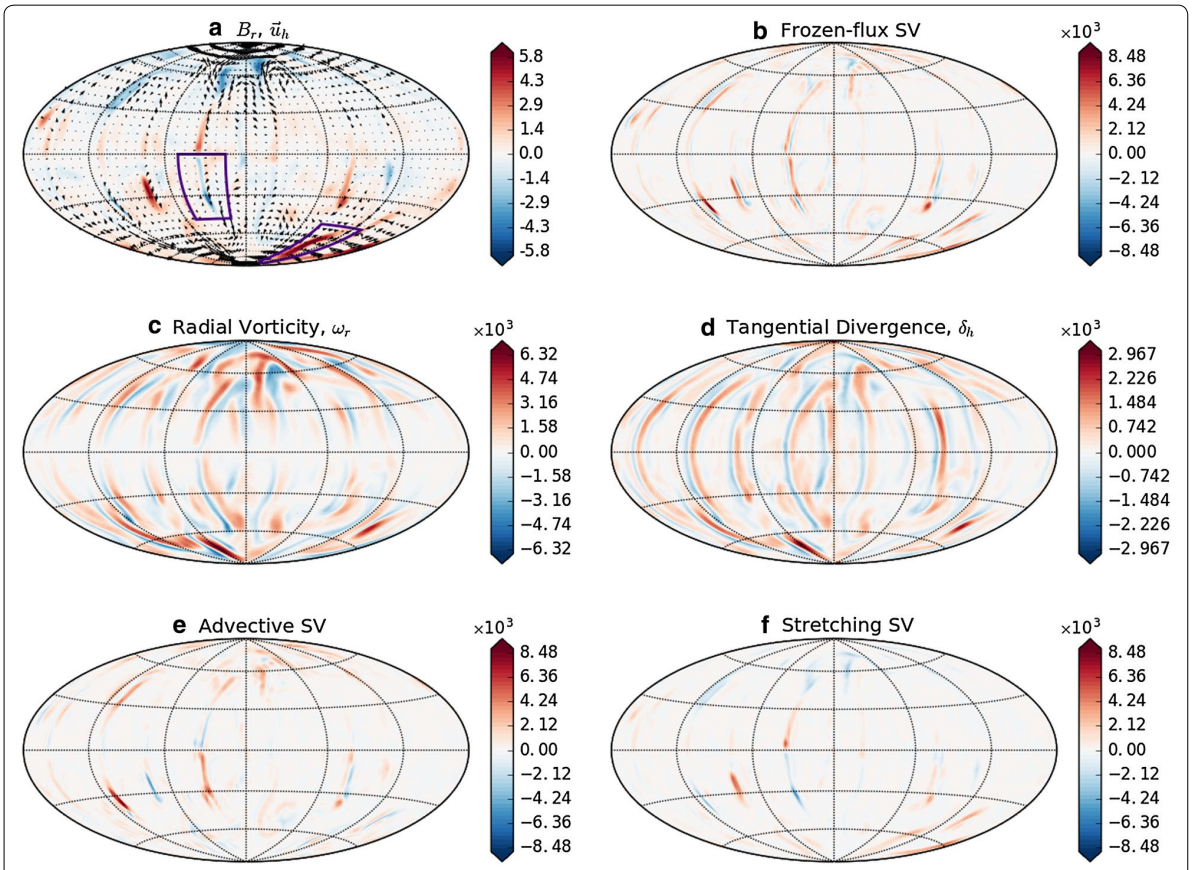

Fig. 4 As in Fig. 1 for a snapshot from model 6. The *upper* and *lower polygons* denote the zoom-in zones shown in Figs. 6 and 5, respectively. The statistics for this snapshot are: St/Ad = 0.75; $\mathcal{P}/\mathcal{T} = 0.39$; $H_u = 0.84$; corr$(|B_r|, \delta_h^-) = 0.42$; corr$(|B_r|, \delta_h^+) = -0.11$

Considering the modified Rayleigh number $Ra' = \frac{E \cdot Ra}{Pr}$ (e.g., Olson et al. 1999), and $Pr = 1$, Eq. (29) could be written as

$$\mathrm{St/Ad} \approx 2.996 (Ra' Pm^3)^{-\frac{1}{6}} \tag{30}$$

Globally, relative stretching in the dynamo models increases with increasing rotation (decreasing E), but decreases when convection (Ra) and electrical conductivity (Pm) increase. The dependence is strongest on Pm (30).

We followed a similar fitting process for the St/Ad ratio of HN. The parameter dependence of St/Ad of HN is given by (Fig. 10b)

$$\mathrm{St/Ad} \approx 10.489 (Ra' Pm^2)^{-\frac{1}{3}} \tag{31}$$

In qualitative agreement with the global case (Fig. 10a), relative stretching increases with rotation, but decreases when convection and electrical conductivity increase. In high-latitude normal intense flux patches (HN), relative stretching exhibits a strong dependence on Pm, but less than in global.

We also attempted to find power law fits for St/Ad of LN and LR, but no satisfactory fit (large σ_r) was found. The same holds for the other statistical quantities. Fits were therefore obtained for global and HN but not for LN and LR.

Next we fitted the global $\mathcal{P}/\mathcal{T}$ ratio. The best fit is

$$\mathcal{P}/\mathcal{T} = 0.373 \cdot E^{-0.002} \cdot Ra^{-0.008} \cdot Pm^{0.153} \tag{32}$$

with $\sigma_r = 0.021$. The Pm power is dominant, motivating

$$\mathcal{P}/\mathcal{T} \approx 0.321 Pm^{0.175} \tag{33}$$

with $\sigma_r = 0.022$. Then (33) may be approximated in logarithmic scale as

$$\log(\mathcal{P}/\mathcal{T}) \approx \log C + \frac{1}{6} \log(Pm) \tag{34}$$

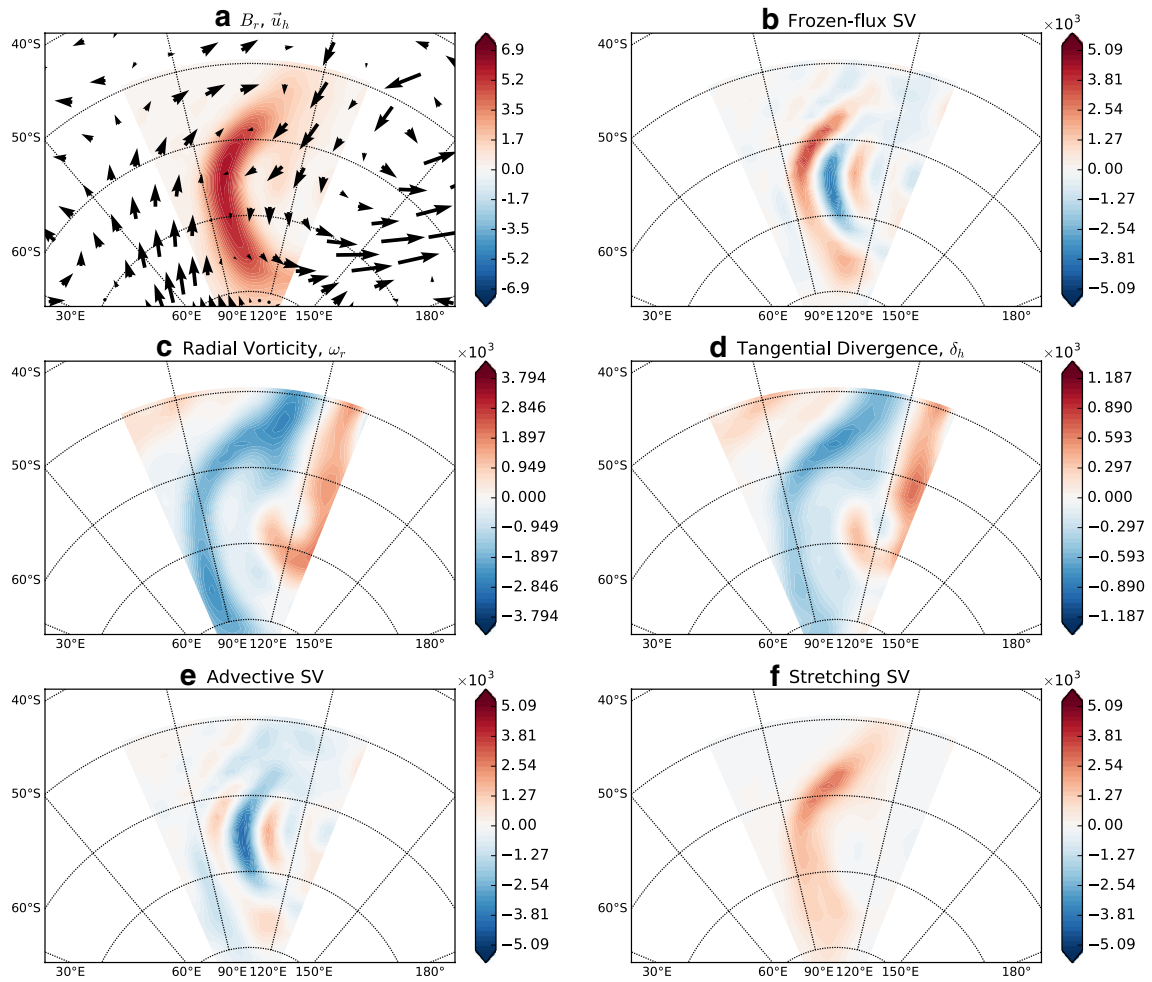

Fig. 5 As in Fig. 2 for an intense high-latitude normal polarity flux patch (HN) in dynamo model 6 (*lower polygon* in Fig. 4a). The statistics for this patch are: St/Ad = 0.87; $\mathcal{P}/\mathcal{T} = 0.27$; $H_u = 0.95$; corr($|B_r|, \delta_h^-$) = 0.58; corr($|B_r|, \delta_h^+$) = −0.28; $\xi_a = 0.61$; $\xi_s = 0.88$; $\xi_e = 0.98$

The 0.179 slope in Fig. 11a well approximates the $-\frac{1}{6}$ prediction in (34). Then, the parameter dependence of global $\mathcal{P}/\mathcal{T}$ is approximated by

$$\mathcal{P}/\mathcal{T} \approx 0.319 Pm^{\frac{1}{6}} \tag{35}$$

Globally, the relative poloidal flow is mostly influenced by *Pm*, increasing with increasing electrical conductivity.

We followed similar fitting process for the $\mathcal{P}/\mathcal{T}$ ratio of HN. The parameter dependence of $\mathcal{P}/\mathcal{T}$ in HN is given by (Fig. 11b)

$$\mathcal{P}/\mathcal{T} \approx 0.261 Pm^{\frac{1}{6}} \tag{36}$$

In HN, the relative poloidal flow also increases when electrical conductivity increases.

We also attempted to fit the global and local H_u ratio. In both cases, we found much lower powers than in (30), (31), (35) and (36), indicating that the parameter dependence of H_u is weak. We therefore do not plot this parameter dependence.

The St/Ad ratio is a good measure of the stretching influence in the SV, but it is not enough to measure the stretching efficiency. In Fig. 12 we compare the St/Ad and the $\mathcal{P}/\mathcal{T}$ ratios, globally and locally (HN, LN and LR). Although poloidal flow is necessary to produce stretching, Fig. 12a shows that global St/Ad is larger than global

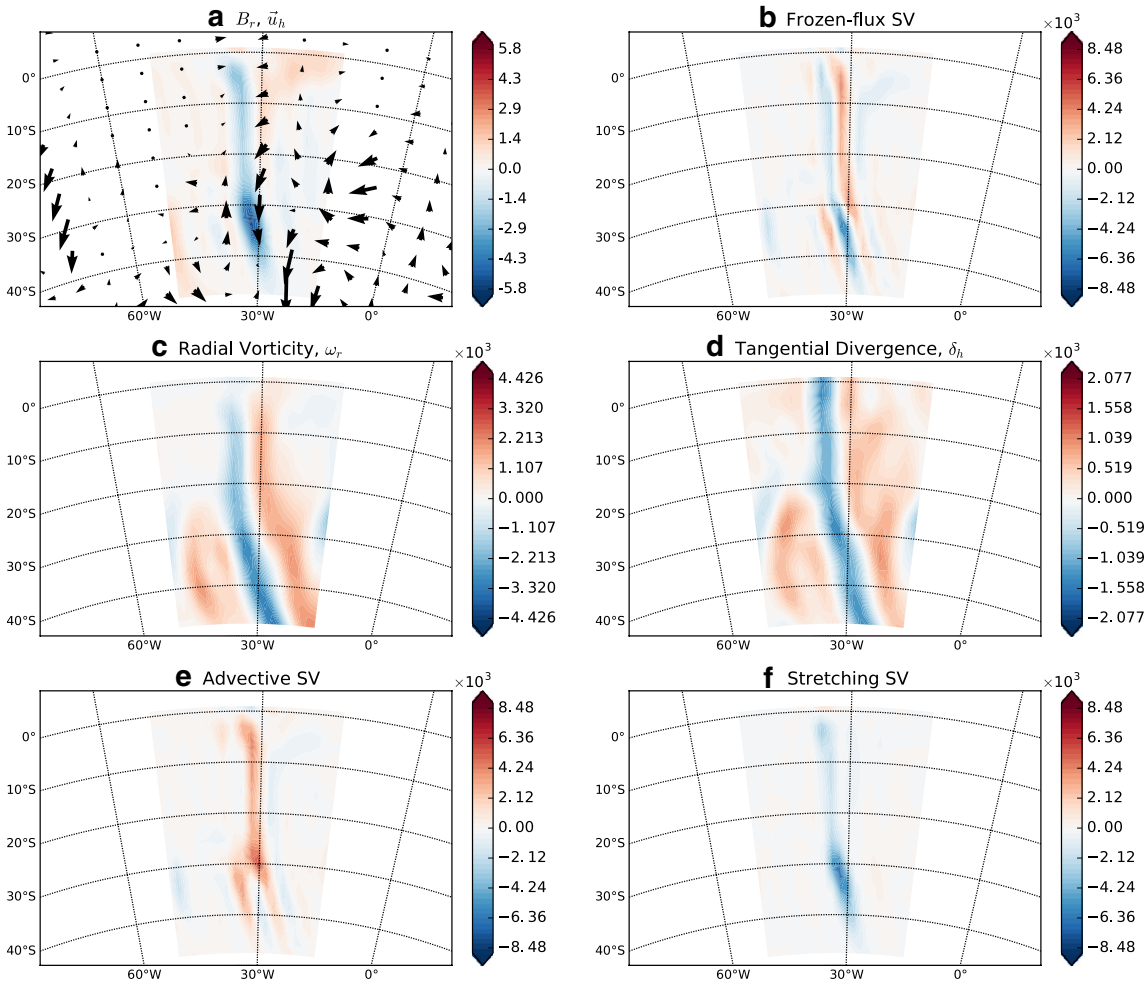

Fig. 6 As in Fig. 2 for an intense low-latitude reversed polarity flux patch (LR) in dynamo model 6 (*upper polygon* in Fig. 4a). The statistics for this patch are: St/Ad = 0.83; $\mathcal{P}/\mathcal{T} = 0.56$; $H_u = 0.83$; corr($|B_r|, \delta_h^-$) = 0.70; corr($|B_r|, \delta_h^+$) = −0.18; $\xi_a = 0.48$; $\xi_s = 0.80$; $\xi_e = 0.87$

$\mathcal{P}/\mathcal{T}$ except for the large *Pm* case 2 where the two quantities are nearly identical. The larger St/Ad is an evidence for the presence of an important stretching contribution even when the toroidal flow dominates. Locally, HN shares the global behavior with even larger difference between the values of St/Ad and $\mathcal{P}/\mathcal{T}$ (Fig. 12b). In all dynamo models St/Ad is larger in HN than in global despite $\mathcal{P}/\mathcal{T}$ being smaller in HN than in global, evidence for the particularly high stretching efficiency in HN. LN exhibits higher values of $\mathcal{P}/\mathcal{T}$ in some of dynamo models but in most models St/Ad is larger (Fig. 12c). LR exhibits an opposite behavior: $\mathcal{P}/\mathcal{T}$ is larger in most models (Fig. 12d). In addition, the $\mathcal{P}/\mathcal{T}$ values in LR are significantly larger than in global or in the other patch types.

Figure 13 shows the efficiency of advection ξ_a and stretching ξ_s in each intense B_r patch type. In all dynamo models the stretching appears more efficient than the advection. The highest efficiency is found in all dynamo models for the magnetic flux intensification ξ_e.

Discussion

Globally, in our dynamo models stretching varies between half to comparable of advection SV, whereas the toroidal flow is 2–3 times larger than the poloidal flow (Table 3). Locally, stretching may dominate SV in field-aligned flow regions where advection is not effective. Such stretching dominance is found at high-latitude normal polarity flux patches in some dynamo models. The

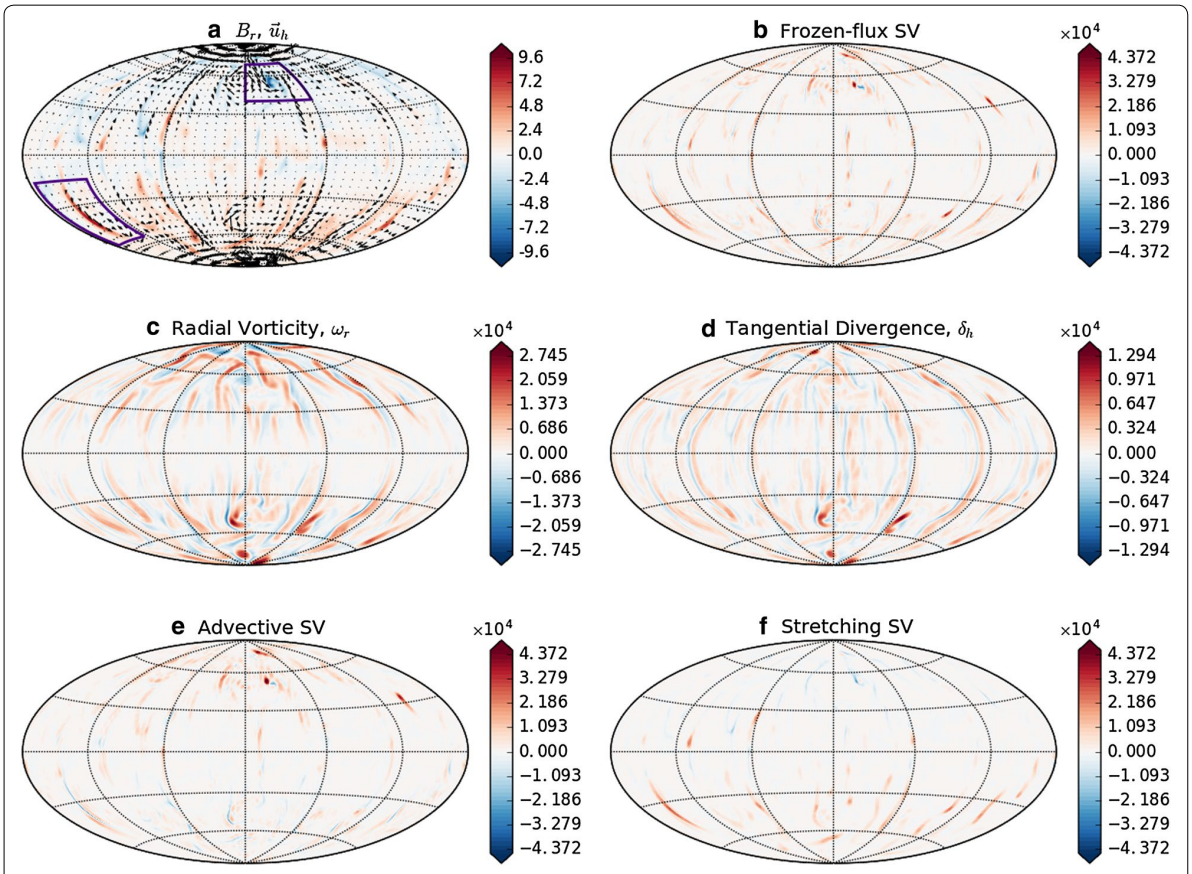

Fig. 7 As in Fig. 1 for a snapshot from model 9. The *upper* and *lower polygons* denote the zoom-in zones shown in Figs. 8 and 9, respectively. The statistics for this snapshot are: St/Ad = 0.67; $\mathcal{P}/\mathcal{T} = 0.37$; $H_u = 0.83$; corr$(|B_r|, \delta_h^-) = 0.43$; corr$(|B_r|, \delta_h^+) = -0.13$

stretching contribution varies depending on the patch type. On average, stretching to advective SV RMS ratio in HN is 0.82, whereas the poloidal to toroidal flow RMS ratio is only 0.32 (Fig. 12b; Table 4), i.e., St/Ad $> \mathcal{P}/\mathcal{T}$ and hence stretching is much more efficient than advection in these patches. Stretching is also more efficient than advection in LN, though to a lesser extent (St/Ad is 0.61, whereas $\mathcal{P}/\mathcal{T}$ is 0.49 on average, Fig. 12c; Table 4). In contrast, stretching to advective SV RMS ratio in LR is 0.68, and the poloidal to toroidal flow RMS ratio is 0.72 (Fig. 12d; Table 4), so advection and stretching are comparably efficient in regions of reversed flux patches at low latitudes.

The magnetic field in our models is generated by the α -dynamo mechanism via a helical flow (Olson et al. 1999). The surface expression of this process is a high correlation between tangential divergence and radial vorticity, providing a useful way to couple toroidal and poloidal motions at the top of the shell (Olson et al. 2002; Amit and Olson 2004). In our dynamo models, helical flow is a very good approximation (correlations of 0.78–0.87, see Table 3). The helical flow approximation is especially applicable at high latitudes where axial convective columns impinge the CMB (Amit et al. 2010, Table 4).

Positive/negative correlations of magnetic flux with downwelling/upwelling, respectively, indicate that the magnetic field is concentrated by downwelling (Christensen et al. 1998) and dispersed by upwelling (Olson and Aurnou 1999). Moderate correlations appear because as downwellings are advected, magnetic field structures persist and diffuse slowly (Amit et al. 2010) causing a phase shift between the field concentrations and the cyclones that maintain them (Olson and Christensen 2002; Aubert et al. 2007; Takahashi et al. 2008).

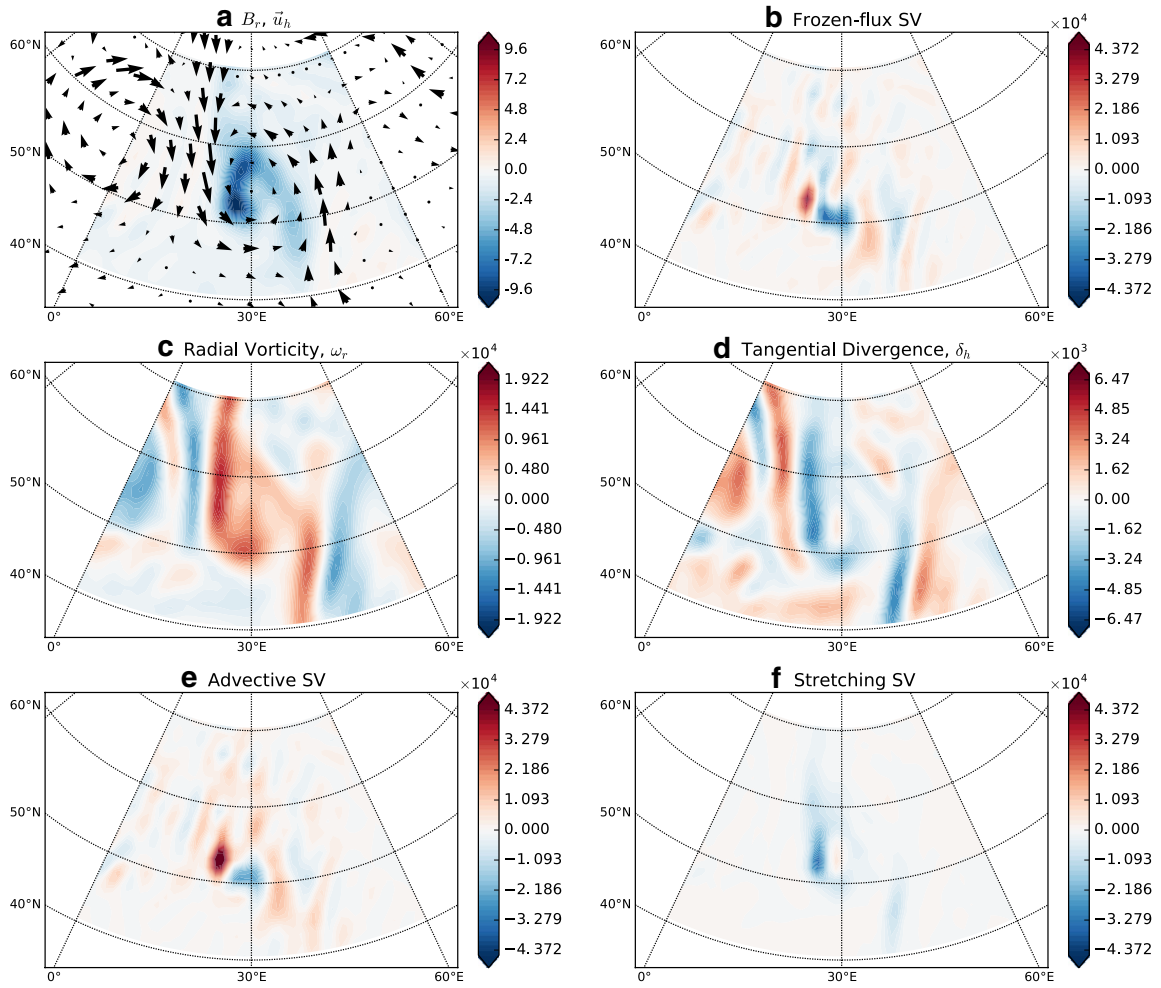

Fig. 8 As in Fig. 2 for a high-latitude normal flux patch (HN) in dynamo model 9 (*upper polygon* in Fig. 7a). The statistics for this patch are: $St/Ad = 0.62$; $\mathcal{P}/\mathcal{T} = 0.23$; $H_u = 0.88$; $\mathrm{corr}(|B_r|, \delta_h^-) = 0.40$; $\mathrm{corr}(|B_r|, \delta_h^+) = -0.24$; $\xi_a = 0.37$; $\xi_s = 0.73$; $\xi_e = 0.91$

The level of cancellation of the SV structures at high-latitude normal polarity flux patches shows that stretching is more efficient than advection (Fig. 13a). This results in a highly effective local magnetic flux intensification by stretching ($\xi_e = 0.9$ on average). In LN, the efficiency of stretching and advective structures as well as the stretching efficiency to locally intensify the magnetic flux in these patches are lower (Fig. 13b). The advective bipolar structures seen in LR are more balanced (hence the lowest ξ_a value) and the intensification of the magnetic field by stretching is less effective than at other patch types ($\xi_e = 0.66$ on average).

Globally, relative stretching increases with increasing rotation, but decreases when convection and electrical conductivity increase, with the strongest dependence being on *Pm* (Fig. 10a). The relative global poloidal flow is also influenced by *Pm*, increasing with increasing electrical conductivity. The helical flow correlation H_u depends on *Pm* and *Ra* (stronger dependence on *Pm*). However, the much lower powers of H_u compared to the powers of the St/Ad and $\mathcal{P}/\mathcal{T}$ fits indicate that its parameter dependence is much weaker.

It is tempting to insert Earth-like control parameters to our power laws. This yields stretching that is much larger

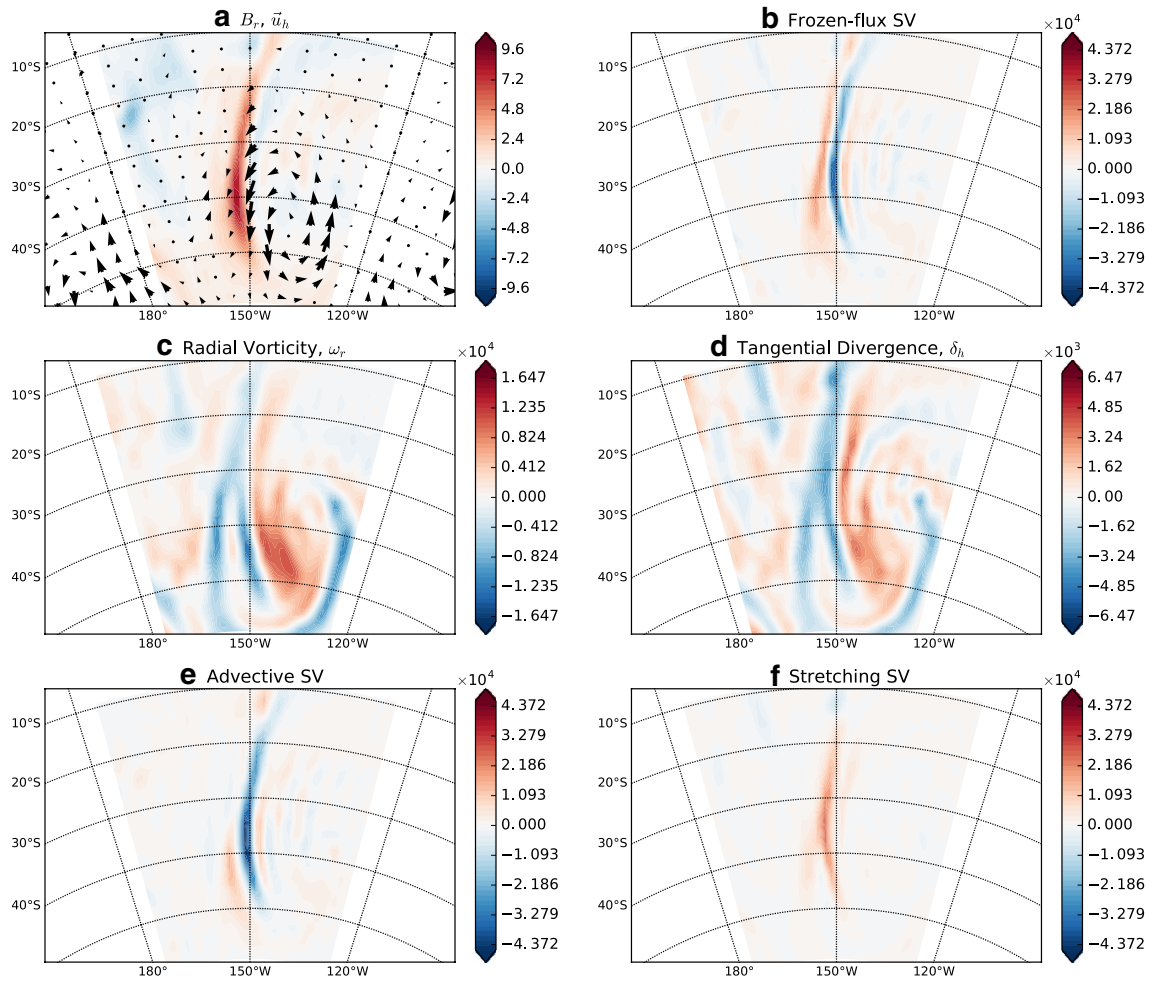

Fig. 9 As in Fig. 2 for a low-latitude normal flux patch (LN) in dynamo model 9 (*lower polygon* in Fig. 7a). The statistics for this patch are: St/Ad $= 0.54$; $\mathcal{P}/\mathcal{T} = 0.43$; $H_u = 0.87$; corr $(|B_r|, \delta_h^-) = 0.56$; corr $(|B_r|, \delta_h^+) = -0.22$; $\xi_a = 0.44$; $\xi_{str} = 0.78$; $\xi_e = 0.88$

(by two orders of magnitude) than advective SV. This is obviously unrealistic and may result from the small number of dynamo models studied which led to a poor extrapolation. Nevertheless, qualitatively we may hypothesize that stretching at the top of Earth's core is even stronger than in our dynamo models.

Conventional magnetic Reynolds number estimates might not represent the induction accurately because field–flow interactions are not considered. The $\cos\gamma$ values in Table 5, which represent the level of field-aligned flow, are in agreement with the values found by Finlay and Amit (2011). This means that the advective effective magnetic Reynolds number Rm_a is about 30 % lower than the conventional Rm. The stretching effective magnetic Reynolds number Rm_s varies between half to one Rm_a. Finally, Rm_e, which combines the effective advective and stretching magnetic Reynolds numbers, is about two-thirds of the conventional Rm (Table 5). This 50 % increase is the level of overestimation of the magnetic Reynolds number when field–flow interactions are ignored for both advection and stretching.

We note that surprisingly the two quantities $\cos\gamma$ and ξ_{Rm} are very similar (Table 5). Our synthetic tests of these quantities clearly show that there is no apparent

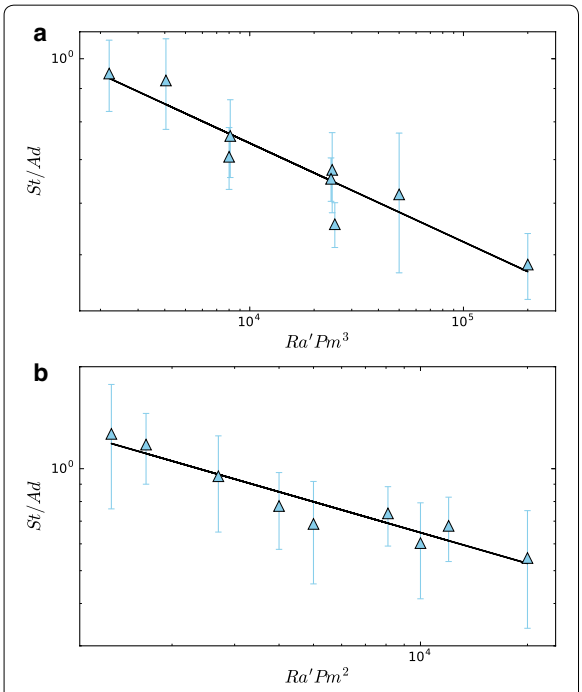

Fig. 10 Stretching/Advection RMS ratio parameter dependence. Each *point* represents the **a** global mean value and **b** HN mean value of each dynamo simulation. *Error bars* represent time-dependence

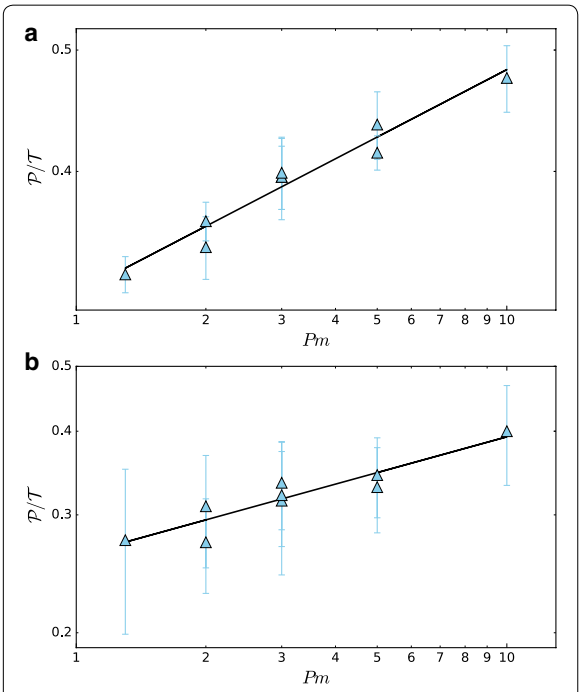

Fig. 11 Poloidal/toroidal flow RMS ratio parameter dependence. Each *point* represents the **a** global mean value and **b** HN mean value of each dynamo simulation. *Error bars* represent time-dependence

reason for this similarity (Table 2). This suggests that the particular field–flow interactions in the dynamo models produce same field–flow alignment (represented by $\cos\gamma$) and advection/stretching interference (represented by ξ_{Rm}). The intermediate $\cos\gamma$ values arise from low contributions at high latitudes where the flow is nearly aligned with the radial field, balanced by large contributions at low latitudes where the flow is nearly perpendicular to the radial field (Finlay and Amit 2011). The intermediate ξ_{Rm} values stem from the nearly non-correlated advection and stretching SV patterns. Indeed, for RMS ratio St/Ad $\sim$ 0.5–1 the purely non-correlated relation gives $\sim$0.7–0.75, while some overlap introduces some anti-correlation with lower ξ_{Rm} contributions (see expressions after 21). At the moment, however, the precise reason for this similarity between $\cos\gamma$ and ξ_{Rm} in the dynamo models is still unknown to us.

Resemblance between the stretching signature in our dynamo models and local geomagnetic SV structures may provide some evidence for the existence of stretching and hence upwelling/downwelling at the top of the Earth's core. We find same sign radial field and stretching SV signatures in zones of intense flux patches (see Figs. 2, 3, 5, 6, 8, 9). Amit (2014) found same sign persistent radial field and total SV below the Indian Ocean. In the same region, studies of geomagnetic field models identified formation of flux patches (Jackson et al. 2000; Finlay and Jackson 2003) and studies of core flow models reported strong poloidal flows (e.g., Amit and Pais 2013; Baerenzung et al. 2016). Overall, local morphological similarities between stretching SV in our dynamo models and total SV in the geomagnetic field (Amit 2014) may suggest that the whole of the outer core convects.

Naively it may be expected that the role of stretching would be represented by the relative size of poloidal flow. However, we found that the global ratio of RMS stretching to RMS advection is systematically larger than the ratio of RMS poloidal flow to RMS toroidal flow. The

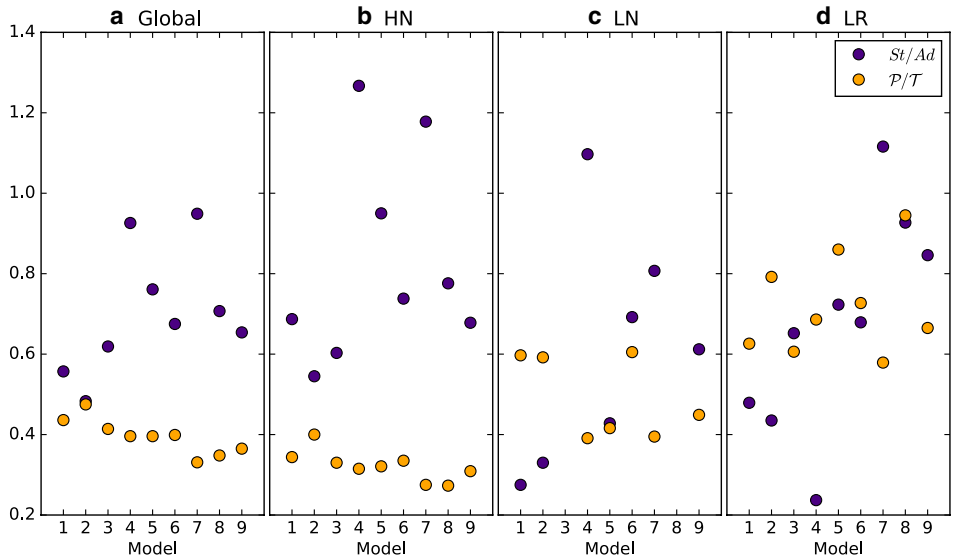

Fig. 12 St/Ad and $\mathcal{P}/\mathcal{T}$ ratios: **a** Global, **b** HN, **c** LN, and **d** LR for each dynamo model. No intense LN patches were detected in the snapshots of dynamo models 3 and 8

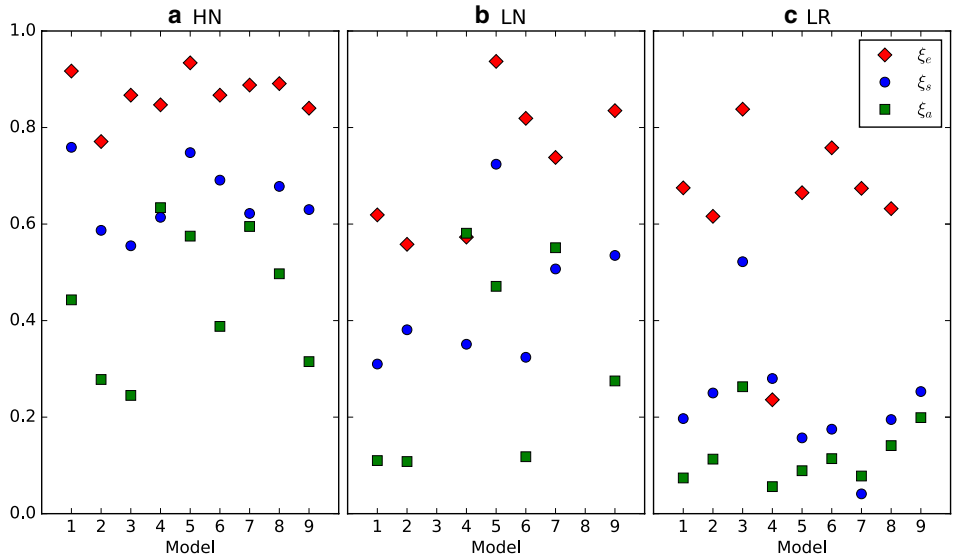

Fig. 13 Advective ξ_a and stretching ξ_s efficiency and magnetic field intensification ξ_{e^*} **a** HN, **b** LN, **c** LR for each dynamo model. No intense LN patches were detected in the snapshots of dynamo models 3 and 8

Table 5 Alternative *Rm* numbers

Model	cos γ	Rm_a	Rm_s	ξ_{Rm}	Rm_e	Rm
1	0.65	88.37	49.22	0.65	89.98	137
2	0.65	166.77	80.55	0.68	167.44	255
3	0.66	146.20	89.88	0.66	155.15	219
4	0.59	48.71	45.10	0.59	55.44	82
5	0.64	79.88	60.78	0.61	86.51	125
6	0.66	155.15	104.72	0.65	169.17	234
7	0.64	80.01	75.93	0.60	93.72	126
8	0.65	140.70	100.18	0.63	151.66	218
9	0.66	294.81	192.80	0.66	321.33	446

cos γ is the field–flow alignment factor. Rm_a and Rm_s are the advective and stretching effective magnetic Reynolds numbers, respectively. The effective magnetic Reynolds number Rm_e was calculated using the advection/stretching interference factor ξ_{Rm}. For comparison the conventional Rm number is reproduced from Table 1

larger relative stretching than relative poloidal flow is even more pronounced at zones of high-latitude normal polarity intense flux patches. In these regions the toroidal flow is often aligned with B_r-contours and hence it produces little advection (Finlay and Amit 2011). In contrast, downwelling is often correlated with these patches, rendering stretching efficient in concentrating and maintaining these robust features. Lesur et al. (2015) argued that the geomagnetic SV requires weak poloidal flow, which led them to conclude that the top of the core is weakly stratified. According to our dynamo models, even if the poloidal flow is weak stretching SV may be significant in the kinematics at the top of the core.

Authors' contributions

HA ran the dynamo simulations. DP analyzed the models' output, produced the graphics, calculated the statistics and wrote the paper. All authors read and approved the final manuscript.

Author details

[1] Geophysics Department, Observatório Nacional, CEP: 20921-400 Rio de Janeiro, Brazil. [2] Laboratoire de Planétologie et de Géodynamique, UMR CNRS 6112, Nantes Atlantiques Universités, Université de Nantes, CNRS, 2 rue de la Houssinière, 44000 Nantes, France.

Acknowledgements

We thank two anonymous reviewers for constructive comments that improved the paper. This study was supported by the Centre National d'Etudes Spatiales (CNES). D.P. was supported by a Ph.D. research grant from Coordenação de Aperfeiçoamento de Pessoal de Nível Superior (CAPES) and a grant by LPG-Nantes. K.P. was supported by la Région des Pays de la Loire and Coordenação de Aperfeiçoamento de Pessoal de Nível Superior (CAPES- Proc no BEX 2498/13-8).

Competing interests

We confirm that we read SpringerOpen's guidance on competing interests. We declare that none of the authors have any competing interests in the manuscript.

Appendix: Variables

See Table 6.

Table 6 Variables used in this paper

Symbol	Meaning
$\vec{u}$	Velocity
$\vec{B}$	Magnetic field
t	Time
P	Pressure
T	Temperature (or co-density)
ϵ	Heat (or buoyancy) source or sink
Ra	Rayleigh number
E	Ekman number
Pr	Prandtl number
Pm	Magnetic Prandtl number
Rm	Magnetic Reynolds number
Rm_a	Effective advective magnetic Reynolds number
Rm_s	Effective stretching magnetic Reynolds number
Rm_e	Effective magnetic Reynolds number
α	Thermal expansivity
g_o	Gravitational acceleration on the outer boundary at radius r_o
q_o	Mean heat flux across the outer boundary
D	Shell thickness
k	Thermal conductivity
κ	Thermal diffusivity
ν	Kinematic viscosity
Ω	Rotation rate
λ	Magnetic diffusivity
U	Typical velocity scale
L	Typical length scale
$\hat{z}$	Unit vector in the direction of the rotation axis
r	Radial coordinate
$\hat{r}$	Unit vector in the radial direction
$\vec{r}$	Position vector
r_o	Earth's core radius
r_e	Radial level at which the simulations were analyzed
$\bar{\delta\tau}$	Average time difference between snapshots in units of magnetic advection time

Table 6 continued

Symbol	Meaning
B_r	Radial component of the magnetic field on the CMB
$\vec{u}_h$	2D velocity vector tangent to the CMB spherical surface
St/Ad	Ratio of stretching RMS to advection RMS
$\mathcal{P}/\mathcal{T}$	Ratio of poloidal flow RMS to toroidal flow RMS
δ_h	Tangential divergence
ω_r	Radial vorticity
H_u	Helical flow correlation
δ_h^-	Downwelling process ($\delta_h < 0$)
δ_h^+	Upwelling process ($\delta_h > 0$)
ξ_a	Normalized integrated advective
ξ_s	Normalized integrated stretching
ξ_e	Normalized integrated magnetic field intensification by stretching
γ	Angle between the vectors $\vec{u}_h$ and $\nabla_h B_r$
cos γ	Field–flow alignment factor
ξ_{Rm}	Advection/stretching interference factor
f	Statistical quantity
C, a, b, c	Generic power law fitting coefficients
σ_r	Relative misfit of the power law
f^{dyn}	Statistical quantity in dynamo models
n	Number of dynamo models analyzed
$\mathcal{T}_1$	Large-scale degree-1 toroidal synthetic flow
$\mathcal{P}_1$	Large-scale degree-1 poloidal synthetic flow

Received: 11 January 2016 Accepted: 21 April 2016
Published online: 14 May 2016

References

Amit H (2014) Can downwelling at the top of the earth's core be detected in the geomagnetic secular variation? Phys Earth Planet Int 229:110–121
Amit H, Aubert J, Hulot G (2010) Stationary, oscillating or drifting mantle-driven geomagnetic flux patches? J Geophys Res 115(B7):1978–2012
Amit H, Christensen UR (2008) Accounting for magnetic diffusion in core flow inversions from geomagnetic secular variation. Geophys J Int 175(3):913–924
Amit H, Olson P (2004) Helical core flow from geomagnetic secular variation. Phys Earth Planet Int 147:1–25
Amit H, Olson P, Christensen UR (2007) Tests of core flow imaging methods with numerical dynamos. Geophys J Int 168:27–39
Amit H, Pais MA (2013) Differences between tangential geostrophy and columnar flow. Geophys J Int 194(1):145–157
Aubert J, Amit H, Hulot G (2007) Detecting thermal boundary control in surface flows from numerical dynamos. Phys Earth Planet Int 160:143–156
Aubert J, Amit H, Hulot G, Olson P (2008b) Thermochemical flows couple the earth's inner core growth to mantle heterogeneity. Nature 454(7205):758–761
Aubert J, Aurnou J, Wicht J (2008a) The magnetic structure of convection-driven numerical dynamos. Geophys J Int 172(3):945–956
Aubert J, Finlay CC, Fournier F (2013) Bottom up control of geomagnetic secular variation by the earth's inner core. Nature 502:219–223
Baerenzung J, Holschneider M, Lesur V (2016) The flow at the earth's core–mantle boundary under weak prior constraints. J Geophys Res doi:10.1002/2015JB012464
Bloxham J (1986) The expulsion of magnetic flux from the earth's core. Geophys J R Astr Soc 87:669–678
Bloxham J, Jackson A (1991) Fluid flow near the surface of earth's outer core. Rev Geophys 29(1):97–120
Buffett B (2014) Geomagnetic fluctuations reveal stable stratification at the top of the earth's core. Nature 507(7493):484–487
Christensen UR (2006) A deep dynamo generating Mercury's magnetic field. Nature 444:1056–1058
Christensen UR, Aubert J (2006) Scaling properties of convection-driven dynamos in rotating spherical shells and application to planetary magnetic fields. Geophys J Int 166:97–114
Christensen UR, Aubert J, Hulot G (2010) Conditions for earth-like geodynamo models. Earth Planet Sci Lett 296(3):487–496
Christensen UR, Olson P (2003) Secular variation in numerical geodynamo models with lateral variations of boundary heat flow. Phys Earth Planet Int 138(1):39–54
Christensen UR, Olson P, Glatzmaier G (1998) A dynamo model interpretation of geomagnetic field structures. Geophys Res Lett 25(10):1565–1568
Christensen UR, Wicht J (2007) Numerical dynamo simulations. In: Olson P (ed) Treatise on geophysics, vol 8. Elsevier Science, Amsterdam, pp 245–282
Chulliat A, Hulot G, Newitt LR (2010) Magnetic flux expulsion from the core as a possible cause of the unusually large acceleration of the north magnetic pole during the 1990s. J Geophys Res 115(B7):1978–2012
Chulliat A, Olsen N (2010) Observation of magnetic diffusion in the earth's outer core from magsat, Ørsted, and champ data. J Geophys Res doi:10.1029/2009JB006994
de Koker N, Steinle-Neumann G, Vlcek V (2012) Electrical resistivity and thermal conductivity of liquid fe alloys at high p and t, and heat flux in earth's core. Proc Natl Acad Sci USA 109(11):4070–4073
Finlay CC (2008) Historical variation of the geomagnetic axial dipole. Phys Earth Planet Int 170(1–2):1–14
Finlay CC, Amit H (2011) On flow magnitude and field flow alignment at earth's core surface. Geophys J Int 186:175–192
Finlay CC, Jackson A (2003) Equatorially dominated magnetic field change at the surface of earth's core. Science 300(5628):2084–2086
Finlay CC, Maus S, Beggan CD, Bondar TN, Chambodut A, Chernova TA, Chulliat A, Golovkov VP, Hamilton B, Hamoudi M, Holme R, Hulot G, Kuang W, Langlais B, Lesur V, Lowes FJ, Løhr H, Macmillan S, Mandea M, McLean S, Manoj C, Menvielle M, Michaelis I, Olsen N, Rauberg J, Rother M, Sabaka TJ, Tangborn A, Tøffner-Clausen L, Thébault E, Thomson AWP, Wardinski I, Wei Z, Zvereva TI (2010) International geomagnetic reference field: the eleventh generation. Geophys J Int 183(3):1216–1230
Gillet N, Pais MA, Jault D (2009) Ensemble inversion of time dependent core flow models. Geochem Geophys Geosyst 10:Q06004. doi:10.1029/2008GC002290
Gubbins D (2003) Thermal core–mantle interactions: theory and observations. In: Dehant V, Creager KC, Karato SI, Zatman S (eds) Earth's core: dynamics, structure, rotation. American Geophysical Union, Washington, DC, pp 163–179
Gubbins D, Davies CJ (2013) The stratified layer at the core–mantle boundary caused by barodiffusion of oxygen, sulphur and silicon. Phys Earth Planet Int 215:21–28
Hartmann GA, Pacca IG (2009) Time evolution of the South Atlantic magnetic anomaly. Ann Acad Bras Ciênc 81(2):243–255
Helffrich G, Kaneshima S (2010) Outer-core compositional stratification from observed core wave speed profiles. Nature 468:807–810
Holme R (2007) Large-scale flow in the core, Ch. 4. In: Olson P (ed) Treatise on geophysics, vol 8. Elsevier Science, Amsterdam, pp 107–130
Holme R, Olsen N, Bairstow FL (2011) Mapping geomagnetic secular variation at the core–mantle boundary. Geophys J Int 186(2):521–528
Jackson A, Jonkers ART, Walker MR (2000) Four centuries of geomagnetic secular variation from historical. Philos Trans R Soc Lond A 358(1768):957–990
Kutzner C, Christensen UR (2002) From stable dipolar towards reversing numerical dynamos. Phys Earth Planet Int 131(1):29–45
Lesur V, Whaler K, Wardinski I (2015) Are geomagnetic data consistent with stably stratified flow at the core–mantle boundary? Geophys J Int. 201:929–946
Mininni PD (2011) Scale interactions in magnetohydrodynamic turbulence. Ann Rev Fluid Mech 43:377–397
Moffatt HK (1978) Magnetic field generation in electrically conducting fluids. Cambridge University Press, London, New York, Melbourne

Olsen N, Lühr H, Finlay CC, Sabaka T, Michaelis I, Rauberg J, Toffner-Clausen L (2014) The chaos-4 geomagnetic field model. Geophys J Int 197(2):815–827
Olsen N, Mandea M (2008) Rapidly changing flows in the earth's core. Nat Geosci 1(6):390–394
Olson P, Amit H (2006) Changes in earth's dipole. Naturwissenschaften 93(11):519–542
Olson P, Aurnou J (1999) A polar vortex in the earth's core. Nature 402(6758):170–173
Olson P, Christensen UR (2002) The time averaged magnetic field in numerical dynamos with non uniform boundary heat flow. Geophys J Int 151(3):809–823
Olson P, Christensen UR, Glatzmaier GA (1999) Numerical modeling of the geodynamo: Mechanisms of field generation and equilibration. J Geophys Res 104(B5):10383–10404
Olson P, Sumita I, Aurnou J (2002) Diffusive magnetic images of upwelling patterns in the core. J Geophys Res 107(B12):801–813
Pais MA, Jault D (2008) Quasi-geostrophic flows responsible for the secular variation of the earth's magnetic field. Geophys J Int 173(2):421–443
Pozzo M, Davies C, Gubbins D, Alfe D (2012) Thermal and electrical conductivity of iron at earth's core conditions. Nature 485(7398):355–358
Roberts PH, Scott S (1965) On analysis of the secular variation, 1, a hydromagnetic constraint: theory. J Geomagn Geoelectr 17:137–151
Takahashi F, Matsushima M, Honkura Y (2008) Scale variability in convection-driven MHD dynamos at low Ekman number. Phys Earth Planet Int 167:168–178
Takehiro S, Lister JR (2001) Penetration of columnar convection into an outer stably stratified layer in rapidly rotating spherical fluid shells. Earth Planet Sci Lett 187(3–4):357–366
Whaler K (1980) Does the whole of the earth's core convect? Nature 287(5782):528–530
Whaler K, Holme R (2007) Consistency between the flow at the top of the core and the frozen-flux approximation. Earth Planets Space 59:1219–1229
Wicht J (2002) Inner-core conductivity in numerical dynamo simulations. Phys Earth Planet Int 132:281–302
Zhang P, Cohen R, Haule K (2015) Effects of electron correlations on transport properties of iron at earth's core conditions? Nature 517:605–607